Acoustical Physics, Vol. 47, No. 2, 2001, pp. 115–139. Translated from Akusticheskiĭ Zhurnal, Vol. 47, No. 2, 2001, pp. 149–177.

REVIEWS

Acoustics of Shells[1]

H. Überall

Department of Physics, Catholic University of America, Washington, DC 20064, USA

Received May 25, 2000

Abstract—We discuss the physical phenomena that arise in the scattering of acoustic waves from fluid-immersed elastic (metal) shells which may be either evacuated or filled with the same or with a different fluid. The phenomena occurring here include the formation of circumferential (peripheral, or "surface") waves that circumnavigate the shells, propagating either as elastic waves in the shell material or as fluid-borne waves of the Scholte–Stoneley type in the external or the internal fluid. By phase matching along a closed circuit, these waves may lead to prominent resonances in the acoustic scattering amplitude, and we demonstrate how the set of observed resonance frequencies is related to the dispersive phase velocities of the surface waves, so that one can be determined from the other. In addition, we discuss how the dispersion curves (phase velocity plotted vs. frequency) of the various types of surface waves show repulsion phenomena due to their coupling through the boundary conditions. The cases of spherical and cylindrical shells are investigated here as typical examples, and as an introductory topic we additionally mention surface waves on plates where related phenomena also occur. Both the theoretical and the experimental aspects of the present subject will be considered, including the experimental visualization of the surface waves. *© 2001 MAIK "Nauka/Interperiodica".*

INTRODUCTION

We consider the process of acoustic interactions with elastic (metal) shells of a cylindrical or spherical shape, these examples being sufficient to exhibit the essential physical phenomena arising in the acoustic interaction process. They were found to be qualitatively similar to those in metal plates, the effects of curvature in the shells not having caused any major differences [1] as long as the radius of curvature is large compared to the wavelength. We assume the shells to be fluid-loaded on the exterior or on both the exterior and the interior with the same or with different fluids. Acoustic interaction, e.g., by an incident plane wave (or, if there is no external fluid, assuming some mechanical interaction) will cause the excitation of waves in the shell material which, in analogy to similar waves in elastic plates, can be referred to as Lamb-type (pseudo-Lamb or, simply, Lamb) waves; the lowest-order wave is related to the Rayleigh wave on an elastic half space [2–4] and has often been referred to by this name [5]. In distinction from the analogous plate waves, these waves on a shell may propagate in a "circumferential" fashion along a closed "peripheral" path and can then be referred to under these names or, alternately, as "surface waves"; the circumferential Lamb waves have also been called "Whispering Gallery waves" [5], from Lord Rayleigh's observations in the dome of St. Paul's cathedral [6] in London. The distinguishing feature from plate waves appears here as the possibility that surface waves may match phases over their closed paths and thus form standing circumferential waves, which leads to a resonant reinforcement of their amplitudes and, hence, to acoustic scattering resonances. Due to the dispersive nature of the waves, these will occur at well-defined resonance frequency values which, owing to attenuation, have an imaginary component. The latter is often small, in which case, spectacularly high and narrow resonance features may appear in the scattering amplitude; see, e.g., [7]. Closed-path phase-matching resonances will also occur on elastic bodies of more general shapes, such as spheroids or finite-length cylinders; some of these cases have been discussed in [8, 9].

The presence of fluid loading causes the appearance of additional surface waves during the excitation process which, in contrast to the shell-borne Rayleigh and Lamb-type waves, are predominantly fluid-borne and which are often referred to as Scholte–Stoneley waves, in analogy to related geophysical waves introduced by Stoneley [10] and by Scholte [11]. Their phase-velocity dispersion curves tend asymptotically, for high frequencies, to the sound velocity in the fluid loading(s) while those of the Rayleigh or Lamb waves tend towards the Rayleigh-wave speed c_R or the bulk shear speed c_T in the shell material, respectively; but the situation is complicated here by the coupling of the Scholte–Stoneley waves with the lowest-order Lamb (or Rayleigh) wave; this has been analyzed by Bao *et al.* [12]. The acoustic coupling phenomena have first been clarified for the case of an elastic plate [13]. For this reason we shall, in the following, first present a brief overview of the related surface-wave dispersion phenomena on plates, before proceeding to the analogous, more complicated phenomena on cylindrical and spherical shells, for which the discussion of the plate case furnishes a first step towards their understanding.

[1] This article was submitted by the author in English.

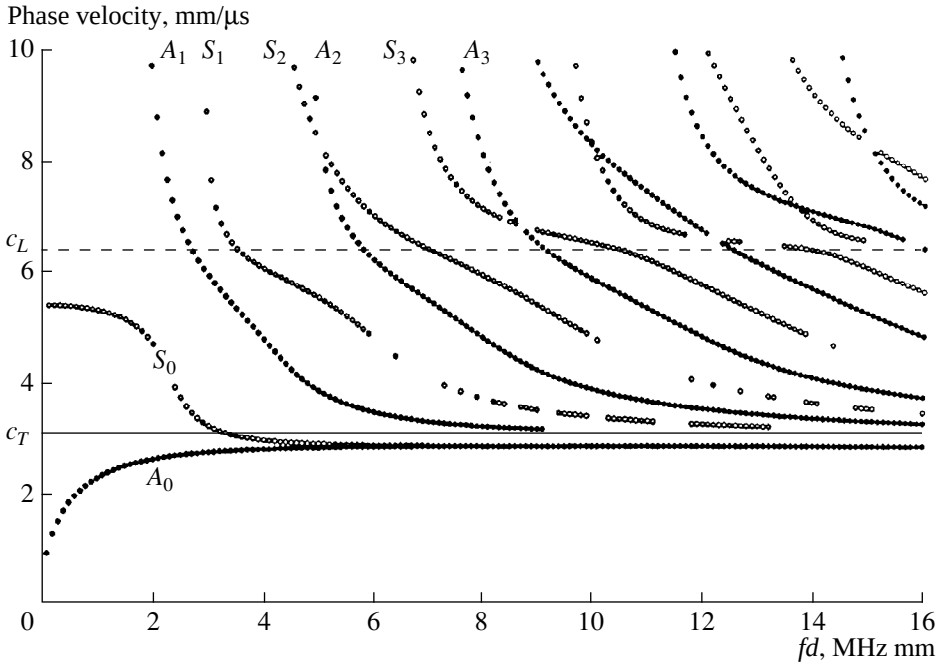

Fig. 1. Phase velocity dispersion curves of Lamb waves on a free aluminum plate (from [13]).

A more complete discussion of plate wave dispersion phenomena can be found in [14], which is a review paper devoted exclusively to plate waves.

PLATE WAVE DISPERSION

Phase velocity dispersion curves for the waves on an elastic plate are given, e.g., for a free plate by Brekhovskikh [15] or for a plate loaded by two different fluids on one or both sides by Talmant [16], see also [13]. They are obtained from solving the characteristic equation for plate vibrations. Figure 1 shows the dispersion curves for an aluminum plate in vacuo in a version obtained by [13]; see also [4]. Phase velocities are plotted vs. the product of frequency f and plate thickness d, and the compressional (c_L) and shear velocity (c_T) of bulk waves in aluminum are indicated by horizontal lines. Lamb-wave modes indexed by i correspond to either symmetric (S_i) or antisymmetric or flexural (A_i) plate displacements, and the phase velocities of the lowest-order ($i = 0$) Lamb waves (or Rayleigh-type waves) S_0 or A_0 (flexural wave) tend asymptotically for $fd \longrightarrow \infty$ towards the Rayleigh wave velocity c_R on a half-space (lying just below c_T), while the higher-order ($i \geq 1$) Lamb waves tend towards the shear speed c_T, the S_i waves having lingered around the compressional-wave speed c_L before eventually dropping down to the shear speed also.

The pattern of A_i and S_i wave dispersion curves in Fig. 1 has been explained by [13] in the following fashion. One may, as in Fig. 2, calculate the dispersion curves for a free aluminum plate for which either the shear waves were assumed absent ($c_T = 0$) or the compressional waves were assumed absent ($c_L = 0$). This yields the two families of intersecting curves of Fig. 2, which lead to the following interpretation for the curves of an actual plate shown in Fig. 1 (except for those of S_0 and A_0 waves): descending from certain individual cutoff positions, the A_i curves drop down to their asymptotic value c_T in a fairly straightforward fashion, and may be identified with the (purely shear) $c_L = 0$ curves in Fig. 2. The S_i curves, after descending from their individual cutoffs, try to form horizontal curve segments around c_L before asymptotically dropping down to c_T also. One notices, however, that the horizontal curve segments of neighboring S_i waves may be thought to be connected from one wave to the next, so that such a connected curve (with gaps) approaches a (purely compressional) $c_T = 0$ curve of Fig. 2. This was studied in detail in [13] by changing the plate parameters but is most easily seen in Fig. 1 when advancing, e.g., from the horizontal portion of the S_3 to that of the S_4 wave. These gap-forming phenomena are caused by the coupling between the $c_T = 0$ and the $c_L = 0$ waves (caused by the plate boundary conditions), and we conclude that each wave in Fig. 1 changes its nature as one goes along its dispersion curve: in its steep portion it largely has the nature of a shear ($c_L = 0$) mode; in its flat portion, largely that of a compressional ($c_T = 0$) mode. When now, e.g., the S_3 curve in its flat, compressional portion ($c_T = 0$) approaches the downward-coming shear ($c_L = 0$) S_4 curve, it then turns downward itself and changes into a shear ($c_L = 0$) mode, asymptoting to c_T, undergoing a curve repulsion which at the same time converts the S_4 curve into a flatter, compressional

($c_T = 0$) mode. The curve repulsions caused by the coupling of waves thus break up the basic ($c_L = 0$ or $c_T = 0$) uncoupled curves into segments with gaps, with each wave changing its physical nature when passing a point of curve repulsion.

One may now consider the case of a fluid-loaded plate. Figure 3 shows [4] the phase velocities, divided by the sound speed c_w in the one-sided water loading, of the S_0 and A_0 Lamb waves of an aluminum plate. In addition, the phase-velocity dispersion curve of the Scholte–Stoneley wave (which we shall call the "*A* wave") that now appears [17] due to the fluid loading, and which is largely water-borne, is shown also. (These curves would be essentially unchanged with two-sided water loading, the A_0 and S_0 curves being essentially the same as those for a free plate; there only appear now some imaginary parts of the phase speeds due to the waves radiating off into the water, the imaginary parts doubling for two-sided vs. one-sided water loading [16].) One notices a repulsion phenomenon between the A_0 and the *A* wave around $fd \cong 30$ MHz mm, which means not only that these two waves are coupled, but also that they exchange their physicals nature while passing through the repulsion region: the A_0 wave as it approaches c_R for $fd \longrightarrow \infty$ is plate-borne there, while the *A* wave as it approaches c_w is fluid-borne there. To the left of the repulsion region, the A_0 wave is now fluid-borne there and the *A* wave is plate-borne [4].

The case of two-sided fluid loading of a plate has been investigated in [18, 19]; see also [1]. Figure 4 shows a result for an aluminum plate water-loaded on one side and alcohol-loaded on the other. It is seen that here two Scholte–Stoneley waves appear which tend asymptotically to the sound velocity in water (c_w = 1483 m/s) and in alcohol (c_a = 1200 m/s), respectively. This limiting behavior has been noted earlier [20]. We also see that the dispersion curve of the wave that tends to the higher-lying fluid sound speed forms a loop to the left of point *M*; the existence of such a loop in a dispersion curve has been noted before [21], and it was shown that the wave in the loop region propagates without attenuation.

The foregoing discussion of the basic features of surface waves in fluid-loaded plates will help us understand similar phenomena in fluid-loaded thin shells, to which we shall turn our attention in the following.

SURFACE WAVES AND RESONANCES ON FLUID-LOADED THIN ELASTIC CYLINDRICAL SHELLS

Our discussion of the physical phenomena involving elastic shells will deal with the interplay of surface waves on the shell, of the circumferential (peripheral) type, and of the resonances caused by them; but we shall also mention resonant processes dealing with longitudinal (axially propagating) shell waves. These waves are generally assumed here to be excited acoustically by an incident plane wave that gets scattered by the shell (requiring the shell to be immersed in an external fluid whose influence on these processes needs to be considered in addition), but the literature also contains examples of their excitation by (point) mechanical forces [22, 23]. The study of acoustic shell interactions goes back to the work of Lyamshev [24–29]. His and other related works have been reviewed by Muzychenko and Rybak [30], and we may also mention here as relevant the book on thin-shell theory by Gol'denveĭzer [31]. This earlier work also involves [30] the effects of plane acoustic waves obliquely incident on a finite-length cylindrical shell and a discussion of the excitation of normal modes of axial shell waves by their coincidence with the trace of the incident wave on the shell (sometimes referred to as Cremer's coincidence

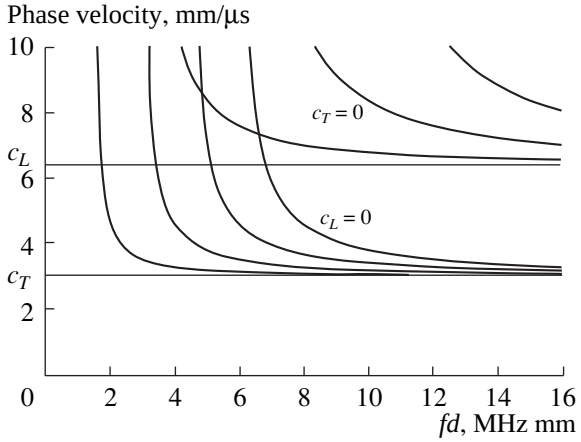

Fig. 2. Phase velocity dispersion curves of Lamb waves on a free aluminum plate for which either c_T or c_L were set equal to zero, as indicated (from [13]).

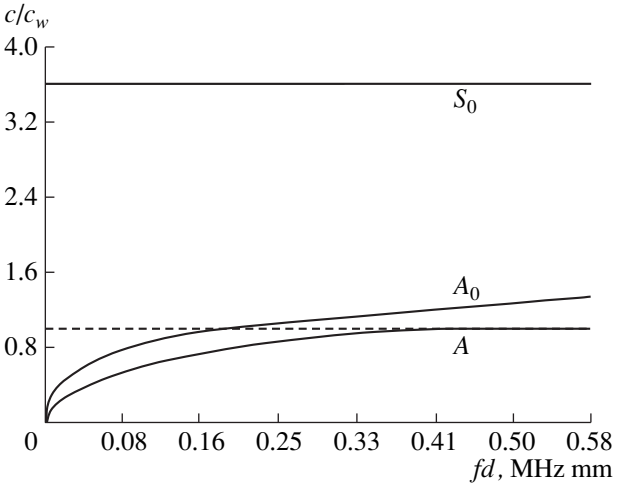

Fig. 3. Phase velocity dispersion curves of S_0 and A_0 Lamb waves in an aluminum plate with one-sided water loading, together with that of the *A* (Scholte–Stoneley) wave from [13].

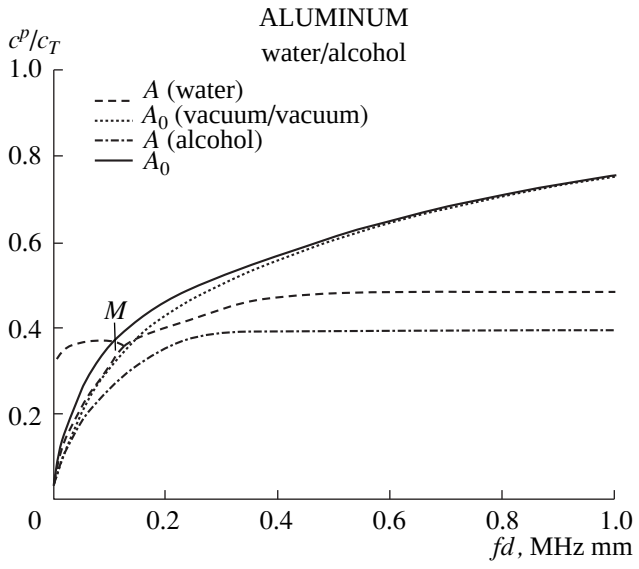

Fig. 4. Phase velocity dispersion curves (normalized by shear speed c_T) of the A_0 wave for an aluminum plate in vacuum, and of the A_0 wave and two Scholte–Stoneley waves A and S for an aluminum plate loaded by water on one side and by alcohol on the other (from [18, 19]).

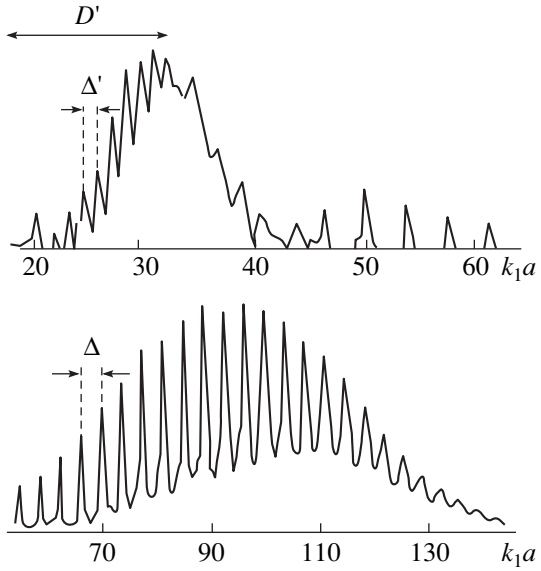

Fig. 5. Resonance contribution to the far-field backscattering amplitude of an evacuated cylindrical aluminum shell in water, plotted vs. ka (k is the propagation constant in water, a is the outer shell radius) (from [34]).

condition [15]), but a discussion of resonances in the frequency space is also given in [30].

The shell resonances can be calculated and observed as distinct features, often of a quite narrow width in frequency, in the acoustic scattering amplitude, with striking examples of both shown, e.g., in [32, 33] and in [34], respectively, Fig. 5 (from [34]) illustrating these resonances. Their physical origin lies in the (acoustic) excitation of surface waves on the shell which, e.g., for an acoustic signal incident normally to the cylinder axis, will circumnavigate the shell in a peripheral fashion along a closed circumferential path. If upon each circumnavigation they match phases with themselves at their point of origin (i.e., forming circumferential standing waves with an integer number of wavelengths spanning the circumference), this will lead to their resonant reinforcement and to a resonance in the scattering amplitude. The resonances plotted vs. frequency can be quite narrow but are of a finite height due to damping introduced by radiation of the surface wave as it circumnavigates the shell. Because of the dispersive nature of the surface waves, phase matching takes place at a series of well-defined resonance frequencies. This explanation of the (circumferential-wave) resonance spectrum of a cylindrical shell (or generally, of an elastic object on which surface waves can circumnavigate along a closed path) was put forward by Überall *et al*. [35, 36] in 1977 and has been generally followed (see, e.g., [32]). This tight interplay of resonances and surface waves will allow a determination of the surface wave phase velocity dispersion curves from a known corresponding subset of the resonance spectrum, or, conversely, it will allow a determination of the corresponding resonance spectrum from known (e.g., calculated) surface wave dispersion curves.

For a cylinder of finite length, another set of resonances arises from the formation of longitudinal standing waves in the axial direction, which also amounts to a phase matching [37]. These were studied, e.g., in [38], and for an oblique direction of the incident wave [23] both longitudinal and circumferential waves can be excited simultaneously in a combined fashion, generating resonances from the formation of helical waves [39–41].

As to the scattering from a spherical shell (or a sphere, in general), circumferential surface waves excited, e.g., by an incident acoustic wave, can likewise match phases and form standing peripheral waves. It should be noted here, however, that in this case the circularly peripheral waves will pass through two focal points, one towards the source and one on the opposite side, at which a quarter-wave phase jump occurs [42]. Phase matching then takes place here in integer-number-plus-half wavelengths of the surface wave span on the circumferential path [43].

A. Circumferential Waves on Infinite Cylindrical Shells with External Fluid Loading

Figure 3 showed the lowest (S_0 and A_0 or "flexural") Lamb waves on an aluminum plate and the additional (A) Scholte–Stoneley wave which is introduced by a one-sided water loading of the plate. The appearance of such a Scholte–Stoneley wave on a water-immersed, evacuated shell was first shown by Subrahmanyam [44]; see also [34]. (Note, however, that the first resonance and dispersion analysis of immersed cylindrical

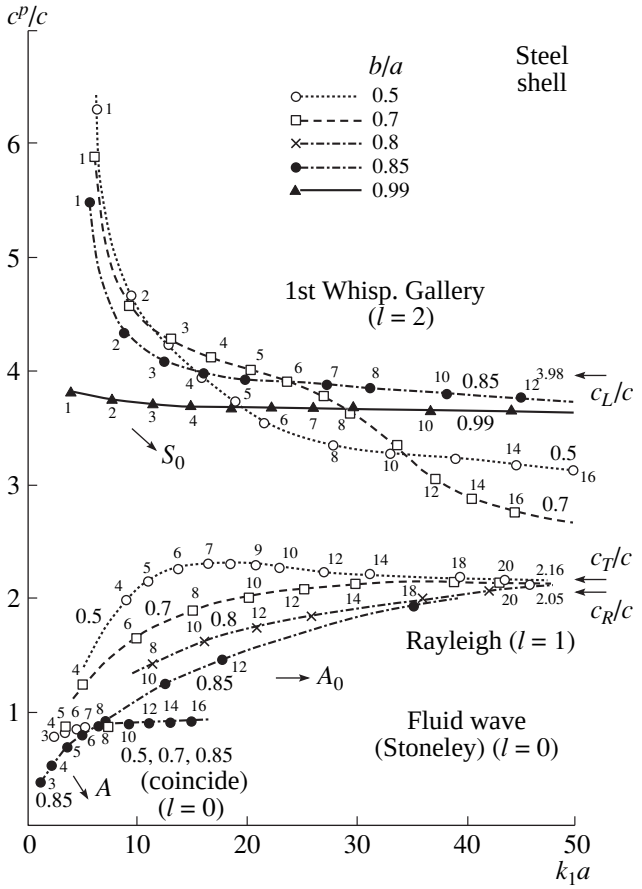

Fig. 6. Phase velocity dispersion curves (normalized by sound speed in water) of pseudo S_0 ($l = 2$), A_0 ($l = 1$), and A waves ($l = 0$) for the air-filled steel shell in water for various shell thickness ratios b/a (from [34]).

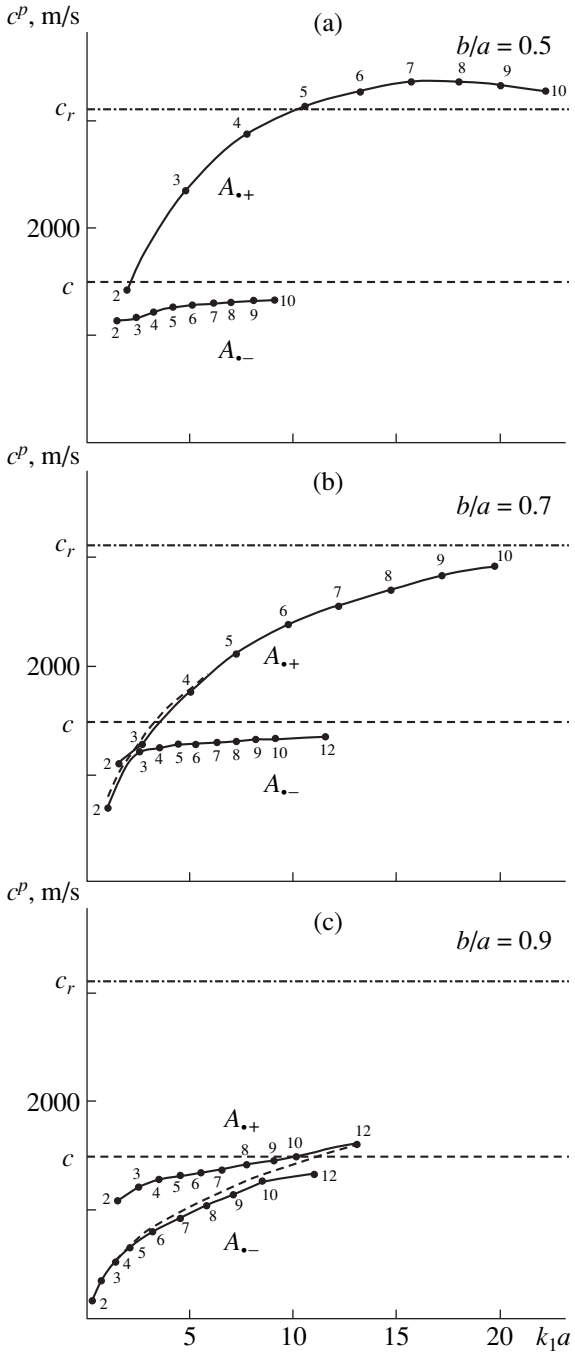

Fig. 7. Phase velocity dispersion curves for A_0 and A waves on evacuated steel shells in water, of various thickness ratios b/a = (a) 0.5, (b) 0.7, and (c) 0.9 (from [48]).

shells is due to [45], and it was followed up by the work of [46].) Figure 6 shows Subrahmanyam's calculated results [44] for water-loaded, air-filled steel shells of various thickness b/a. The figure displays the phase-velocity (c^p) dispersion curves, normalized by the sound speed in water (c), for circumferential waves analogous to the plate waves: the S_0-Lamb analog ($l = 2$ or first Whispering Gallery wave, in cylinder terminology); the A_0-Lamb analog ($l = 1$ or Rayleigh wave); and the Scholte–Stoneley analog ($l = 0$). Present knowledge (see above) tells us that the A_0 wave, descending from the right, continues as the white circles to the left of $ka \cong 5$, while the A wave, coming in horizontally from the right, continues as indicated by the descending black dots to the left of $ka \cong 5$. The two curves come close but repel each other at $ka \cong 5$. Physically, however, the continuous-looking black dot curve (A_0 to the right, A to the left) is shell-borne in its entirety, and the near-horizontal, continuous-looking curve (black dots to the right, white circles to the left) is water-borne entirely.

The mentioned repulsion of the A_0 and the A wave dispersion curves, not well discernible in Fig. 6, is visible for a plate in Fig. 3 and has been studied for cylindrical shells in [47, 48]. Figure 7, from [48], shows calculated dispersion curves for A_0 and A waves on water-immersed steel shells of various thickness, b/a = 0.5, 0.7, and 0.9, indicating the repulsion phenomenon between these two curves. Note that the dashed curve, representing the A_0 wave on a shell without fluid loading and thus entirely shell-borne, clearly indicates the shell-borne nature of the lower curve to the left of the repulsion region and of the upper curve to the right of it.

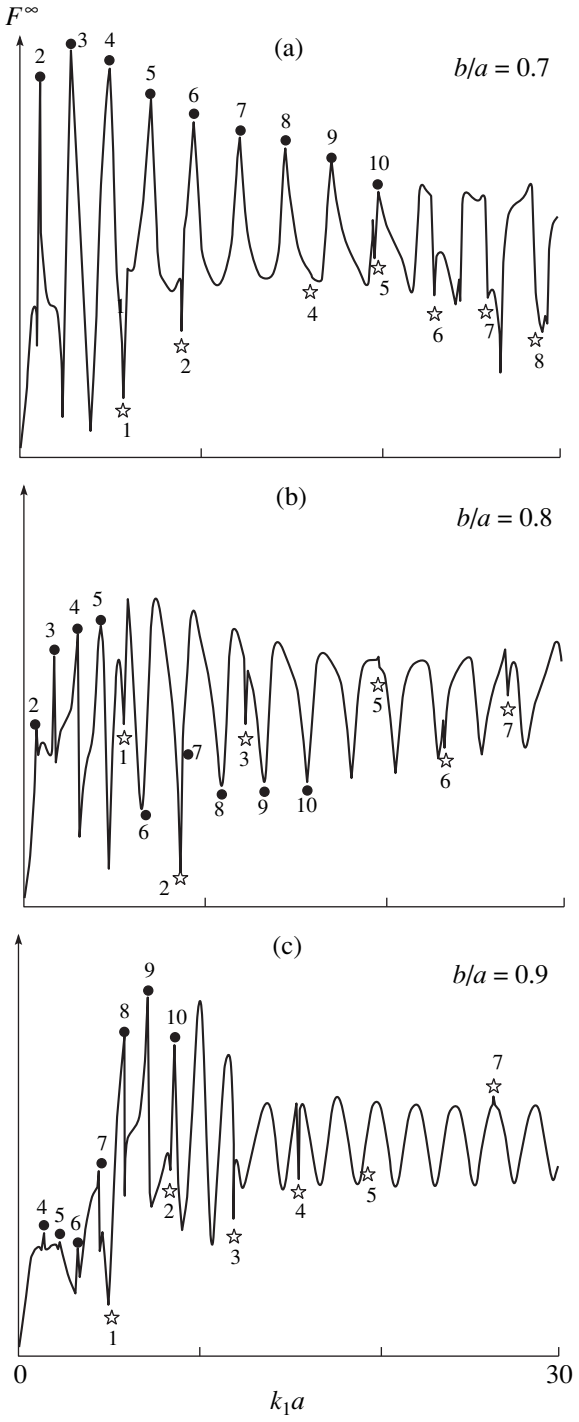

Fig. 8. Far-field backscattering amplitude plotted vs. k_1a, from evacuated steel shells in water of thickness ratios b/a = (a) 0.7, (b) 0.8, and (c) 0.9 (from [48]).

Far-field acoustic scattering amplitudes from such cylindrical shells of various thickness, calculated for normal incidence, are shown in Fig. 8, from [48]. The various visible resonances were attributed here to the S_0 (*), A_0 (■), and A wave (●) as indicated. One can notice the following features: (i) S_0 resonances, the numbers indicating their order number n, occur at all thicknesses of the shell; (ii) A_0 resonances are visible at all remaining resonance features for $b/a = 0.7$, at all but one of these for $b/a = 0.8$, and at only one single resonance feature for $b/a = 0.9$, while (iii) no A resonance occurs among the non-S_0, $b/a = 0.7$ resonance features, only one is visible at $b/a = 0.8$, and at $b/a = 0.9$ all but one of the non-S_0 resonance features are A-wave resonances. These and other observations (e.g., [49]) show that while the A resonances are visible on thin shells ($b/a \geq 0.9$), the A_0 resonances are harder and harder to observe the thinner the shell becomes. The reason for this non-observability of the A_0 wave (via its resonances) on very thin shells was recognized by Talmant and Quentin [16, 50] to lie in the fact that at low frequencies the attenuation (caused by re-radiation) of the A_0 wave, especially for frequency-thickness values $fd \leq 1$ MHz mm, is an order of magnitude higher than, e.g., that of the S_0 wave, due to the transverse (flexural) nature of the A_0 wave. It was also shown [16] that the attenuation coefficient is inversely proportional to $(1 - b/a)$, so that the thinner the shell, the larger the attenuation (and reradiation) of the wave. In the experiments of Talmant and Quentin [50, 51], which were done observing the radiation from multiply circumnavigating pulses on the shells, one single (non-identified) circumnavigating pulse was seen on a steel shell (but not on duraluminum shells) in addition to those of the S_0 and A waves, which might have been an example of the A_0 wave.

Experimental observations of the A_0 wave on very thin shells have been carried out, however [52], by utilizing ultra-short, spark-generated sound pulses exciting the A_0 wave on the cylindrical shell and observing only a short initial portion of just its first circumnavigation, before it had any time to decay. The visualization of the A_0 wave propagation was achieved by the shadowgraph method [53]. Figure 9 presents the shadowgraph of a $b/a = 0.94$ water-immersed, evacuated steel shell insonified by a spark acoustic source (top), which shows the incident (I) and specularly reflected pulse (SR), turning into the fluid-borne Franz or "creeping" wave [35, 36, 54, 55] as it wraps around the cylinder. It also shows the re-radiation in water of two kinds of shell waves which have traveled ahead of the incident pulse: the S_0 wave (fastest) and the A_0 wave (as indicated), which has been clearly observed here. Its identification occurred via spectral analysis of its observed re-radiation, permitting the extraction of its phase-velocity dispersion curve which closely agreed with the calculated dispersion curves [47, 48].

The mentioned Franz waves are entirely fluid-borne and exist even if the (cylindrical or general) scattering object is impenetrable (rigid or soft); the A wave is also largely fluid-borne although its existence depends on the scatterer being elastic. It stands to reason, therefore, that a possible interplay of the Franz waves and the A wave should be discernible. This has been brilliantly demonstrated in [56], where it was shown for water-immersed, evacuated aluminum and steel shells that for

varying values of the shell curvature, the water-borne (Stoneley) wave and the succession ($F_1, F_2, \ldots$) of water-borne Franz waves cross over and often exchange roles with each other. This study also includes the shell-borne (A_0) wave and the attenuation of these waves. Figure 10 shows the phase velocities in an aluminum plate and shell of the following situations: of the A_0 wave for a plate in vacuum (A_0^{PV}); on a one-sidedly water-loaded plate both A_0^P and A^P (here called S^P) are shown, and on a water-immersed shell with $(a+b)/2(a-b) = 45$ the figure shows the A_0, A (here called S), and the first two Franz waves F_1 and F_2. One notices the role F_1 plays in the repulsion region of the A_0 and A waves. This analysis is based on the Timoshenko–Mindlin shell theory and the Watson transformation.

In Fig. 5, one can notice a series of approximately evenly spaced resonances in the acoustic scattering amplitude for an immersed empty aluminum shell ($b/a = 0.96$). This is also seen [57] in Fig. 11 for a steel shell ($b/a = 0.99$), the frequency domain being indicated in (a). If an incident pulse is assumed rather than a steady plane wave, it can be described by a Fourier transform which then is also applied to the scattered wave. The nearly even spacing of the resonances allows us to approximate the scattered-wave Fourier integral by a summable series in the time domain, with the result shown in (b). This simple mathematics furnishes a series of evenly spaced pulses, which obviously physically represent the observation of the radiation from circumferential-wave pulses that encircle the shell a number of times.

A definitive theoretical study on the observability of the A_0 wave for thin evacuated, water-immersed metal shells has appeared very recently [58] based on filtering of the backscattered amplitude in the frequency and in the time domain. Figure 12 displays the calculated backscattering acoustic pressure spectrum for a $b/a = 0.94$ steel shell vs. ka, indicating (*a*) *A*-wave resonances which appear in the frequency window $10 \le ka \le 25$ (see also Fig. 5), (*b*) an oscillation with a constant period in $25 \le ka \le 70$, and (*c*) a large amplitude variation at $ka \sim 195$ which constitutes the so-called "thickness resonance," at a frequency where a resonating standing wave can be formed across the shell thickness. The *A*-wave resonances have been known to appear [45, 46, 59, 60] for an immersed, evacuated shell only in a well-defined "frequency window" (for a 0.94 steel shell at $10 \le ka \le 25$; for a 0.96 shell at $20 \le k/a \le 40$; for a 0.98 shell at $45 \le ka \le 70$). The spectrum of Fig. 12 is Fourier-analyzed to obtain the time-domain response of a short (Dirac) pulse. Suppressing the specular echo and applying an inverse Fourier transform gives the resonance spectra without the specular-echo "background," which always needs to be eliminated [60, 61] in order to display the true resonances. This pure resonance spectrum is now frequency-filtered to eliminate the *A*-wave resonances in their frequency window.

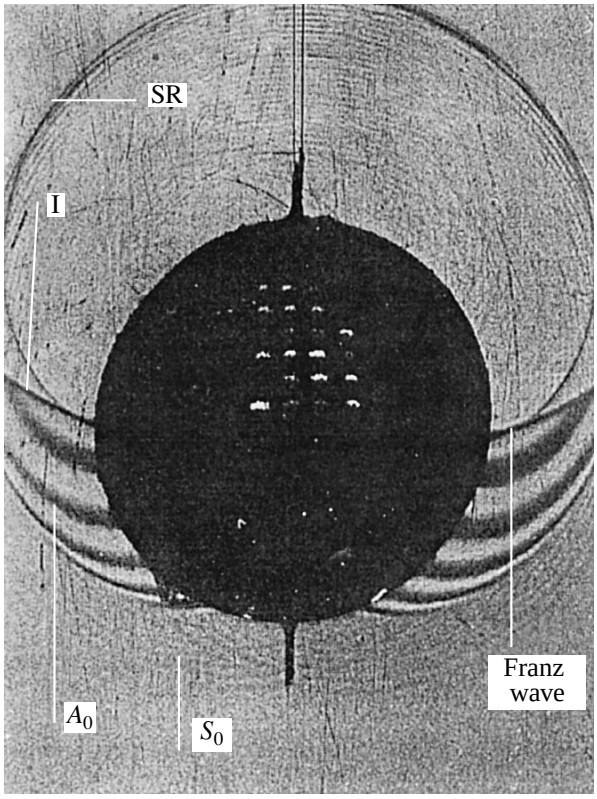

Fig. 9. Shadowgraph of ultrashort sound pulses propagating around water-immersed steel shell ($b/a = 0.94$), showing S_0, A_0, and Franz waves (from [52]).

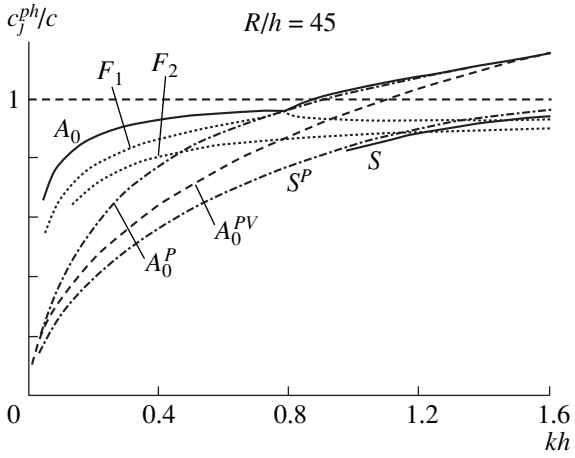

Fig. 10. Phase velocity dispersion curves of A_0, *A*, and Franz waves on aluminum plates and shells, water-loaded from one side. Here, $h = a - b$ and $R = (a + b)/2$ (from [56]).

Another Fourier transform furnishes the time-filtered signal in which a series of circumferential S_0 pulses appears quite similar to Fig. 11, but the earliest appearing pulse is recognized [58] as an A_0-wave pulse, which thus is seen to correspond to the constant-period oscillation in $25 \le ka \le 70$ of Fig. 12.

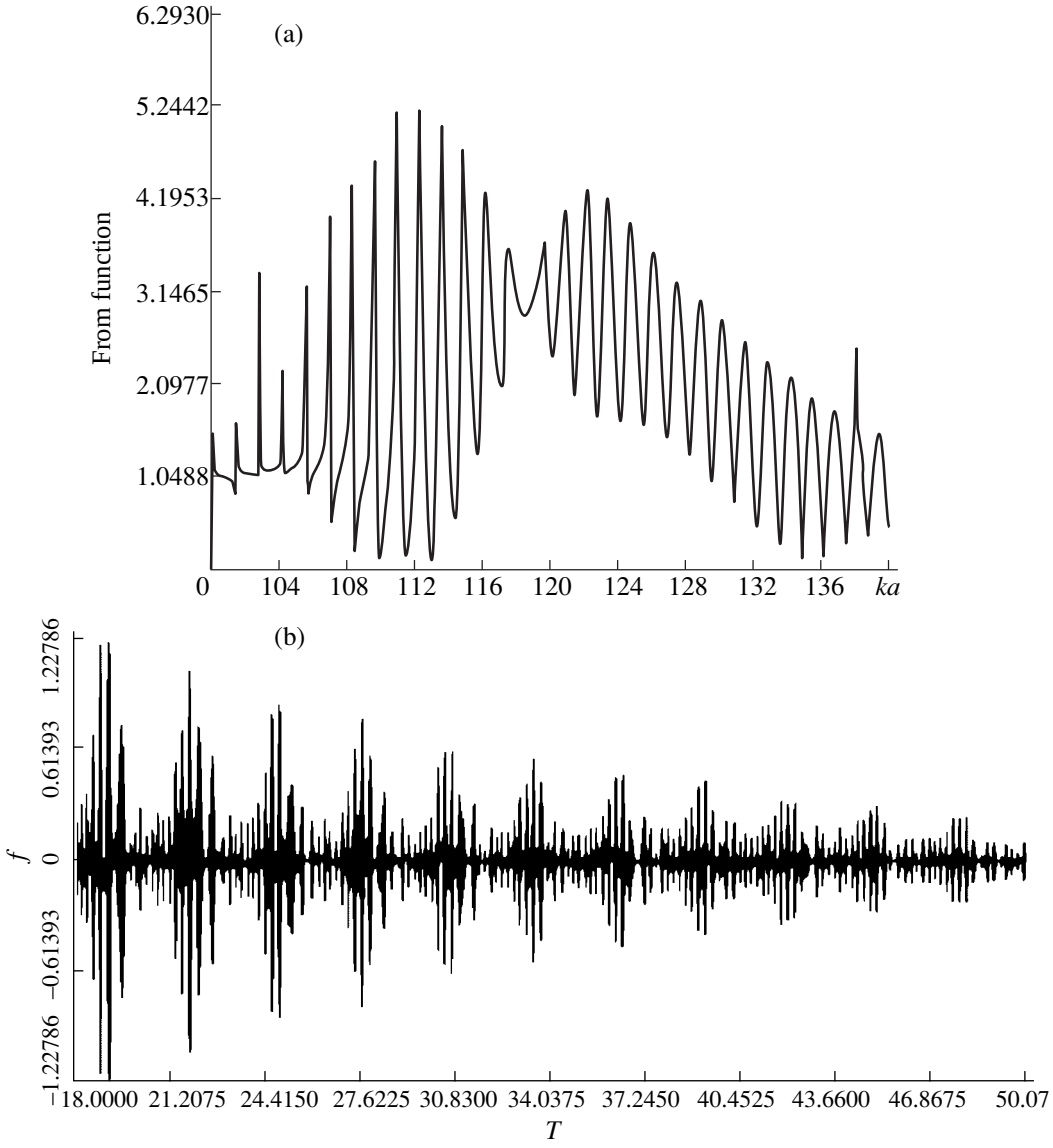

Fig. 11. (a) Resonant backscattered amplitude vs. *ka* of an immersed steel shell with $b/a = 0.99$ and (b) time-domain response to a short incident pulse (from [57]).

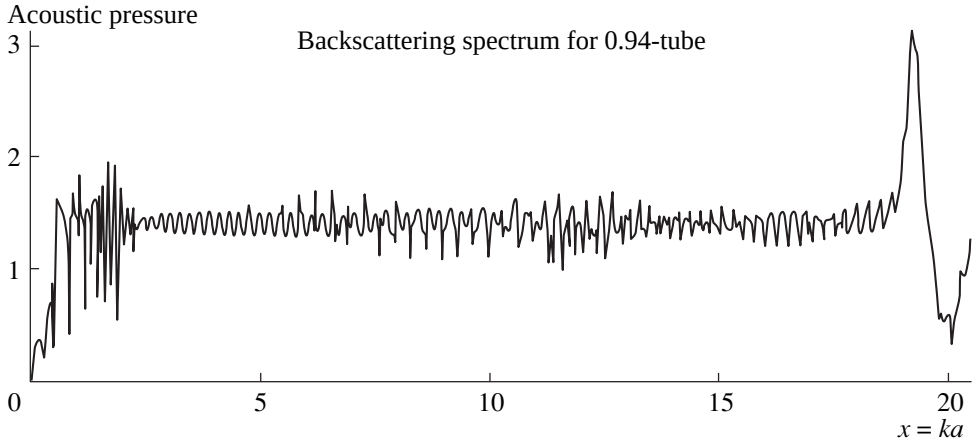

Fig. 12. Backscattered amplitude vs. *ka* from a $b/a = 0.94$ steel shell in water, containing S_0, A, A_0 and thickness resonances (from [58]).

The above-described discussion of shell scattering and the ensuing extraction of shell-borne surface waves have ultimately been based on far-field analysis. Guo [62] has, starting from asymptotics, derived near-field pressure and shell responses in terms of the shell waves.

B. Circumferential Waves on Infinite, Fluid-Filled Cylindrical Shells

Unlike the above-described investigations of empty shells subject to fluid immersion, the study of fluid-filled shells in air or vacuum is of much more recent origin [37]. Figure 13a shows circumferential-wave phase

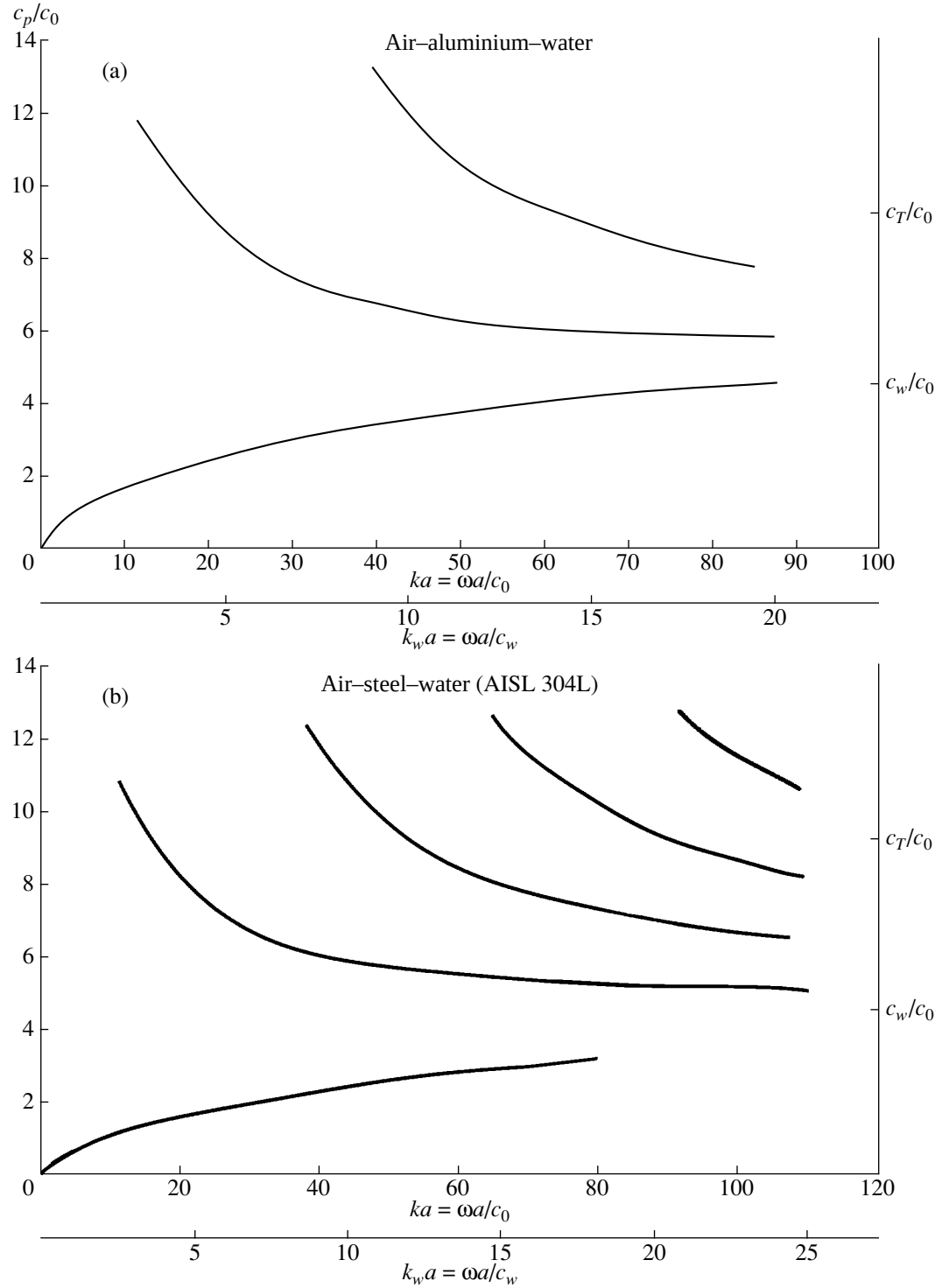

Fig. 13. Phase-velocity dispersion curves for (a) the water-filled $b/a = 0.92$ aluminum shell and of (b) the $b/a = 0.963$ steel shell in air (from [37]).

velocity (c_p) dispersion curves on a water-filled, b/a = 0.92 aluminum shell in air, and Fig. 13b shows the same for a water-filled, b/a = 0.963 AISL 304L steel shell in air. They are normalized by the sound velocity in air, $c_0 \equiv 340$ m/s, and are plotted against both $ka \equiv \omega a/c_0$ and against $k_w a = \omega a/c_w$ where the sound speed in water is $c_w = 1483$ m/s. We see the lowest-order curve starting out from the origin and asymptotically tending towards c_w/c_0. A series of higher-order curves descends from certain lower frequency cutoffs, also appearing to tend towards c_w/c_0 although this would be seen clearly only if the figures extended to higher frequency regions. However, the asymptotics identify well enough all of these waves to be fluid-borne in the filler fluid [18–20], and this will be confirmed in the following section where shells with both external and internal fluid loading are considered.

C. Circumferential Waves on Infinite Cylindrical Shells with Both External and Internal Fluid Loading

This case considered here, double fluid loading with two different fluids, represents the most general situation of fluid loading on a shell. After a brief study of this case [1], a complete investigation was carried out by Bao *et al.* [12]. Their results are shown in Fig. 14a for a water-immersed, alcohol-filled aluminum shell with b/a = 0.92. The phase velocities c_p are normalized by the sound speed in water, $c_0 = 1483$ m/s. The dashed curve shows the A_0 wave dispersion curve for a free shell without any fluid loading (denoted $A_{0\text{free}}$), and the A_0 and A wave dispersion curves for an evacuated, water-loaded shell (denoted by $A_{0\text{evac}}$ and A_{evac}, respectively) are indicated by diamonds. These are the waves that have been discussed in Section *A* above. The shell-borne disjoint portions of these curves are here indicated by the letter a_0, and the water-borne portions, by the letter a. If the alcohol filling is added, the results corresponding to a double-loading of the shell are obtained as the curves indicated by asterisks. Here, we immediately find the dispersion curves of the circumferential waves propagating in the filler fluid, which are very similar to those shown in Fig. 13. While the lowest curve corresponds to the A wave, which shows a possible asymptotic limit at $c_a/c_0 = 0.81$ where $c_a = 1200$ m/s is the sound speed in alcohol, all the higher curves labeled F_1, F_2, F_3, … correspond to the filler-fluid-borne waves that descend from their low-frequency cutoffs and possibly tend toward c_a/c_0 also, although the right end of the figure at $ka \equiv \omega a/c_0 = 50$ does not allow a firm conclusion on this.

What is seen, however, is the repulsion phenomenon of the filler-borne waves already familiar from Fig. 1. We have labeled each continuous curve by F_i. What is clear, however, is that without the interaction mechanism that causes the repulsions, we would have the continuous curves we called f_i (as indicated in Fig. 14a). The repulsion causes a gap in all f_i curves, reconnecting them along the $A_{0\text{free}}$ line to form the continuous F_i curves, all of which have a short segment that follows the $A_{0\text{free}}$ line. The sequence of these segments can now be recognized as the A_0 curve which has been segmented by the interaction mechanism that also segmented (and reconnected) the f_i curves.

This interaction mechanism can be identified from Fig. 14b in which the dispersion curves have been drawn for the same doubly fluid loaded aluminum shell, but assuming "liquid aluminum" in which c_T was taken as zero. This assumption is seen to have eliminated all the curve repulsions, so that now the dispersion curves of the filler-fluid-borne waves coincide with the f_i curves of Fig. 14a; likewise, no A-wave curve appears at all since the "liquid" shell won't support any. This clarified the interaction mechanism causing the curve repulsions in Fig. 14a as being due to the elasticity of the shell (see the equivalent situation when comparing Figs. 1 and 2 for a plate). The onset of the coupling for a fluid-filled aluminum shell in air, Fig. 13a, cannot be seen in that figure since the figure cuts off at $k_w a = 20$ while the first curve repulsion in Fig. 14a commences at about this value (note $k_w a$ in Fig. 13a is the same as ka in Fig. 14a).

D. Determination of the Resonance Frequency Spectrum of Shells

Practical applications often require a knowledge of the eigenfrequency spectrum of fluid-filled cylindrical metal shells in air. The eigenfrequencies corresponding to circumferential waves can be obtained from the above-given dispersion curves by using the principle of phase matching [35], in which a circumferential wave closes into itself with the same phase after each circumnavigation of a cylinder or cylindrical shell, leading to the formation of standing waves and hence resonant eigenfrequencies. The condition for phase matching, i.e., n wavelengths spanning the circumference, is $2\pi a = n\lambda$ (for a thin shell) or

$$c_p/c_0 = ka/n = (2\pi a/nc_0) f \qquad (1)$$

(where $k \equiv \omega/c_0$ is the wave number in the air). This equation represents a straight-line plot of c_p/c_0 vs. k_a, and its intersections with the dispersion curves, e.g., those of Fig. 13, furnish the portion of the eigenfrequency spectrum of the fluid-filled cylindrical shell corresponding to the circumferential waves. Table 1 lists the eigenfrequencies of the water-filled cylindrical aluminum shell corresponding to Fig. 13a, obtained in this way, and Table 2, those of the AISL 304L steel shell of Fig. 13b. The graph of Fig. 15 shows the straight lines of Eq. (1) intersecting with the dispersion curves of Fig. 13a, indicating how the entries of Table 1 were found. For completeness, we also list in Table 3 the values obtained from Fig. 14a for the eigenfrequen-

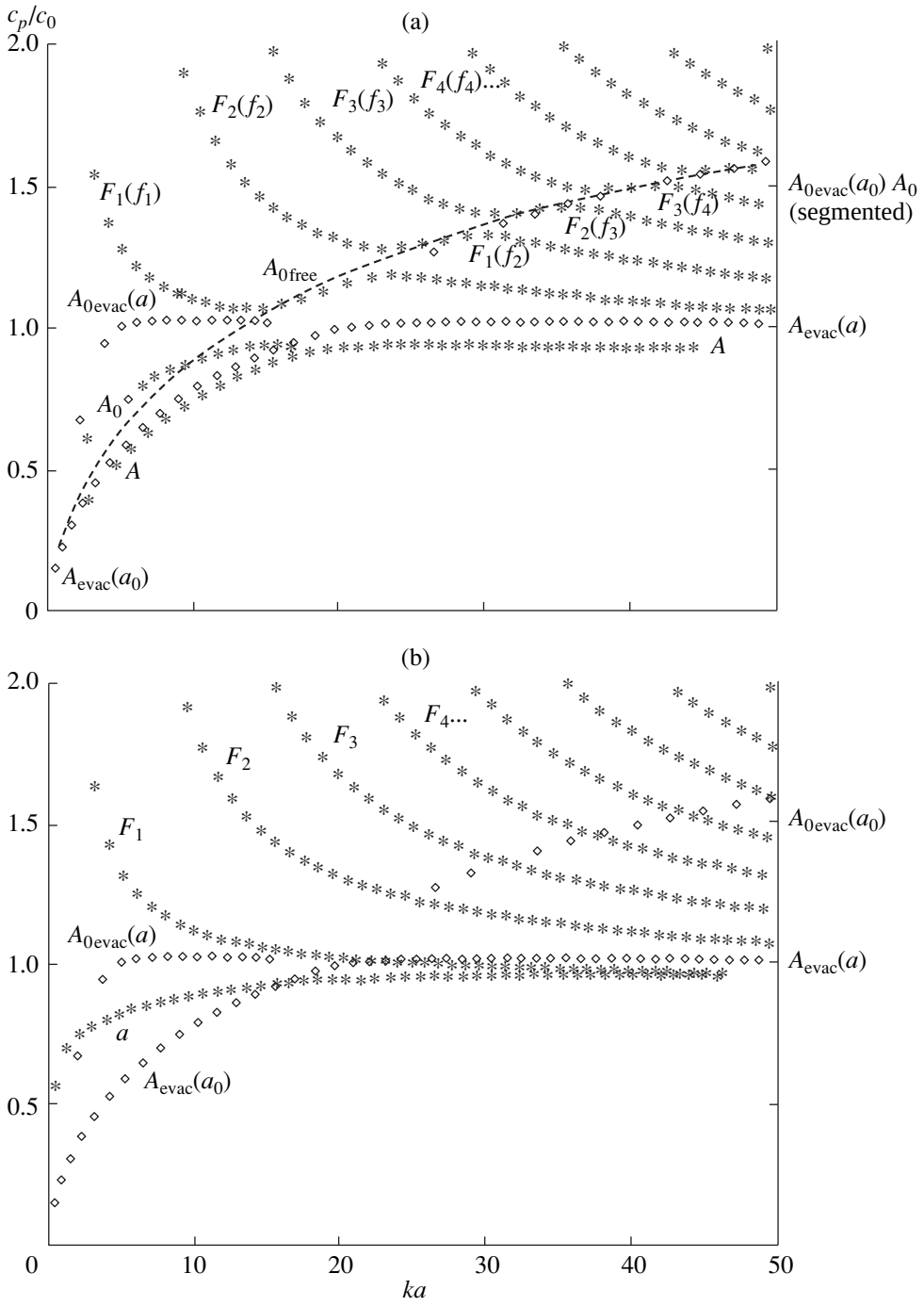

Fig. 14. Phase-velocity dispersion curves (a) for water-immersed, alcohol-filled aluminum shell with $b/a = 0.92$ and (b) for aluminum shell with c_T set equal to zero (from [12]).

cies of the alcohol-filled, water-immersed aluminum shell with $b/a = 0.92$.

E. Determination of Shell Characteristics: Inverse Scattering

Acoustic scattering can be used for purposes of object recognition and material characterization; for this application it is known as "Inverse Scattering." In a series of publications, Professor Quentin and collaborators [63–66] have devised several inverse scattering schemes in order to determine the material and/or size parameters of water-immersed metal cylinders or air-filled metal cylindrical shells via acoustic reflections therefrom, primarily from the scattering resonances of

Table 1. Circumferential wave eigenfrequencies f_l (in kHz) of water-filled cylindrical aluminum shell in air (shell radius a = 5 cm) corresponding to the three waves in Fig. 13a labeled l = 1, 2, 3 (from below)

n	$f(1)$	$f(2)$	$f(3)$
1	–	12.7	
2	–	20.5	
3	0.93	26.6	42.9
4	4.92	32.4	48.6
5	7.69	38.2	56.1

Table 2. Circumferential wave eigenfrequencies f_l (in kHz) of water-filled cylindrical AISL 304L-steel shell in air (shell radius a = 5.4 cm) corresponding to the waves in Fig. 13b labeled l = 1, 2, … (from below)

n	$f(2)$	$f(3)$	$f(4)$
1	11.11		
2	17.89		
3	23.24	38.13	
4	28.21	44.34	
5	33.27	49.91	64.74

Table 3. Circumferential wave eigenfrequencies f_n (in kHz) of alcohol-filled, water-immersed cylindrical Al shell (shell radius a = 5 cm) corresponding to the waves A, A_0, F_1, F_2, and F_3 of Fig. 14a

n	A	A_0	F_1	F_2	F_3
2			14.65		
3			19.88		
4		11.38	24.26		
5		15.41	28.82	45.01	
6		19.51	33.38	50.08	
7	13.13	24.55	37.85	55.01	
8	18.10	29.91	42.26	60.02	75.02

circumferential waves. Our present review of this topic will be restricted only to the case of shells.

In the mentioned references, it has been noticed that the resonances of such cylindrical shells can be seen to fall into two families which are termed as follows:

(a) Shear resonances (T): their frequencies depend only on the shear speed c_T (not on the longitudinal speed c_L) of bulk waves in the shell material; they are of narrow width [note that all resonance widths depend mainly on the density ratio ρ/ρ_0 of the shell (ρ) and the ambient fluid (ρ_0), rather than on c_L and c_T].

(b) Longitudinal resonance (L): these are wide-band and depend only on c_L (not on c_T).

The corresponding c_L or c_T dependence was found to be approximately linear, following the empirical equations ($x = ka$, $k = \omega/c_0$):

$$x^T_{n,i} = (\pi/c_0)[ai/(a-b) + \beta(n)]c_T, \quad i = \text{integer} \quad (2a)$$

for shear resonances and

$$x^L_{n,j} = (\pi/c_0)[aj/(a-b) + \beta(n)]c_L, \quad j = \text{integer} \quad (2b)$$

for longitudinal resonances. Here, n is the standing-wave order number and i, j label the resonance modes of a given n with respect to increasing frequency. The constant $\beta(n)$ depends on n and on b/a. The resonance widths Γ_L are found to be given by

$$\Gamma_L \cong 2(\rho_0/\rho)[a/(a-b)][1-(c_0/c_L)^2]^{-1/2}. \quad (3)$$

Figure 16, from [66], shows the calculated longitudinal resonance frequencies, plotted vs. n, of b/a = 0.5 shells of steel (c_L = 5790 m/s), aluminum (c_L = 6370 m/s), bronze (c_L = 4550 m/s), and copper (c_L = 4600 m/s), divided by the corresponding values of c_L. The resonances $L_1 \ldots L_4$ associated with these four materials and corresponding to the same values of n and L_j appear at the same normalized frequencies.

For certain values of c_T and c_L there occur coincidences between a certain shear and a certain longitudinal resonance. Figure 17, from [66], shows the variation of calculated shear resonance frequencies (linear) and longitudinal resonance frequencies (independent of c_T, hence horizontal) with c_T. One notices near-crossover points where, due to the elastic-wave coupling, a repulsion phenomenon occurs, familiar from Figs. 1 and 14a, that prevents an actual crossing of the curves, but instead creates what [66] terms "hybrid modes."

The three unknowns in the inverse problem of the shell are c_L, c_T, and ρ of the shell material. From a measured sequence of circumferential shell resonances (their frequencies and widths), these three quantities are determined from Eqs. (2) and (3) provided a and b of the shell are known, in addition to the L_j (and T_j) labels and of the mode number n. Determining the latter requires bistatic scattering experiments [67] (while the L_j or T_j labels can be assigned considering the widths of the resonances).

In order to avoid such complications, Batard *et al.* [66] have devised a different, statistical method (MECA) based only upon the measurement of the resonance frequencies in acoustic backscattering. This method allows the determination of c_T and c_L, when a and are known; but for thin shells it allows the determination of c_T without knowing b/a and the determination of this quantity b/a subsequently. A detailed discussion of MECA lies beyond the scope of this review.

F. Axially Propagating Waves on Finite-Length Cylindrical Shells

Besides the circumferential waves, cylindrical shells also support waves propagating in the axial direction. The dispersion curves for such waves were obtained by Kumar [68] for empty or water-filled brass shells in vacuum (restricted to axially symmetric waves, i.e., with a circumferential symmetry index n = 0), and by Kumar and Stephens [69] for empty shells

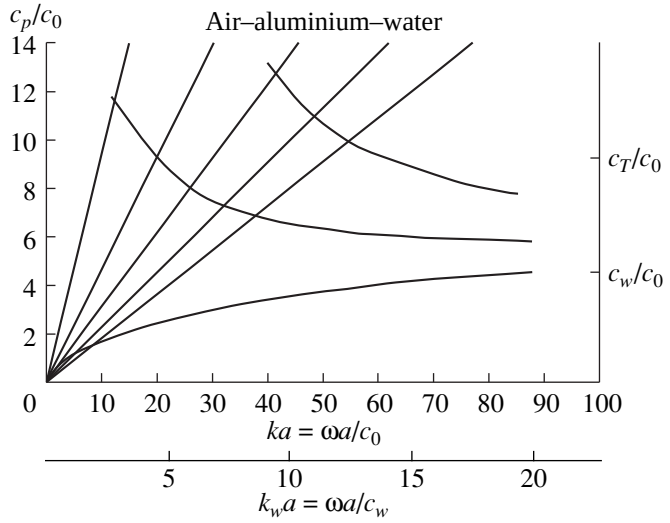

Fig. l5. Determination of the eigenfrequencies of the water-filled cylindrical aluminum shell of Fig. 13a (from [37]).

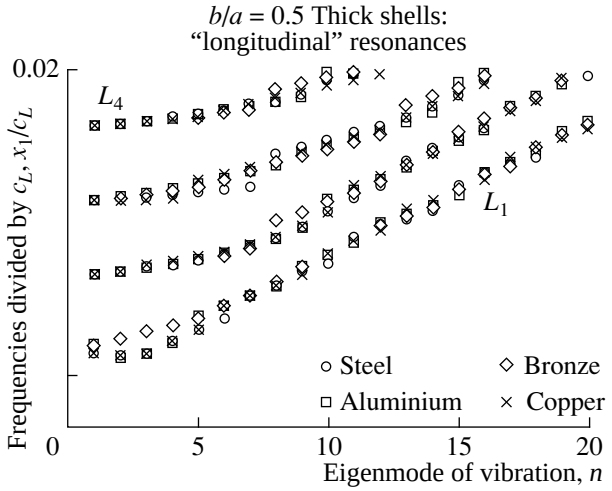

Fig. 16. Longitudinal-resonance frequencies of b/a = 0.5 steel, aluminum, bronze, and copper steel shells plotted vs. n (from [66]).

(restricted to flexural waves with $n = 1$). The dispersion curves are similar to those on the flat plate (with appropriate loading) since the transverse curvature is of little influence for axial propagation on a cylinder [70]. An example of this is the propagation of the Scholte–Stoneley wave on a fluid-loaded plate which is known to be nonradiating (i.e., it has a real propagation constant). The same was shown to be the case for the axial propagation of this wave on a fluid-immersed cylindrical shell [71].

If the cylindrical shell is not infinitely long as assumed before, but is terminated at both ends (the shell being assumed here to be water-filled and in a vacuum) and having a length L, then the phase matching condition for axially propagating waves (furnishing the resonant eigenfrequencies) leads to the formation of standing waves (assuming fixed terminations):

$$L = n\lambda/2, \quad n = 1, 2, 3, \ldots \tag{4a}$$

or

$$c_p/c_w = (k_w d/n)(L/\pi d) = (2L/nc_w) f \tag{4b}$$

(where k_w is the wave number in the water filling, and we use $k_w d$ as the frequency variable, with $d = a - b$. This equation represents a straight-line plot of c_p/c_w vs. $k_w d$, and its intersection with the dispersion curves of axially propagating waves again furnishes a portion of the eigenfrequency spectrum of the fluid-filled cylindrical shell that corresponds to the axially-propagating waves. For aluminum and steel, these dispersion curves are not available from the literature regarding fluid-filled cylindrical shells, but as said above, it may be sufficient here to use the dispersion curves on plates fluid-loaded on one side (aluminum: [18, 19, 56]; steel: [56]). These curves (restricted to the A_0 wave, the S_0 wave, and the Scholte–Stoneley wave A) are shown in Fig. 3 for the one-sidedly water-loaded aluminum plate. Intersection with Eq. (4b) leads to the eigenfrequencies shown in Table 4 for an aluminum shell of length L = 960 mm. The intersection with the higher-lying S_0 wave dispersion curve (see Fig. 3) leads to much higher lying eigenfrequencies. Note that at higher frequencies, curve repulsion effects would appear in the dispersion curves [68].

The acoustic resonances of cylindrical shells with flat or hemispherical endcaps were obtained and analyzed [72–74] employing, among other approaches, the Finite Element/Boundary Element Method [75]. This was done for axial incidence, where the corresponding phase matching condition, e.g., for a cylindrical shell with hemispherical endcaps was obtained [43] for propagation along the meridian circumference (the term 1/2 appearing here due to the quarter-wavelength

Table 4. Eigenfrequencies f_n (in kHz) of S_0, A_0, and A standing waves in the longitudinal direction on a water-filled aluminum shell in vacuum, of length 960 mm (fixed end pieces), outer radius a = 5 cm and wall thickness 4 mm, corresponding to Fig. 3

n	S_0	A_0	A
1	2.85		
2	5.69		
3	8.52		
5	14.21	0.967	
10	28.41	2.58	
20	56.82	7.74	1.81
30	85.19	16.45	6.77
40	113.58	26.06	12.38
50	141.90	35.47	19.35

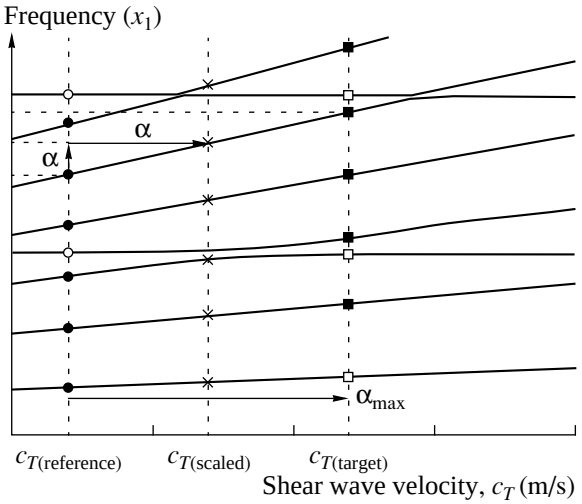

Fig. 17. Shear- and longitudinal-resonance frequencies of shells plotted vs. c_T (from [66]).

phase jump at the focal points on each of the hemispheres):

$$[(2L/c_{cyl}) + (2\pi a/c_{sph})]\, f - 1/2 = n. \qquad (5)$$

Here, c_{cyl} is the phase velocity of the axially propagating wave and c_{sph} the phase velocity of a circumferential wave on the spherical shell. For a tungsten carbide (WC) spherical shell ($b/a = 0.97$) and infinite cylindrical shell, c_{cyl} and c_{sph} are shown [74] plotted vs. ka in Fig. 18a; the resonance (n, l) predictions (arrows) and the observed resonance spectrum (displaying the $l = 2$ peaks of the S_0 wave) for a shell of total overall length L and diameter D with a ratio $L/D = 2$ are shown [74] in Fig. 18b.

G. Surface Waves and Resonances on Submerged Cylindrical Shells Subjected to Oblique Acoustic Incidence

An early theoretical investigation by Veksler [33] of circumferential waves on cylindrical shells was subsequently succeeded by a similar study of surface waves and their resonances generated by oblique acoustic incidence [76]. This latter study found an excitation of axially propagating waves (called T_i), in addition to that of the circumferential waves. Experimentally detected axially propagating waves on cylinders [77–79] have been referred to as "guided waves." The shell problem with oblique incidence was investigated using finite-length cylindrical shells [23, 38]. For oblique incidence, circumferential, and guided waves combine to form helical waves [80, 81]. The physical basis of the corresponding experimentally observed scattering resonances [39] was lucidly explained [40] on the basis of phase matching of a helical wave with itself during its propagation on an infinite cylinder, as shown in Fig. 19.

These resonances were observed at the Institute LAUE at Le Havre, France [82], for infinite cylindrical shells, as shown in Fig. 20 for a $b/a = 0.9$ air-filled aluminum shell in water at an angle of incidence from the normal $\alpha = 5°$. The resonances of the A wave [n], $n = 8$–11; of the S_0 wave (n, 0), $n = 3$–5; and of the new guided wave T_0, $\langle n, 0\rangle$, $n = 2$–7, have been identified and the mode number n has been determined via bistatic scattering measurements (for a full circuit of the receiver

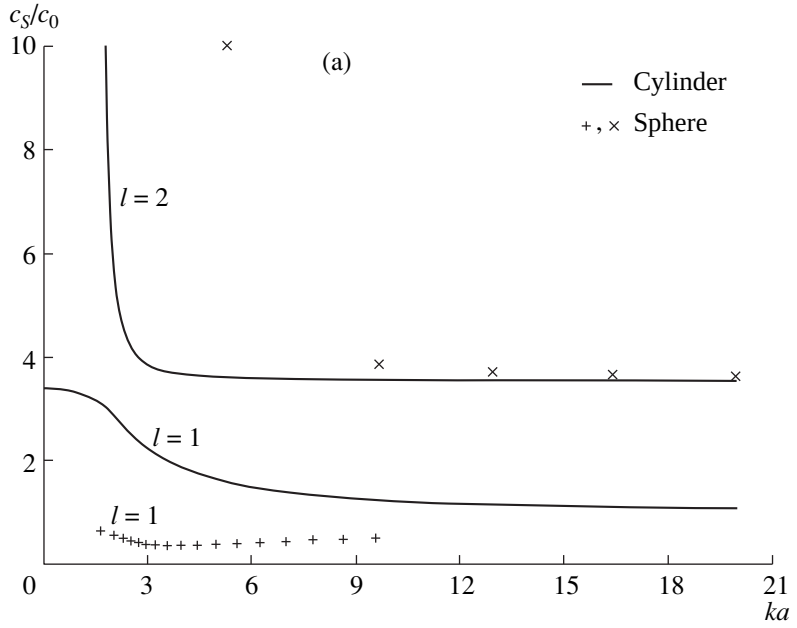

Fig. 18. (a) Phase velocity dispersion curves for a $b/a = 0.97$ spherical and cylindrical shell of tungsten carbide (WC).

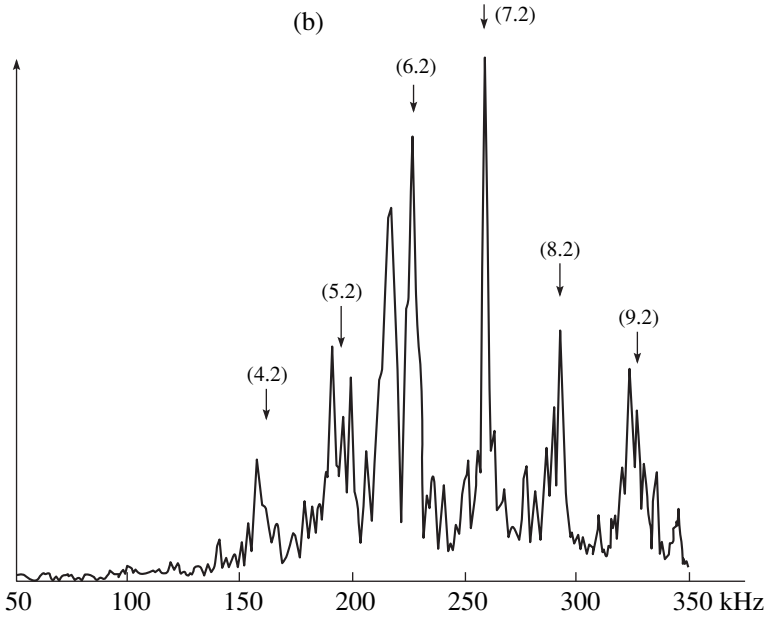

Fig. 18. (b) Measured and predicted resonances for $b/a = 0.97$ tungsten carbide steel with hemispherical end caps and length/diameter ratio of 2 (from [74]).

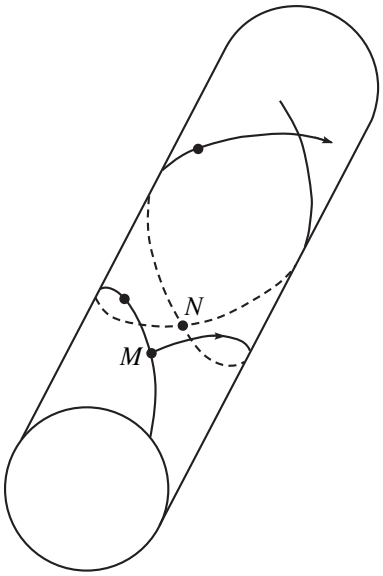

Fig. 19. Helical wave on a cylindrical object generated by oblique acoustic-wave incidence and resonances created by phase matching of the helical wave with itself (from [40]).

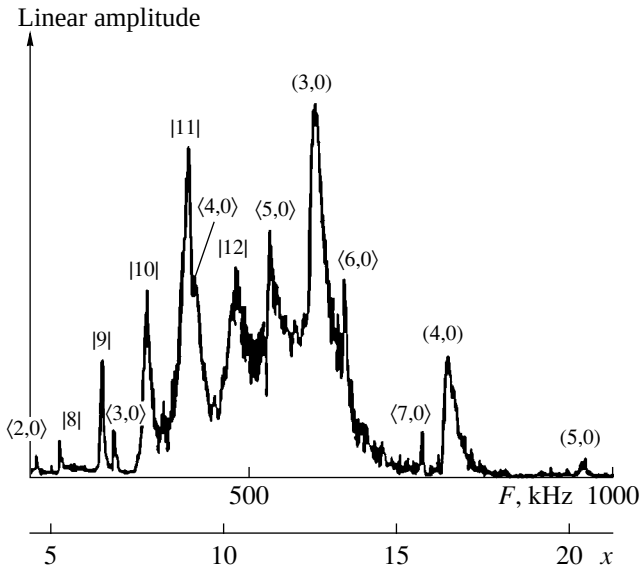

Fig. 20. Observed resonances in the acoustic scattering amplitude of a cylindrical shell showing circumferential-wave and T_0 guided-wave resonances for 5° oblique incidence (from [82]).

around the cylinder axis, the number of lobes in the observed angular scattering pattern is $2n$).

In the same laboratory [82], results were also obtained for finite-length cylindrical shells terminated by plane disks [38]. Figure 21a shows for a $b/a = 0.89$ aluminum shell with $L/2a = 1.66$ the measured backscattering spectrum at normal incidence (A, before, and B, after removal of the specular reflection background) where only the $n = 2\ldots8$ resonances of the $l = 2$ (S_0) Whispering Gallery wave are seen. Part C of the figure displays the resonance spectrum at $\alpha = 4°$ incidence showing, besides the S_0 resonances (which have shifted upwards in frequency), the $n = 6\ldots10$ resonances of the T_0 guided wave. These also shift upwards in frequency when observed (or calculated) at increasing angles α; in addition, a frequency doubling of many of the S_0 as

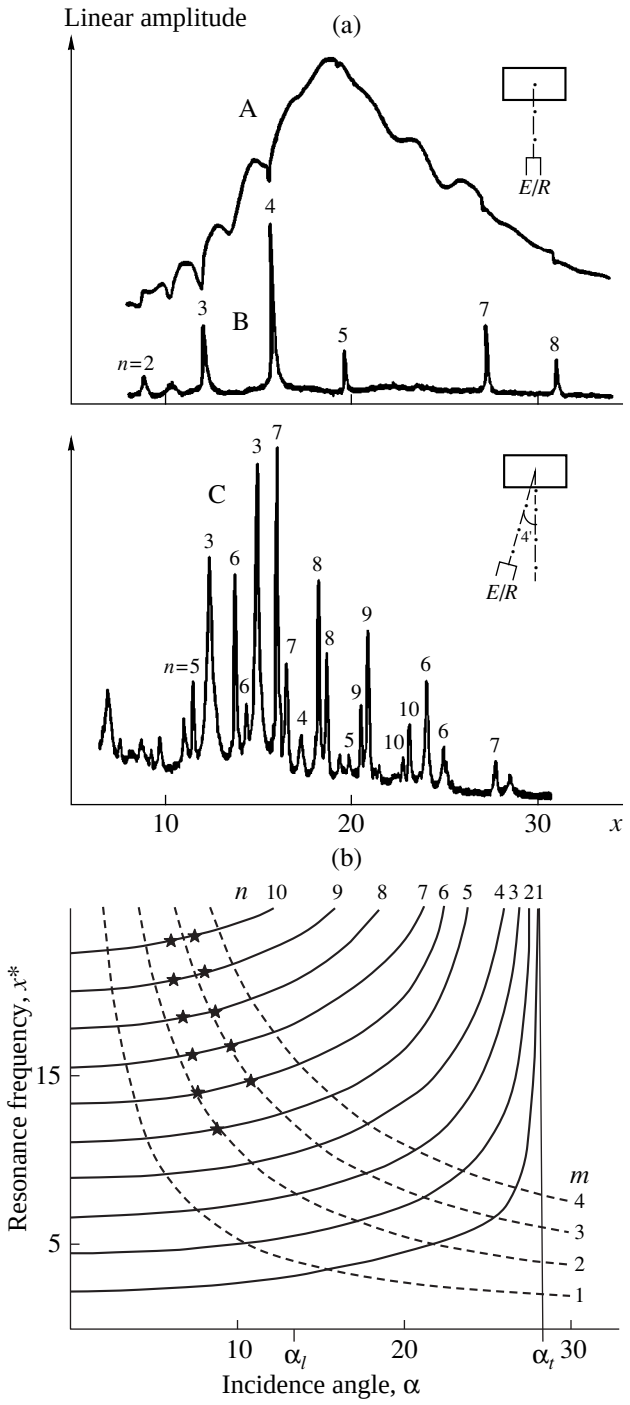

Fig. 21. (a) Observed resonances on a $b/a = 0.89$ aluminum shell terminated by plane disks. A, before and B, after removal of specular background, and C, $\alpha = 4°$ off-normal incidence. (b) Shift of T_0 resonances vs. α (solid curves) and phasematching condition (dashed curves) (from [38]).

well as the T_0 peaks is observed. This can be explained as follows. Figure 21b shows as solid lines the shift of the T_0 peaks as a function of α. The finite length of the shell imposes the phase matching (stationary) condition

$$ka = m\pi a/L\sin\alpha, \quad m = \text{integer} \qquad (6)$$

shown in Fig. 21b as dashed curves. Their intersections with the solid curves predict the resonances, with experimental values indicated as asterisks. We see that for a given n, two (or in principle, several) resonances exist, which explains the observed frequency doubling due to various values of m, the number of standing wavelengths over the length of the finite shell.

H. Scattering from Cylindrical Shells with Internal Reinforcements

The topic of cylindrical shells containing internal structures quite obviously constitutes a problem of great practical importance, both as a vibration problem and as one of acoustic scattering. There exists ample literature on this topic, of which because of space limitation, we can discuss in detail only some selected examples.

The acoustic radiation problem from cylindrical shells with ribs has been studied by Bernblit [83, 84] in the USSR and by Burroughs [85, 86] and others [87] in the US; Burrough's investigations also included experimental measurements. Acoustic scattering from the same cylinder with doubly-periodic ring supports that had been considered by Burroughs [85] was studied theoretically by Moser *et al.* [88].

Additional theoretical investigations of the scattering from shells with internal structures are due to Guo [89–92] and Felsen and Guo [93]. The internal structures considered in these studies are diametrical or off-diameter elastic plates, with the internal masses attached to the shell walls directly or by means of springs, possibly attached at several internal points. The vibrations of a cylindrical shell with a floor partition were studied by Missaoui *et al.* [94]. The acoustic excitation of Scholte–Stoneley and Lamb waves on a shell containing an internal attachment was considered by Poncelet *et al.* [95].

A series of experimental investigations of sound scattering by a reinforced shell, accompanied by the relevant theory, was carried out at the LAUE laboratory at Le Havre, France [96–98]. In these studies, a diametrical lengthwise rib was considered, attached to either one shell wall with a gap towards the opposite wall or diametrically attached to both shell walls. The results of these studies will be shown below.

The ribbed cylinder considered in [85, 88] is a finite-length MK-35 shell of a 21 inch diameter with ribs spaced in a 7 inch, 8 inch, 8 inch, 7 inch, 8 inch, and 8 inch sequence; in addition, an ensemble of five such shells end-to-end is also considered. The shell is 0.325 inches thick, which is small compared to the wavelength, hence it is assumed to be describable by a soft cylinder. The scattering amplitude of the body of the shell is obtained from the Geometrical Theory of Diffraction [99] (GTD) and stems mainly from its edges (whose curvature was taken into account) with the edge diffraction coefficient obtained from GTD. In

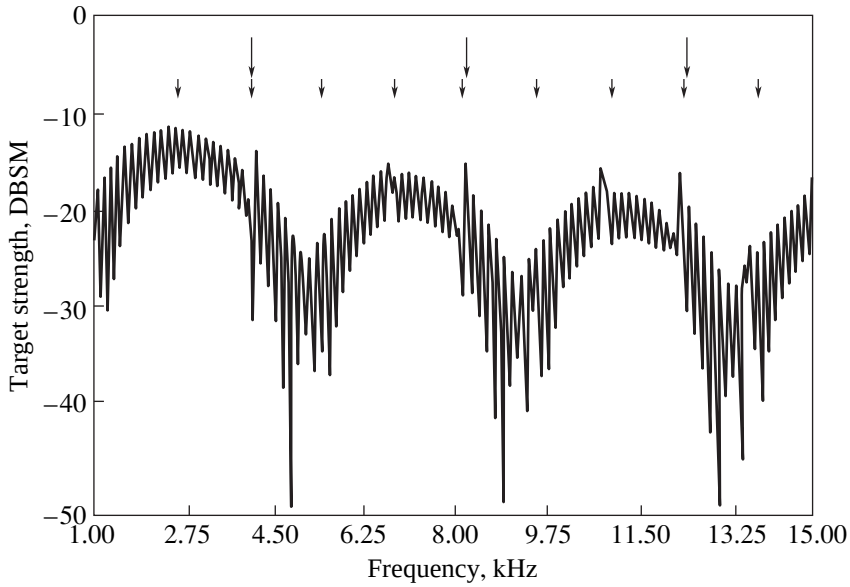

Fig. 22. Backscattering amplitude from a ribbed shell, showing a Bragg diffraction pattern (from [88]).

this way an analytical expression for the scattering amplitude is obtained. The rib scattering amplitude for a single rib in a shell is adapted from Wooley's solution for a rib on a plate [100] (with a curvature correction) and is summed over the MK-35 ensemble. Figure 22 shows the target strength (backscattering amplitude) vs. frequency at the 5-shell ensemble at an angle of incidence of the acoustic signal of 20° from the cylinder axis. The underlying pattern is caused by the shell's edge diffraction; two sets of arrows indicate the Bragg diffraction pattern due to the ribs. Short arrows point at maxima every 1.37 kHz which, by Bragg's law, stem from the 23 inch repeat factor of the assembly; long arrows indicate primary maxima every 4.10 kHz which stem from an overlap of the 7.667 inch average rib spacing and every third 23 inch repeat. It is indicated that the average spacing and the repeat pattern of the ribs contribute most to the diffraction pattern grating portion of the target strength, rather than the actual rib spacings [88]. The rib scattering effects are apparent at all frequencies considered here, as well as at all incident angles (10°–70°), and their positions are in perfect agreement with the prediction of Bragg's law.

The Tallinn-Le Havre collaboration [96–98, 101, 102] has produced a large amount of illuminating results regarding the topic of scattering from a shell reinforced by a lengthwise plate ("stringer") attached along the shell wave from one side. Figure 23a from [96] shows the backscattering amplitude vs. ka for a $b/a = 0.98$ aluminum shell with one internal lengthwise aluminum stringer of dimensions relative to the radius $h_s = 0.02$ (thickness in the azimuthal direction) and $l_s = 0.07$ (radial dimension). The dashed curve in part (A) refers to a smooth shell, the solid curve to the shell with stringer. Parts (B) and (C) present the stringer-generated contributions of vibrations symmetric (B) and antisymmetric (C) relative to the stringer; in these parts, solid curves refer to an aluminum stringer and dashed curves to a rigid stringer. Comparison of the corresponding curves in (B) vs. (C) reveal a doubling of the resonance frequencies, which has been explained in [95] as being due to a foreshortening of the path of phase-matching circumferential waves that either pass through or are reflected by the stringer (Fig. 23b). These waves, responsible for the extra resonances in Fig. 23a, are A waves whose "frequency window" has been opened up by the interaction with the stringer.

With a stringer that diametrically traverses the shell but avoids touching the opposite wall [97] (Fig. 24), the scattering resonances of a smooth shell are observed coming from the S_0 wave (top portion, A) and the extra resonances seen for the stiffened shell (bottom portion) are due to the A wave [95] again. Short-pulse backscattering results [97] (Fig. 25a) show a series of pulses that can be explained (Fig. 25b) by the incident pulse being reflected from the apex of the cylinder (I), from the stringer junction (II), traveling across the stringer and being back-reflected from its rear edge (III), or circumnavigating the shell as if it were smooth (IV).

Similar approaches were used in [98] where a shell was considered that was diagonally traversed by a plate attached to both walls of the shell. The plate-shell junctions were shown to act as reflectors for circumferential waves; these were excited on the shell surface by the incident wave at the known critical angle, traveled to the junction where they were reflected, and returned the same way they came in. If the plate was not in a position normal to the direction of incidence, but inclined,

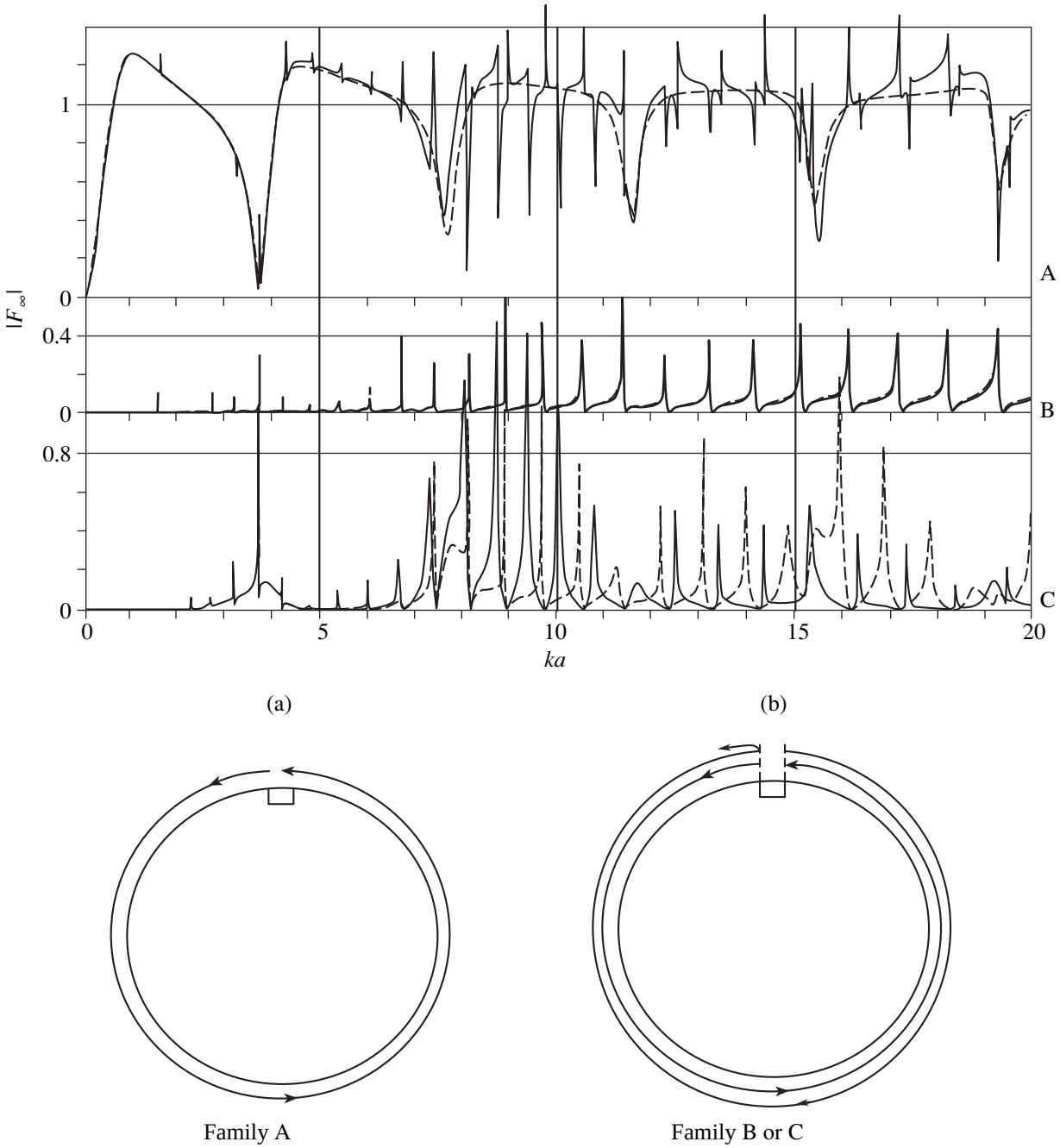

Fig. 23. (a) Backscattering amplitude vs. *ka* for a $b/a = 0.98$ aluminum shell with lengthwise stringer, from [96]; (b) explanation of frequency doubling in (a) by phase matching with and without reflection from the stringer, from [95].

the wave's surface path could be made very short and in this way, it was possible to observe the A_0 wave before it had time to decay. This approach is an alternative to observing the A_0 wave by visualization shortly after its creation [52]; see Fig. 9. It should be noted that [98] contains more useful information on A_0, A, and S_0 waves on smooth shells such as phase and group velocity dispersion curves, attenuation of these waves, and their critical angles.

SURFACE WAVES AND RESONANCES ON FLUID-LOADED THIN ELASTIC SPHERICAL SHELLS

The scattering amplitude for submersed spherical shells has been calculated and experimentally measured as a function of frequency, in a fashion that involved both the resonances of the target and the surface waves [7, 57, 103–111]. We might also mention

some calculations for spheroidal shells [112, 113] which can, however, not be discussed by us in detail here.

A series of publications on the scattering of waves from a spherical layer [114–118], which have been intended for geophysical applications, will however be discussed here to some extent since they provide us with the opportunity to familiarize the reader with a method called the "Generalized Debye Series Method" [119] that has also been applied to plates and to cylindrical shells [120, 121]. This analytic method can be used for the scattering from multilayered objects, provided all layer boundaries correspond to the coordinate surfaces of any of the eleven coordinate systems in which the wave equation is separable [122]. The basis of the method is a replacement of the known standard solution, obtained by Kramer's rule as the quotient of two huge determinants that each stem from satisfying the boundary conditions at all of the layer boundaries, by a solution that only contains the known ("local") transmission and reflection coefficients between layers and that is developed into a series of powers of matrices (the Generalized Debye series) which have immediate physical (geometrical) significance, as illustrated in Fig. 26.

If, for the multilayer case, the layers are labeled, starting from the top, by m, $m-1$, …, and $m+1$ labeling the overlying ambient medium, the solution satisfies

$$S_m = R_{m+1,m} + T_{m,m+1} S_m (1 - R_{m,m+1} S_m)^{-1} T_{m+1,m}, \tag{7a}$$

where 1 indicates the 4×4 unit matrix and S_{m+1} is

$$S_{m+1} = \begin{pmatrix} a_{m+1} & 0 & & \\ 0 & a'_{m+1} & & \\ & & a_{m+1} & 0 \\ & & 0 & a'_{m+1} \end{pmatrix}, \tag{7b}$$

a_{m+1} (and a'_{m+1}) being the amplitude of outgoing P waves (or SV waves, respectively) and the quantities R and T being reflection and transmission matrices defined in [114] or [119]. The resonances of the mth layer are obtained as the roots of the equation

$$\det(1 - R_{m,m+1} S_m) = 0. \tag{8}$$

If the multiply-reflected amplitudes are desired (Fig. 26), one may expand then using the Cayley–Hamilton theorem [123]:

$$(1 - R_{m,m+1} S_m)^{-1} = \sum_{p=1}^{\infty} (R_{m,m+1} S_m)^{p-1}. \tag{9}$$

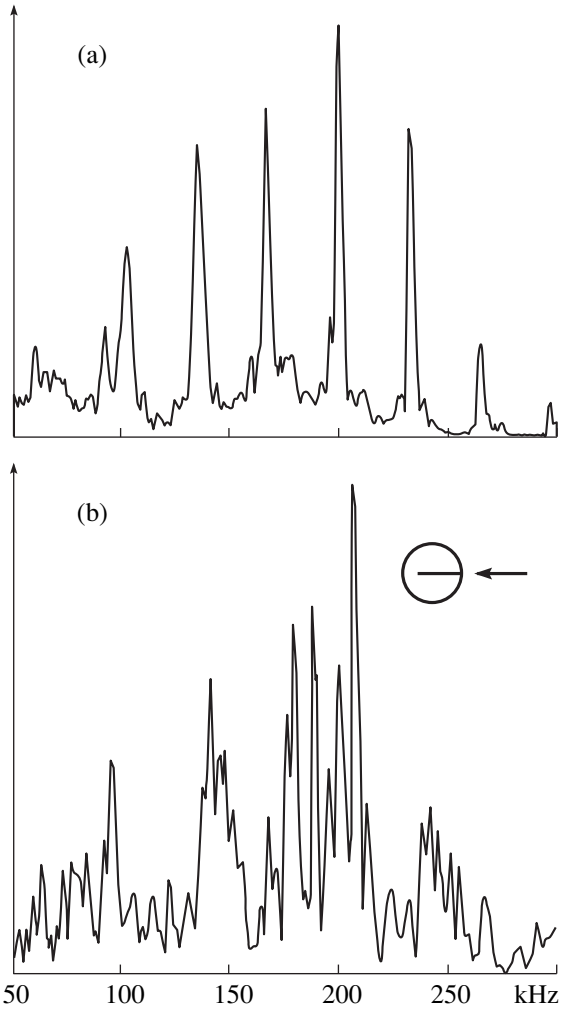

Fig. 24. Observed resonance amplitudes for (A) smooth and (B) stringer-reinforced stainless-steel cylindrical shell (from [97]).

This is the Generalized Debye series [119], which leads to a representation of the scattering solution in the ambient medium in terms of the various known "local" reflection and transmission coefficients at all the interfaces of the multilayer system, in a fashion symbolized by Fig. 26. Note, however, that the Debye series accomplishes this decomposition in an automatic fashion, without having to go through the detailed steps implied by Fig. 26.

An interpretation of calculated scattering amplitudes from a spherical shell, showing the scattering resonances and associating them with the phase matching of surface waves, was given, e.g., by [7, 103]. Figure 27 (from [7]) shows the resonances in the backscattering amplitude from a $b/a = 0.975$ thick evacuated spherical aluminum shell of outer radius a plotted vs. ka, with $k = \omega/c$ (c = sound velocity in the ambient water). Notice the similarity of this curve with those of a cylindrical shell, Fig. 5 (top portion) or Fig. 12 (leftmost portion). The analysis of the resonances was carried out

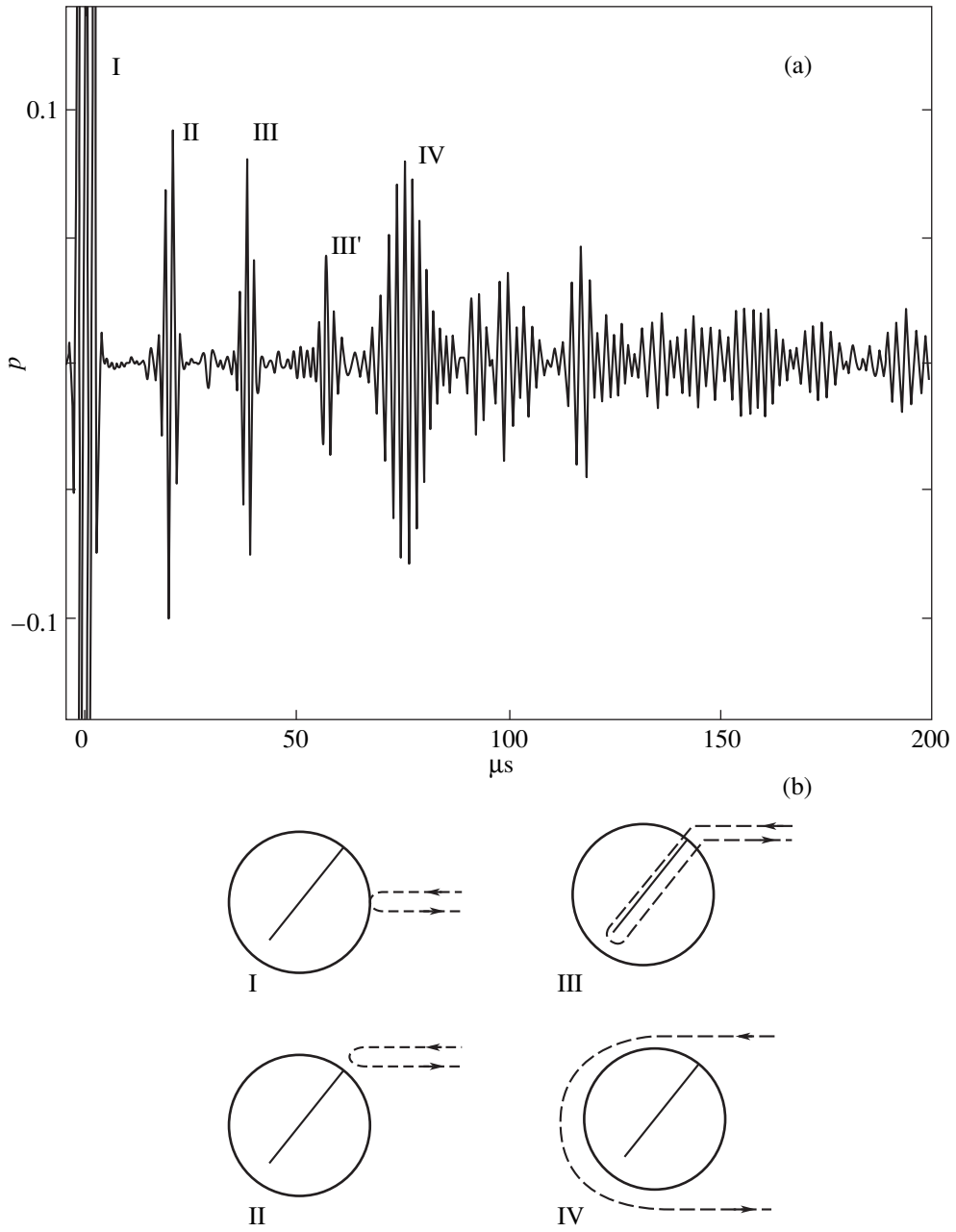

Fig. 25. (a) Short-pulse backscattering from a stringer-reinforced stainless-steel cylindrical shell, both (A) calculated and (B) observed, and (b) explanation of backscattering pulses by interaction with the stringer (from [97]).

using the plate dispersion curves of Fig. 3, to sufficient accuracy. The scale conversion from *fd* of the plate to *ka* is given by [1, 7, 51]

$$ka = (2\pi/c)\, fd/(1 - b/a). \tag{10}$$

For spherical geometry, the condition for the phase matching of circumferential waves that causes the resonances is (at the discrete resonance points)

$$c_p/c = (ka)^*/(n + 1/2), \tag{11}$$

c_p being the phase velocity of the circumferential wave and k^* the resonant wave number. Incidentally, the group velocity c_g of these waves, which in general is given by

$$c_g = [d/d(fd)(fd/c_p)]^{-1}, \tag{12a}$$

can also be obtained from the spacing $\Delta(ka)^*$ of the resonances [1, 16, 50, 51]

$$c_g/c = \Delta(ka)^* \tag{12b}$$

(at the discrete resonance points) and, alternately, from the arrival times of pulses in a transient experiment or calculation. Equation (11) represents a straight line

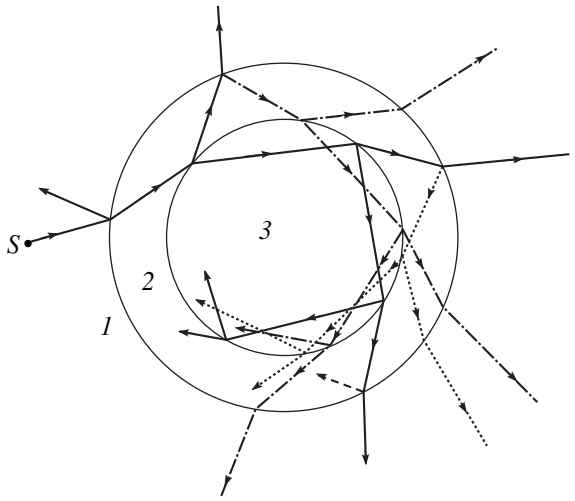

Fig. 26. Geometrical resolution of scattering process on a spherical shell by the Generalized Debye series (from [115]).

through the origin in Fig. 3 which, intersected with the c_p curve, predicts the resonance frequency k_n^* together with the mode number [1] n (as before for the cylindrical case), or, conversely, a known series of resonances k_n^* leads to a determination of c_p.

It should be noted that in calculated or measured backscattering amplitudes, a useful display of the scattering amplitudes can only be made if the background amplitude stemming from the wave geometrically reflected from the apex of the scatterer is coherently subtracted (e.g., going from part A to part B of Fig. 21). The prescription for this is given by the Resonance Scattering Theory [5] (RST) where it is suggested to subtract the scattering amplitude of a rigid object, for the case of a solid metal scatterer or a thick metal shell, or that of a soft object for a very thin evacuated or air filled shell. For the intermediate case of a not-so-thin shell, an exact intermediate background has been derived for the spherical case by Werby [61] or the use of the scattering amplitude for a corresponding fluid object has been suggested [124, 125]. Earlier suggestions for intermediate backgrounds are contained in [126, 127].

The result of an interpretation of Fig. 27 is the identification of resonances numbered $n = 40\ldots63$ in the frequency window of the Scholte–Stoneley wave (A), and of $n = 8\ldots20$ due to the S_0 Lamb wave. No individual A_0-wave resonances are visible. This wave, being flexural, is not excited below the coincidence frequency [109] (defined by $c_{p,A} = c$), and just above this frequency, the imaginary part of its wave vector is exceedingly large [16, 50, 51, 98] so that it will not propagate very far. Alternately speaking, it will give rise to resonances that are exceedingly wide. Many of these broad resonances overlap coherently.

The A wave does get excited below the coincidence frequency, but its resonances are visible only in a limited frequency window [45] (of about $ka = 30$–70 for the case of [7], Fig. 27). The reason for this is as follows: if the group velocity c_{gA} is obtained from Eq. (12), it is found to have a plateau over such a frequency region (i.e., if is rather nondispersive there) and circumnavigating wave packets interfere constructively to form resonances. Outside the region, the wave packets disperse. For the A_0 wave, no plateau of c_g is found, which is the same reason for its nonappearance in Fig. 27 as that given above (dispersive wave packets indicate $\mathrm{Im}k \neq 0$).

It should be noted that at very low frequencies, the plate model dispersion curves are not applicable to the spherical shell: an exact calculation shows [106] that here the A-wave curve (see Fig. 3) ceases to tend to zero, but instead turns up toward infinity (as does the A_0 curve for the case of no fluid loading, Fig. 28). The corresponding additional intersections with the straight-line

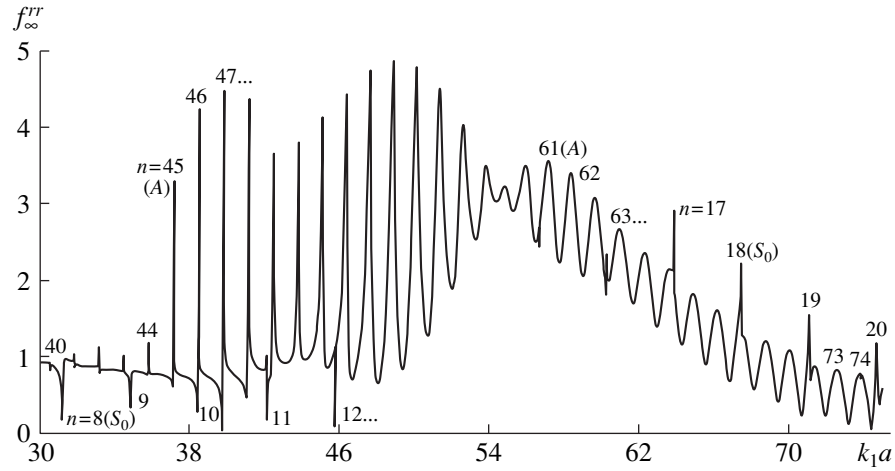

Fig. 27. Scattering-amplitude resonances for a $b/a = 0.975$ spherical aluminum shell in water (from [7]).

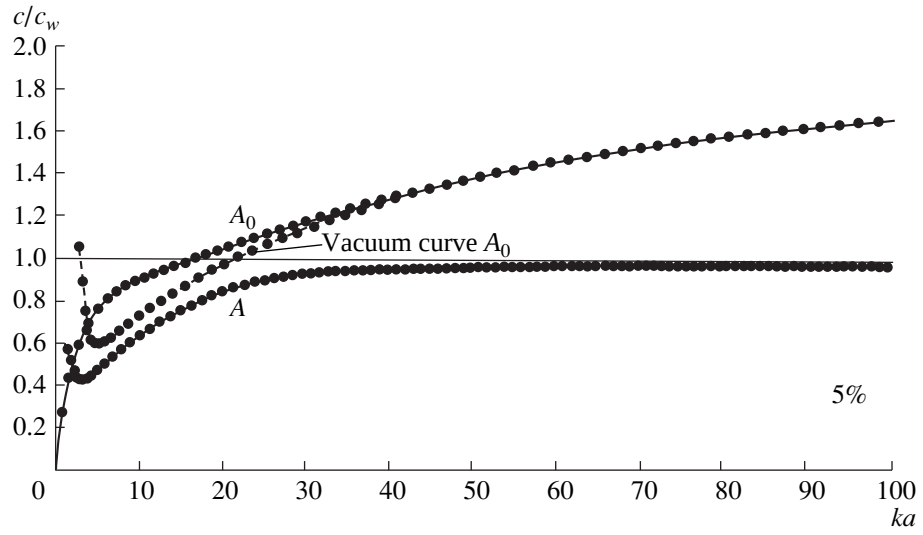

Fig. 28. A_0 and A wave phase velocity dispersion curves for a 5% thick spherical aluminum shell in water, and of the A_0 wave for a shell in vacuum (from [106] or [13]).

curve of Eq. (11) were shown [7] to give rise to what Junger and Feit [128] termed the lower ($j = 1$) branch of spherical shell vibration modes. More details on this will be given below.

The first resonance calculations for spherical shells [103, 104] have represented the resonances in a form where the resonance frequencies k^*a are plotted vs. the mode number n. The resulting curves are termed "Regge trajectories," after the way elementary particle masses (resonances) are plotted vs. the angular momentum quantum numbers [129]. Resonances of the A_0 ($l = 1$), S_0 ($l = 2$), and A_1 ($l = 3$) waves were found, and for the case of a spherical Fortal shell of $b/a = 0.80$ (Fig. 29), the A wave ($l = 0$) has also been found.

The most recent calculation of the resonances and circumferential-wave dispersion curves for spherical shells has interpreted [111] the phenomenon of low-frequency upturning of the A wave dispersion curve for fluid-immersed spherical shells (or of the A_0 wave for the case of a shell in vacuum) that was mentioned in connection with Fig. 28. These A wave (solid-line) curves were calculated [106] for 5 and 2% thick aluminum shells as shown in Fig. 30, and the points of a resonance calculation [7] for the 5% shell are entered here and show perfect agreement. For the case of steel

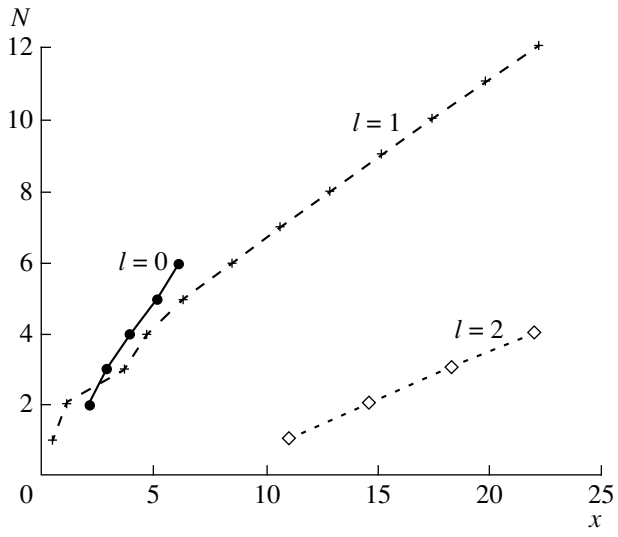

Fig. 29. Regge trajectories of surface waves on a $b/a = 0.80$ spherical Fortal shell (from [104]).

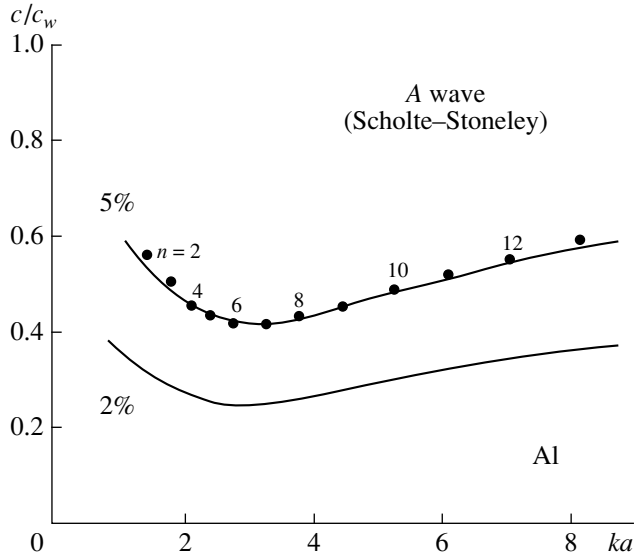

Fig. 30. A wave dispersion curves for 5 and 2% thick spherical aluminum shells in water (from [111]).

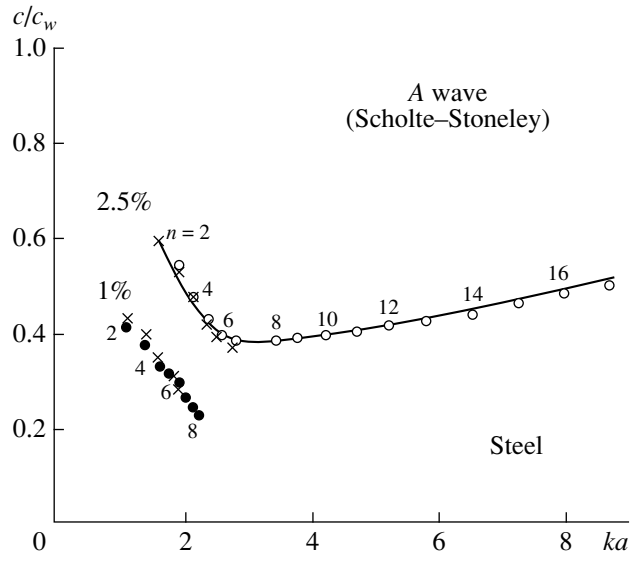

Fig. 31. A-wave dispersion curves for 2.5 and 1% thick spherical steel shells in water (from [111]).

shells, the corresponding results were formerly still unavailable since in fact, some results in the earlier literature contradict the interpretation offered by Fig. 30. The study of [111] has now presented 2.5- and 1%-thickness steel-shell results (Fig. 31) in complete analogy with those of the aluminum shell shown in Fig. 30. The calculated solid-line *A* wave dispersion curve is due to [130]; it has been extended here to a lower frequency, drawn through the resonance points to provide an analogy to the aluminum curve of Fig. 30. The circles are resonance frequencies from the calculations of [131]. The low-frequency upturn of the *A* wave dispersion curves is thus confirmed here for the 2.5% steel shell also, and the Junger resonances [128] (dark points) for the 1% steel shell are, by a comparison with the aluminum case of Fig. 30, recognized here as belonging to the *A* wave and, in particular, corresponding to the low-frequency upturn of the *A* wave dispersion curve for the 1% steel shell.

CONCLUSIONS

Over the last several decades, the study of acoustic-wave scattering from elastic shells has led to a unified picture of the physical phenomena involved, due to the understanding that has been gained regarding the role played by the surface waves (circumferentially or axially propagating) when they are excited in the scattering process, and of the prominent resonances which they engender by phase matching. The main progress in shell scattering can thus be summarized as our acquired understanding of the resonance phenomena and their causes, rather than as simply verifying their existence. The resonances can be used to furnish information on the properties of the surface waves due to the one-to-one relationship between these two phenomena, this in a sense providing a solution of the inverse scattering problem or at least of one important aspect of it.

REFERENCES

1. J. P. Sessarego, J. Sageloli, C. Gazanhes, and H. Überall, J. Acoust. Soc. Am. **101**, 135 (1997).
2. H. Überall, in *Physical Acoustics*, Ed. by W. P. Mason and R. N. Thurston (Academic Press, New York, 1973), Vol. 10, pp. 1–60.
3. H. Überall, P. P. Delsanto, J. D. Alemar, *et al.*, Appl. Mech. Rev. **43**, 235 (1990).
4. H. Überall, A. Gérard, A. Guran, *et al.*, Appl. Mech. Rev. **49**, S63 (1996).
5. L. Flax, L. R. Dragonette, and H. Überall, J. Acoust. Soc. Am. **63**, 723 (1978).
6. Lord Rayleigh, *Theory of Sound* (reprinted) (Dover, New York, 1945).
7. M. Talmant, H. Überall, R. D. Miller, *et al.*, J. Acoust. Soc. Am. **86**, 278 (1989).
8. J. M. D'Archangelo, P. Savage, H. Überall, *et al.*, J. Acoust. Soc. Am. **77**, 6 (1985).
9. H. Überall, P. J. Moser, B. L. Merchant, *et al.*, J. Appl. Phys. **58**, 2109 (1985).
10. R. Stoneley, Proc. R. Soc. London, Ser. A **106**, 416 (1924).
11. J. C. Scholte, Proc. K. Ned. Akad. Wet. **45**, 20 (1942); **45**, 159 (1942).
12. X. L. Bao, P. K. Raju, and H. Überall, J. Acoust. Soc. Am. **105**, 2704 (1999).
13. H. Überall, B. Hosten, M. Deschamps, and A. Gérard, J. Acoust. Soc. Am. **96**, 908 (1994).
14. A. Guran and H. Überall, in *Elastic Waves*, Ed. by A. Guran (Birkhäuser, Basel, Switzerland, 2000).
15. L. M. Brekhovskikh, *Waves in Layered Media*, 1st ed. (Academic Press, New York, 1960).
16. M. Talmant, PhD Thesis (Univ. of Paris VII, 1987); M. Talmant and G. Quentin, J. Acoust. **1**, 153 (1988); M. Talmant, J. M. Conoir, and J. L. Rousselot, Acta Acust. **3**, 509 (1995).
17. A. Grabovska, Arch. Acoust. **4**, 57 (1979).
18. X. L. Bao, H. Franklin, P. K. Raju, and H. Überall, J. Acoust. Soc. Am. **102**, 1246 (1997).
19. X. L. Bao, H. Franklin, P. K. Raju, *et al.*, Acta Acust. **84**, 823 (1998).
20. J. Dickey, G. Maidanik, and H. Überall, J. Acoust. Soc. Am. **98**, 2365 (1995).
21. A. Freedman, J. Sound Vibr. **183**, 719 (1995).
22. A. D. Pierce and H. G. Kil, J. Vib. Acoust. **112**, 399 (1990).
23. H. Überall, X. L. Bao, R. D. Miller, and M. F. Werby, in *Proceedings of Second International Congress on Recent Developments in Air- and Structure-Borne Sound and Vib.* (Auburn Univ., Auburn, AL, 1992), pp. 1195–1202.
24. L. M. Lyamshev, *Sound Reflection by Thin Plates and Shells in a Fluid* (Akad. Nauk SSSR, Moscow, 1955), p. 73.
25. L. M. Lyamshev, Akust. Zh. **2**, 188 (1956) [Sov. Phys. Acoust. **2**, 198 (1956)].

26. L. M. Lyamshev, Dokl. Akad. Nauk SSSR **115**, 271 (1957) [Sov. Phys. Dokl. **2**, 332 (1957)].
27. L. M. Lyamshev, Akust. Zh. **4**, 51 (1958) [Sov. Phys. Acoust. **4**, 50 (1958)].
28. L. M. Lyamshev, Akust. Zh. **4**, 161 (1958) [Sov. Phys. Acoust. **4**, 161 (1958)].
29. L. M. Lyamshev, Dokl. Akad. Nauk SSSR **125**, 1231 (1959) [Sov. Phys. Dokl. **4**, 406 (1959)].
30. V. V. Muzychenko and S. A. Rybak, Akust. Zh. **34**, 561 (1988) [Sov. Phys. Acoust. **34**, 325 (1988)].
31. A. L. Gol'denveĭzer, *Theory of Thin Elastic Shells* (Nauka, Moscow, 1976).
32. N. D. Veksler and V. M. Korsunskii, Acoust. Lett. **6**, 70 (1982).
33. N. D. Veksler, Acustica **69**, 63 (1989).
34. M. Talmant, G. Quentin, J. L. Rousselot, *et al.*, J. Acoust. Soc. Am. **84**, 681 (1988).
35. H. Überall, L. R. Dragonette, and L. Flax, J. Acoust. Soc. Am. **61**, 711 (1977).
36. L. Flax, L. R. Dragonette, and H. Überall, J. Acoust. Soc. Am. **63**, 723 (1978).
37. X. L. Bao, H. Überall, P. K. Raju, *et al.*, *Waves on Fluid-loaded Shells and Their Resonance Frequency Spectrum* (Preprint).
38. F. Lecroq, G. Maze, D. Décultot, and J. Ripoche, J. Acoust. Soc. Am. **95**, 762 (1994).
39. F. Léon, F. Lecroq, D. Décultot, and G. Maze, J. Acoust. Soc. Am. **91**, 1388 (1992).
40. J. M. Conoir, P. Rembert, O. Lenoir, and J. L. Izbicki, J. Acoust. Soc. Am. **93**, 1300 (1993).
41. J. M. Conoir, P. Rembert, and J. L. Izbicki, in *Acoustic Interactions with Submerged Elastic Structures (Series on Stability, Vibration, and Control of Structures)*, Ed. by A. Guran *et al.* (World Sci., Singapore and New York, 1996), Vol. 1, pp. 81–128.
42. A. Sommerfeld, *Optics* (Academic Press, New York, 1967).
43. H. Überall, Y. J. Stoyanov, A. Nagl, *et al.*, J. Acoust. Soc. Am. **81**, 312 (1987).
44. J. V. Subrahmanyam, PhD Thesis (Catholic Univ. of America, Washington, DC, 1983).
45. J. D. Murphy, E. D. Breitenbach, and H. Überall, J. Acoust. Soc. Am. **64**, 677 (1978).
46. E. D. Breitenbach, H. Überall, and K. B. Yoo, J. Acoust. Soc. Am. **74**, 1267 (1983).
47. G. Maze, F. Léon, J. Ripoche, *et al.*, Acustica **81**, 201 (1995).
48. G. Maze, F. Léon, J. Ripoche, and H. Überall, J. Acoust. Soc. Am. **105**, 1695 (1999).
49. D. Royer, M. H. Noroy, and M. Fink, J. Phys. III **4**, 673 (1994).
50. G. Quentin and M. Talmant, in *Elastic Wave Propagation*, Ed. by M. F. McCarthy and M. A. Hayes (Elsevier Sci., North Holland, Amsterdam, 1989), pp. 477–482.
51. M. Talmant and G. Quentin, J. Appl. Phys. **63**, 1857 (1988).
52. A. C. Ahyi, P. Pernod, O. Gatti, *et al.*, J. Acoust. Soc. Am. **104**, 2727 (1998); A. C. Ahyi, PhD Thesis (Univ. of Science and Technology of Lille I, 1997).
53. C. Cranz and H. Schardin, Z. Phys. **56**, 147 (1929).
54. H. Überall, R. D. Doolittle, and J. V. McNicholas, J. Acoust. Soc. Am. **39**, 561 (1966).
55. P. Uginčius and H. Überall, J. Acoust. Soc. Am. **43**, 1025 (1968).
56. J. Metsaveer and A. Klauson, J. Acoust. Soc. Am. **100**, 1551 (1996).
57. M. F. Werby and H. Überall, in *Proceedings of Second International Conference on Recent Developments in Air- and Structure-Borne Sound and Vib.* (Auburn Univ., Auburn, AL, 1992), p. 1653.
58. G. Maze, A. Baillard, V. Latard, *et al.*, in *Proceedings of the 1999 ASME Design Engineering Technical Conferences* (Las Vegas, NV, 1999), DETC99/VIB-8090.
59. A. Gérard, J. L. Rousselot, J. L. Izbicki, *et al.*, Rev. Phys. Appl. **23**, 289 (1988).
60. N. D. Veksler, J. L. Izbicki, and J. M. Conoir, J. Acoust. Soc. Am. **96**, 287 (1994).
61. M. F. Werby, Acoust. Lett. **15**, 65 (1991).
62. Y. P. Guo, J. Acoust. Soc. Am. **95**, 2006 (1994).
63. H. Batard, G. Quentin, J. M. Conoir, and J. L. Rousselot, J. Acoust. **3**, 337 (1990).
64. H. Batard and G. J. Quentin, J. Acoust. Soc. Am. **91**, 581 (1992).
65. H. Batard, G. J. Quentin, and M. Talmant, J. Acoust. **5**, 493 (1992).
66. H. Batard, M. Talmant, and G. J. Quentin, Acta Acust. **2**, 333 (1994).
67. G. J. Quentin and A. Cand, Electron. Lett. **25**, 353 (1989).
68. R. Kumar, Acustica **27**, 317 (1972).
69. R. Kumar and R. W. B. Stephens, Proc. R. Soc. London, Ser. A **329**, 283 (1972).
70. H. Hönl, A. W. Maue, and K. Westpfahl, in *Handbuch der Physik XXV/l, Kristalloptik-Beugung* (Springer, Berlin, 1956), pp. 218–591; W. Franz and K. Deppermann, Ann. Phys. **10**, 361 (1952); W. Franz and K. Klante, IRE Trans. Antennas Propag. **7**, S68 (1959).
71. B. P. Belinskiy, J. P. Dauer, and H. Überall, Acta Mech. (in press).
72. R. D. Miller, X. L. Bao, and H. Überall, in *Proceedings of Meeting of the American Society of Mechanical Engineers: Structural Acoustics*, Ed. by R. F. Keltie *et al.* (1991), NCA **12**/AMD **128**, pp. 251–257.
73. M. F. Werby, R. D. Miller, G. Maze, *et al.*, in *Computational Acoustics*, Ed. by R. L. Lau, D. Lee, and A. R. Robinson (Elsevier, North Holland, Amsterdam, 1993), Vol. 1, pp. 285–291.
74. D. Décultot, F. Lecroq, G. Maze, *et al.*, in *Theoretical and Computation Acoustics*, Ed. by J. E. Ffowcs Williams, D. Lee, and A. D. Pierce (World Sci., Singapore, 1994), Vol. 1, pp. 163–175.
75. R. D. Miller, E. T. Moyer, H. Huang, and H. Überall, J. Acoust. Soc. Am. **89**, 2185 (1991).
76. J. D. Kaplunov and N. D. Veksler, Acustica **72**, 131 (1990).
77. G. Maze, J. L. Izbicki, and J. Ripoche, J. Acoust. Soc. Am. **77**, 1352 (1985).
78. J. Ripoche and G. Maze, in *Acoustic Resonance Scattering*, Ed. by H. Überall (Gordon and Breach, Newark, NJ, 1992), pp. 69–103.

79. F. Léon and G. Maze, in *Acoustic Interactions with Submerged Elastic Structures*, Series on Stability, Vibration and Control of Structures, Ed. by A. Guran *et al.* (World Sci., Singapore, 2000), Vol. 2.
80. A. Nagl, H. Überall, P. P. Delsanto, *et al.*, Wave Motion **5**, 235 (1983).
81. H. Überall, Trait. Signal **2** (5), 381 (1985).
82. G. Maze, and J. Ripoche, in *New Perspectives on Problems in Classical and Quantum Physics*, Ed. by P. P. Delsanto and A. W. Sáenz (Gordon and Breach, Newark, NJ, 1998), pp. 157–200.
83. M. V. Bernblit, Sov. Phys. Acoust. **20**, 414 (1975).
84. M. V. Bernblit, Sov. Phys. Acoust. **21**, 518 (1975).
85. C. B. Burroughs, J. Acoust. Soc. Am. **75**, 715 (1984).
86. C. B. Burroughs and J. E. Hallander, J. Acoust. Soc. Am. **91**, 2721 (1992).
87. M. El-Raheb and P. Wagner, J. Acoust. Soc. Am. **85**, 2452 (1989).
88. P. J. Moser, H. Überall, and J. R. Yuan, J. Acoust. Soc. Am. **94**, 3342 (1993).
89. Y. P. Guo, J. Acoust. Soc. Am., Part 1 **90**, 2342 (1991).
90. Y. P. Guo, J. Acoust. Soc. Am., Part 2 **90**, 2342 (1991).
91. Y. P. Guo, J. Acoust. Soc. Am. **91**, 926 (1992).
92. Y. P. Guo, J. Acoust. Soc. Am. **93**, 1936 (1993).
93. L. B. Felsen and Y. P. Guo, J. Acoust. Soc. Am. **94**, 888 (1993).
94. J. Missaoui, L. Cheng, and M. J. Richard, J. Sound Vibr. **190**, 21 (1996).
95. O. Poncelet, A. Gérard, M. Deschamps, *et al.*, J. Comput. Acoust. (in press).
96. A. Klauson and J. Metsaveer, J. Acoust. Soc. Am. **91**, 1834 (1992).
97. A. Klauson, J. Metsaveer, D. Décultot, *et al.*, J. Acoust. Soc. Am. **100**, 3135 (1996).
98. A. Baillard, J. M. Conoir, D. Décultot, *et al.*, in *Proceedings of the 1999 ASME Design Engineering Technical Conferences* (Las Vegas, NV, 1999), DETC 99/VIB-8092.
99. J. B. Keller, J. Opt. Soc. Am. **52**, 116 (1962).
100. B. L. Woolley, J. Acoust. Soc. Am. **67**, 1642 (1980).
101. A. Klauson and J. Metsaveer, Sov. Phys. Acoust. **35**, 42 (1989).
102. J. Chiumia, N. Touraine, A. Klauson, *et al.*, Acoust. Lett. **20**, 162 (1997).
103. A. Gérard and J. L. Rousselot, Rev. Cethedec **78**, 121 (1984).
104. J. L. Rousselot, A. Gérard, J. P. Sessarego, and J. Sagéloli, Acustica **66**, 204 (1988).
105. M. Zakharia, P. Flandin, J. Sagéloli, and J. P. Sessarego, J. Acoust. **1**, 185 (1988).
106. G. S. Sammelmann, D. H. Trivett, and R. H. Hackman, J. Acoust. Soc. Am. **85**, 114 (1989).
107. M. F. Werby and J. W. Dickey, in *Acoustic Resonance Scattering*, Ed. by H. Überall (Gordon and Breach, Newark, NJ, 1992), pp. 257–275.
108. M. F. Werby, in *Acoustic Resonance Scattering*, Ed. by H. Überall (Gordon and Breach, Newark, NJ, 1992), pp. 277–303.
109. M. F. Werby and H. Überall, J. Phys. IV **2**, 1087 (1992).
110. J. D. Kaplunov, E. V. Nolde, and N. D. Veksler, Acustica **76**, 10 (1992).
111. H. Überall, I. K. Bjørnø, and L. Bjørnø, Ultrasonics (in press).
112. M. F. Werby and L. H. Green, J. Acoust. Soc. Am. **81**, 783 (1987).
113. M. F. Werby and R. B. Evans, IEEE J. Ocean Eng. **12**, 370 (1987).
114. A. Gérard, C. R. Acad. Sci., Paris **278**, 1055 (1974).
115. A. Gérard, Int. J. Eng. Sci. **17**, 313 (1979).
116. A. Gérard, C. R. Acad. Sci., Paris **290**, B43 (1980).
117. A. Gérard, Int. J. Eng. Sci. **18**, 583 (1980).
118. A. Gérard, J. Acoust. Soc. Am. **73**, 13 (1983).
119. A. Gérard, H. Überall, and A. Guran, Acta Mech. **132**, 147 (1999).
120. J. M. Conoir, A. Gérard, and A. Derem, J. Acoust. **4**, 159 (l991).
121. A. Grosse-Tête, A. Gérard, and J. L. Rousselot, Trait. Signal **2**, 397 (1985).
122. P. M. Morse and H. Feshbach, *Methods of Theoretical Physics* (McGraw Hill, New York, 1953).
123. R. Courant and D. Hilbert, *Methods of Mathematical Physics* (Interscience, New York, 1953), Vol. 1.
124. N. D. Veksler, Acustica **76**, 1 (1992).
125. L. G. Zhang, N. H. Sun, and P. L. Marston, J. Acoust. Soc. Am. **91**, 1862 (1992).
126. J. D. Murphy, J. George, and H. Überall, Wave Motion **1**, 141 (1979).
127. J. D. Murphy, J. George, A. Nagl, and H. Überall, J. Acoust. Soc. Am. **65**, 368 (1979).
128. M. C. Junger and D. Feit, *Sound, Structures and Their Interaction*, 2nd ed. (MIT, Cambridge, MA, 1986), p. 282.
129. R. G. Newton, *Scattering Theory of Waves and Particles* (McGraw Hill, New York, 1966).
130. G. Kaduchak and P. L. Marston, J. Acoust. Soc. Am. **93**, 224 (1993).
131. P. L. Marston and N. H. Sun, J. Acoust. Soc. Am. **92**, 3315 (1992).

Acoustical Physics, Vol. 47, No. 2, 2001, pp. 140–144. Translated from Akusticheskiĭ Zhurnal, Vol. 47, No. 2, 2001, pp. 178–182.

REVIEWS

Mechanisms of Interaction between Ultrasound and Sound in Liquids with Bubbles: Singular Focusing

I. Sh. Akhatov and D. B. Khismatullin

Institute of Mechanics, Ufa Scientific Center, Russian Academy of Sciences, ul. K. Marksa 12, Ufa, 450000 Russia

e-mail: damir-k@anrb.ru

Received December 14, 1999

Abstract—A two-dimensional interaction between long-wave (sound) and short-wave (ultrasound) pressure perturbations in a rarefied monodisperse mixture of a weakly compressible liquid with gas bubbles is considered. The conditions at which this interaction leads to a singular focusing (an explosive instability) of ultrasound are determined. A numerical study of the defocusing and the singular focusing in a bubbly liquid is carried out. The effect of the long-wave–short-wave resonance on the development of two-dimensional disturbances is studied. © *2001 MAIK "Nauka/Interperiodica".*

A liquid with gas bubbles exhibits pronounced nonlinear acoustic properties due to the nonlinear character of the bubble oscillations and the high compressibility of the bubbles. The theoretical and experimental studies performed in the last few decades revealed many types of nonlinear wave phenomena in bubbly liquids: the self-focusing of ultrasound [1, 2], the self-clarification of sound [3], wavefront reversal [4], the acoustic echo [5], subharmonic wave generation [6, 7], the focusing and amplification of waves in inhomogeneous bubbly liquids [8, 9], and pattern formation in acoustic cavitation [10–12].

For a bubbly liquid, the dispersion curve representing the frequency dependence of the wave number of the disturbance consists of two branches [13]: the low-frequency branch and the high-frequency one. Therefore, in this medium, a simultaneous propagation of long (sound) and short (ultrasound) waves is possible. The propagation of these waves in the medium is accompanied by the energy transfer between them through the mechanism of the long-wave–short-wave interaction [14]. This interaction is most pronounced when the group velocity of the short waves coincides with the phase velocity of the long wave (the long-wave–short-wave resonance [15]). The physical systems in which the long-wave–short-wave resonance can occur include, e.g., waves on the water surface [16] and plasma [17]. Our recent studies [18] show that bubbly liquids also belong to such systems.

In the one-dimensional case, the nonresonance long-wave–short–wave interaction is described by the nonlinear Schrödinger equation for the short-wave envelope [19] and the resonance interaction is described by the Zakharov system of equations [17]. Both these systems have a solution in the form of the envelope soliton [20, 21], which is known to be an example of the one-dimensional focusing of perturbations. In the case of a two-dimensional nonresonance interaction, the Davey–Stewartson system of equations [22] also describes the focusing process. As a rule, the two-dimensional focusing is singular; i.e., it leads to the development of an explosive instability [23, 24]. Only with specially selected coefficients, does the Davey–Stewartson system of equations become integrable and have localized bounded solutions.

In our previous paper [25], we showed that, in a bubbly liquid, the two-dimensional interaction of long and short waves is described by equations that can be reduced to the Davey–Stewartson system and, for some parameters of the liquid, to one of its integrable versions (the Davey–Stewartson equations). In this paper, we derive the conditions for the singular focusing of ultrasound in bubbly liquids and perform its numerical study. We analyze the effect of the long-wave–short-wave resonance on the development of singular focusing.

Let us consider the conditions of a singular focusing. The equations describing the two-dimensional interaction between ultrasound and sound in bubbly liquids were obtained in our previous paper [25] by the multiscale method:

$$\begin{aligned}(c_g^2 - c_e^2)L_{\xi\xi} - c_e^2 L_{\zeta\zeta} &= \alpha(|S|^2)_{\xi\xi},\\ iS_\tau + \beta S_{\xi\xi} + \varrho S_{\zeta\zeta} + \gamma|S|^2 S &= \delta LS.\end{aligned} \tag{1}$$

Here, L is the profile of the long (sound) wave, S is the short (ultrasound) wave envelope, $\xi = \varepsilon(x - c_g t)$, $\zeta = \varepsilon y$, and $\tau = \varepsilon^2 t$ (ε is the parameter characterizing the smallness of the short-wave amplitude). The group velocity of the short waves c_g; the equilibrium velocity of the long wave c_e; and the coefficients α, β, ϱ, γ, and δ depend on the polytropic index κ, the parameter b =

$\sqrt{p_0\rho_{l0}^{-1}\alpha_{g0}^{-1}C_l^{-2}}$, the wave number of the short wave k_s, and its cyclic frequency ω_s [25].

Applying the substitution $L \longrightarrow \delta^{-1}\partial\psi/\partial\xi$ ($\delta \neq 0$) and introducing the notation $\sigma = c_e^{-2}(c_e^2 - c_g^2)$, we reduce the system of Eqs. (1) to the Davey–Stewartson equations:

$$\begin{aligned} \sigma\Psi_{\xi\xi} + \Psi_{\zeta\zeta} &= -\alpha\delta c_e^{-2}(|S|^2)_\xi, \\ iS_\tau + \beta S_{\xi\xi} + \varrho S_{\zeta\zeta} + \gamma|S|^2 S &= S\Psi_\xi. \end{aligned} \tag{2}$$

It is known [23, 24] that, in the nonintegrable case, if the coefficients β, ϱ, σ, and $\alpha\delta/c_e^2$ are positive and $\gamma > 0$ or $|\gamma| < \alpha\delta/c_e^2$, the solution to Eqs. (2) with the boundary condition

$$|S| \longrightarrow 0 \quad \text{for} \quad \xi^2 + \zeta^2 \longrightarrow \infty$$

tends to infinity for sufficiently large amplitudes within a finite time interval (the effect of singular focusing or an explosive instability). The existence of the singular focusing in nonlinear optics is confirmed by the experimental data [26]. For another choice of coefficients, any initially localized solutions to this system are defocused, i.e., spread in space.

If the solution to system (2) exists and tends to zero when $\xi^2 + \zeta^2 \longrightarrow \infty$, the following conservation laws are valid [27]:

$$M = \int\int_{-\infty}^{+\infty} |S|^2 d\xi d\zeta,$$

$$P_x = \int\int_{-\infty}^{+\infty} \left(S^*\frac{\partial S}{\partial\xi} - S\frac{\partial S^*}{\partial\xi}\right) d\xi d\zeta,$$

$$p_y = \int\int_{-\infty}^{+\infty} \left(S^*\frac{\partial S}{\partial\zeta} - S\frac{\partial S^*}{\partial\zeta}\right) d\xi d\zeta,$$

$$E = \int\int_{-\infty}^{+\infty} \left[\beta\left|\frac{\partial S}{\partial\xi}\right|^2 + \varrho\left|\frac{\partial S}{\partial\zeta}\right|^2 - \frac{1}{2}\left(\gamma|S|^4 + \frac{\sigma c_e^2}{\alpha\delta}\left|\frac{\partial\Psi}{\partial\xi}\right|^2 + \frac{c_e^2}{\alpha\delta}\left|\frac{\partial\Psi}{\partial\zeta}\right|^2\right)\right] d\xi d\zeta.$$

The first of these integrals can be interpreted as the "mass" of the short wave, the second and third integrals as the components of the "momentum" of the short wave, and the fourth integral as the "energy" of the long-wave–short-wave system, although these integrals have nothing to do with the physical conservation laws [23].

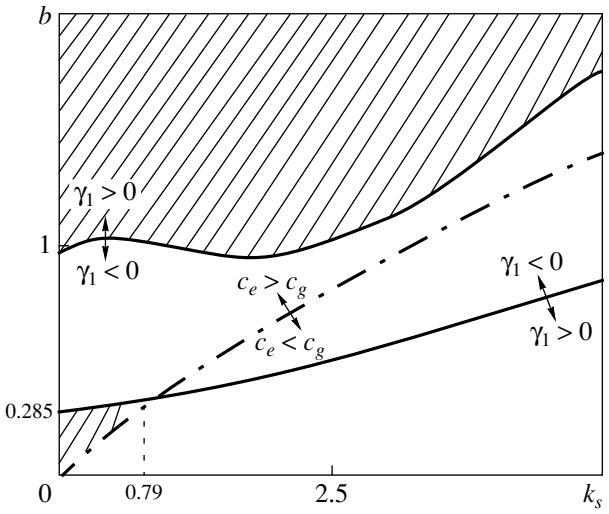

Fig. 1. Regions of explosive instability (hatched) in the (k_s, b) plane. The coefficient is $\gamma_l = \gamma + \alpha\delta/c_e^2$.

For the Davey–Stewartson equations (2), the following relationship is valid [27]:

$$\frac{d^2}{dt^2}\int\int_{-\infty}^{+\infty}\left(\frac{\xi^2}{\varrho} + \frac{\zeta^2}{\beta}\right)|S|^2 d\xi d\zeta = 8E.$$

This relationship can be easily integrated:

$$I = \int\int_{-\infty}^{+\infty}\left(\frac{\xi^2}{\varrho} + \frac{\zeta^2}{\beta}\right)|S|^2 d\xi d\zeta = 8Et^2 + At + B \tag{3}$$

(A and B are the integration constants). In terms of the above representation, the integral I can be considered as the "moment of inertia" of the short wave. Then, Eq. (3) will be an example of the virial theorem.

In the conditions of singular focusing (see above) and for sufficiently large wave amplitudes, the "energy" E can be negative [23]. Then, according to Eq. (3), the integral I, which is a positive definite quantity, will become zero at some instant of time. Since the "mass" of the short wave is conserved, its "moment of inertia" can become zero, if the short-wave perturbation will be concentrated near a single point (a focus). Such a redistribution of the "mass" of the wave leads to a sharp increase in the wave amplitude at this point and, finally, to an explosive instability.

The existence of a "negative-energy" wave and, as a consequence, the development of the singular focusing is caused by the instability of the solitons of the nonlinear Schrödinger equation envelope to transverse long-wave perturbations. This statement is confirmed experimentally for waves on the water surface [28]. Therefore, the theory developed for one-dimensional enve-

lope waves does not apply to waves with dimension 2 and higher.

For a bubbly liquid, the coefficients β and ρ are always positive and α and δ are of the same sign. Hence, in such a liquid, a singular focusing of an ultrasonic wave is possible, provided that the following conditions are satisfied:

$$c_e > c_g, \quad \gamma > -\left|\alpha\delta/c_e^2\right|. \tag{4}$$

Figure 1 shows (by hatching) the explosive instability zones determined by conditions (4) in the (k_s, b) plane.

Figures 2–5 present the results of the numerical analysis of Eqs. (1). The numerical integration of this system of equations was performed using the Fourier transform method [29] for the first equation and the variable directions scheme [11, 30] for the second equation. We considered the boundary conditions

$$L(\xi, \zeta), \quad S(\tau, \xi, \zeta) = 0,$$
$$\text{for } \xi^2 + \zeta^2 \longrightarrow \infty$$

and the initial condition

$$S(\tau = 0, \xi, \zeta) = S_0 \exp\{-(\xi^2 + \zeta^2)\}.$$

Here, S_0 is the real amplitude. The coefficients were selected so as to satisfy the condition $c_e > c_g$ (in this case, the first equation is an elliptic one). We analyzed

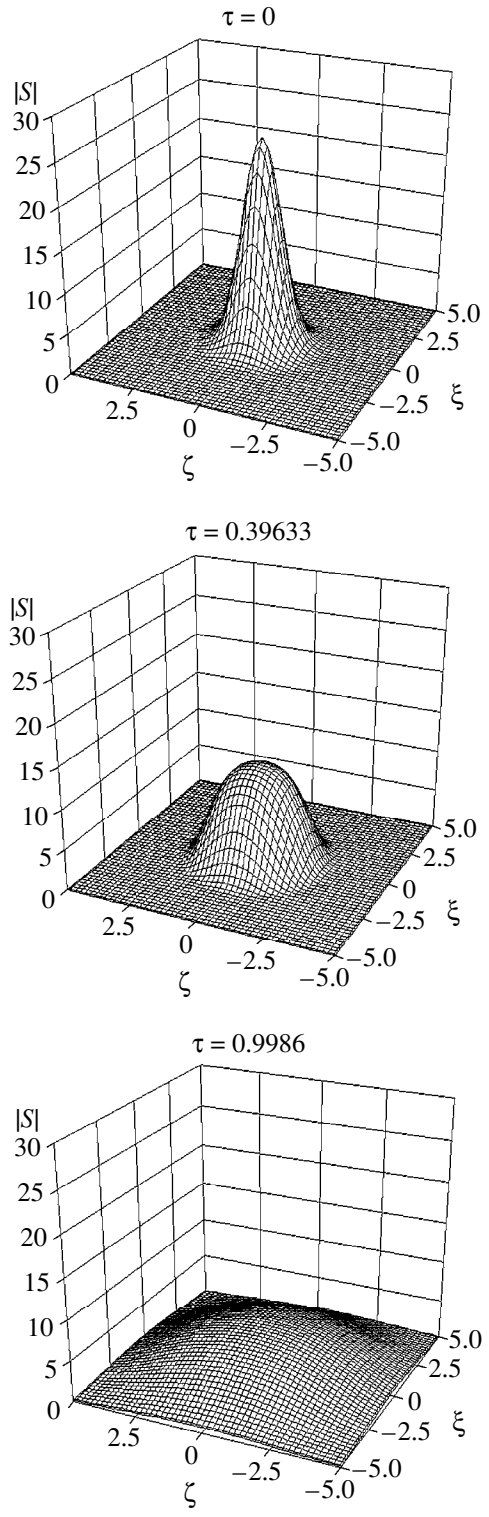

Fig. 2. Nonresonance focusing of the short-wave envelope $|S|$.

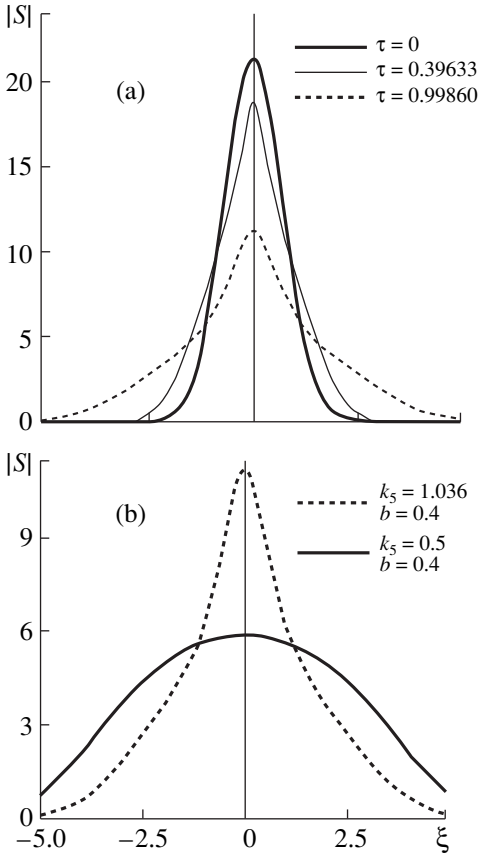

Fig. 3. Effect of the long-wave–short-wave resonance on the defocusing process in a bubbly liquid: (a) dependence of the short-wave envelope $|S|$ on the spatial coordinate ξ ($\zeta = 0$) at various instants of time; (b) comparison of the dependences of $|S|$ on ξ in the nonresonance (the solid line) and resonance (the dashed line) cases at $\tau = 0.9986$.

four cases: (1) $k_s = 0.5$, $b = 0.4$; (2) $k_s = 1.036$, $b = 0.4$; (3) $k_s = 0.5$, $b = 0.25$; and (4) $k_s = 0.574$, $b = 0.25$. The first case corresponds to a nonresonance stable interaction, because $c_g \neq c_e$ and the point (0.5, 0.4) lies in the stability zone (see Fig. 1). The numerical analysis confirms the analytical results: in this case, a defocusing occurs for both long and short waves (Fig. 2).

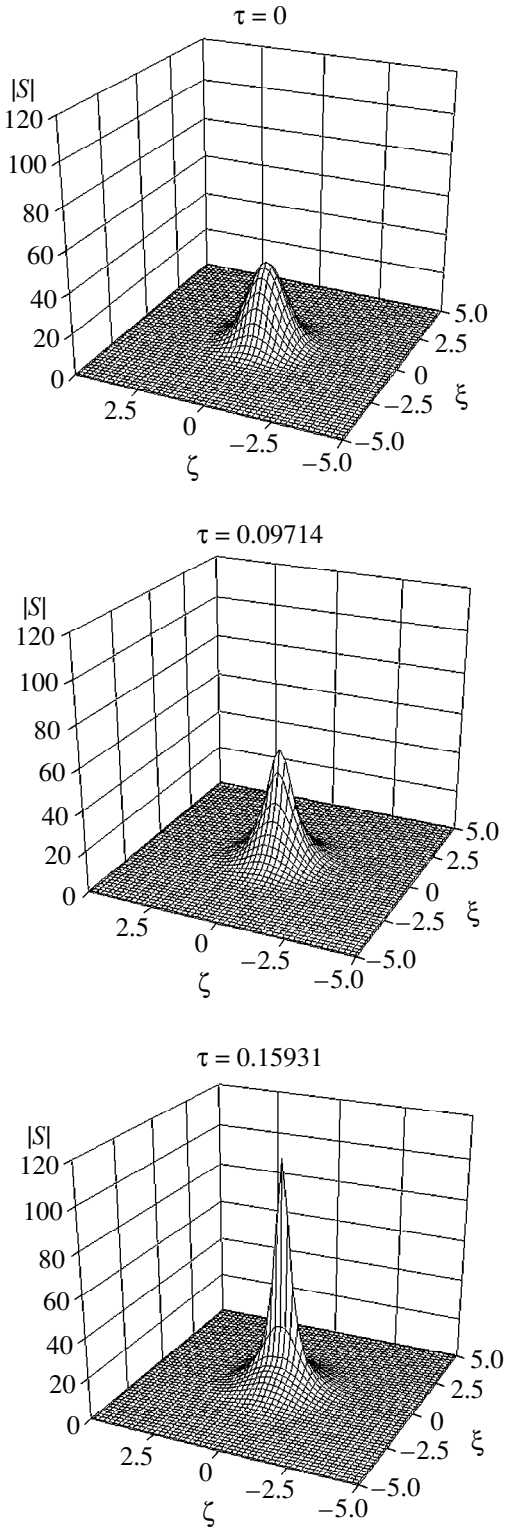

Fig. 4. Nonresonance singular focusing of the short-wave envelope $|S|$.

In the second case, we also deal with the stability zone, but in this case we approach the resonance curve ($c_g \longrightarrow c_e$). From Fig. 3a, one again can see a defocusing of the solution. However, the defocusing process is decelerated and accompanied by a change in the wave form (Fig. 3b).

In the third case, an unstable nonresonance interaction takes place. With time, the solution to Eq. (1) shrinks to a point and increases in amplitude (Fig. 4). At some instant of time, this results in the appearance of an explosive instability.

A singular focusing is also observed in the fourth (unstable resonance) case. In this case, the focusing is accelerated and accompanied by a strong deformation of the wave profile (Fig. 5). It is significant that the minimal amplitude necessary for the development of the singular focusing decreases in the resonance case: $S_0 = 30$ away from the resonance and $S_0 = 20$ at resonance. Therefore, the long-wave–short–wave resonance increases the probability of the singular focusing.

Thus, on the basis of the analysis of the coefficients in the model of a two-dimensional long-wave–short-wave interaction, we determined the conditions for a singular focusing (an explosive instability) in bubbly liquids. The existence of a two-dimensional defocusing and a singular focusing in such liquids is confirmed by the numerical integration of the interaction equations. We also analyzed the effect of the long-wave–short-wave resonance on the two-dimensional interaction of long and short waves. It was shown that, in the resonance case, the defocusing process is decelerated and accompanied by changes in the wave form. By contrast, the singular focusing is accelerated with the develop-

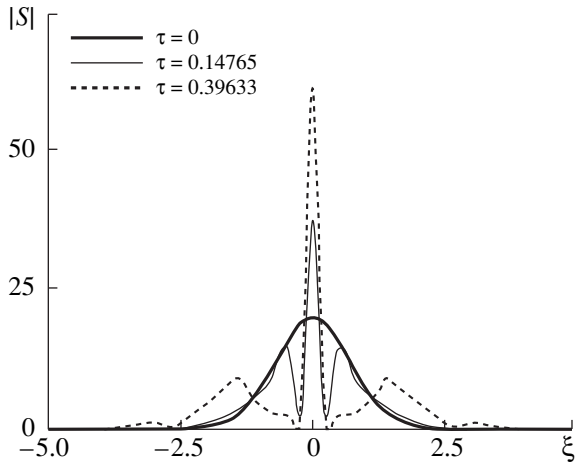

Fig. 5. Dependence of the short-wave envelope $|S|$ on the spatial coordinate ξ at various instants of time in the case of the resonance singular focusing.

ment of a strong distortion of the wave profile. Moreover, the resonance leads to a decrease in the amplitude threshold of the singular focusing.

REFERENCES

1. G. A. Askar'yan, Pis'ma Zh. Éksp. Teor. Fiz. **13**, 395 (1971) [JETP Lett. **13**, 283 (1971)].
2. P. Giuti, G. Iernetti, and M. S. Sagoo, Ultrasonics **18**, 111 (1980).
3. Yu. A. Kobelev, L. A. Ostrovskiĭ, and A. M. Sutin, Pis'ma Zh. Éksp. Teor. Fiz. **30**, 423 (1979) [JETP Lett. **30**, 395 (1979)].
4. Yu. A. Kobelev and L. A. Ostrovsky, J. Acoust. Soc. Am. **85**, 621 (1989).
5. S. L. Lopatnikov, Pis'ma Zh. Éksp. Teor. Fiz. **36**, 623 (1980) [JETP Lett. **36** (1980)].
6. E. A. Zabolotskaya, Tr. Inst. Obshch. Fiz., Akad. Nauk SSSR **18**, 121 (1989).
7. K. A. Naugol'nykh and L. A. Ostrovskiĭ, *Nonlinear Wave Processes in Acoustics* (Nauka, Moscow, 1990).
8. I. Sh. Akhatov and V. A. Baĭkov, Inzh.-Fiz. Zh. **50** (3), 385 (1986).
9. I. Sh. Akhatov, V. A. Baĭkov, and R. A. Baĭkov, Izv. Akad. Nauk SSSR, Mekh. Zhidk. Gaza **21**, 180 (1986).
10. I. Akhatov, U. Parlitz, and W. Lauterborn, J. Acoust. Soc. Am. **96**, 3627 (1994).
11. I. Akhatov, U. Parlitz, and W. Lauterborn, Phys. Rev. E **54**, 4990 (1996).
12. U. Parlitz, R. Mettin, S. Luther, *et al.*, Philos. Trans. R. Soc. London, Ser. A **357**, 313 (1999).
13. R. I. Nigmatulin, *Dynamics of Multiphase Media* (Nauka, Moscow, 1987), Vol. 2.
14. D. J. Benney, Stud. Appl. Math. **55**, 93 (1976).
15. D. J. Benney, Stud. Appl. Math. **56**, 81 (1977).
16. V. D. Djordjevic and L. G. Redekopp, J. Fluid Mech. **79**, 703 (1977).
17. V. E. Zakharov, Zh. Éksp. Teor. Fiz. **62**, 1745 (1972) [Sov. Phys. JETP **35**, 908 (1972)].
18. I. Sh. Akhatov and D. B. Khismatullin, Prikl. Mat. Mekh. **63**, 980 (1999).
19. H. Hasimoto and H. Ono, J. Phys. Soc. Jpn. **33**, 805 (1972).
20. V. E. Zakharov and A. B. Shabat, Zh. Éksp. Teor. Fiz. **61**, 119 (1971) [Sov. Phys. JETP **34**, 62 (1971)].
21. Y.-C. Ma, Stud. Appl. Math. **59**, 201 (1978).
22. A. Davey and K. Stewartson, Proc. R. Soc. London, Ser. A **338**, 101 (1974).
23. M. J. Ablowitz and H. Segur, J. Fluid. Mech. **92**, 691 (1979).
24. G. C. Papanicolaou, C. Sulem, P. L. Sulem, and X. P. Wang, Physica D (Amsterdam) **72**, 61 (1994).
25. I. Sh. Akhatov and D. B. Khismatullin, Akust. Zh. (in press).
26. S. A. Akhmanov, A. P. Sukhorukov, and R. V. Khokhlov, Usp. Fiz. Nauk **93**, 19 (1967) [Sov. Phys. Usp. **10**, 609 (1967)].
27. J.-M. Chidaglia and J.-C. Saut, Nonlinearity **3**, 475 (1990).
28. M. J. Ablowitz and H. Segur, *Solitons and the Inverse Scattering Transform* (SIAM, Philadelphia, Pa., 1981; Mir, Moscow, 1987).
29. G. I. Marchuk, *Methods of Numerical Mathematics* (Springer-Verlag, New York, 1975; 2nd ed., Nauka, Moscow, 1980).
30. C. A. J. Fletcher, *Computational Techniques for Fluid Dynamics* (Mir, Moscow, 1981; Springer-Verlag, Berlin, 1991), Vol. 1.

Translated by E. Golyamina

Acoustical Physics, Vol. 47, No. 2, 2001, pp. 145–149. Translated from Akusticheskiĭ Zhurnal, Vol. 47, No. 2, 2001, pp. 183–188.

REVIEWS

Nonlinear Equations for a Slow Magnetogasdynamic Quasi-Monochromatic Wave in a Medium with Dispersion and Dissipation

A. G. Bagdoev* and S. G. Saakyan**

** Institute of Mechanics, National Academy of Sciences of Armenia, pr. Marshala Bagramyana 24b, Yerevan, 375019 Armenia*

*** Yerevan Institute of Architecture and Construction, ul. Teryana 105, Yerevan, 375015 Armenia*

e-mail: mechins@sci.am

Received September 6, 1999

Abstract—Evolutionary equations are obtained in the vicinity of a singularity for a slow wave with allowance for the quadratic nonlinearity, dispersion, and dissipation. It is demonstrated that the propagation of quasi-monochromatic waves in a current-conducting gas–liquid mixture is described by ordinary differential equations for the amplitudes in the aforementioned region. © *2001 MAIK "Nauka/Interperiodica"*.

Nonlinear equations describing the behavior of a slow magnetoacoustic wave in the vicinities of singularities have been given by Bagdoev [1]. It was demonstrated that, unlike the equations describing waves near caustics, they are partial differential equations of the third order. At the same time, their linear solution near a singularity that does not lie at the axis coinciding with magnetic field is expressed through the Airy function [1, 2], although the amplitude of the solution is in this case multiplied by the imaginary unit. In this paper, we derive the equations for short waves in a conducting gas–liquid mixture in the vicinity of a singularity with allowance for the quadratic nonlinearity, dispersion, and dissipation. From these equations, we obtain ordinary differential equations for the amplitude of a quasi-monochromatic wave in the vicinity of a singularity.

For a planar problem in the x–y plane, linear equations of magnetogasdynamics have the form [1]

$$\frac{\partial \rho}{\partial t} + \rho_0\left(\frac{\partial v_x}{\partial x} + \frac{\partial v_y}{\partial y}\right) = q(t)\delta(x)\delta(y),$$

$$\frac{\partial v_x}{\partial t} = -\frac{1}{\rho_0}\frac{\partial P}{\partial x}, \quad \frac{\partial v_y}{\partial t} = -\frac{1}{\rho_0}\frac{\partial P}{\partial y} + a_1^2\left(\frac{\partial b_y}{\partial x} - \frac{\partial b_x}{\partial y}\right), \quad (1)$$

$$\frac{\partial P}{\partial t} = a_0^2\frac{\partial \rho}{\partial t}, \quad \frac{\partial b_x}{\partial t} = -\frac{\partial v_y}{\partial y}, \quad \frac{\partial b_y}{\partial t} = \frac{\partial v_y}{\partial x},$$

where P is the pressure, ρ is the density, v_x and v_y are the components of the particle velocity, the magnetic field is $B_\perp = B_0 + B_0 b_x$ and $B_y = B_0 b_y$, $q(t) = q_0 t^{k_0 - 1}\dfrac{\sigma(t)}{\Gamma}$ is the source of mass, $\delta(x)$ is the delta-function, $\sigma(t)$ is the unit function, Γ is the coefficient characterizing the medium, $a_1^2 = \dfrac{B_0^2}{4\pi\rho_0}$, a_1 is the Alfven velocity, and a_0 is the sound velocity.

The solution to Eq. (1) is sought using the Laplace integral transformation with respect to t and the Fourier transformation with respect to x and y by assuming that, for the transformation with respect to t, we have

$$\bar{P} = \int_{-\infty}^{\infty} d\alpha_1 \int_{-\infty}^{\infty} e^{i(\alpha_1 x + \beta_1 y)} A'(\alpha_1, \beta_1) d\beta_1, \quad (2)$$

where $\alpha_1 = \omega\alpha$, $\beta_1 = \omega\beta$, ω is the frequency, and $i\omega$ is the parameter of the Laplace transformation. From the equation for P obtained according to the set of Eqs. (1) after substituting Eq. (2) into it, we derive the relationships

$$A' = -\frac{a_0^2(1 - a_1^2\alpha^2 - a_1^2\beta^2)}{\Pi(\alpha, \beta)}\frac{1}{4\pi^2}\frac{q_0}{(-i\omega)^{k_0 - 1}}, \quad (3)$$

$$\Pi(\alpha, \beta) = (1 - a_1^2\alpha^2 - a_1^2\beta^2)(1 - a_0^2\alpha^2) - a_0^2\beta^2.$$

Substituting Eq. (3) into Eq. (2) and calculating the residue with respect to β at the point $\beta = \beta(\alpha)$ determined by the dispersion equation $\Pi(\alpha, \beta) = 0$, we obtain an expression for the linear solution $P = P_0$:

$$e^{st}\bar{P}_0 = -\frac{q_0}{(-i\omega)^{k_0 - 1}}\frac{i}{2\pi} \times \int_{-\infty}^{\infty} \frac{a_0^2\{1 - a_1^2\alpha^2 - a_1^2\beta^2(\alpha)\}^{-i\omega T}}{\Pi'_\beta} d\alpha, \quad (4)$$

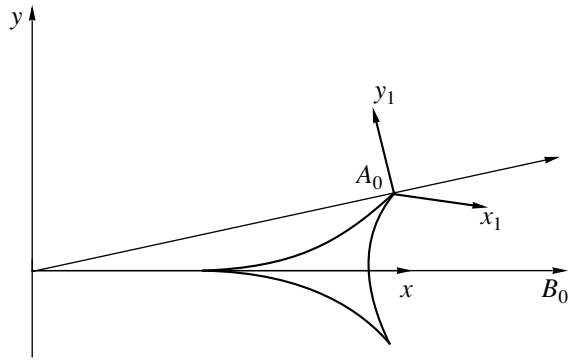

Form of a slow magnetogasdynamic wave near the singularity A_0.

where $T = t - \alpha x - \beta(\alpha)y$.

At the singular point A_0 (see figure), the wave has an infinite curvature and, therefore, $\beta''(\alpha_0) = 0$. In order to obtain a solution in the vicinity of the singularity, we can use an expansion within a small vicinity of $\alpha = \alpha_0$:

$$T \approx t - \alpha_0 x - \beta(\alpha_0)y - \{x + \beta'(\alpha_0)y\}(\alpha - \alpha_0) - \frac{1}{6}\beta'''(y_0)(\alpha - \alpha_0)^3. \quad (5)$$

Substituting Eq. (5) into Eq. (4) and introducing the Airy function $v(\eta) = \frac{1}{2\sqrt{\pi}}\int_{-\infty}^{\infty} e^{i\eta\xi + i\frac{\xi^3}{3}} d\xi$, where $\eta = \omega^{\frac{2}{3}} y_1$, we obtain

$$e^{st}\bar{P}_0 = e^{-i\frac{\pi}{4}} 2A_1 v\left(\omega^{\frac{2}{3}} y_1\right) \frac{\omega^{\frac{1}{6}}}{(-i\omega)^{k+1}} e^{i\omega x_1}. \quad (6)$$

Here, $k = k_0 + 3/2$,

$$A_1 = -\frac{1}{2\sqrt{\pi}} q_0 a_0^2 \frac{1 - a_1^2\alpha_0^2 - a_1^2\beta^2(\alpha_0)}{\Pi'_\beta\{\alpha_0, \beta(\alpha_0)\}} \left\{\frac{2}{\beta'''(\alpha_0)y}\right\}^{\frac{1}{3}} i, \quad (7)$$

$$y_1 = \left\{\frac{2}{\beta'''(\alpha_0)y}\right\}^{\frac{1}{3}} \{x + \beta'(\alpha_0)y\}, \quad x_1 = \alpha_0 x + \beta(\alpha_0)y - t, \quad (8)$$

x_1 is the eikonal, and y_1 characterizes the distance from the ray passing through the point A_0. Thus, the linear solution near the singularity A_0 is written in the form of Eq. (6), which differs from the solution near a caustic [1] by a factor of i.

Now, we consider the derivation of a nonlinear equation in the vicinity of a singularity without taking into account the dissipation and the dispersion for a nonstationary point wave. As Eq. (6) shows, the solution in the vicinity of a singularity is determined in the principal orders by the coordinates x_1, y_1 (Eq. (8)). Since the relationship $y = \frac{t}{\beta(\alpha_0) - \alpha\beta'(\alpha_0)}$ is satisfied for the wave, we obtain

$$x_1 = \alpha_0 x + \beta(\alpha_0)y - t, \quad y_1 = \frac{x + \beta'(\alpha_0)y}{t^{\frac{1}{3}}} K, \quad K^3 = \frac{2}{\beta'''(\alpha_0)}\{\beta(\alpha_0) - \alpha_0\beta'(\alpha_0)\}. \quad (9)$$

In the equation for small perturbations in the vicinity of the point A_0, we take into account the nonlinear term in which only the derivatives with respect to the fast coordinate x_1 are retained [1]:

$$A_0\frac{\partial U}{\partial t} + A_1\frac{\partial U}{\partial x} + A_2\frac{\partial U}{\partial y} = K_1 P\frac{\partial P}{\partial x}. \quad (10)$$

Here, the pressure $P = U_1$ is taken as one of the functions, $U = \{U_i\}$ is the vector of the desired quantities, $K_1 = \{K_{1i}\}$ is the vector determined from the matching conditions for the linear wave [1], and $A_{0,1,2}$ are the coefficients of the linear part of the initial equations.

Solving the set of equations given by Eq. (10) with respect to P, we obtain the equation

$$\Delta(p, q, S)P = A_{i1}K_{1i}P\frac{\partial P}{\partial x_1}. \quad (11)$$

Here, Δ is the characteristic determinant for the left-hand side of the set of Eqs. (10), this left-hand side being a homogeneous function of $p = \frac{\partial}{\partial x}$, $q = \frac{\partial}{\partial y}$, and $S = \frac{\partial}{\partial t}$; A_{i1} are the cofactors of the first row elements of Δ.

From the linear solution (6), by analogy with the solution of the problem with the caustic [1], we obtain the relationships

$$x_1 \sim y_1^{\frac{3}{2}}, \quad t \sim 1. \quad (12)$$

Proceeding from Eq. (11), introducing the function $\frac{u'}{t^{\frac{1}{3}}} = P$ (one can see from Eq. (7) that $u' = u'(x_1, y_1)$), and taking into account Eq. (9), we arrive at the expressions

$$p = \alpha_0\frac{\partial}{\partial x_1} + \frac{K}{t^{\frac{1}{3}}}\frac{\partial}{\partial y_1}, \quad q = \beta_0\frac{\partial}{\partial x_1} + \beta'(\alpha_0)\frac{K}{t^{\frac{1}{3}}}\frac{\partial}{\partial y_1}, \quad S = -\frac{\partial}{\partial x_1} - \frac{1}{3}\frac{y_1}{t}\frac{\partial}{\partial y_1} - \frac{1}{3t}. \quad (13)$$

Assuming that $p_0 = \alpha_0 \frac{\partial}{\partial x_1}$, $q_0 = \beta_0 \frac{\partial}{\partial y_1}$, $S_0 = -\frac{\partial}{\partial x_1}$, and $\beta_0 = \beta(\alpha_0)$ and expanding $\Delta(p, q, S)$ in the powers of the operators $\frac{\partial}{\partial y_1} \ll \frac{\partial}{\partial x_1}$, we obtain

$$\begin{aligned}\Delta(p, q, S) &= \Delta(p_0, q_0, S_0) + (\Delta_{p_0} + \beta'\Delta_{q_0})\frac{K}{t^{\frac{1}{3}}}\frac{\partial}{\partial y_1} \\ &+ \Delta_{S_0}\left(-\frac{1}{3t}y_1\frac{\partial}{\partial y_1} - \frac{1}{3t}\right) + \frac{1}{2}\frac{K^2}{t^{\frac{2}{3}}} \\ &\times (\Delta_{p_0p_0} + 2\Delta_{p_0q_0}\beta' + \Delta_{q_0q_0}\beta'^2)\frac{\partial^2}{\partial y_1^2} + \frac{1}{6}\frac{K^3}{t} \\ &\times (\Delta_{p_0p_0p_0} + 3\Delta_{p_0p_0q_0}\beta' + 3\Delta_{p_0q_0q_0}\beta'^2 + \Delta_{q_0q_0q_0}\beta'^3)\frac{\partial^3}{\partial y_1^3}.\end{aligned} \tag{14}$$

The subscript marking the quantity Δ denotes the differentiation.

Taking into account the homogeneity of Δ and the fact that $\Delta(\alpha, \beta, -1) = 0$ is the dispersion equation of a linear problem, we differentiate it with respect to α and obtain

$$\begin{aligned}\Delta_\alpha + \beta'(\alpha)\Delta_\beta &= 0, \\ \Delta_{\alpha\alpha} + 2\beta'\Delta_{\alpha\beta} + \Delta_{\beta\beta}\beta'^2 + \Delta_\beta\beta'' &= 0, \\ \Delta_{\alpha\alpha\alpha} + 3\Delta_{\alpha\alpha\beta}\beta' + 3\Delta_{\alpha\beta\beta}\beta'^2 + \Delta_{\beta\beta\beta}\beta'^3 + 2\Delta_{\alpha\beta}\beta'' \\ + 2\Delta_{\beta\beta}\beta'\beta'' + \beta''(\Delta_{\alpha\beta} + \Delta_{\beta\beta}\beta') + \beta'''\Delta_\beta &= 0.\end{aligned} \tag{15}$$

Here, one should take into account that, at the singularity, $\beta'' = 0$.

Then, Eq. (14) takes on the form

$$\begin{aligned}\Delta(p, q, S) = \left(\frac{\partial}{\partial x_1}\right)^{m-3}\Bigg\{(\alpha\Delta_\alpha + \beta\Delta_\beta)\Bigg(-\frac{1}{3t}y_1\frac{\partial^3}{\partial y_1\partial x_1^2} \\ -\frac{1}{3t}\frac{\partial^2}{\partial x_1^2}\Bigg) - \frac{1}{6}\frac{K^3}{t}\beta'''\Delta_\beta\frac{\partial^3}{\partial y_1^3}\Bigg\},\end{aligned} \tag{16}$$

where the fact that $\Delta_{S_0} = \frac{\partial^{m-1}}{\partial x_1^{m-1}}(\alpha\Delta_\alpha + \beta\Delta_\beta)$ is taken into account and m is the power of the operator polynomial Δ.

Substituting Δ into Eq. (11) and taking into account the fact that $A_{i1}(p_0, q_0, s_0) = \left(\frac{\partial}{\partial x_1}\right)^{m-1} A_{i1}(\alpha_0, \beta_0, -1)$, we obtain

$$\begin{aligned}\frac{1}{3t}y_1\frac{\partial^4 P}{\partial y_1\partial x_1^3} + \frac{1}{3t}\frac{\partial^3 P}{\partial x_1^3} + \frac{1}{3t}\frac{\partial^4 P}{\partial x_1\partial y_1^3} \\ = -\frac{\partial^3}{\partial x_1^3}\left\{\frac{A_{i1}(\alpha_0, \beta_0, -1)K_{1i}}{\alpha\Delta_\alpha + \beta\Delta_\beta}P\frac{\partial P}{\partial x_1}\right\}.\end{aligned} \tag{17}$$

To determine the coefficient on the left-hand side of Eq. (17), we have to allow for the fact that it is the same as the coefficient of the nonlinear term in the evolutionary equations describing the vicinities of the tangency points of the waves [1] in the form of Eq. (11), where

$$\Delta = (\alpha\Delta_\alpha + \beta\Delta_\beta)\left(\frac{\partial}{\partial\tau}\right)^{m-1}\frac{\partial}{\partial t} - \frac{1}{2}\Delta_\alpha L\left(\frac{\partial}{\partial\tau}\right)^{m-2}, \tag{18}$$

L is the transverse operator containing the derivatives in the direction tangential to the wave, and $\tau = x_1$ is the eikonal. In the coordinate system connected with the wave, we can take $\beta = 0$ and $\alpha = \frac{1}{H_1}$.

Writing Eqs. (11) and (18) for the problem that is one-dimensional with respect to τ, we obtain an equation for the nonlinear characteristics

$$\frac{\partial\tau}{\partial t} = -\frac{1}{\alpha\Delta_\alpha + \beta\Delta_\beta}A_{i1}(\alpha_0, \beta_0, -1)K_{1i}P. \tag{19}$$

On the other hand, in the one-dimensional problem, the following relationship for the normal velocity of a nonlinear wave [1] is valid in the first order with respect to P:

$$c_n + v_n = H_1 + \Gamma u = H_1 + H_1\frac{\partial\tau}{\partial t}, \tag{20}$$

where H_1 is the normal velocity of the wave in the linear problem, u being the particle velocity normal to the wave and $u = \frac{Pc_0}{\rho_0 a_0^2}$ in magnetogasdynamics. Then, we obtain

$$\frac{\partial\tau}{\partial t} = \Gamma\frac{P}{\rho_0 a_0^2} \tag{21}$$

and the comparison with Eq. (19) yields

$$\frac{A_{i1}(\alpha_0, \beta_0, -1)K_{1i}}{\alpha\Delta_\alpha + \beta\Delta_\beta} = -\Gamma\frac{1}{\rho_0 a_0^2}. \tag{22}$$

Expressing Eq. (17) in terms of u, we obtain a nonlinear equation

$$\frac{\partial}{\partial y_1}\left(\frac{\partial^2 u}{\partial x_1^2}y_1 + \frac{\partial^2 u}{\partial y_1^2}\right) = \frac{\partial^2}{\partial x_1^2}\left(\frac{3t\Gamma}{H_1}u\frac{\partial u}{\partial x_1}\right). \tag{23}$$

Following the results of the previous studies [1, 3], we write the expression for the coefficient Γ in the form

$$\Gamma = \alpha^0 \frac{H_1^2 - a_1^2}{2H_1^2 - a_0^2 - a_1^2} + \frac{3}{2}\frac{H_1^2 - a_0^2}{2H_1^2 - a_0^2 - a_1^2}.$$

Here, $\alpha^0 = \left(\frac{\partial \rho a}{a \partial \rho}\right)_{\rho = \rho_0}$. For the problem with the adiabatic exponent n, we have $\alpha^0 = \frac{n+1}{2}$.

At the next stage, we consider the nonlinear equations for waves with allowance for the dissipation and dispersion. The linear solution in the vicinity of the point A_0 has the form of Eqs. (6) and (7) in which $A_1 = iA_3$, where A_3 is the real amplitude of the wave far from the singularity. The meaning of this amplitude is revealed when the asymptotics of the function $\nu(\eta)$ for large η is used [1].

A nonlinear equation taking into account the dispersion and dissipation can be obtained directly from the equations of magnetogasdynamics. However, it is easier to take into account the necessary terms with the help of three-dimensional equations of short waves. These equations have the following form in the system of coordinates connected with the wave [1]:

$$\begin{aligned}&\frac{\partial^2 u}{\partial t \partial \tau} - \frac{1}{2}H_1 L(u)\\ &= -\frac{1}{H_1}\frac{\partial}{\partial \tau}\left(\Gamma u \frac{\partial u}{\partial \tau}\right) - \frac{E}{H_1}\frac{\partial^4 u}{\partial \tau^4} - \frac{D}{H_1}\frac{\partial^3 u}{\partial \tau^3},\end{aligned} \tag{24}$$

where $\tau = x_1$ is the eikonal, $L(u)$ is the transverse operator with respect to the coordinates tangential to the wave, and E and D are the dispersion and dissipation coefficients given in [3]. Comparing Eqs. (24) and (23) and taking into account the fact that $\tau = x_1$, it is possible to obtain an equation near the singularity A_0:

$$\begin{aligned}&\frac{\partial^3 u}{\partial x_1^2 \partial t} - \frac{1}{3t}\frac{\partial}{\partial y_1}\left(y_1 \frac{\partial^2 u}{\partial x_1^2} + \frac{\partial^2 u}{\partial y_1^2}\right)\\ &= -\frac{\Gamma}{H_1}\frac{\partial^2}{\partial x_1^2}\left(u\frac{\partial u}{\partial x_1}\right) - \frac{E}{H_1}\frac{\partial^5 u}{\partial x_1^5} - \frac{D}{H_1}\frac{\partial^4 u}{\partial x_1^4}.\end{aligned} \tag{25}$$

This equation takes into account that, in Eqs. (24) and (25), the terms that are one-dimensional with respect to τ and x_1 must coincide.

In the case of a quasi-monochromatic wave, we assume

$$\begin{aligned}u &= U_0 + U_1 e^{i(\omega x_1 - \omega_1 t) - \nu_1 t}\\ &+ U_2 e^{2i(i\omega x_1 - \omega_1 t) - 2\nu_1 t} + \text{c.c.},\end{aligned} \tag{26}$$

where U_0 is the constant term, $U_{1,2}$ are the amplitudes of the first and second harmonics, ω is the fundamental frequency, ω_1 is the modulation frequency, and ν is the linear attenuation. Substituting Eq. (26) into Eq. (25) and equating the terms describing the first harmonic, we obtain

$$\omega_1 = -\frac{E}{H_1}\omega^3, \quad \nu_1 = -\frac{D}{H_1}\omega^2. \tag{27}$$

Equating the terms with the second harmonic in Eq. (25) for high frequencies when $|\omega_1|t \gg 1$, it is possible to eliminate the derivatives of the amplitude of the second harmonic and obtain in the basic approximation

$$U_2 = -\frac{\Gamma\omega}{2H_1(3\omega_1 - i\nu_1)}U_1^2. \tag{28}$$

Since, in the diffraction problem under consideration, $U_1 \sim \varepsilon$ and $U_0 \sim \varepsilon^3$, where ε is the small parameter, the terms with U_0 can be eliminated from the equation for the first harmonic. In this case, we obtain

$$\begin{aligned}&-\omega^2\frac{\partial U_1}{\partial t} - \frac{1}{3t}\frac{\partial}{\partial y_1}\left(-y_1\omega^2 U_1 + \frac{\partial^2 U_1}{\partial y_1^2}\right)\\ &= \frac{i\omega^3\Gamma}{H_1}U_2 U_1^* e^{-2\nu_1 t},\end{aligned} \tag{29}$$

where the asterisk means a complex conjugate quantity.

Since, according to Eq. (12), we have $x_1 \sim y_1^{\frac{3}{2}}$ and $y_1 \sim \varepsilon$, the first term in Eq. (29) can be eliminated and the weak time dependence of the coefficients in Eqs. (6), (9), and (29) can be ignored. Then, taking into account Eq. (28), we obtain for a quasi-monochromatic wave near the point A

$$u = \psi(y_1)e^{i\omega x_1}, \quad U_1 e^{-i\omega_1 t - \nu_1 t} = \psi, \tag{30}$$

$$\frac{d}{dy_1}\left(-y_1\psi + \frac{1}{\omega^2}\frac{d^2\psi}{dy_1^2}\right) = (\tilde{\chi}_1 + i\tilde{\chi}_2)\psi|\psi|^2, \tag{31}$$

where

$$\tilde{\chi}_1 = -\frac{3t\omega^2\Gamma^2\nu_1}{2H_1^2(9\omega_1^2 + \nu_1^2)}, \quad \tilde{\chi}_2 = \frac{9t\omega^2\Gamma^2\omega_1}{2H_1^2(9\omega_1^2 + \nu_1^2)}. \tag{32}$$

In the coordinate system $\omega^{\frac{2}{3}}y_1 = y'$, $\psi = \tilde{\psi}|\tilde{\chi}|^{-\frac{1}{2}}$, Eq. (31) has the form

$$\frac{d}{dy'}\left(\frac{d^2\tilde{\psi}}{dy'^2} - y'\tilde{\psi}\right) = \pm\left(i + \frac{\tilde{\chi}_1}{\tilde{\chi}_2}\right)\tilde{\psi}|\tilde{\psi}|^2, \tag{33}$$

where the plus sign corresponds to $\tilde{\chi}_2 > 0$ and the minus sign corresponds to $\tilde{\chi}_2 < 0$.

According to Eq. (6), in the linear problem, we have

$$U_0 = \frac{e^{-i\omega t}\bar{P}_0}{\rho_0 a_0^2} H_1, \quad \psi_0 = e^{i\varphi_0}\psi_0', \qquad \varphi_0 = \frac{k+1}{2}\pi + i\frac{\pi}{4}, \tag{34}$$

where ψ_0' is a real quantity and

$$\psi_0' = \frac{2A_3 H_1}{\rho_0 a_0^2}\omega^{-k-\frac{5}{6}} v(y') = Cv(y'). \tag{35}$$

Then, in view of Eq. (33), the following equation is valid for the function $\tilde{\psi}' = \tilde{\psi} e^{-i\varphi_0}$:

$$\frac{d}{dy'}\left(\frac{d^2\tilde{\psi}'}{dy'^2} - y'\tilde{\psi}'\right) = \pm\left(i + \frac{\tilde{\chi}_1}{\tilde{\chi}_2}\right)\tilde{\psi}'|\tilde{\psi}'|^2. \tag{36}$$

Unlike a caustic [1] in a nondissipative medium ($\nu_1 = 0$), here $\tilde{\psi}' = |\tilde{\chi}_2|^{\frac{1}{2}}\psi'$ is a complex quantity. Setting $\tilde{\psi}' = A + Bi$, we obtain from Eq. (36)

$$\frac{d}{dy'}\left(\frac{d^2A}{dy'^2} - y'A\right) = \pm\left(\frac{\tilde{\chi}_1}{\tilde{\chi}_2}A - B\right)(A^2 + B^2),$$
$$\frac{d}{dy'}\left(\frac{d^2B}{dy'^2} - y'B\right) = \pm\left(A + \frac{\tilde{\chi}_1}{\tilde{\chi}_2}B\right)(A^2 + B^2). \tag{37}$$

By analogy with the solution of the problem [1] near the caustic, the set of Eqs. (37) should be solved with the boundary conditions set far from the singularity, e.g., at $y' = \pm 5$:

$$A(\pm 5) = C|\chi_2|^{\frac{1}{2}} v(\pm 5), \quad B(\pm 5) = 0,$$
$$A(\pm 5) = C|\tilde{\chi}_2|^{\frac{1}{2}} v(\pm 5), \quad B(\pm 5) = 0. \tag{38}$$

We denote $\tilde{A} = A - C|\bar{\chi}_2|^{\frac{1}{2}} v(y')$. Then, we have zero boundary conditions for $\tilde{A}$ at $y' = \pm 5$. Denoting the right-hand sides of Eqs. (37) by f_1 and f_2 with allowance for the fact that far from the singularity a linear variant for Eq. (36) takes place, we can write Eqs. (37) in the form

$$\frac{d^2\tilde{A}}{dy'^2} - y'\tilde{A} = \int_{-5}^{y'} f_1 dy',$$
$$\frac{d^2B}{dy'^2} - y'B = \int_{5}^{y'} f_2 dy' \tag{39}$$

with two zero boundary conditions at $y' = \pm 5$ for each of the two equations.

The solution can be sought by reducing Eqs. (39) to a set of integral equations with respect to $\tilde{A}$ and B. Two Airy functions, $v(y')$ and $u(y')$, are involved in the kernels of these equations. The process of iterations starting from a linear solution for the right-hand sides of Eqs. (39) is performed in the same way as in the case of a single equation [1]. As in the case of a caustic [1], one should distinguish focusing ($\chi_2 < 0$) and defocusing ($\chi_2 > 0$) media, depending on the sign of dispersion. In the first case, noticeable distinctions from the solution of the linear problem exist for small values of $\frac{A_1}{\rho_0 a_0^2}$. In the second case, the nonlinear solution differs little from the corresponding linear solution.

Thus a linear solution for a quasi-monochromatic wave in the vicinity of a singularity of a slow magnetogasdynamic wave is obtained. Using the values of the parameters of motion and the coordinates x_1, y_1 obtained from the linear solution, we obtained a nonlinear equation in the region under consideration for a nonstationary wave in a nondissipative medium without dispersion. This equation is complemented by taking into account the dispersion and dissipation. An additional complete equation for a medium with a quadratic nonlinearity and with dissipation and dispersion is obtained in the vicinity of a singularity for a nonstationary problem. Two ordinary differential equations for the real and imaginary parts of the amplitude are derived from the aforementioned equation for a quasi-monochromatic wave, and the problem of solving these equations with the boundary conditions taken from the linear solution is formulated. An expression for the amplitude of the second harmonic is obtained. As in the case of a caustic [1], the amplitude of the first harmonic increases by a factor of $\omega^{\frac{1}{6}}$ due to the presence of a singularity and the amplitude of the second harmonic increases by a factor of $\omega^{\frac{1}{3}}$.

REFERENCES

1. A. G. Bagdoev, *Wave Propagation in Continuous Media* (Akad. Nauk Arm. SSR, 1981).
2. Yu. A. Kravtsov, Izv. Vyssh. Uchebn. Zaved., Radiofiz. **7** (4), 664 (1964).
3. A. G. Bagdoev and L. G. Petrosyan, Izv. Akad. Nauk Arm. SSR, Mekh. **36** (5), 3 (1983).
4. W. Moon and I. J. Busch-Vishniac, J. Acoust. Soc. Am. **101**, 1398 (1997).
5. W. Moon and I. J. Busch-Vishniac, J. Acoust. Soc. Am. **101**, 1408 (1997).

Translated by M. Lyamshev

Acoustical Physics, Vol. 47, No. 2, 2001, pp. 150–159. Translated from Akusticheskiĭ Zhurnal, Vol. 47, No. 2, 2001, pp. 189–199.

REVIEWS

Long-Range Sound Propagation in the Central Region of the Baltic Sea

R. A. Vadov

Andreev Acoustics Institute, Russian Academy of Sciences, ul. Shvernika 4, Moscow, 117036 Russia

e-mail: bvp@akin.ru

Received April 19, 2000

Abstract—The data obtained from a set of experiments on the long-range, low-frequency (<5 kHz) sound propagation in the central region of the Baltic Sea are analyzed. The experiments were carried out in the summer season, with a fully developed underwater sound channel. Experimental data on the sound attenuation are presented. A significant excess of the attenuation coefficients over the predicted absorption coefficients is obtained. The quantitative estimates indicate that the sound scattering by internal waves is the most probable mechanism responsible for the observed excessive sound attenuation. The frequency dependence of the attenuation coefficient exhibits a minimum whose position on the frequency axis at the beginning of the summer season noticeably differs from that at the end of summer. The analysis of the propagation conditions allows one to relate the position of this minimum to the critical frequency of the water modes. In addition to the intensity parameters of the sound field, the formation of the time structure of explosion-generated signals propagating in the Baltic underwater sound channel is considered for the case of the sound propagation along the 360-km path crossing the Gotland Hollow. The specific role of the bottom waves in the time structure formation at short distances from the sound source is demonstrated. © *2001 MAIK "Nauka/Interperiodica"*.

For a number of years, the researchers from the Acoustics Institute studied the structure and intensity characteristics of the sound fields generated by point sources in the underwater sound channel of the Baltic Sea. The waters of this sea are rather desalinated. The salinity significantly varies: from 15–21% in the vicinity of the Dutch Straits to 3–5‰ near the Gulf of Bothnia. Salt waters of the North Sea are desalinated under the influence of numerous rivers that fall into the Baltic Sea. In addition to desalination, a stratification of the waters takes place: the dense salt waters are spread near the sea floor, the light-weight desalinated ones lie over them. In the central region of the Baltic Sea, the water salinity increases with the depth from 6–8‰ near the surface to 12–14‰ near the bottom [1, 2].

A well-pronounced underwater sound channel (USC) seldom exists in a shallow sea. In this respect, the Baltic Sea is an exception. A stable USC, with the axis at a depth of about 50 m, can be observed here for 6 to 8 months a year. The difference between the sound speeds at the channel boundaries and at its axis is higher than 8–10 m/s. With a sea depth of approximately ~100 m, this channel captures the rays that cross the USC axis at angles exceeding 6°–7°. The vertical profiles $C(z)$ of the sound speed are noticeably different for the spring and autumn seasons (Fig. 1). In May, the weak warming of the upper water layer corresponds to the discontinuity layer at a depth of 5–15 m, with a sound speed difference of 10–15 m/s. With the colder near-surface waters that are intermixed by the winter storms up to depths of 60–70 m, the weak spring warming of the very upper layers leads to a minimum in the sound speed, which is spread in depth and corresponds to a nearly isospeed 40- to 50-m layer of the intermediate waters. By August or September, the intense warming of the near-surface waters leads to the formation of the temperature discontinuity layer with a sound speed difference of 50–55 m/s. During the summer, the multiple storm-induced mixing of the warm near-surface waters leads to their penetration down to the 40-m depth. By August or September, the USC is formed with a sharply pronounced minimum in the sound speed. Independently of the season, as the depth increases from 60–70 to 150–200 m, both the salinity and temperature increase (by 4–6‰ and 1–2°C, respectively). Hence, the sound speed increases as well (by 8–12 m/s). In addition to the seasonal variability of the water parameters in the Baltic Sea, a year-to-year variability takes place that is associated with the corresponding variations in the water exchange with the North Sea and in the water supply from the rivers.

The ray patterns shown in Fig. 2 illustrate the general features of the sound propagation in the central region of the Baltic Sea. The patterns are calculated for the environmental conditions that were experimentally observed at the beginning and end of the summer season. In May (Fig. 2a), with the 50-m source depth (near the USC axis) and the 80–85-m sea depth, the "water" rays insonify the layer from 10 m to the bottom. With the same conditions in August (Fig. 2b), these rays insonify a thinner layer (from 45–50 m to the bottom). In both cases, the length of the full ray cycle is 1.5–2.5 km

1063-7710/01/4702-0150$21.00

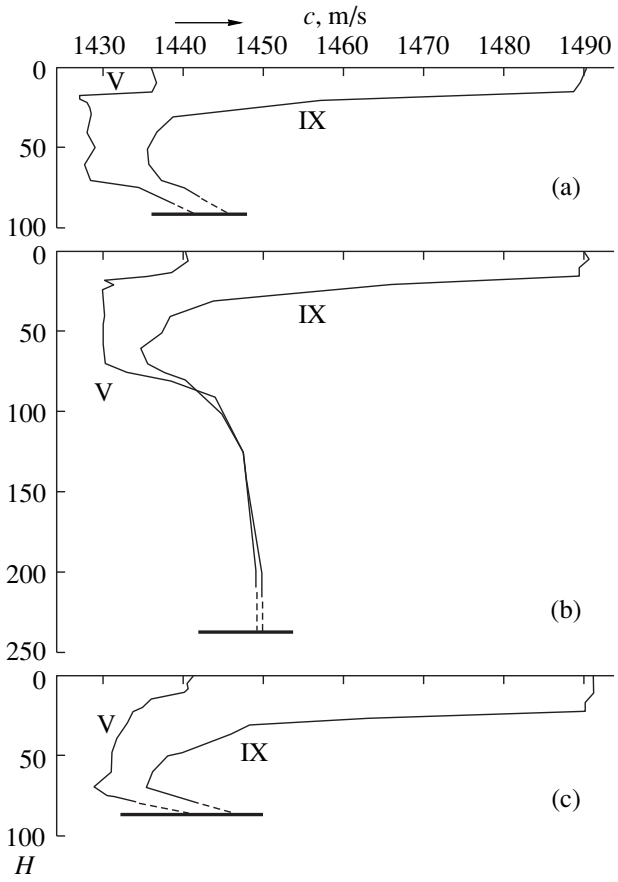

Fig. 1. Sound speed profiles on the propagation paths of the May (V) and September (IV) experiments: (a) at the southern path end; (b) in the middle of the path; and (c) at the northern path end.

for the water rays. On the average, the 100-km propagation path includes 50 such ray cycles; the number of bottom reflections is higher than 50 (for the bottom-reflected rays).

The main studies of the long-range propagation were carried out on the 350–400-km path whose southern point was 120–130 km northwest of Kaliningrad. The path crossed the 20° meridian (in the vicinity of the Gotland Hollow), at an angle of about ~20°.

At the initial 70-km-long part of the path, the sea depth was within 80–85 m, then it slowly increased to 140 m at a distance of 195 km from the reception point, and up to 240–250 m in the region of the Gotland Hollow (at a distance of 250 km). At the terminal part of the path, the sea depth decreased from 210 m (at a distance of 290 km) to 105 m (at a distance of 305 km), and to 80–85 m at the path end.

According to the auxiliary measurements accompanying the acoustic experiments, the sound speed in the 1.5–2.5-m upper layer of the bottom sediments was 1500 m/s at the northern part of the path, the sediment density being 1.3 g/cm^3. At the southern part of the path, the corresponding sound speed increased to 1545 m/s, with the density being 1.5 g/cm^3. The bottom sediments consisted of the pelitic silt. Closer to the southern point of the path, traces of sand were observed in the sediments.

The intensity characteristics of the sound field were studied in the USC of the Baltic Sea with the use of both cw sound sources (within the kilohertz frequency band) and explosive ones with pressure-sensitive detonators. The source was towed and the charges were exploded at the depth 50 m, near the USC axis.

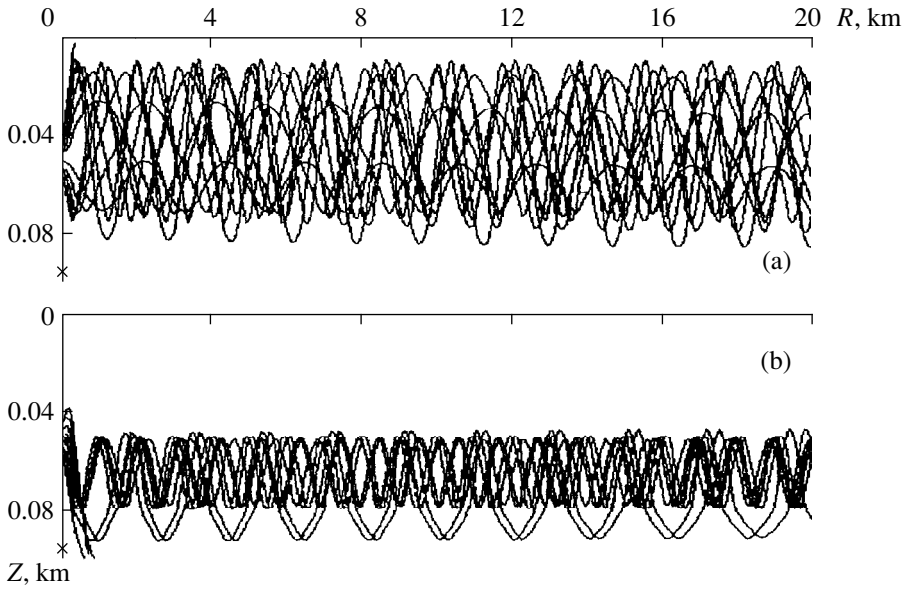

Fig. 2. Ray patterns plotted for the conditions of the (a) May and (b) September experiments. The sea depth is 80–90 m, the source depth is 50 m.

The signals were received by omnidirectional systems, one of which was also at the USC axis.

By analogy with a deep sea, the following intensity parameters were chosen to characterize the sound propagation in the shallow sea: the propagation anomaly, the attenuation coefficient, and the transition distance.

In a deep sea, the attenuation is usually interpreted as the change in the sound field with distance due to the sound absorption and the scattering in the medium. For a shallow sea, apart from the geometric spread, the losses caused by bottom reflections substantially contribute to the sound field decay. However, for the USC-propagation in the Baltic Sea, the main part of the sound field is formed by "purely water" rays that do not touch the bottom and propagate within the USC. In this case, just as in a deep sea, the range decay of the sound field is governed by the geometric spread and the attenuation in the water medium, including both absorption and scattering of sound.

According to this deep-sea analogy, we define the propagation anomaly $A(R)$ for the Baltic Sea as the excess of the sound field level produced by a sound source in the sea medium over the mean sound level of the same source in an unbounded medium, with the attenuation coefficient β that characterizes the actual propagation conditions in the specific sea region. Thus, the decay law of the sound field can be described by the following relation:

$$I = \frac{I_0}{R^2} A(R) \times 10^{-0.1\beta R}, \quad (1)$$

where I_0 is the sound field intensity produced by the source at the unit distance in an unbounded uniform medium.

If one excludes the attenuation-caused losses of the sound energy, the sound field decay in the USC will follow the cylindrical law, provided that the distance from the source is sufficiently long, and the propagation anomaly will change proportionally to the distance: $A(R) = kR$. The quantity $1/k$ is called the transition distance (R_0). For ranges $R \gg R_0$, by substituting the anomaly value determined from the transition distance into Eq. (1), one obtains a relation that describes the decay law of the sound field at large distances from the source:

$$I = \frac{I_0}{RR_0} \times 10^{-0.1\beta R}.$$

In the experiments performed in the kilohertz frequency band, the sound source was used that consisted of a set of cylindrical piezoceramic transducers placed into a towed body. The transmitting vessel went about 3 knots, away from the receiving vessel or toward it. In these experiments, the distance between the vessels was less than 80–100 km: this value was limited by the signal-to-noise ratio which was higher than 10–15 dB in all measurements. A continuous noise signal was transmitted within the 1/3-octave band. On the receiving vessel, the sound signal was continuously recorded, with reference to the distance between the vessels (at long distances) or between the transmitting and receiving systems (at shorter distances). The stability of the transmitted signal was monitored by measuring the level of the electric signal applied to the piezoceramic transducer.

As the initial data for estimating the attenuation, the experimentally obtained decay law of the sound field level was used. The attenuation coefficient was determined by measuring the deviation of the range-dependent sound level recorded at long distances from the cylindrical law. In addition to the experimental level decay, the data of calibrating the source, which were obtained in a deep sea, were used in determining the transition distance R_0 and the propagation anomaly $A(R)$.

In the experiments with the source and receiver close to the USC axis, which were carried out by us in the summer months of different years, we obtained the values from 200 to 350 m for the transition distance R_0.

In Fig. 3, the range dependence of the propagation anomaly is shown that was obtained in an experiment carried out in the summer season (in June). In the same figure, in addition to the experimental dependence (the solid curve), the calculated range dependence (the dotted curve) of the propagation anomaly is plotted. The calculation was performed with the computer code by Tebyakin [3].

With the explosion-generated signals, the following quantity was used to characterize the sound field:

$$E_f = \int_0^T p_f^2(t)dt,$$

where $p_f(t)$ is the time-dependent sound pressure in the explosion-generated signal upon filtering within 1/3-octave frequency bands, and T is the signal duration. This quantity is equivalent to the energy of the received signal, which is normalized to the associated frequency band.

The signals received at distances longer than 20–30 km ($\geqslant R_0$) were processed to determine the parameter β governing the decay law:

$$E_f \sim \frac{1}{R} \times 10^{-0.1\beta R}.$$

The frequency dependence $\beta(f)$ was obtained for the attenuation coefficient.

All experimental data on the sound attenuation in the central region of the Baltic Sea are summarized in Fig. 4. The values of the low-frequency (100–2500 Hz) attenuation coefficient are shown for two experiments carried out in May (in different years), at different sea states (Beoufort 3 and dead calm), and for an experiment performed in September. Explosions were used as

the sound sources in these experiments. In the figure, the attenuation coefficients for the kilohertz frequency band are also shown; they were obtained in different years with the use of cw sound sources. Most of the entire set of data on the frequency dependence of the low-frequency attenuation coefficient, which was obtained in the USC of the Baltic Sea, is bounded by two curves described by the expressions $\beta = 0.04f^{0.65}$ ∂B/km (the solid curve) and $\beta = 0.06f^{0.65}$ ∂B/km (the dashed curve), where f is the frequency (in kHz).

In the experiments of May (the full circles), the attenuation coefficients obtained at a sea state of Beoufort 3 are (on average) by a factor of 1.5 higher than those obtained for a dead calm sea.

In the data of September (the squares), a pronounced minimum in the attenuation can be seen at the frequencies 400–600 Hz. At the same time, the data of May exhibit only a trend to forming the attenuation minimum at 100–200 Hz. The analysis of the difference in the propagation conditions for the beginning and end of summer allows one to assume that the position of the minimum is governed by the critical frequency of the water modes. For example, for the sound speed profiles $C(z)$ of May, at the sea depth 80–90 m, the calculated value of the critical frequency is 80–110 Hz for the first mode, while it is 180–220 Hz for September. For the second, third, and higher modes, the critical frequencies are higher by a factor of two, three, and so on. It is hardly probable that the sound field is formed solely by the first mode. Hence, at frequencies lower than 400–600 Hz in September and lower than 100–200 Hz in May, the attenuation was caused by the losses of the sound energy in the sea floor, in addition to the absorption in the water medium. The contribution of the bottom-associated losses must increase as the frequency decreases, just in accordance with the experimental data.

For the sake of comparison, Fig. 4 also shows the experimental results obtained by Schneider *et al.* [4] in summer (August) on a 70-km path, with the sea depth about 120 m (see the full triangles). These data agree well with our results. The authors of the cited publication attempted to explain the observed attenuation in the Baltic Sea by the relaxation absorption associated with boron that is present in the sea water. To estimate the absorption coefficient, they used the formulas given in [5], which unfortunately are incorrect in describing the actual dependence of this quantity on the boron concentration.

Nowadays, the relaxation absorption associated with boron is used to explain the low-frequency sound attenuation in relatively "calm" regions of the ocean, i.e., in the regions that are not influenced by intense currents, mixing of different-origin waters, or straits. The boron content in ocean waters is approximately constant and equals 4.6 mg/l. This content varies proportionally to the water salinity. In this respect, we can say that the law of constancy for the salt content of the

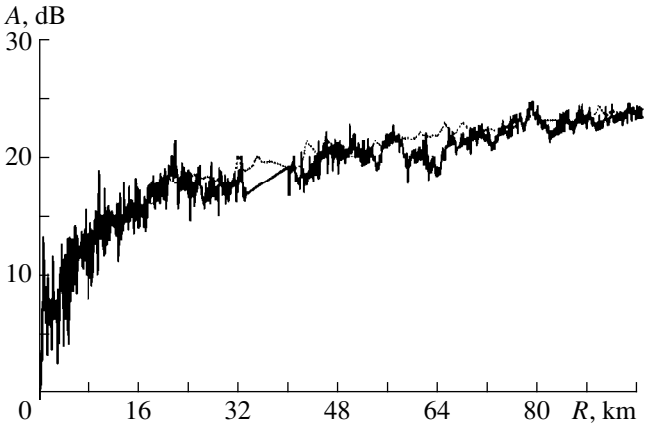

Fig. 3. Propagation anomaly for an experiment with the cw sound source. The transmission and reception depths are 56 and 52 m, respectively. The dotted curve is computed with the code by Tebyakin [3].

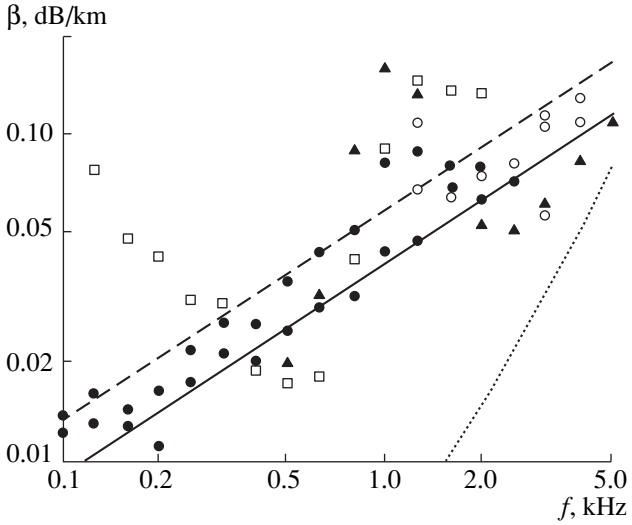

Fig. 4. Experimental data on the sound attenuation in the central region of the Baltic Sea.

sea water (the Marcette principle [6]) is valid for boron as well. In spite of the significant desalination (6–14‰), the Baltic waters are not an exception, with respect to both their main components [7] and boron [8]. For the Baltic Sea, the proportions in the salt water content are the same as for the ocean: the deviations are lower than 5–10%. Thus, the considerable change in salinity of the Baltic waters, as compared to the ocean, leads to a proportional change in the boron content.

To estimate the low-frequency absorption coefficient, we use the expression [9]

$$\alpha = \frac{A_B f}{f/f_{rB} + f_{rB}/f} + \frac{A_{MgSO_4} f}{f/f_{rMgSO_4} + f_{rMgSO_4}/f} + Kf^2,$$

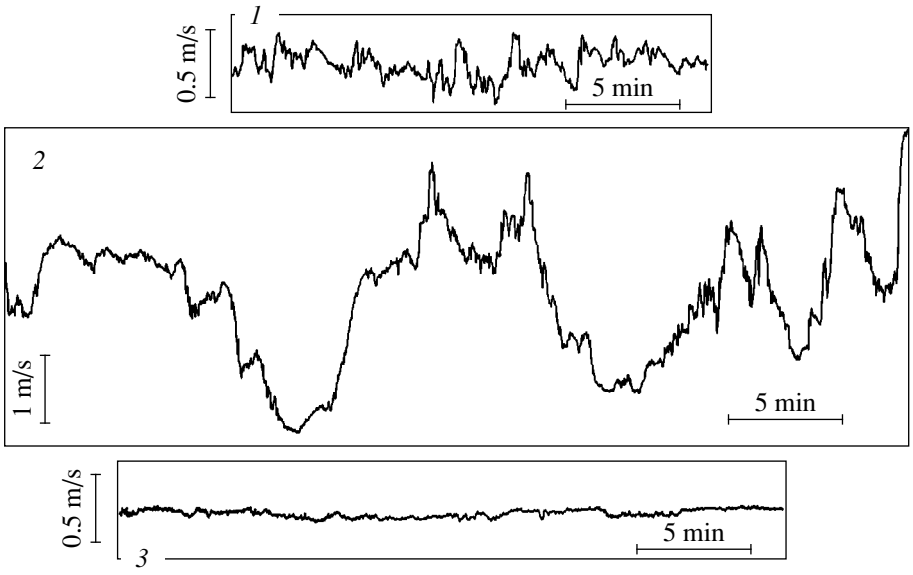

Fig. 5. Time variations of the sound speed at three fixed depths corresponding to (*1*) the mixed upper layer, (*2*) the temperature discontinuity layer, and (*3*) the axis of the underwater sound channel.

where f is the frequency (kHz), $K = 1.42 \times 10^{-8} \times 10^{1240/T}$ dB/km kHz^2, $f_{r\mathrm{MgSO_4}} = 1.125 \times 10^{(9-2038/T)}$ kHz, $A_{\mathrm{MgSO_4}} = 62.5ST \times 10^{-6}$ dB/km kHz, $f_{rB} = 37.9S^{0.8} \times 10^{-780/T}$ kHz, $A_B = 1.65S \times 10^{(4+0.78\mathrm{pH}-3696/T)}$ dB/km kHz, S is the salinity (‰), T is the temperature (K), and pH is the hydrogen ion exponent.

For the central region of the Baltic Sea (at the depth close to the USC axis), the temperature 4–5°C, the salinity 6–10‰, and the hydrogen ion exponent 7.8–8.0 are typical. The frequency dependence of the absorption coefficient, which was calculated for these mean values of the parameters, is shown by the dotted curve in Fig. 4. For the low-frequency sound attenuation in the Baltic Sea, one can see a significant excess of its value over the absorption caused by the relaxation processes associated with magnesium sulphate and boron that are present in the sea water. Such an excess indicates that there are additional mechanisms responsible for the main part of the losses in the sound propagation in the USC of the Baltic Sea.

In the literature, numerous mechanisms are discussed that lead to an additional sound attenuation in the ocean (the scattering by various inhomogeneities of the medium [10, 11], the losses of the sound energy in the suspension of sediment particles [12], etc.).

In one of the acoustic experiments, we monitored the fluctuations of the sound speed by cyclically measuring it at characteristic horizons. The data obtained in this experiment show relatively high rms values of the measured sound speed fluctuations. For example, according to the data of one set of the measurements, the rms values of the refractive index fluctuations $\sqrt{\langle \mu^2 \rangle}$ were 9×10^{-5} in the upper water layer, 12×10^{-4} in the temperature discontinuity layer, and 35×10^{-6} at the USC axis. If the additional attenuation in the Baltic Sea is associated with the sound scattering by thermal inhomogeneities of the water medium off the USC (according to [10]), then, with the inhomogeneities of about 30 cm in size, it is sufficient to specify the value 10^{-3} for $\sqrt{\langle \mu^2 \rangle}$. We observed such values of $\sqrt{\langle \mu^2 \rangle}$ only in the temperature discontinuity layer. However, the records shown in Fig. 5, which were obtained in a set of the sound speed observations, exhibit a behavior that is typical of internal waves rather than of random inhomogeneities. The data of the measurements confirm the existence of internal waves in the temperature discontinuity layer, the periods of these waves being about 10–20 min. The magnitude of the sound speed fluctuations reaches 4 m/s in this layer. With a sound speed gradient of about 0.8 1/s in the layer, this magnitude corresponds to a height of approximately 5 m of the internal wave (from its crest to foot). If we specify a value of ~0.4 m/s for the propagation velocity of the internal waves, the wavelength will be about 360 m.

To estimate the losses associated with the sound scattering by internal waves, we carried out a computer simulation. We used a sinusoidal internal wave with the parameters close to the experimentally observed ones. The changes were calculated in the angle at which the ray crosses the USC axis after turning in the temperature discontinuity layer perturbed by the internal wave. On the assumption of equally probable positions of the internal wave (in its phase) relative to the source, a distribution was estimated for the deviations of the angle of the ray intersection with the USC axis, as measured relative to the initial value (i.e., the one unperturbed by the internal wave). The obtained distribution was recal-

culated to the scattering diagram. The redistribution of the sound energy was computed for each of the selected ray tubes (about 100 tubes), after each ray turning in the discontinuity layer. In this procedure, the energy scattered beyond the angle range of the water rays was treated as lost. The coefficient of losses estimated in such a way proved to be 1–2 dB/km for the conditions of the May experiment.

For the attenuation coefficient due to the sound scattering by internal waves, off the USC, a more rigorous ray-approximation estimate was reported in [13, 14]. A solution was used for the equation of the ray diffusion caused by the medium inhomogeneities represented by internal waves with the Munk spectrum [15]. As applied to the equatorial Atlantic, the obtained relations led to rather low values of the attenuation coefficient ($\sim 5 \times 10^{-4}$ dB/km), which are comparable with the absorption in the ocean only at frequencies lower than 50 Hz. On the other hand, the recalculation performed by us for the Baltic Sea leads to attenuation coefficients that have the same order of magnitude as those observed experimentally at frequencies of about 1 kHz.

The obtained estimates are somewhat rough and yield an order of magnitude for the attenuation caused by internal waves rather than its frequency dependence. However, these estimates show that the sound scattering by internal waves is the most probable explanation for the observed increased level of the attenuation.

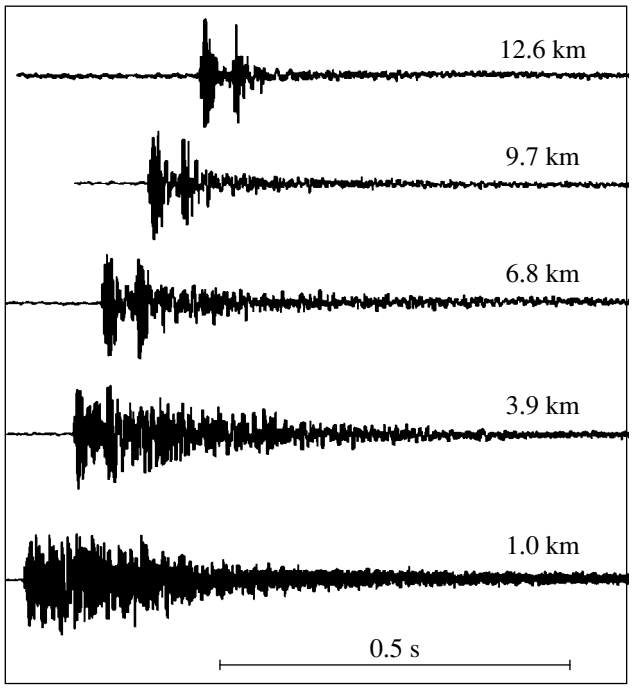

Fig. 6. Time structure of the explosion-generated signals received at short (<13 km) distances from the source. The source–receiver distance is indicated on the right for each signal.

The time structure of the sound field was studied with the use of explosive sound sources. Let us recall that the initial ("single-ray") explosion-generated signal that serves as the "sounding" one in our experiments consists of a train of short pulses: the shock wave and several fluctuations of the gas bubble. If the spectrum of the explosion-generated signal is limited by 3–5 kHz from above, the pulses of the shock wave and the first fluctuation have comparable amplitudes, which considerably exceed those of subsequent fluctuations of the gas bubble. The time delay between the pulses of the shock wave and the first fluctuation (the period of the first fluctuation T_0) depends on the charge weight and the depth of the explosion. If small charges (the pressure-sensitive detonators that we used in our experiments) are exploded at a depth of 50 m, the bubble fluctuation period is 40 ms.

In the studies of region-dependent features of the time structure of the sound field in deep-water regions of the ocean, the greatest attention has been paid to the positions of the "classical" quartets of signals whose relative time delays are determined by the sound propagation over the whole water column of the ocean (or over the major part of it) [16]. In such an approach, the conservative characteristics of deep waters (deeper than 200–300 m) played the decisive role in forming the time delays between the quartets, this conservation providing the reliability and stability of the regional classification. The Black Sea is the only region where the stability and reproducibility of the time structure has been observed in the sound field formed within the 200-m subsurface layer. Highly ordered arrival times were observed in the sound field that was formed by signals propagating along the near-axis rays in the 200-m subsurface layer of the Black Sea. This property of being highly ordered manifested itself in a specific form of the terminal part of the explosion-generated signal propagating in the USC. Such a form has been never observed in other seas.

In the Baltic Sea (in contrast to a deep sea), the time structure of the sound field is completely formed by signals that propagate in the shallow 100- to 150-m water layer whose characteristics are strongly variable in time and space.

The time structure of the sound field was calculated for the path in the Baltic Sea with the sea depths smaller than 90 m. The calculation yields a complex pattern: the signal quartets that differ in a number of full ray cycles overlap, and the sequence of single arrivals, which is typical of a deep sea, is violated. With the sea depth up to 250 m, the ordered arrivals are observed only for the signals that have lower turning points at horizons deeper than 90–100 m.

The key features of forming the structure of the sound field in the Baltic Sea can be illustrated by the data of a May experiment. In Fig. 6, the signals are shown that were received at a distance of 13 km from the source. In this figure and the following ones, the amplitude of each signal is normalized to its maximal

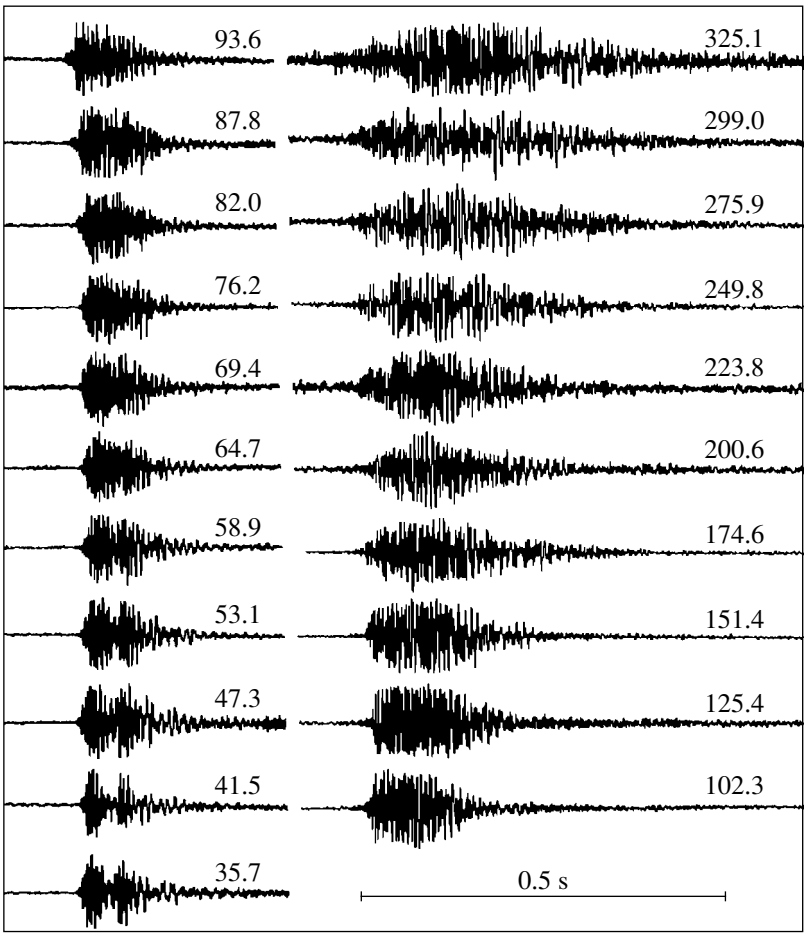

Fig. 7. Time structure of the explosion-generated signals received at long (>35 km) distances from the source. The source–receiver distance (in km) is indicated on the right for each signal.

value. At distances up to 6–8 km from the source, a reverberation-like protraction of the signal can be noticed that nearly vanishes at 12 km. In the multiray signals received at the distances 4–13 km, two compact groups are well-resolved that are separately formed by the pulses of the shock wave and the first gas-bubble fluctuation. Within each group, single signals are unresolvable. The duration of each group is by a factor of 3–4 less that the period of the first bubble fluctuation. As the distance increases, the two resolved groups of signals become broader and begin to overlap; they become nearly unresolved starting from the distance 55–60 km (Fig. 7). The duration of the groups becomes approximately equal to the bubble fluctuation period at 50–55 km.

A characteristic feature of the signals received at the distances up to 175 km is their sharp fronts. At the distances 200–225 km and longer, the signal front is spread, and a smooth increase in the signal level is observed (Fig. 7). Such changes in the signal shape can be explained by the sound scattering from internal waves. Starting from 150–175 km relative to the reception point, the sea depth smoothly increases from 120–130 to 240 m at the distance 250 km. A possibility arises for the sound to propagate at horizons deeper than 80–100 m without contacts with the bottom, along the rays that cross the USC axis at the angles greater than 6°–7°. With the scattering by internal waves, such a propagation is quite feasible. Figure 8 presents the reduced *t–R*-diagram calculated for the Baltic Sea. According to this diagram, the signals propagating along the aforementioned rays are ahead of the signals propagating along the main energy-carrying ray beam formed at the 100-km part of the path that is closest to the reception point. As a result, the front of the multiray explosion-generated signal is spread. With an inaccuracy determined by the time spreads of the leading and trailing edges of the multiray signal, one can estimate the signal duration at different distances from the source. The factor of proportionality is equal to 0.0012 s/km for the signal protraction on the path at hand.

In analyzing the time structure of the sound field, one should also consider the low-frequency waves propagating in the sea bottom. To observe and record

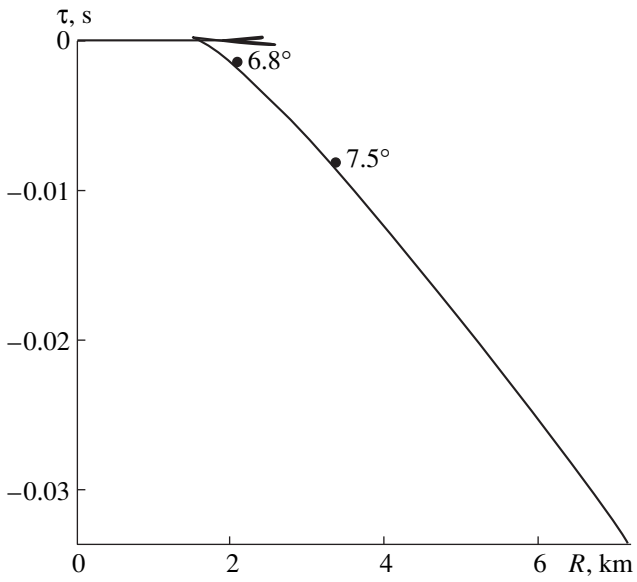

Fig. 8. Reduced *t*–*R*-diagram computed for the central region of the Baltic Sea. The two points of the diagram (6.8° and 7.5°) correspond to the limiting water signal at the sea depths 80 and 90 m, respectively.

these bottom waves, in some experiments we used a special receiving device whose frequency response was extended down to the infrasound frequencies (5–6 Hz) with a noticeably reduced noise level at these frequencies. The bottom waves generated by the explosive sound source were observed up to the distances 10–15 km.

To visualize the bottom waves, the received explosion-generated signal was preliminarily filtered by a two-band filter with pass frequencies of 7–35 and 140–180 Hz. The time structure of the bottom waves was analyzed in view of the arrival time of the water waves and, hence, in view of the time structure of the entire received signal. Figure 9 shows a set of the recorded explosion-generated signals received by a bottom-moored hydrophone in one of the measurements. The water signal was recorded with some overload (it is symbolically shown by the black spot); the bottom signals were received with a sufficient excess over the interfering noise.

The time structure of the bottom waves strongly depends on the properties of the sea floor. The group velocity of the signal is a function of frequency and changes from the value of the sound speed in the bottom material to the 0.7- to 0.9-fraction of the sound speed in water. For the simplest model of a two-layer sea medium (a water layer above a half-infinite liquid bottom), the group velocity U of sound is given by the expression [18]

$$\frac{1}{U} = \frac{1}{C_0\cos\theta}\left[\cos^2\theta + \frac{\sin\theta}{\dfrac{1}{\sin\theta} + \dfrac{m(1-n^2)}{\left(\dfrac{2l-1}{2}\pi + \arctan\dfrac{\sqrt{\cos^2\theta - n^2}}{m\sin\theta}\right)(m^2\sin^2\theta + \cos^2\theta - n^2)\sqrt{\cos^2\theta - n^2}}}\right],$$

where C_0 is the sound speed in water, $n = C_0/C_b$, C_b is the sound speed in the bottom material, $m = \rho_0/\rho_b$, ρ_0 and ρ_b are the densities of water and bottom material, and θ is the grazing angle of the plane waves that constitute the lth normal wave. From this expression, one obtains $U = C_b$ for the critical grazing angle θ_{cr} ($\cos\theta_{cr} = n$). The sound speed in the bottom is the maximal velocity for the signal transmission in such a waveguide. Thus, from the arrivals of the explosion-generated signals received at different distances from the source, one can estimate the sound propagation velocity in the sea floor. At $\theta \longrightarrow 0$, the group velocity tends to the sound speed in water. However, it is not the minimal group velocity. It is the propagation velocity of the Airy wave which is the last to arrive at the receiver, and the minimal group velocity is somewhat lower than this value. The Airy wave also carries information on the bottom material. The propagation velocity and the frequency of the Airy wave depend on the ordinal number of the exited wave, as well as on the ratios of the densities and sound speeds for the bottom material and the water. Upon determining the sound speed in the sea floor (from the time analysis of the signal), one can attempt to estimate the density of the bottom material. However, the accuracy of such an estimate will be rather low. Thus, with $C_0/C_b = 0.75$, a change from 1 to 2 in the ratio ρ_b/ρ_0 of the densities leads to only a 1.5%-change in the propagation velocity of the Airy wave and to a frequency change by 15%.

For a multilayer model of the medium, the dispersion phenomena are more complicated. However, if the upper sediment layer is much thicker than the water one, the three-layer model allows one to use the relations obtained for the simplest two-layer model, with a

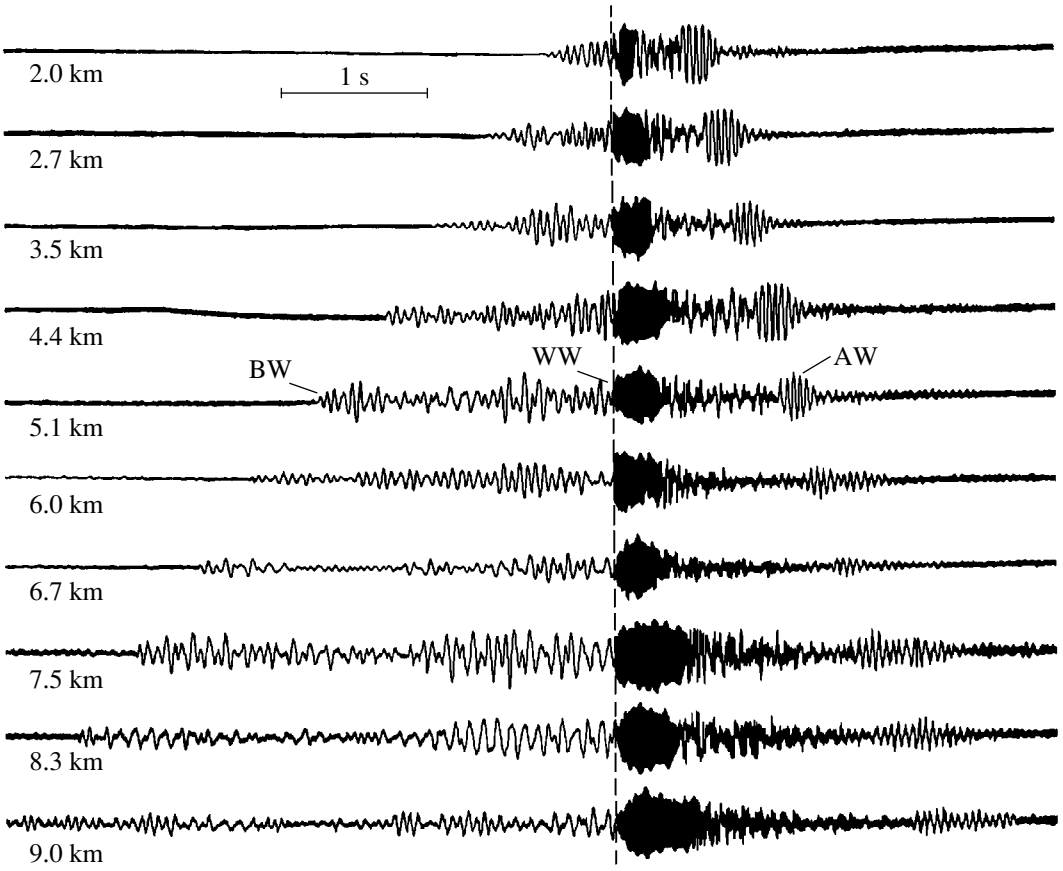

Fig. 9. Time structure of the explosion-generated signals received at short (2 to 9 km) distances from the source by the bottom-moored hydrophone in the frequency band 7–35 Hz. The vertical dashed line indicates the arrival time of the water signal that is schematically shown by the black spot. The following abbreviations are used: BW for the bottom wave, AW for the Airy wave, and WW for the water waves.

sufficient degree of reliability. On the other hand, by measuring the arrival times of single bottom waves that correspond to separate layers of the bottom sediments, one can estimate the thicknesses of these layers, e.g., with the use of the technique described in [19]. With the multilayer model, it is much more difficult to identify single Airy waves associated with each layer boundary. The Airy wave which propagates with the minimal velocity is the only one that can be well detected.

The ten records shown in Fig. 9 correspond to ten explosions produced at the distances 2 to 9 km from the receiver. The bottom signal becomes split starting from the second explosion and remains such up to the tenth one. At some distances, several time-separated bottom waves arrive. However, for most explosions, only the arrivals of two bottom waves that can be associated with two separate layers of the bottom sediments can be observed.

On the basis of the analysis of the experimental time structure of the bottom waves for two parts of the studied path of long-range sound propagation, we estimated the structure of the bottom sediments. Within the central part of the path, the 360-m sediment layer with a sound speed of about 1900 m/s overlies a layer of a more rigid bottom material with a sound speed of about 4600 m/s in it. For the southern end of the path, two sediment layers were identified (the 650-m upper layer with the sound speed ~1540 m/s and the 800-m lower one with the sound speed ~2100 m/s) that lie above the layer of a rigid material with a sound speed of approximately 4900 m/s.

ACKNOWLEDGMENTS

I am grateful to V.V. Nemchenko, A.V. Mikryukov, and N.K. Abakumova from the Acoustics Institute for the assistance in the experiments and for useful discussions. The work was supported by the Russian Foundation for Basic Research, project no. 99-02-18359.

REFERENCES

1. V. F. Sukhoveĭ, *Seas of the World Ocean* (Gidometeoizdat, Leningrad, 1986).
2. T. A. Bernikova, *Hydrology and Industrial Oceanology* (Moscow, 1980).

3. V. P. Tebyakin *et al.*, A Report (Akust. Inst. Akad. Nauk SSSR, Moscow, 1990).
4. H. G. Schneider, R. Thiel, and P. C. Wille, J. Acoust. Soc. Am. **77**, 1409 (1985).
5. R. E. Francois and G. R. Garrison, J. Acoust. Soc. Am. **72**, 1879 (1982).
6. R. Horne, *Marine Chemistry* (Wiley, New York, 1969; Mir, Moscow, 1972).
7. E. Zarins and J. Ozolins, J. Cons. (Copenhagen) **10** (3) (1935).
8. D. W. Dyrssen and L. R. Uppstrom, J. Hum. Env. Res. Man. **3** (1) (1974).
9. R. A. Vadov, Akust. Zh. **46**, 624 (2000) [Acoust. Phys. **46**, 544 (2000)].
10. L. A. Chernov, *Wave Propagation in a Random Medium* (Akad. Nauk SSSR, Moscow, 1958; McGraw-Hill, New York, 1960).
11. Yu. P. Lysanov and L. M. Lyamshev, in *Proceedings of the Fourth European Conference on Underwater Acoustics* (Rome, 1998), p. 801.
12. S. D. Richards, J. Acoust. Soc. Am. **103**, 205 (1998).
13. *Sound Transmission through a Fluctuating Ocean*, Ed. by S. Flatte (Cambridge Univ. Press, Cambridge, UK, 1979; Mir, Moscow, 1982).
14. R. H. Mellen, D. G. Browning, and L. Goodman, J. Acoust. Soc. Am. **60** (5) (1976).
15. C. Garret and W. H. Munk, J. Geophys. Res. **80**, 291 (1975).
16. R. A. Vadov, Akust. Zh. **40**, 930 (1994) [Acoust. Phys. **40**, 824 (1994)].
17. R. A. Vadov, Akust. Zh. **44**, 749 (1998) [Acoust. Phys. **44**, 651 (1998)].
18. M. A. Isakovich, *General Acoustics* (Nauka, Moscow, 1973).
19. C. Pekeris, Mem.–Geol. Soc. Am., No. 27 (October 15, 1948).

Translated by E. Kopyl

Acoustical Physics, Vol. 47, No. 2, 2001, pp. 160–168. Translated from Akusticheskiĭ Zhurnal, Vol. 47, No. 2, 2001, pp. 200–209.

REVIEWS

Interaction of a Shear Wave with a Moving Domain Wall in an Iron Garnet Crystal

E. A. Vilkov*, V. G. Shavrov, and N. S. Shevyakhov***

** Institute of Radio Engineering and Electronics, Ul'yanovsk Branch, Russian Academy of Sciences, ul. Goncharova 48, Ul'yanovsk, 432700 Russia*

*** Institute of Radio Engineering and Electronics, Russian Academy of Sciences, ul. Mokhovaya 11, Moscow, 103907 Russia*

Received September 25, 1998

Abstract—The boundary-value problem of the interaction of a plane monochromatic shear wave with a moving Bloch wall in an iron garnet crystal is solved in the framework of the nonexchange magnetostatic approximation on the basis of the method of phase invariants for wave problems with moving boundaries. For a shear wave incident on the domain wall, the possibility of the reflectionless birefringence is demonstrated. Numerical results illustrating the resonance properties of the magnetic subsystem are presented. It is established that, at the upper bound of the reflectionless birefringence range, the interaction of the shear wave with the domain wall manifests itself as a degenerate resonance with the solution in the form of two combined antiphase, collinearly propagating shear waves of infinitely large amplitudes, which form a zero resulting field. © *2001 MAIK "Nauka/Interperiodica".*

In our recent publication [1], we reported on the possibility of a reflectionless birefringence for a shear wave incident on a moving 180° domain wall (DW) in an iron garnet crystal. However, it was found that, for obtuse refraction angles $\theta' > \pi/2$, which are characteristic of this phenomenon (Fig. 1), it is of fundamental importance to take into account the effective changes that are implicitly introduced in the dispersion law of the refracted waves by the motion of the DW. Therefore, a more detailed study of this problem is required.

This paper continues the previous study [2] and the aforementioned publication [1]. We note that the problem of the interaction of acoustic waves with moving domain walls in ferrites was to some extent initiated by the study of the parametric interaction of electromagnetic radiation with moving mirror boundaries in optics and in electrodynamics [3]. In particular, the reflection of electromagnetic waves from moving magnetic "mirrors" (magnetic steps) in ferrites was considered by Freidman [4].

For acoustic waves, the first results were obtained by Auld and Tsai [5] who pointed out the possibility of an adiabatic interbranch transformation of magnetoelastic waves incident on a moving magnetic step in a ferrite, this transformation being a result of the Doppler shift. A rigorous evaluation of the efficiency of such processes proved to be possible for the case of a plane Bloch wall after the theoretical study by Nedlin and Shapiro [6] who considered the reflection of an acoustic wave from a moving DW of the aforementioned type in a cubic ferrite. However, in the cited paper and in the following publications [7, 8], the analysis was performed for a normal incidence of waves on the DW, when, in iron garnets in the frequency range $\omega \lesssim 10^{10}$ s^{-1}, the acoustodomain interaction, which is caused mainly by the contribution of the nonuniform exchange to magnetostriction, is weak.[1] As was noted in [2], this interaction can noticeably increase owing to the resonance response of the magnetic subsystem through the magnetostatic scattering fields of the poles of alternating signs, which are induced at the DW by an obliquely incident wave. It is essential that the aforementioned possibility of an increase in the interaction of the incident wave with a DW allows one to considerably simplify the procedure of constructing the solution for the case of iron garnets by using the nonexchange approximation and by eliminating the short-wave (exchange) part of the spectrum, so that the DW can be considered as a structureless, infinitely thin boundary.

It should be noted that, after the aforementioned publication [2], no papers concerned with the problem of acoustodomain interaction in iron garnets in the conditions of an oblique incidence of waves on a moving DW appeared in the literature. The structureless representation of a DW as a geometric domain boundary implies that it cannot be excited in its internal (structural) degrees of freedom at the expense of the motion, which, hence, can be considered as preset. Otherwise, one has to consider the typical problem of the magnetodynamics of domain walls that consists in the self-

[1] This does not apply to the case of antiferromagnets characterized by a strong magnetoelastic coupling [8]. However, for the latter materials, it also seems important to take into account the response of magnetostatic scattering fields to the acoustodomain interaction in the conditions of an oblique incidence of acoustic waves.

1063-7710/01/4702-0160$21.00 © 2001 MAIK "Nauka/Interperiodica"

consistent description of the acoustic fields (not necessarily in the presence of external sources of radiation, if one is interested in the acoustic generation [9–11]) and the motion of the DW with allowance for different aspects of its dynamic stability [12–14].

Let us assume that shear waves propagate in the (001) plane of an iron garnet with the displacements $\mathbf{u}_j$ collinear with the spontaneous magnetizations $\mathbf{M}_0^{(j)}$ in the domains ($\mathbf{M}_0^{(1)} \uparrow\downarrow \mathbf{M}_0^{(2)} \parallel [001]$; $j = 1, 2$ is the domain number). The domains are separated in the (010) plane by a geometrically thin, structureless Bloch wall with the current coordinate $y_D = V_D t$, where $V_D < 0$ is the velocity of the Bloch wall motion and t is time. Correspondingly, we assume that the spontaneous magnetizations $M_0^{(j)}$ and the internal magnetic fields $H_i^{(j)}$ in the domains have the form $M_0^{(j)} = (-1)^{j+1} M_0$ and $H_i^{(j)} = (-1)^{j+1} H_i$, where $M_0 > 0$, $H_i > 0$, $j = 1$ for $y > y_D$, and $j = 2$ for $y < y_D$. Since we use the nonexchange magnetostatic approximation, the adopted model of the DW is adequate for the interval of the wave numbers k and frequencies ω up to the values slightly exceeding the "forbidden" gap in the spectrum of magnetoelastic waves [15]. In addition to the condition $k\Delta \ll 1$ (Δ is the DW thickness) satisfied in the aforementioned interval, we also imply a low structural sensitivity of the domain walls to external actions [16], which is characteristic of iron garnets away from the phase transition. To exclude the magnetostrictive (Cherenkov) instability of the DW, we assume that $|\mathbf{V}_D| < c_t$, where c_t is the velocity of shear waves without regard for the magnetoelastic coupling.

With the conditions specified above, we arrive at the following initial equations (see [2]):

$$\nabla^2 u_j + (\rho\Omega^2/\lambda_\Omega^*) u_j = 0,$$
$$\nabla^2 \varphi_j = (-1)^{j+1} \frac{4\pi\gamma\beta\omega_0}{\Omega^2 - \omega_k^2} \nabla^2 u_j. \qquad (1)$$

Here, Ω is the frequency of the incident or refracted wave, φ_j is the magnetostatic potential, $\lambda_\Omega^* = \lambda + \gamma\beta^2\omega_0/[M_0(\Omega^2 - \omega_k^2)]$, $\omega_0 = \gamma H_i$ is the uniform precession frequency, $\omega_M = 4\pi\gamma M_0$ is the magnetization frequency, $\omega_k = [\omega_0(\omega_0 + \omega_M)]^{1/2}$ is the magnetoacoustic resonance frequency, γ is the gyromagnetic ratio, β is the magnetoelastic interaction coefficient, λ is the shear modulus, and ρ is the density of the ferrite.

The first of Eqs. (1) is the Helmholtz equation the solution to which can be represented in the form of plane harmonic waves with the dispersion law

$$k^2 \equiv k^2(\Omega) = \frac{\rho\Omega^2}{\lambda_\Omega^*}. \qquad (2)$$

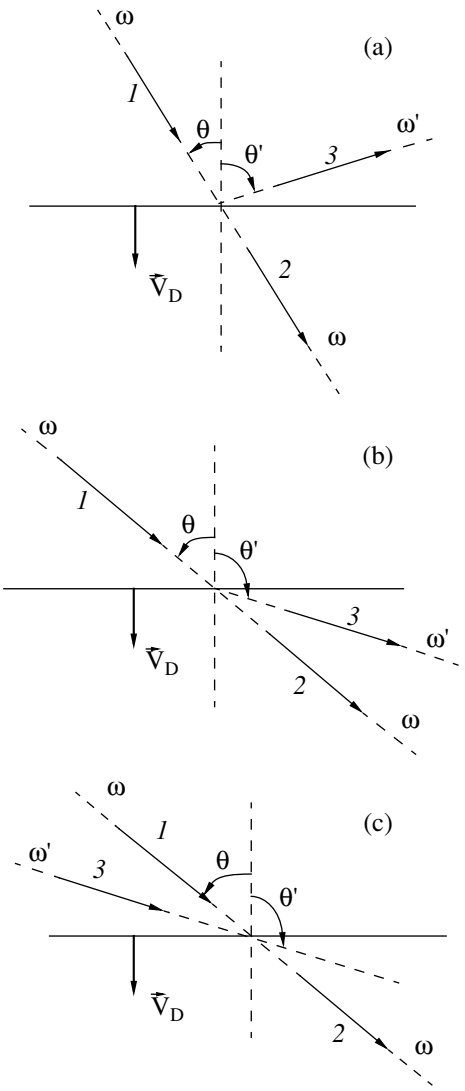

Fig. 1. Refraction of a shear wave by a moving DW for (a) acute and (b, c) obtuse refraction angles: (*1*) the wave vector of the incident wave, (*2*) the wave vector of the directly transmitted wave, and (*3*) the wave vector of the refracted wave.

The second of Eqs. (1) allows us to write the expressions

$$\varphi_j = (-1)^{j+1} \frac{4\pi\gamma\beta\omega_0}{\Omega^2 - \omega_k^2} u_j + \Phi_j, \quad \nabla^2 \Phi_j = 0, \qquad (3)$$

where Φ_j is the potential of the scattering field of the magnetic poles.

Following the usual procedure of solving the refraction problems, we set the frequency ω and the wave vector of the incident wave $\mathbf{k} = \mathbf{n}k$, where $\mathbf{n} = (\sin\theta, -\cos\theta)$, θ is the angle of incidence, and $k = k(\omega)$ is the wave number determined from Eq. (2) in which Ω is replaced by ω. The wave refracted by the moving DW is characterized by the frequency ω' and the wave vec-

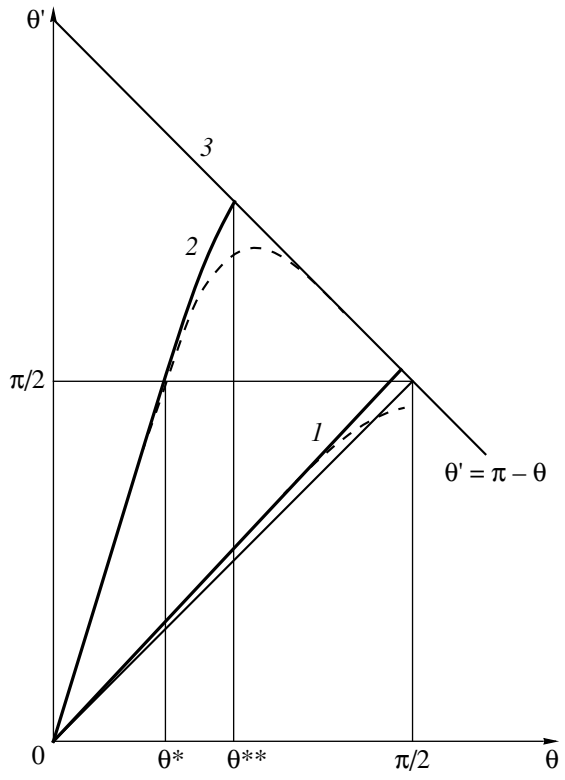

Fig. 2. Typical refraction dependences in the vicinities of the frequencies ω_0 (the solid curves) and ω_k (the dashed curves): (*1*) the case of low velocities $|V_D| \ll c_t$, (*2*) the case of moderate velocities $|V_D| < c_t$, and (*3*) the refraction dependence $\theta' = \pi - \theta$ for the directly transmitted wave.

tor $\mathbf{k}' = \mathbf{n}'k'$ with the wave normal $\mathbf{n}' = (\sin\theta', \cos\theta')$ and the wave number $k' = k(\omega')$, which is obtained from Eq. (2) with Ω being replaced by ω'. Here, θ' is the refraction angle from the interval $[0, \pi)$.

The relationship between the frequencies ω and ω' and the angles θ and θ' can be determined from the condition of the conjunction of the wave fields at the DW by the phase invariant method [3]. Namely, from the equality of the projections of the wave vectors of the incident and refracted waves at $y = y_D$, we obtain

$$\frac{\omega}{v}\sin\theta = \frac{\omega'}{v'}\sin\theta' \equiv k_\tau \qquad (4)$$

and the temporal matching of the phases of oscillations at the DW is provided by the relationships

$$\omega\left(1 + \frac{V_D}{v}\cos\theta\right) = \omega'\left(1 - \frac{V_D}{v'}\cos\theta'\right) \equiv \tilde{\omega}. \qquad (5)$$

In Eqs. (4) and (5), $v = \omega/k$ and $v' = \omega'/k'$ are the phase velocities of the incident and refracted waves, respectively.

Taking into account Eq. (2), one can prove that Eqs. (4) and (5) are equivalent to the system of equations

$$\sin\theta' + \frac{V_D}{v}\sin(\theta + \theta') = \frac{\sin\theta}{v}c_t\left[1 + \frac{\chi\omega_0^2}{\omega^2 f^2(\theta, \theta') - \omega_k^2}\right]^{1/2}, \qquad (6)$$

$$\frac{\omega'}{\omega} = 1 + \frac{V_D}{v}\frac{\sin(\theta + \theta')}{\sin\theta'} \equiv f(\theta, \theta'). \qquad (7)$$

The quantity $\chi = \gamma\beta^2/(\lambda M_0\omega_0)$ is the dimensionless (and usually small, $\chi \ll 1$) parameter of magnetoelastic coupling, and $c_t = (\lambda/\rho)^{1/2}$.

Since θ, ω, and, hence, $v = v(\omega)$ are known, Eq. (6) determines θ' as the root of a transcendental equation. Then, the corresponding value of ω' can be easily calculated by Eq. (7), which exhibits the presence of the Doppler shift in the refracted wave. The first of the two solutions to Eq. (6), $\theta' = \pi - \theta$, exists only for obtuse refraction angles $\theta' > \pi/2$ and does not depend on V_D. The wave refracted in such a way has the characteristics ω, ν, and $\mathbf{k}$ that are identical to the characteristics of the incident wave. It is evident that, in the conditions in which the refraction problem has a physical meaning, this wave should be associated with the propagation region $y < y_D$. As a result, the root $\theta' = \pi - \theta$ of Eq. (6) will correspond to the directly transmitted shear wave represented in the refraction diagrams of Fig. 1 by arrows *2* (in terms of the wave vectors).

The second solution to Eq. (6), $\theta' \neq \pi - \theta$, can be obtained only by the numerical method. In [2], the solution was obtained by applying the iteration procedure directly to Eqs. (4) and (5). Because of the possibility for the iterated values of the frequency ω' to fall into the "forbidden" gap of spectrum (2) of magnetoelastic waves at the intermediate stages of calculation, a strict limitation was imposed on the region of calculation: $|V_D|/c_t \ll 1$. This condition considerably narrowed the region of calculation and made it impossible to consider in detail the refraction of the shear wave by the DW for obtuse angles $\theta' \neq \pi - \theta$. To avoid this disadvantage, here we will use a more general procedure of an exhaustive search to determine the root θ' [17].

The refraction dependences $\theta'(\theta)$ obtained with this method are shown in Fig. 2 for small ($|V_D| \ll c_t$, curves *1*) and moderate ($|V_D| < c_t$, curves *2*) fixed values of $V_D < 0$ for frequencies close to ω_0 and for frequencies $\omega \gtrsim \omega_k$ by solid and dashed curves, respectively. The difference observed between these curves at $\theta' \longrightarrow \pi - \theta$ (line *3* in Fig. 2 corresponds to the refraction law $\theta' = \pi - \theta$ for the directly transmitted wave) is explained by the considerable frequency dispersion of the refracted wave due to the Doppler-related approach of ω' to ω_k, which occurs in the case of the dashed curves according to Eqs. (6) and (7). The dashed curves have the form typ-

ical of the refraction dependences for waves in the conditions of a complex aberration effect [18].

If we ignore the nearly grazing incidence of waves with the frequencies $\omega \gtrsim \omega_k$ (see dashed curve *1* in Fig. 2), we will have $\theta' > \theta$ and, according to Eq. (7), $\omega' < \omega$. In such conditions, the refraction curves shown in Fig. 2 demonstrate the possibility of a transition from acute refraction angles $\theta' < \pi/2$ (see Fig. 1a where refracted wave *3* represents a reflected wave) to obtuse angles $\theta' > \pi/2$ with increasing θ (Figs. 1b, 1c). We restrict our consideration to the case $\theta' > \pi/2$ when $\theta \in [\theta^*, \theta^{**}]$; the reflective refraction for $\theta < \theta^*$ was considered in [2].

To estimate the lower bound θ^* of the interval under study, it is convenient to assume that the frequencies ω are close to ω_0 and, without noticeably reducing the precision of our estimate, to set $v \approx c_t$, which corresponds to neglecting the term with χ in Eq. (6). Since, at $\theta = \theta^*$, we have $\theta' = \pi/2$, from Eqs. (6) and (7) we derive $\cos\theta^* \approx -2(V_D/c_t)(1+V_D^2/c_t^2)^{-1}$. The intersection of the solid refraction curves with the straight line *3* in Fig. 2 means that θ^{**} is determined in the conditions of a multiple degeneracy of the roots θ' of Eq. (6). To eliminate the degeneracy, we set $\theta + \theta' \approx \pi - \alpha$, $\alpha \ll \pi$. Then, we expand $\sin(\theta + \theta')$ and $\sin\theta'$ on the left-hand side of Eq. (6) in powers of α and retain the linear terms; assuming that $\omega' \approx \omega$ in Eq. (7) and taking into account the equality $v = c_t[1 + \chi\omega_0^2(\omega^2 - \omega_k^2)^{-1}]^{1/2}$, which follows from Eq. (2), we derive the expression

$$\cos\theta^{**} \simeq -\frac{V_D}{c_t}\left[1 + \frac{\chi\omega_0^2}{\omega^2 - \omega_k^2}\right]^{-1/2}. \qquad (8)$$

Here, ω must be sufficiently small in comparison with ω_k. As in the case of the solutions obtained for relativistic problems [3, 19–21], starting from the angle θ^{**}, the incident signal in the form of a pulse (group) of shear waves ceases to catch up with the DW moving away from it. Hence, the angular region $\theta > \theta^{**}$ is excluded from our consideration.

The problem of correctly constructing the solution within the interval $\theta^* < \theta < \theta^{**}$ formally consists in choosing between the alternative refraction variants presented in Figs. 1b and 1c. In the first case (Fig. 1b), refracted wave *3* complements the directly transmitted wave *2* in the region $y < y_D$, which was interpreted in [1] as the reflectionless birefringence experienced by the shear wave at a moving DW. In the second case (Fig. 1c), the orientation of the wave vector of the refracted wave *3* relative to the DW is the same as in Fig. 1b, but in this case the refracted wave "complements" the incident wave *1*. At first glance, this defies common sense. However, exactly this type of refraction is considered in the known solutions of the optics and electrodynamics problems with moving boundaries [3, 19] for the angles $\theta' > \pi/2$. The same results were obtained in other studies [20, 21].

By analogy with the cited papers [3, 19–21], wave *3* in Fig. 1c can be considered as an infinitely long (because we consider monochromatic waves) stub of radiation of Huygens sources from the DW surface, so that this stub is continuously generated but more and more lags behind the DW because of its relatively fast motion at $\theta > \theta^*$. Such a choice is based on the fact (mentioned in [3, 19]) that wave *3* in Fig. 1c provides the energy transfer away from the DW precisely because of the fast motion of the latter, which complies with the Mandelshtam radiation principle [22]. By contrast, in the first case (Fig. 1b), the choice of the solution was made in [1] on the basis of the seemingly evident fact of the normal dispersion of magnetoelastic waves [15] (see Eq. (2)) in compliance with the Sommerfeld radiation principle, which is suitable in these conditions. However, this approach [1] does not take into account that the DW is continuously displaced, which, according to the relativity principle, is equivalent to the opposite motion, or drift, of the medium as a whole with the velocity $|V_D|$ through the DW.

From the viewpoint of an observer resting in the DW frame of reference, such an "ether wind" makes the ferrite an anisotropic nonstationary medium with both frequency and spatial dispersion properties. In such a medium, the Mandelshtam condition of the energy transfer from the boundary by the refracted wave should be compatible with the possible existence of the states with both positive and negative energy densities [23]. According to Bolotovskiĭ and Stolyarov [24], in this case, the causality requirement will be satisfied for the waves with a positive projection of their group velocity $\mathbf{V}_g = \partial\tilde{\omega}/\partial\tilde{\mathbf{k}}'$ on the direction the energy transfer, independently of the type of the energy state of the medium. Here, $\tilde{\omega}$ and $\tilde{\mathbf{k}}'$ denote the frequency and the wave vector of the refracted wave in the DW frame of reference, $\tilde{x}\,0\tilde{y}\tilde{z}$, related to the laboratory frame of reference, $x0yz$, by the Galilean transformation $\tilde{x} = x$, $\tilde{y} = y - V_D t$, $\tilde{z} = z$, and $\tilde{t} = t$.

If we take into account the invariance of the wave numbers as a consequence of the general invariance of the Helmholtz equation (1) under the Galilean transformation, then, on the basis of the above consideration, we obtain the following criterion for the choice of the solution in the case under study, i.e., in the case of the reflectionless birefringence (Fig. 1b): $\partial\tilde{\omega}/\partial k' > 0$. When $\partial\tilde{\omega}/\partial k' < 0$, the refracted wave should complement the incident wave according to the diagram shown in Fig. 1c. In this case, we do not need to solve the boundary-value problem, because now the results obtained in [2] are also valid for the angular region $\theta > \theta^*$ ($\theta' > \pi/2$, $V_D < 0$). Evidently, this does not eliminate the necessity to draw a distinction between the ordinary reflected wave and the refracted wave complementing the incident one.

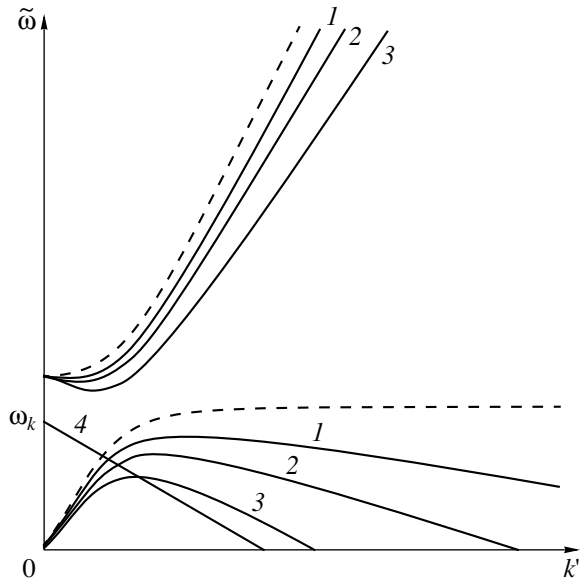

Fig. 3. Dispersion branches of the refracted wave in the DW frame of reference at a fixed value of $V_D < 0$ in the nonexchange approximation: (*1*) $\theta' \gtrsim \pi/2$, (*2*) $\theta' > \pi/2$, and (*3*) $\theta' = \pi - \theta^{**}$. The dashed curves correspond to the value $\theta' = \pi/2$ or $V_D = 0$. The straight line (*4*) represents the dependence $\tilde{\omega}(k')$ obtained from the time invariant of the phase of oscillations, Eq. (5), at $\theta = \theta^{**}$.

The quantity $\tilde{\omega}$ is a time invariant of the phase of oscillations at the DW [3]. Therefore, from Eq. (5) we obtain $\tilde{\omega} = \omega' - \mathbf{k}'\mathbf{V}_D$. Here, according to the rule that determines the real direction of motion of the DW by the sign of V_D, we have $\mathbf{k}'\mathbf{V}_D = k'V_D\cos\theta'$. The desired dependence $\tilde{\omega}(k')$ can be derived by using the explicit expression for ω' according to Eq. (2):

$$\tilde{\omega} = \frac{1}{\sqrt{2}}\left[\Omega_+^2 \pm \sqrt{\Omega_-^4 + 4k'^2c_t^2\chi\omega_0^2}\right]^{1/2} - \mathbf{k}'\mathbf{V}_D, \qquad (9)$$

where $\Omega_\pm^2 = \omega_k^2 \pm k'^2c_t^2$. From the ordinary (nonexchange) representation of the spectral branches of magnetoelastic waves [15, 25], this dependence differs by the term $\mathbf{k}'\mathbf{V}_D$, which expresses the effect of the "ether wind."

Figure 3 shows the typical spectral curves of Eq. (9) for a given $V_D < 0$; the curves are numbered in order of increasing values of θ' from $\theta' = \pi/2$ and $\theta = \theta^*$ (the dashed curves) to $\theta' = \pi - \theta^{**}$ and $\theta = \theta^{**}$ (curves *3*). The series of the upper curves corresponds to the plus sign in Eq. (9) and represents the high-frequency ($\omega' \geq \omega_k$) spectral branches of magnetoelastic waves. The low-frequency ($\omega' < \omega_k$) spectral branches are represented by the lower curves in Fig. 3 and correspond to the minus sign in Eq. (9). Evidently, the dashed curves coincide with the real behavior of the spectral dependences $\omega' = \omega(k')$ for magnetoelastic waves in the laboratory frame of reference. The effect of the "ether wind" can be revealed by comparing the solid curves with the dashed ones. For example, one can see that both dispersion branches contain segments with a normal ($\partial\tilde{\omega}/\partial k' > 0$) and an anomalous ($\partial\tilde{\omega}/\partial k' < 0$) dispersion. The anomalous (or normal) dispersion manifests itself in those regions of the spectral branches where the magnetoelastic waves predominantly exhibit a spin (or, correspondingly, an acoustic) nature.

Thus, unlike the problems of optics and electrodynamics [3, 19–21] in which the choice of the solution at obtuse refraction angles is uniquely determined in favor of the refraction diagram shown in Fig. 1c (the electrodynamic type of refraction), in the case under study both variants are possible, depending on the values of the parameters ω, V_D, and $\theta^* < \theta < \theta^{**}$. Such a duality of the refraction of magnetoelastic waves at $\theta' > \pi/2$ can be considered as a consequence of the mixed (lattice–field) nature of these waves and, finally, follows from the different roles played by the moving medium ("ether") in the propagation of acoustic and electromagnetic waves [26]. When the magnetoelastic waves behave as spin waves (magnetic, i.e., essentially electromagnetic, waves), the condition $\partial\tilde{\omega}/\partial k' < 0$ is satisfied, which determines the choice of the solution in compliance with the results of the aforementioned studies [3, 19–21]. When magnetoelastic waves behave as acoustic waves, we have $\partial\tilde{\omega}/\partial k' > 0$ and the reflectionless birefringence [1] takes place, which is noncharacteristic of electromagnetic waves at $\theta' > \pi/2$.

Turning to Fig. 3, one can notice that the limitation $k' < k^*$ cuts off the short-wave part of the spectrum, i.e., the spin part of the low-frequency branch and the acoustic part of the high-frequency branch. Correspondingly, in the framework of the approach adopted for describing the acoustodomain interaction, at the angles $\theta' > \pi/2$ it is possible to consider either the reflectionless birefringence for $\omega' < \omega_k$ or the purely electrodynamic-type refraction for $\omega' > \omega_h$. Generally speaking, in the latter case one has to take into account the possible interbranch transformation of modes at the DW [27] (see also [5]), which, in view of the appearance of waves with $k' > k^*$, leads to the violation of the condition $k'\Delta \ll 1$ and requires a revision of the solution [2] of this problem in the spirit of paper [6].

We will restrict our following consideration to the case of the reflectionless birefringence of a shear wave by a moving DW at frequencies ω considerably lower than ω_k. With allowance for Eqs. (3), the solution to Eqs. (1) can be represented in the form

$$u_1 = U\exp[i(\mathbf{kr} - \omega t)],$$
$$\Phi_1 = C\exp(i\xi)\exp[-k_\tau(y - y_D)], \quad y > y_D,$$
$$u_2 = UT\exp[i(\mathbf{kr} - \omega t)] + UT'\exp[i(\mathbf{k}'\mathbf{r} - \omega' t)], \qquad (10)$$

$$y < y_D,$$

$$\Phi_2 = D\exp(i\xi)\exp[k_\tau(y - y_D)], \quad y < y_D.$$

Here, $\xi = k_\tau x - (\omega - \mathbf{kV}_D)t$, k_τ is the projection of the wave vectors of waves on the DW, as determined by Eq. (4); T and T' are the amplitude coefficients of the directly transmitted and the additionally refracted waves; U is the amplitude of the displacements in the incident wave; and C and D are the amplitude coefficients of the potentials of the scattering fields localized by the DW.

The relativistic corrections to the boundary conditions do not exceed the neglected corrections allowing for the magnetic field delays (they are of the order of the ratio $c_t/c = 10^{-5}$, where c is the speed of light). Hence, the boundary conditions at the moving DW are reduced to the classical boundary conditions from the theory of elasticity and magnetostatics [2, 15]:

$$u_1\big|_{y = y_D} = u_2\big|_{y = y_D}, \quad \varphi_1\big|_{y = y_D} = \varphi_2\big|_{y = y_D},$$

$$T_{yz}^{(1)}\big|_{y = y_D} = T_{yz}^{(2)}\big|_{y = y_D}, \qquad (11)$$

$$[4\pi m_y^{(1)} - \partial\varphi_1/\partial y]\big|_{y = y_D} = [4\pi m_y^{(2)} - \partial\varphi_2/\partial y]\big|_{y = y_D}.$$

Taking into account that the y component of the magnetic moment is determined by the expression

$$m_y^{(j)} = \frac{\gamma\beta}{\Omega^2 - \omega_k^2}\left[i\Omega\frac{\partial u_j}{\partial x} + (-1)^{j+1}\omega_0\frac{\partial u_j}{\partial y}\right]$$

$$+ \frac{\omega_M}{4\pi(\Omega^2 - \omega_k^2)}\left[\omega_0\frac{\partial\Phi_j}{\partial y} + (-1)^{j+1}i\Omega\frac{\partial\Phi_j}{\partial x}\right]$$

and the shear stresses $T_{yz}^{(j)}$ have the form

$$T_{yz}^{(j)} = \lambda_\Omega^*\frac{\partial u_j}{\partial y} + (-1)^{j+1}i\Omega\frac{\gamma\beta^2}{M_0(\Omega^2 - \omega_k^2)}\frac{\partial u_j}{\partial x}$$

$$+ \frac{\gamma\beta}{\Omega^2 - \omega_0^2}\left[(-1)^{j+1}\omega_0\frac{\partial\Phi_j}{\partial y} + i\Omega\frac{\partial\Phi_j}{\partial x}\right],$$

we substitute Eqs. (10) in Eqs. (3) and (11) and solve the resulting algebraic system of equations. Then, we obtain the desired result:

$$T' = \frac{i(\gamma\beta^2/\lambda_\omega^* M_0)\Gamma_+(\omega, \omega)\tan\theta}{[1 + (\lambda_{\omega'}^*/\lambda_\omega^*)\tan\theta\cot\theta'] - i(\gamma\beta^2/\lambda_\omega^* M_0)\Gamma_-(\omega', \omega)\tan\theta}, \qquad (12)$$

where $T = 1 - T'$. In Eq. (12), we used the notation

$$\Gamma_\pm(\Omega, \omega)\big|_{\Omega = \omega, \omega'} = \frac{\Omega - \omega_M F(\pm\Omega)}{\Omega^2 - \omega_k^2} \pm \frac{\omega - \omega_M F(-\omega)}{\omega^2 - \omega_k^2},$$

$$F(\Omega) = \frac{\Omega(\omega' - \omega) + \omega_0(\omega' + \omega) - 2\omega_k^2}{2\omega'\omega - (2\omega_0 + \omega_M)(\omega' + \omega) + 2\omega_k^2}.$$

We note that, in the derivation of Eq. (12), the quantity Ω involved in the expressions for $m_y^{(j)}$ and $T_{yz}^{(j)}$ was taken to be equal to ω at $j = 1$ and ω or ω' at $j = 2$, depending on which of the terms of the expression for u_2 from Eqs. (10) was used for the substitution.

Switching to the DW frame of reference and assuming that all frequencies in Eq. (12) are equal to $\tilde{\omega}$ from Eq. (5), one can easily show that, in the conditions of the reflectionless birefringence, the laws determined in [2] for the frequency response of the magnetic subsystem retain their validity. For example, at $\tilde{\omega} = \omega_0$, the ferromagnetic resonance takes place, whereas at

$$\tilde{\omega}(\tilde{\omega} - \omega_0) - \omega_0\omega_M = 0 \qquad (13)$$

we have the ferromagnetic antiresonance at the magnetostatic scattering fields Φ_j from Eqs. (3). The magnetoacoustic resonance that formally is possible at the lower bound of the "forbidden" frequency band $\tilde{\omega}^2 - \omega_k^2 + \chi\omega_0^2 = 0$ [15, 25, 26] (it manifests itself as a result of the spin–phonon coupling in the spectrum of modes of waves (2) propagating in the ferrite) falls within the spin part of the spectrum of the low-frequency branch, i.e., in the region where the solution under consideration is meaningless. It should be noted that the ferromagnetic resonance and antiresonance lines are sensitive to the Doppler shift: with increasing $|V_D|$ or with decreasing ω, they occur at greater angles θ.

Figures 4 and 5 show the dependences $|T'(\theta)|$ for a YIG crystal with the parameters [28, 29]: $\chi\omega_0 = 10^7$ s^{-1}, $M_0 = 140$ Gs, $c_t = 3.8 \times 10^5$ cm/s, $\omega_0 = 1.4 \times 10^{10}$ s^{-1}, and $\omega_M = 3.5 \times 10^{10}$ s^{-1}. The dependences were calculated by Eq. (12) for the frequencies $\omega = 1.4 \times 10^{10}$ s^{-1} (Fig. 4) and 1.7×10^{10} s^{-1} (Fig. 5) and for $V_D/c_t = -0.6$ (curves *1*) and -0.3 (curves *2*) after the preliminary determination of θ' and ω' from Eqs. (6) and (7). At $\omega = \omega_0$, the angular position of the ferromagnetic resonance peak corresponds to the grazing incidence $\theta = \pi/2$ or to a stationary DW. Therefore, in Fig. 4 this peak is absent. Similarly, it falls outside the interval $[\theta^*, \theta^{**}]$, but this time it occurs in the angular region $\theta < \theta^*$, as in the case of curve *2* shown in Fig. 5. The typical form of the ferromagnetic resonance peak observed in the vicinity of the angle $\theta = 36°$ in the conditions of the reflectionless birefringence is demonstrated by curve *1* in Fig. 5.

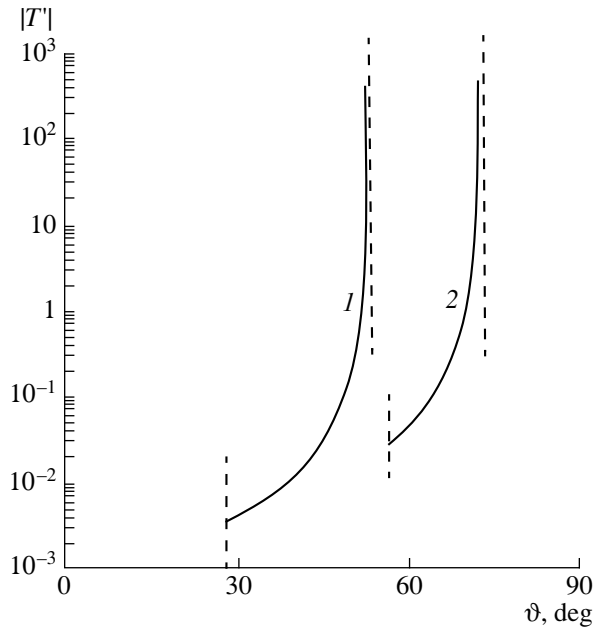

Fig. 4. Dependence $|T'(\theta)|$ for the frequency $\omega = \omega_0$ and for different velocities of the DW motion.

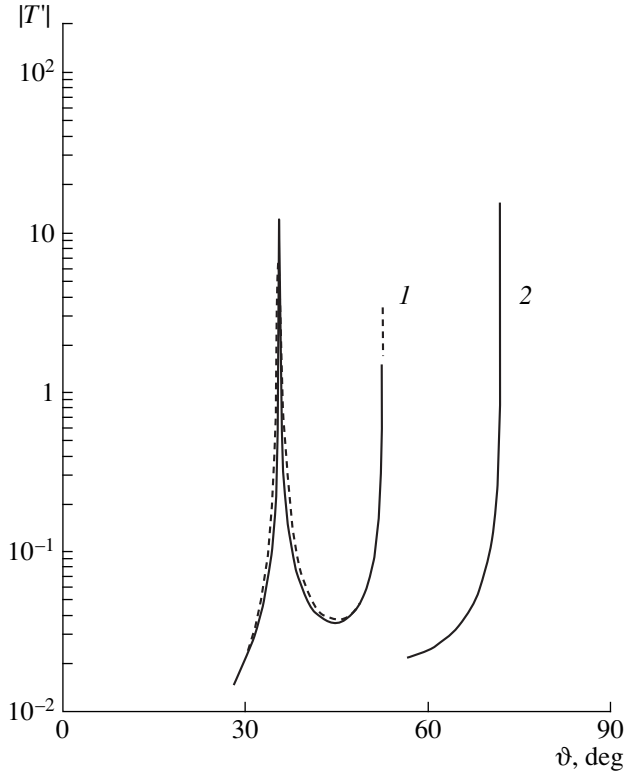

Fig. 5. Dependence $|T'(\theta)|$ for the frequency $\omega = 1.7 \times 10^{10}$ s^{-1} and for different velocities on the DW motion.

The behavior of $|T(\theta)|$ qualitatively does not differ from that of the dependence $|T'(\theta)|$. For the case of curve *1* in Fig. 5, the dependences $|T'(\theta)|$ and $|T(\theta)|$ shown in Fig. 6 (curve *1* and the dashed curve, respectively) coincide in the immediate vicinity of the ferromagnetic resonance and in the limit $\theta \longrightarrow \theta^{**}$. Outside the specified regions, the quantity $|T|$ is close to unity, being much greater than $|T'|$. Curve *2* in Fig. 6 represents the dependence $|T'(\theta)|$ calculated for the inverted directions of the spontaneous magnetization in the domains, as compared to the case of curve *1*. The zero value of the function $|T'(\theta)|$, which lies to the right of the ferromagnetic resonance peak of curve *1* within approximately 7°, here represents the ferromagnetic antiresonance line in the angular spectrum, this line being determined by Eq. (13) at $\omega_0 \longrightarrow -\omega_0$ and $\omega_M \longrightarrow -\omega_M$ or $\tilde{\omega} \longrightarrow -\tilde{\omega}$. The ambiguity of the result, which is evident from the difference between curves *1* and *2* of Fig. 6 obtained by the magnetic inversion procedure $\mathbf{M}_0^{(j)} \longrightarrow -\mathbf{M}_0^{(j)}$, expresses the inherent nonreciprocity of ferrites [15, 28].

It is remarkable that the ferromagnetic antiresonance line of the angular spectrum of the quantity $|T'(\theta)|$ can be interpreted as the consequence of the existence of a proper solution in the form of a plane monochromatic shear wave engaged with the moving DW and propagating in the direction of its motion. To prove the existence of a proper solution of this kind, we switch to the DW frame of reference and, according to the aforesaid, consider the solution to Eqs. (1) not in the form of Eqs. (10) but in the form

$$\begin{aligned} u_j &= U_j \exp[i(k_\parallel \tilde{x} - \tilde{\omega} t)] \exp(-ik_\perp \tilde{y}), \\ \Phi_j &= F_j \exp[i(k_\parallel \tilde{x} - \tilde{\omega} t)] \exp[(-1)^j k_\parallel \tilde{y}], \end{aligned} \tag{14}$$

where $k_\parallel$, $k_\perp > 0$. In the DW frame of reference, the expressions for $m_y^{(j)}$ and $T_{yz}^{(j)}$ and the boundary conditions (11) (at $\tilde{y} = 0$) are obtained by the substitutions $\Omega \longrightarrow \tilde{\omega} = \omega - \mathbf{k}\mathbf{V}_D$ and $\partial/\partial x, y \longrightarrow \partial/\partial \tilde{x}, \tilde{y}$, where $\mathbf{k}\mathbf{V}_D = -k_\perp V_D$, $V_D < 0$. Taking into account the equality of the amplitudes of the shear displacements $U_1 = U_2 \equiv U$, which follows from the first of Eqs. (11), we substitute Eqs. (14) in Eqs. (11) with allowance for Eqs. (3) and for the inequality $\tilde{\omega} \neq \omega_0 + \omega_M$. As a result, we obtain $F_1 = -F_2 \equiv F$. Thus, we arrive at a system of homogeneous algebraic equations

$$\frac{4\pi\gamma\beta\omega_0}{\tilde{\omega}^2 - \omega_k^2} U + F = 0, \quad \frac{\chi\omega_0\lambda\tilde{\omega}}{\tilde{\omega}^2 - \omega_k^2} U + \frac{\gamma\beta}{\tilde{\omega} - \omega_0} F = 0.$$

As the condition of the nontriviality of the solution for $\tilde{\omega} > 0$, this system yields the frequency of the engaged wave $\tilde{\omega} = [\omega_0 + \sqrt{\omega_0(\omega_0 + 4\omega_M)}]/2$. One can easily see that this expression represents a root of Eq. (13) that belongs to the physical sheet of the solution. Thus, when the wave frequency $\tilde{\omega}$ coincides with the root of Eq. (13), a total direct transmission of a wave through

the DW ($T' \longrightarrow 0$, $T \longrightarrow 1$) occurs as a kind of spatial resonance of the incident wave with the engaged wave given by Eq. (14). The specific manifestation of this resonance does not crucially depend on the DW motion[2] but is determined exclusively by the ability of the incident wave to be, in contrast to the spatial resonance types known in acoustics (see, e.g., [30]), an integral part (the field u_1 in Eqs. (14)) of the proper solution.

In addition to the ferromagnetic resonance and antiresonance lines, the angular spectra of the wave amplitudes in Figs. 4–6 show the presence of a pole at the point $\theta = \theta^{**}$. The elimination of this singularity of the solution by taking into account the magnetic losses with the substitution $\omega_0 \longrightarrow \omega_0 - i\omega_R$ (ω_R is the magnetic attenuation frequency, which for YIG is about 10^{-6} s^{-1} [28]) does not provide the desired result. For example, from the behavior of the dashed curve *1* in Fig. 5, which was obtained in the approximation of small losses $\omega_R/\omega_0 \sim 10^{-2}$ and for frequencies close to ω_0, one can see that the magnetic attenuation, which broadens and lowers the ferromagnetic resonance peak, almost does not affect the behavior of $|T'(\theta)|$ at other angles of incidence.

When $\theta \longrightarrow \theta^{**}$, the waves u_T and u'_T combine ($\theta' \longrightarrow \pi - \theta^{**}$, $\omega' \longrightarrow \omega$). This process is accompanied by an infinite growth of amplitudes because of the termination of the decelerating effect of magnetic poles induced at the DW by the incident wave. When $\theta < \theta^{**}$, by virtue of the relation $v\cos\theta > |V_D|$, the incident wave catches up with the moving DW and interacts with it. In the limit $\theta \longrightarrow \theta^{**}$, such an advanced propagation of the incident wave relative to the DW is almost terminated:[3] $v_g\cos\theta^{**} = |V_D|$, where $v_g \lesssim v$. The corresponding energy matching of the propagating waves $u_{T,T'}$ with the moving DW is expressed by the equality $v'_g\cos\theta' = V_D$. In combination with the retained engagement of each individual wave with the DW, this condition provides an infinite growth of the wave amplitudes.

Since $v'_g\cos\theta' = \partial\omega'/\partial(k'\cos\theta')$, the latter equality with allowance for Eq. (5) for $\tilde{\omega}$ can be interpreted as the requirement that the energy transfer across the DW by the wave $u_{T'}$ be absent in the DW frame of reference, $\partial\tilde{\omega}/\partial(k'\cos\theta') = 0$. In the case of Fig. 3 where θ' plays the role of a fixed parameter, this requirement is equivalent to the condition $\partial\tilde{\omega}/\partial k' = 0$. Hence, in Fig. 3, the point that corresponds to the pole $\theta = \theta^{**}$ will be precisely the point of intersection of curve *3* (for $\theta' = \pi - \theta^{**}$, i.e., at $\theta = \theta^{**}$) with the straight line *4* (determined according to Eq. (5) by the equation $\tilde{\omega} = \omega + k'\cos\theta^{**}V_D$) at which the tangent to curve *3* is strictly horizontal.

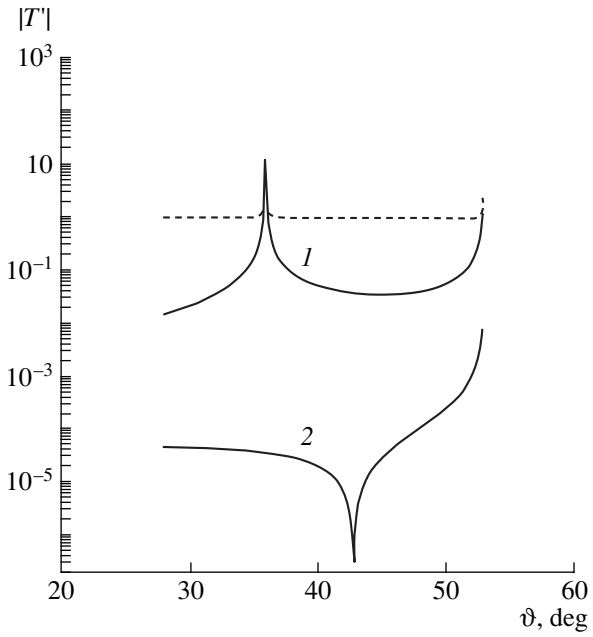

Fig. 6. Dependences $|T'(\theta)|$ (the solid curves) and $|T(\theta)|$ (the dashed curves) for the frequency $\omega = 1.7 \times 10^{10}$ s^{-1} and for $V_D/c_t = -0.6$. Curve *2* represents the dependence $|T'(\theta)|$ calculated for the inverted directions of the spontaneous magnetization in the domains, as compared to the case of curve *1*.

In refraction problems, the usual practice is to relate the poles of the amplitude coefficients to the presence of a proper solution in the absence of the incident wave. Therefore, in the DW frame of reference, it is convenient to represent the proper solution for the pole $\theta = \theta^{**}$ of the coefficients T and T' from Eq. (12) in the form of Eqs. (10) at $u_1 = 0$:

$$u_1 = 0, \quad \Phi_1 = C\exp[i(k_\parallel\tilde{x} - \tilde{\omega}t)]\exp(-k_\parallel\tilde{y}), \quad \tilde{y} > 0$$

$$u_2 = \exp[i(k_\parallel\tilde{x} - \tilde{\omega}t)][U\exp(-ik_\perp\tilde{y}) + U'\exp(-ik'_\perp\tilde{y})], \quad \tilde{y} < 0$$

$$\Phi_2 = D\exp[i(k_\parallel\tilde{x} - \tilde{\omega}t)]\exp(k_\parallel\tilde{y}), \quad \tilde{y} < 0.$$

Here, $k_\parallel$, $k_\perp$, and $k'_\perp$ are positive and $V_D < 0$. Following the procedure used for the transformation of the boundary conditions (11) in considering the proper solution in the form of the engaged wave (14), we substitute Eqs. (15) in them, and, equating the determinant of the resulting system of equations to zero, we obtain $k'_\perp - k_\perp = 0$. This condition means a collinear propagation of the partial waves of proper solution (15) in front of the moving DW, and, as one would expect, in view of the relations $k'_\perp = -k'\cos\theta'$ and $k_\perp = k\cos\theta$ and with allowance for Eqs. (4) and (5), it determines the coordinates

[2] This spatial resonance is also possible in the case of the ordinary reflective refraction of the shear wave by the DW, including the case of a stationary DW [2].

[3] For the region of a weakly pronounced dispersion of magnetoelastic waves, when the replacement of their group velocity v_g by the phase velocity v is appropriate, this expression leads to Eq. (8).

of the pole of the coefficients T and T' from Eq. (12): $\theta = \theta^{**}$, $\omega' = \omega$.

It should be noted that, although, according to the requirement U, $U' \neq 0$, solution (15) is nontrivial, the condition $k'_\perp - k_\perp = 0$ in combination with the equality $U' = -U$, which expresses the antiphase character of oscillations in the partial waves determined by Eqs. (15),[4] and with the corresponding absence of magnetic poles at the DW, $C = D \equiv 0$ (the contributions made by the partial waves to the poles compensate each other), yields a proper solution of a degenerate zero type: $u_j \equiv 0$, $\Phi_j \equiv 0$ for all space–time points. This result eliminates the logical contradiction between the fact of the infinite (resonance, if we keep in mind the presence of the proper solution given by Eqs. (15)) growth of the amplitudes T, T' for $\theta \longrightarrow \theta^{**}$ and the termination (in terms of the signal) of the interaction of the incident wave with the moving DW precisely at these conditions. In fact, the resulting field $u_2 = u_T + u_{T'}$ excited in the resonance way proves to be zero at $\theta \longrightarrow \theta^{**}$, in accord with the degeneracy of the proper solution (15). In this case, the oscillations of the waves u_T and $u_{T'}$ are combined in antiphase, no matter how large their amplitudes.

In closing, we note that, in the immediate vicinity of the angle θ^{**}, because of the violation of the spatial synchronism and the slight frequency mismatch of the waves u_T and $u_{T'}$, the oscillations in these waves will not fully compensate each other. The beats that occur in this case can be used for detecting the conditions of the reflectionless birefringence and for studying the effects associated with this phenomenon.

ACKNOWLEDGMENTS

This work was supported by the Federal Program "Integratsiya," project no. KO 179.

REFERENCES

1. N. S. Shevyakhov and E. A. Vilkov, *Acoustics at the Threshold of the 21st Century* (Mosk. Gorn. Univ., Moscow, 1997), pp. 27–30.
2. N. S. Shevyakhov, Akust. Zh. **36**, 760 (1990) [Sov. Phys. Acoust. **36**, 427 (1990)].
3. B. M. Bolotovskiĭ and S. N. Stolyarov, Usp. Fiz. Nauk **159**, 155 (1989) [Sov. Phys. Usp. **32**, 813 (1989)].
4. G. I. Freĭdman, Zh. Éksp. Teor. Fiz. **41**, 226 (1961) [Sov. Phys. JETP **14**, 165 (1962)].
5. B. A. Auld and C. S. Tsai, Appl. Phys. Lett. **9** (5), 192 (1966).
6. G. M. Nedlin and R. Kh. Shapiro, Fiz. Tverd. Tela (Leningrad) **18**, 1696 (1976) [Sov. Phys. Solid State **18**, 985 (1976)].
7. E. A. Turov and A. A. Lugovoĭ, Fiz. Met. Metalloved. **50**, 903 (1980).
8. L. V. Panina and V. L. Preobrazhenskiĭ, Fiz. Met. Metalloved. **60**, 455 (1985).
9. E. Schlömann, J. Appl. Phys. **31** (9), 1647 (1960).
10. A. V. Mitin and V. A. Tarasov, Zh. Éksp. Teor. Fiz. **72**, 793 (1977) [Sov. Phys. JETP **45**, 414 (1977)].
11. A. V. Andrianov, V. D. Buchel'nikov, A. N. Vasil'ev, *et al.*, Zh. Éksp. Teor. Fiz. **97**, 1674 (1990) [Sov. Phys. JETP **70**, 944 (1990)].
12. J. M. Winter, Phys. Rev. **124**, 452 (1961).
13. F. B. Hagedorn, J. Appl. Phys. **41** (3), 1161 (1970).
14. B. A. Ivanov and A. L. Sukstanskiĭ, Zh. Éksp. Teor. Fiz. **94**, 204 (1988) [Sov. Phys. JETP **67**, 1201 (1988)].
15. A. I. Akhiezer, V. G. Bar'yakhtar, and S. V. Peletminskiĭ, *Spin Waves* (Nauka, Moscow, 1967; North-Holland, Amsterdam, 1968).
16. V. S. Gornakov, L. M. Dedukh, and Yu. P. Kabanov, Fiz. Tverd. Tela (Leningrad) **26**, 648 (1984) [Sov. Phys. Solid State **26**, 391 (1984)].
17. L. I. Turchak, *Foundations of Numerical Methods* (Nauka, Moscow, 1987).
18. Yu. M. Sorokin, Izv. Vyssh. Uchebn. Zaved., Radiofiz. **36** (7), 635 (1993).
19. S. N. Stolyarov, in *The Einstein's Collection of Papers 1975–1976* (Nauka, Moscow, 1978), pp. 152–215.
20. A. Mor and S. Gavril, Int. J. Electron. **63**, 643 (1987).
21. Y.-X. Huang, J. Appl. Phys. **76** (5), 2575 (1994).
22. L. I. Mandel'shtamm, *Lectures on Optics, Relativity Theory, and Quantum Mechanics* (Nauka, Moscow, 1972).
23. M. V. Nezlin, Usp. Fiz. Nauk **120**, 481 (1976) [Sov. Phys. Usp. **19**, 946 (1976)].
24. B. M. Bolotovskiĭ and S. N. Stolyarov, in *Einstein's Collection of Papers 1974* (Nauka, Moscow, 1976), pp. 179–275.
25. J. P. Parekh and H. L. Bertoni, J. Appl. Phys. **44** (6), 2866 (1973).
26. V. Yu. Zavadskiĭ, *Modeling of Wave Processes* (Nauka, Moscow, 1991).
27. R. L. Comstock and N. Kusnezov, Appl. Phys. Lett. **8** (5), 126 (1966).
28. Yu. M. Yakovlev and S. Sh. Gendelev, *Ferrite Single Crystals in Radio Electronics* (Sov. Radio, Moscow, 1975).
29. B. A. Goldin, L. N. Kotov, L. K. Zarembo, and S. N. Karpachev, *Spin-Phonon Interactions in Crystals (Ferrites)* (Nauka, Leningrad, 1991).
30. L. M. Lyamshev, *Sound Reflection from Thin Plates and Shells in a Liquid* (Akad. Nauk SSSR, Moscow, 1955).

[4] A similar conclusion can be made for the oscillations in the waves u_T and $u_{T'}$ from the solution to the refraction problem, because, according to Eq. (12), the relationship $T' = -T$ becomes valid in the vicinity of the pole.

Translated by E. Golyamina

Acoustical Physics, Vol. 47, No. 2, 2001, pp. 169–177. Translated from Akusticheskiĭ Zhurnal, Vol. 47, No. 2, 2001, pp. 210–219.

REVIEWS

Sound Fluctuations Caused by Internal Waves in a Shallow Sea

A. M. Derzhavin and A. G. Semenov

Andreev Acoustics Institute, Russian Academy of Sciences, ul. Shvernika 4, Moscow, 117036 Russia

e-mail: bvp@akin.ru

Received July 14, 1999

Abstract—Estimates are presented for the fluctuations of the parameters of low-frequency sound fields in shallow-water regions of the Barents Sea, in the presence of seasonal internal gravity waves. The objective of the experiments is to reveal the main mechanisms that govern the sound fluctuations and their statistical parameters on paths of moderate lengths (50–60 to 100–120 km). Another objective is to determine the features of the sound interaction with internal waves for the sound speed profile of the summer–autumn type for which the water stratification is most pronounced. As the probing signals, continuous tonal ones produced by bottom-moored sources at the frequencies about 100 and 300 Hz are used along with the 1/3-octave noise signals with the central frequency 1000 Hz, which are generated by a source deployed from a vessel. For the signal reception, both fixed bottom-moored hydrophones and a vertical chain of hydrophones are used, the chain also being deployed from the vessel. The water temperature, the salinity, and the thermocline displacements are monitored with standard hydrographic sensors. The following main results are presented: the estimate of the degree of correlation between the sound fluctuations and the parameters of the water layer, the comparison of the fluctuations in the signal amplitude envelope with the data obtained in other regions, and the estimate of the statistical parameters of the signal amplitude fluctuations, including their dependence on the path length. One more result consists in the proof of the wave nature of the interaction of sound and internal waves, which manifests itself in a strong dependence of the sound interaction with internal waves of discrete frequencies on the frequency of the probing signal and on the angle at which these wave beams intersect. An attempt is made to explain the observed phenomena by the synchronism in the interacting sound and gravity waves. The data obtained can be used to analyze and compare the fluctuations of the sound fields in the ocean, especially in shallow-water regions. © *2001 MAIK "Nauka/Interperiodica".*

Internal gravity waves existing in many ocean regions are believed to be the main factor that causes amplitude and phase fluctuations of the underwater sound fields of different frequencies [1–5, 13]. With regard to the problems of acoustic tomography and thermometry, it has become highly urgent to study and predict the sound field fluctuations on propagation paths of various lengths. In recent years, many papers [14–20] were published on sound fluctuations in the presence of internal gravity waves, mainly for deep-water ocean regions and relatively high sound frequencies (several hundreds of hertz). The studies of the laws of sound field formation, which can be associated with the problem of global warming, have also become quite topical. To perform such studies, one often must choose the paths lying in the polar regions of the Earth. In many cases, these paths may run through shallow-water regions, in the shelf zones or in near-pole seas. In such regions, a number of common laws and features are typical of both the field of internal gravity waves and the sound field fluctuations caused by them [1–6, 9, 10, 14–16, 27–29]. Numerous studies [8, 11–13, 17] of sound fluctuations in these regions are purely experimental and, in contrast to the deep-water studies [18], do not reveal the general principles. One of the first attempts to generalize different kinds of data on the fluctuations of low-frequency sound fields in shallow-water polar regions was made by Katsnel'son and Petnikov [9]. By analogy with deep-water ocean regions, they treated the local wave processes induced by internal waves as the key factor responsible for the sound fluctuations. The latter statement seems to be partially true for paths that are shorter than 100 km. [27]. In contrast to deep-water regions, the shallow-sea internal waves usually exhibit no seasonal, temporal, or spatial uniformity [9, 10]. In a number of cases, they are represented by trains of soliton-like waves of high amplitudes on the background of weak internal waves. The periodicity of the solitons observed in a shelf zone is usually associated with tides. Therefore, such processes (along with a number of other mechanisms) can only be used to explain the formation of the sound field fluctuations at frequencies that correspond to a period of about 12 h. They cannot be the cause of regular sound field fluctuations observed on paths running through offshore areas of shallow seas and characterized by circular frequencies of 10^{-4} to 10^{-1} rad/s, within the so-called super-low frequency band [27].

As evidence of the regular spatial structure of internal waves on long paths, the data on the scattering of

electromagnetic waves by the sea surface can be mentioned, this process being influenced by the structure of internal gravity waves that propagate over the shallow-water area. Such observations were performed with the use of a satellite positioned above a region of the North Atlantic, near the New-Jersey coastline, in summer 1995, during the SWARM experiment [1, 2, 28]. From the analysis of the photographs, one can conclude that the structure of the internal-wave field observed on the acoustic path significantly depends on its orientation relative to the propagation direction (orientation of the fronts) of internal waves and that to the coastline. The paths used for the studies in a shelf zone can be differently oriented relative to the fronts of internal waves and to the coastline, which determines different regular structures of the wave field on the path. For instance, the typical size of the photographed sea surface area [28] is about 40 km, and up to several tens of the wave front projections are covered by the image. Evidently, the interaction process may depend on the angle between the propagation directions of the internal and sound waves. Thus, the effects of internal waves on sound can be different in their structures and interaction mechanisms for shallow-water regions (where low frequencies of sound are predominantly used) and deep-water ones (where higher frequencies are commonly used). The latter fact is determined by the statistical parameters of the spectrum and by the nature of the hydrodynamical wave fields that exist in deep-water regions [18]. On the other hand, in forming the sound field fluctuations in shallow-water regions, the deterministic phenomena of interaction between sound and hydrodynamical fields associated with both internal and surface gravity waves are significant. At the same time, according to [27], the stable hydrodynamical fields associated with long-period surface gravity waves are universal, and their parameters are nearly independent of the season and water stratification for a given ocean region. On the contrary, in coastal regions, the manifestations of the hydrodynamical wave fields depend on tidal processes, along with weather conditions for shallow water areas. The same properties seem to be typical for the corresponding fluctuations of the sound fields. On this background, other fluctuations can exist that are even less uniform in space and time. These fluctuations can be governed by local seasonal internal waves, tidal phenomena, and passages of fluctuating front zones, eddies, or soliton-like objects.

In general, one can predict (or model) the effect of the wave field on the received sound signal only if the mode content of the sound field is known in advance or if the reception point is chosen in such a manner that a single mode contributes to the received signal. This is the case, e.g., for shallow-water regions at distances more than 100 km from the sound source, where the sound field structure can be satisfactorily described by two or three initial modes and the aforementioned choice of the reception point is quite feasible [27]. In some cases, one can assume that the mean phase of all power-predominating modes is influenced by the hydrodynamical wave field in a synchronous manner. Then, the choice of the reception point becomes easier: for instance, it can be located at the sea floor within the near-bottom sound channel [13, 14]. The effect of the hydrodynamical waves on each mode of the sound field can be characterized by the depth of the phase modulation for this mode. As to the experimentally measured amplitude modulation, it is often far from being a determinative and objective characteristic of the interaction, because the extent to which it is stressed in the received signal can be governed by the location of the receiver or by the deliberate masking of the lower modes at the very reception point [26].

In this paper, experimental data are reported on the sound fluctuations observed on the background of the aforementioned processes, on shallow-water paths of lengths up to 120 km. The objective of the experiments was to reveal the mechanisms of the formation of the sound fluctuations caused by the interaction of sound with gravity waves, mainly internal ones. The measurements were carried out in the Barents Sea, with the summer–autumn sound field profile, which corresponds to the most pronounced stratification of the layer. The path lengths varied from 50–60 to 100–120 km. The probing signals were continuous tonal signals produced by fixed bottom-moored sound sources with the frequencies 100 and 300 Hz, as well as with 1/3-octave noise signals with a central frequency of about 1000 Hz, which were transmitted from a vessel. A separate objective of this work was to prove the wave nature of the interaction between sound and internal waves in shallow-water regions. This nature manifests itself in the following features:

(i) A noticeable correlation between the spectrum of the envelope of the amplitude fluctuations of the signal (both for tonal and noise signals) generated at different frequencies and the spectrum of the vertical thermocline displacements caused by internal waves;

(ii) A dependence of the efficiency of interaction between sound and internal waves on the frequency of the probing sound signal, on the wavelength of the internal wave, and on the angle of intersection of the wave beam fronts.

Preliminary measurements of sound fluctuations were performed in summer, in a shallow-water region of the Barents Sea, on two paths schematically illustrated in Fig. 1. The first path was formed by two fixed narrow-band sound sources, which were bottom-moored at the same point and had the frequencies 100 and 300 Hz, and a receiving system. The latter was either a broadband sound receiver fixed near the bottom at a distance of 60 km from the sources or a vertical chain of hydrophones deployed from the vessel. The chain was fastened to a drifting buoy and stretched by a load attached to its lower end. From the fixed receiver, the signals were cable-transmitted to a coastal laboratory and recorded. From each hydrophone of the verti-

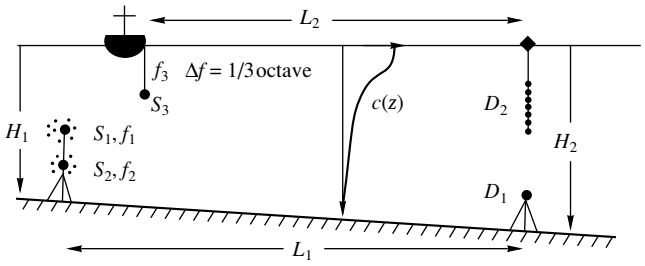

Fig. 1. Layouts of the experiments on measuring the parameters and fluctuations of the sound signal on the shallow-water paths: S_1 and S_2 are the omnidirectional narrow-band (tonal) sound sources of frequencies f_1 = 100 Hz and f_2 = 300 Hz, respectively; the sources are bottom-moored at the beginning of the path; D_1 is the omnidirectional sound receiver (hydrophone) bottom-moored at the opposite end of the path; L_1 = 60 km is the path length between the sources S_1, S_2 and the hydrophone D_1; S_3 is the noise source with the central frequency f_3 = 1000 Hz and the 1/3-octave bandwidth; this source is deployed from the drifting vessel; D_2 is the receiving system (a vertical chain containing N = 7 equidistant hydrophones); the chain is stretched between a surface buoy and a load; it is carried by a vessel; its length is 20 m with the upper hydrophone positioned at a depth of 16 m; the data are transmitted from the buoy to the vessel via a radio channel; L_2 = 50 km is the path length between the vessel and the drifting buoy; H is the thickness of the water layer smoothly varying along the path from H_1 = 60 m to H_2 = 200 m.

cal chain, the received signals were radio-transmitted and recorded in the vessel's laboratory. The second path ran between a transmitter of 1/3-octave band noise with a central frequency of 1000 Hz and the same receivers located at a distance of about 50 km from the source. The sound source was deployed from the anchored research vessel to a depth of 20–30 m. The vertical chain (Fig. 1) consisted of seven equidistant hydrophones, with the depths 16 and 37 m of the uppermost and lowest ones, respectively. At the point where the fixed sound sources were bottom-moored, the sea depth was about 60 m, and it varied reaching 200 m near the receiving systems. During the experimentation, with the use of standard hydrographic probes deployed from the research vessel, vertical profiles of the water temperature, density, and salinity were measured along the path. Simultaneously, the vertically distributed temperature sensors [10] were used to measure the temperature variations in the thermocline, this data serving to subsequently estimate the thermocline displacements. The total duration of the simultaneous measurements of the parameters of sound and internal waves was up to 40 h. The data were recorded by a multi-channel magnetic-tape recorder. Later, the signals were spectrally processed with the use of a special computer code [13]. In the processing, the power spectra and the correlation characteristics (both auto- and cross-correlation) of the signals were estimated along with the vertical displacements of the thermocline. The vertical distributions of

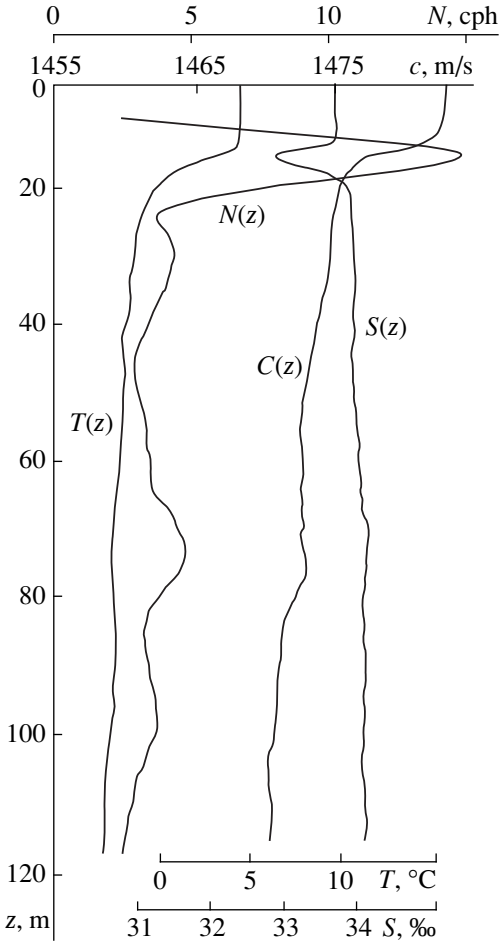

Fig. 2. Typical distributions of the water parameters in depth, which are measured from the vessel in the course of the experiment in summer in a shallow-water region of the north-eastern part of the Barents Sea: the temperature T, the salinity S, the sound speed c, and the Väisälä–Brunt frequency N.

the sound speed and Väisälä–Brunt frequencies were also estimated.

The typical profiles of the temperature $T(z)$, sound speed $c(z)$, salinity $S(z)$, and Väisälä–Brunt frequency $N(z)$ obtained as a result of the data processing are presented in Fig. 2. These data show that the vertical temperature gradient observed within the thermocline reached 0.5°C/m. The thermocline covered the depths from 15 to 20 m, which correspond to the near-bottom channel that is commonly observed in shallow-water regions of the Arctic shelf in summer. The Väisälä–Brunt frequency in the water layer varied within 2.5–14.0 cycles per hour, and it was 4.5 to 14.0 cycles per hour in the layer of the most pronounced thermocline, i.e., at the depths from 8 to 28 m. The parameters of the power spectrum of internal waves were close to those of the well-known Garret–Munk spectrum [18]. At the same time, narrow-band discrete components of high-intensity were also

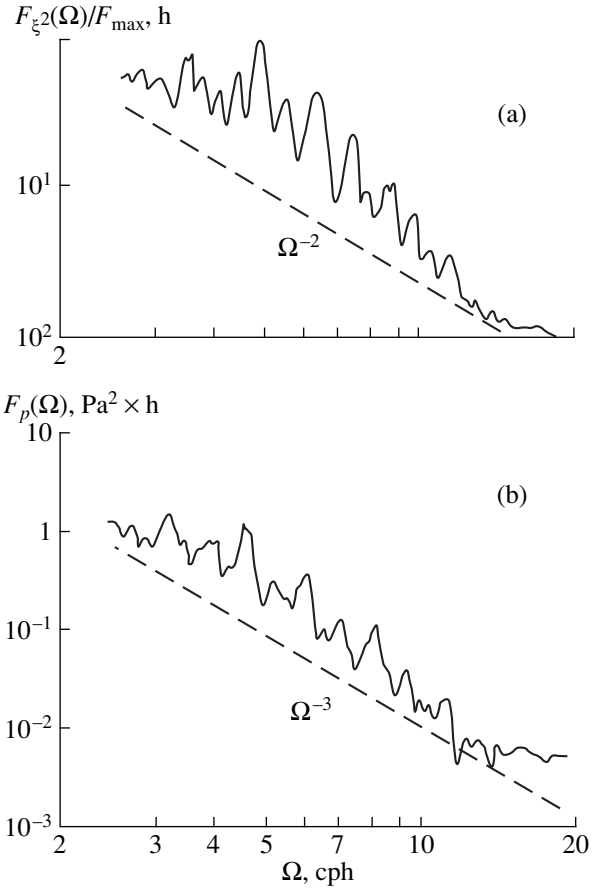

Fig. 3. Power spectra of the amplitude fluctuations for the processes experimentally studied in the shallow-water Arctic region (summer, northeastern part of the Barents Sea): (a) a typical normalized spectrum of the vertical thermocline displacements as measured from the vessel; the straight line corresponds to the law Ω^{-2} for the decay of the power envelope spectrum with frequency; (b) a typical power spectrum of the envelope of the amplitude fluctuations for the electric signal at the output of the band-pass filter with the central frequency 1000 Hz and the bandwidth 15 Hz, as measured with the sound source S_3 on the quasi-stationary path with L_2 = 50 km; the realization duration is 6 h, the spectral resolution of the analysis is about (4–5) × 10^{-5} Hz; the straight line corresponds to the law Ω^{-3} for the mean decay of the power envelope spectrum with frequency.

present in the spectrum. Thus, within a narrow band around 12 cycles per hour, regular oscillations of the thermocline that are caused by internal waves with displacement amplitudes of 10–12 m can be noticed. In addition, within the band 3–12 cycles per hour, short-period quasi-periodic oscillations of the thermocline were observed that were induced by internal waves with the 4- to 5-m displacement amplitudes. The longitudinal correlation lengths R_i of the thermocline displacements were estimated to yield a value close to 10 km. This value agrees well with the data reported in [9, 10].

Figure 3a shows the high-frequency part of a typical normalized power spectrum of thermocline displacements. In Fig. 3b, the corresponding part of a typical normalized power spectrum is presented for the envelope of amplitude fluctuations of the broadband sound signal received by the lower hydrophone (at the depth 37 m) of the vertical chain, upon band-pass filtering within 995–1010 Hz. The typical duration of the recorded envelope realization is 6 h, the spectral resolution of the analysis is (4–5) × 10^{-5} Hz. It is evident that the power-predominating parts of both spectra correspond to frequencies of 2.4 to 9.0 cycles per hour, the spectra rising towards lower frequencies (longer periods), though with different slopes (the corresponding dependences Ω^{-2} and Ω^{-3} are shown by straight lines in Fig. 3). According to the analysis of the data, during the 40-h measurements, the cross-correlation coefficient of these signals (for different receivers of the vertical chain) remained at a level of about 0.7 and reached 0.82–0.87 in the presence of the discrete component. It is worth mentioning that the compared realizations cover a relatively small (limited) number of oscillations (cycles) of the main frequency: from 2.4 to 9 per one-hour realization. Even when averaged over 6 h (over six realizations), the value of the cross-correlation coefficient depends on the change in the relative initial phases of the signals to be compared. The estimate of the maximal correlation coefficient can be obtained by adjusting the relative phase of the processes (signals). This procedure is important in estimating the time cross-correlation coefficient between the thermocline displacements and the envelopes of the amplitude fluctuations of the signals received by the hydrophones of the vertical chain, because the phases of these envelopes depend on the depth of the observation point in the water layer [9]. The aforementioned procedure is the one we used to establish the fact that the compared processes were rather close to each other, especially when the discrete component was present in the spectrum of internal waves. Note that such structure of the spectrum is typical for internal waves in shallow-water regions.

Let us consider the data on the intensity fluctuations of the signals generated by the used sound sources on the studied paths. The analysis resulted in the following values of the fluctuations in the signal level: about 4 dB (which corresponds to the mean variation coefficient up to ±18.3%) at a frequency of 300 Hz for the narrowband signal on the first path; the same value at the output of the 15-Hz filter with a central frequency of 1000 Hz for the broadband signal on the second path; 1.6 dB (the variation coefficient up to ±6.8%) at the output of the 1/3-octave filter with a central frequency of 1000 Hz for the broadband signal on the second path; and less than 1.0 dB (the variation coefficient lower than ±4.2%) at a frequency of 100 Hz for the narrowband signal on the first path. Here, the variation coefficient (V, %) means the relative mean value of the envelope fluctuations $V = 2^{-1/2}(\tilde{a}/\bar{a})$, where $\bar{a}$ is the mean value of the envelope and $\tilde{a}$ is the mean value of its

fluctuations, this coefficient being estimated for the entire realization duration (2500–3600 s in our case). The relative value $\tilde{a}/\bar{a}$ of the fluctuations is directly related to the mean magnitude ΔL_{dB} of fluctuations in the signal level according to the expression

$$\begin{aligned}\Delta L_{\mathrm{dB}} &= L_{\max,\mathrm{dB}} - L_{\min,\mathrm{dB}} = 20[\log(1+\tilde{a}/\bar{a}) \\ &\quad - \log(1-\tilde{a}/\bar{a})] \\ &= 20\log\left[\frac{(1+\tilde{a}/\bar{a})}{(1-\tilde{a}/\bar{a})}\right] \cong 40\log(1+\tilde{a}/\bar{a}),\end{aligned} \tag{1}$$

so that $V(\%) \cong 2^{-1/2}(10^{\Delta L_{\mathrm{dB}}/40} - 1) \times 100\%$. We used this relation in our calculations.

The difference in the fluctuation values at the outputs of the 15-Hz and 1/3-octave filters are quite predictable and can be explained by averaging the out-of-phase components of the noise signal. Recall that, in such a case, the different-frequency spectral levels of the signal are governed by a combination of modes that have different phase increments formed by the field of internal waves. In a narrow band, the phase increments are fixed, thereby leading to the maximum intensity of fluctuations. If the band were broader, a further decrease in the intensity of fluctuations would be observed because of different phase increments. According to our estimates, the magnitude of the fluctuations in the signal level would be no higher than 1.0 dB in an octave band.

For the fluctuations of the signal propagating over the first path, the envelope spectrum proves to be close to that of the fluctuations of the noise signal at the output of the 15-Hz filter (Fig. 4b). The generality of this result is also confirmed by comparing with the data of [9]. Figures 4a and 4b show the envelope spectra for the amplitude fluctuations of the 300-Hz signals for two paths of the same lengths, in the same region of the Barents Sea. These data were obtained in the summer of another year, with similar weather conditions. Even the shape and slope of the spectra are in good agreement for these two data sets. The explanation consists in the closeness of the spectra of internal waves, which can be observed in summer in this region. According to the measurements of different researchers [9], discrete spectral components are more weakly pronounced for deep-water regions, with close mean shapes of the spectra of sound signal amplitudes and thermocline displacements induced by internal waves. Theoretically, in the absence of discrete components in the spectrum of thermocline displacements, the spectrum shape should be close to that of Garret–Munk [18] for this part of the band. Later, we will see that the discrete components also change the form of the statistical distribution of the amplitude sound fluctuations. The distribution of the variation coefficients is nearly Gaussian for deep-water regions, whereas, in shallow-water regions, it is narrower and closer to the Rayleigh form. In addition, the mean values of the variation coefficients differ by a factor of 2–3 in these regions [14]. The experimental data indicate that a narrow-band signal of a frequency that is no lower than 300 Hz coherently images the structure of internal waves, especially if narrow-band discrete components are present in the displacement spectrum. For lack of a noise sound source with a frequency band around 300 Hz, we failed to determine the band of coherency for such a signal in the presence of internal waves. However, this band cannot be higher than 1–2% (in relative units). Thus, at a frequency around 1000 Hz,

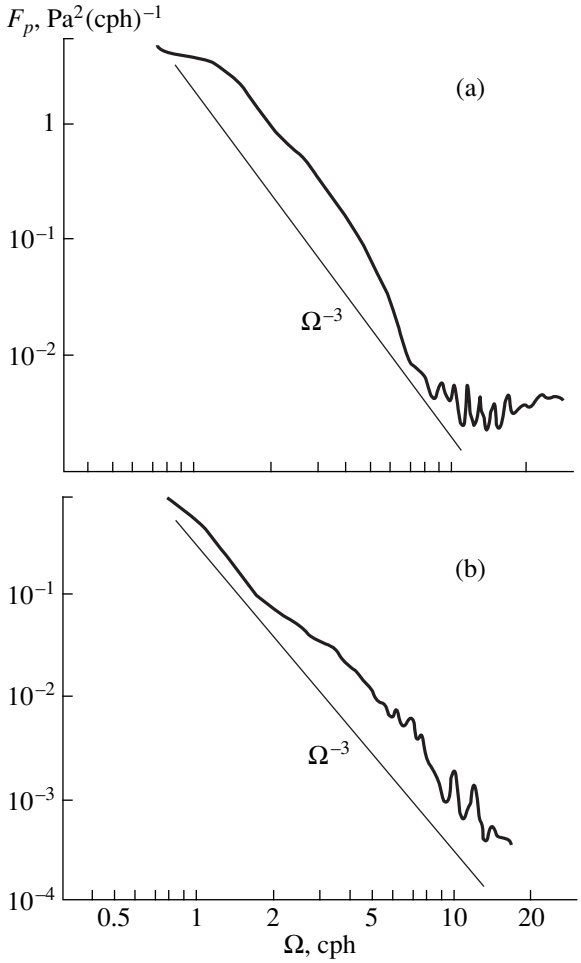

Fig. 4. Power spectra of the amplitude fluctuations for the processes experimentally studied in similar experiments performed by other researchers [9] on fixed paths in the shallow-water Arctic region: (a) a typical power spectrum of the envelope of amplitude fluctuations for the electric signal at the output of the band-pass filter with the central frequency 300 Hz and the relative bandwidth (1–2)%, as measured with the sound source S_2 on a path of about 70 km in length; the spectral resolution of the analysis is approximately 0.07 cycles per hour (2×10^{-5} Hz); (b) the same as in Fig. 4a for the path of comparable length, with the same sound source, but with other position of the receiver within the shelf zone. The straight lines in both plots correspond to the law Ω^{-3} for the mean decay of the power envelope spectrum with frequency.

the 15-Hz band of the analysis should be regarded as the band of coherency for the noise signal envelope [9].

Note that, on the first path where two narrow-band signals (300 and 100 Hz) were received simultaneously, the values of the fluctuation spectra differ by a factor of nearly four from each other. This experimental result is unexpected and requires additional considerations. In that case, the sound beams of different frequencies simultaneously interacted with the gravity waves traveling at the same angle. Hence, the difference in the degree of the interaction cannot be explained in purely geometric terms, i.e., by the difference in the angles of intersection. The first attempt to explain this phenomenon was reported in [13]. There, a preliminary analysis can be found that is based on estimations of the conditions for sound and gravity (internal) waves to interact in a synchronous way. Here, we repeat this analysis with some corrections and generalizations. For the synchronism between the fields of sound and gravity waves to exist, some conditions should be met in space and time [20–22]. The time condition is usually met for a narrow-band sound beam of frequency f ($\Delta f \ll f$) if the bandwidth Δf of the sound signal is higher than the value of the characteristic frequency for the gravity (internal) wave within the domain of interaction Ω ($\Delta f \geq \Omega$).

To evaluate the condition of spatial synchronism, we introduce the angle ϑ between the z axis (directed upwards with the unit vector $\boldsymbol{\nu}$) and the direction of the wave vector $\mathbf{K}$. In view of the well-known dispersion relation $\Omega^2 = N^2\sin^2\vartheta$ for internal waves (N is the Väisälä–Brunt frequency, $\Omega \leq N$), one can find [19] a general relation for the group velocity $\mathbf{U}_{ig}$ to have the form:

$$\mathbf{U}_{ig} = -\frac{N^2}{\Omega K}(\mathbf{n}\boldsymbol{\nu})\{\boldsymbol{\nu} - (\mathbf{n}\boldsymbol{\nu})\mathbf{n}\} \qquad (2)$$

with the unit vector $\mathbf{n} = \mathbf{K}/K$. The velocity $\mathbf{U}_{ig}$ is perpendicular to the vector $\mathbf{K}$, and its magnitude is $U_{ig} = (N/K)\cos\vartheta$. Its vertical and horizontal projections are $U_{igv} = -(N/K)\cos\vartheta\sin\vartheta$ and $U_{igh} = (N/K)\cos^2\vartheta$, respectively. Accordingly, the phase velocity of the wave also does not coincide with the vector $\mathbf{K}$ in its direction, and $U_{if} = (N/K)\sin\vartheta$. Its vertical and horizontal projections are $U_{ifv} = (N/K)\sin^2\vartheta$ and $U_{ifh} = (N/K)\cos\vartheta\sin\vartheta$, respectively. Evidently, the horizontal component of the phase velocity has its maximal value at $\vartheta = \pm\pi/4$, and this value is $U_{ifh} = (N/2K)$. At $\vartheta = 0, \pm\pi/2$, and $\pm\pi$, the horizontal phase velocity is equal to zero. The velocity $\mathbf{u}$ of the fluid particles in the wave proves to be perpendicular to the vector $\mathbf{K}$, so that the entire motion of the fluid occurs in parallel to the surfaces of constant phase, which is typical for transverse waves [19, 22]. Thus, the horizontal projection of the wave vector $\mathbf{K}$ can be expressed as $K_{ih} = \Omega[U_{ifh}/(U_{if})^2] = (\Omega K/N)\cot\vartheta = K\cos\vartheta$. And, in view of the horizontal path orientation determined by the angle φ (varying from 0 to 2π in a cylindrical coordinate system with a vertical axis), the actual value of the projection of the wave vector onto the direction of sound propagation can be expressed as $K^*_{ih} = K\cos\vartheta\cos\varphi$.

For surface gravity waves with frequencies within 2.5–12 cycles per hour, which exist in practice, the phase velocity obeys the relation $U_{sf} = (gH)^{1/2}$ in shallow-water regions. With these waves, the phase velocity coincides with the group velocity in its direction along the water layer. Hence, the horizontal projection of the wave vector $\mathbf{K}$ is given by the expression: $K^*_{sh} = \Omega/U_{sfh} = [\Omega/(gH)^{1/2}]\cos\varphi'$ where φ' is the angle formed by the path with the propagation direction of surface gravity waves; in the general case, we have $\varphi \neq \varphi'$.

For the sound modes of numbers m and n, which propagate along the layer and have horizontal projections ξ_m and ξ_n of the wave vectors, respectively, the space condition takes the form $|\xi_m - \xi_n| = |K_h|$. In the simplest case of a uniform layer of thickness H, the left-hand side of the condition can be expressed as $|\xi_m - \xi_n| = (\pi c/16H^2 f)[(2m-1)^2 - (2n-1)^2]$, where c is the sound speed in the layer [23, 24]. The expression in square brackets is always greater than eight for arbitrary integers $m \neq n \neq 0$. Therefore, for the minimal sound frequency f_1 that allows the synchronism between the gravity waves (internal or surface ones) and the sound waves to occur, we arrive at the estimate:

$$f_1 \geq \frac{\pi c}{2H^2|K^*_h|} = \frac{\pi c|U_f|}{2H^2\Omega|\cos\vartheta\cos\varphi|} \cong \frac{\pi c|U_f|}{\sqrt{2}H^2\Omega|\cos\varphi|}, \qquad (3)$$

where U_f is the phase velocity of the internal or surface wave.

For our experiment ($H = 60$ m, $c = 1500$ m/s, $\cos\vartheta = (2)^{-1/2}$, $\cos\varphi = 1$, $U_{if} = 1$ m/s, and $\Omega = 2$ cycles per hour with a frequency of about 1 mHz), the estimated minimal frequency f_l proves to be approximately 148.5 Hz, which is somewhat higher than 100 Hz but lower than 300 Hz. This result partially explains the difference in the fluctuation intensities at these frequencies on the fixed path [13]. Thus, for a given combination of the parameters H and c, the frequency f of the source, and the sound speed profile that determines the values of U_f, Ω, and ϑ, one can use Eq. (3) to select the angle φ that determines the path orientation relative to the fronts of gravity waves (see, e.g., [28]), at which no synchronism occurs, and the amplitude variations of the sound signal are reduced.

For surface waves, the estimate of the frequency f_l proves to be much higher because, with the same sound frequencies and the same orientations of the propagation path with respect to the propagation direction of the gravity waves of the two types ($\varphi = \varphi'$), the ratio of the corresponding phase velocities ($U_{sf}\cos\vartheta/U_{if}$) is about 20–30. Thus, if the value of $\cos\vartheta$ is not too low

($|\cos\vartheta| \approx 1$), the change from 300 to 100 Hz in the carrier frequency is not critical for the interaction between the surface and sound waves. It looks like only the internal waves are be responsible for the observed phenomena in our experiments. Similar estimations based on the conditions of the synchronism are mainly applicable to narrow-band components in the spectrum of internal waves, and they fail in explaining the interaction of sound with internal waves of a continuous spectrum (similar to the Garret–Munk one), which are also observed in the experiments. Thus, for the experimental conditions, one should observe only a partial interaction of the 100-Hz sound with the internal waves existing on the fixed path. At a frequency of 300 Hz, the interaction proves to be more pronounced. In that case, an additional contribution is made by the regular oscillations of the thermocline, which exist, e.g., around the frequency 12 cycles per second and are caused by internal waves with displacement amplitudes of 10–12 m. Thus, to create a fixed shallow-water tomographic system that can be used to monitor weak phenomena (as in the observations of global warming), one should prefer a carrier frequency lower than 100 Hz. Both the preliminary experiments and the physical considerations evidence in favor of such a choice. Nevertheless, this conclusion requires further analysis and verification.

For this purpose, additional experiments were carried out on fixed paths 60, 90, and 120 km in length, in another shelf region of the Barents Sea, with similar water stratification (the near-bottom sound channel of the summer type). In these experiments, a bottom-moored sound source with the frequency about 100 Hz was used (Fig. 1). Three fixed sound receivers were located at the aforementioned distances. The amplitude envelopes of the received continuous signals were processed with the same technique as above, within the circular frequency band 2.6–15 cycles per hour. The duration of simultaneously received signals that were processed was no less than 52–60 h on each path. In processing, the main attention was paid to the variation coefficient (V, %) that is directly related (see Eq. (1)) to the magnitude ΔL_{dB} of the sound level fluctuations, including the mean value of $\bar{V}$ and its standard deviation σ within the observation time. The data of the statistical processing are summarized in the table.

Figure 5b shows the probability density distributions $\Psi(V)$ of the observed envelopes for all paths, namely, for the 60-km-long, the 90-km-long, and the 120-km-long paths. Figure 5a compares the typical probability distributions for the envelope variations in (*1*) shallow-water and (*2*) deep-water regions. Distribution *1* is based on the data obtained on the 90-km path that is intermediate in length; distribution *2* uses our data [14] obtained in a deep-water region close to the Russian Pacific coastline, on a fixed path of about 400 km between the Sakhalin and Iturup islands, with a narrow-band sound source of about 400 Hz. One can see the evident difference both in the forms of the distributions

Table

Path length, km	$\bar{V}$ (%)	σ (%)
60	4.80	1.20
90	5.90	1.27
120	6.50	1.32

(distributions *1* and *2* are close to the Rayleigh and Gauss ones, respectively) and in the median values of the variation coefficients (they differ by a factor of 2–3 in favor of the deep-water regions). The form of distribution *1* (for which the mean, rms, and most probable values can be generally different) testifies to a residual effect of the aforementioned narrow-band processes on the statistical parameters of the envelope fluctua-

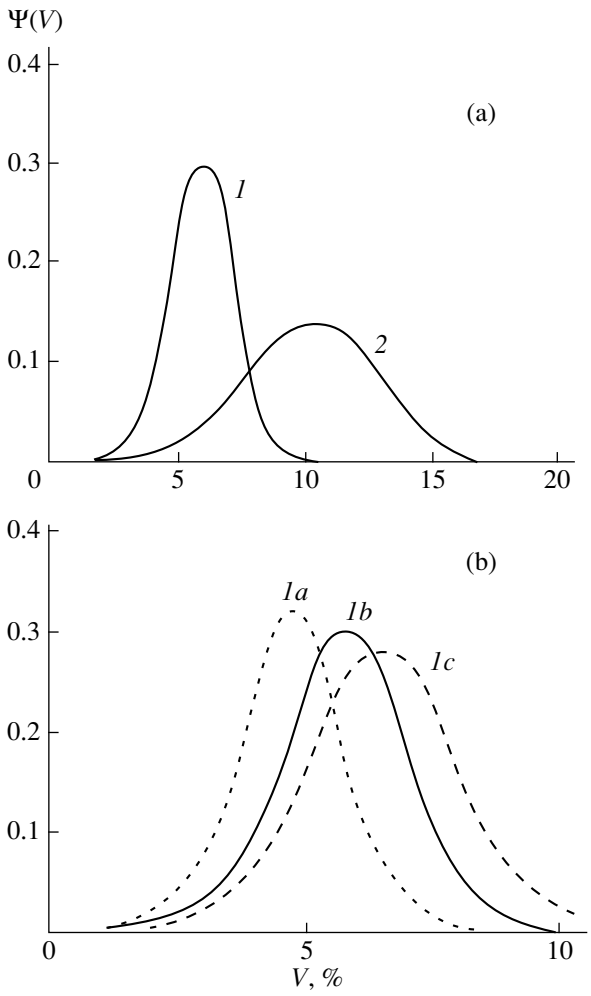

Fig. 5. Probability density distributions $\Psi(V)$ for the observed variations of the envelope on fixed paths of different lengths: (a) (*1*) in shallow-water regions (the data correspond to the intermediate 90-km-long path) and (*2*) in deep-water regions (the data from [14]); (b) in the shallow-water region under study for the path lengths (*1a*) 60 km, (*1b*) 90 km, and (*1c*) 120 km.

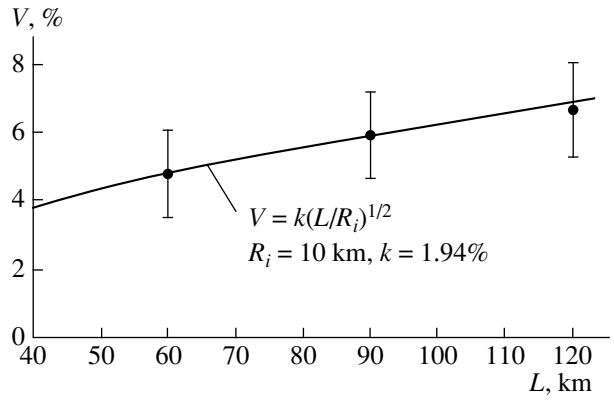

Fig. 6. Experimental dependence of the variation coefficient V (%) of the amplitude fluctuations of sound on the length of shallow-water paths. The data are presented in the form of vertical bars whose centers indicate the mean values of $\bar{V}$ and whose size corresponds to two standard (rms) deviations ($\pm\sigma$). The solid line shows the expected dependence of the fluctuation parameter of the sound signal envelope on the path length. The dependence was sought in the form $V = k(L/R_i)^{1/2}$ [27], and values of R_i and k were chosen according to the experimental data to be 10 km and 1.92%, respectively.

tions in shallow-water regions, although, at the frequency 100 Hz, this effect is lower than at 300 or 1000 Hz (Figs. 3b, 4a, and 4b). In deep-water regions, the observed spectrum of the envelope fluctuations is usually smoother, and the probability density distribution of the fluctuations is nearly Gaussian (with coincident mean, rms, and most probable values). Note that the fluctuations observed on the shortest 60-km path are qualitatively close to the data obtained on the similar path in the aforementioned preliminary experiments [13] carried out in another region. Attention should be paid to the weak dependence of the standard deviation of the variation coefficient (from its mean value) on the path length, with a trend to slowly increase for longer paths.

The experimentally revealed dependence of the fluctuation parameters on the path length is also worth mentioning. This dependence obtained on the basis of the tabulated data is shown in Fig. 6. According to [9, 27], outside the zone (R_i) of the longitudinal correlation of the thermocline displacements, the mean amplitude of the fluctuations is proportional to $(L/R_i)^{1/2}$. In Fig. 6, the solid curve indicates the expected dependence of the fluctuation parameters on the path length, which corresponds to an experimental estimate of about 10 km for the quantity R_i (in agreement with other data [9]). This dependence was approximated by the law $V = k(L/R_i)^{1/2}$ [27], where R_i was specified to be equal to 10 km, and the value of the factor k was selected by fitting. From the experimental data, the latter value was found to be k = 1.92%. The resulting dependences allow one to obtain the prognostic estimates that are required to implement the tomographic system in a shallow-water region of the Arctic shelf. Thus, from the collected data, one can expect that, for a path 200 km in length, the mean value of the correlation coefficient will be about 8.6%, with the associated standard deviation 1.45%. However, these estimates should be complemented with those of the effect of surface waves, which can exceed the predicted contribution of internal waves to the variability of low-frequency sound on longer shallow-water paths [27].

ACKNOWLEDGMENTS

We are grateful to S.A. Rybak for useful discussions and his interest in our studies and to A.N. Serebryanyĭ for his participating in the discussions and attracting our attention to the SWARM experiment [1, 2, 28].

This work was supported by the Russian Foundation for Basic Research (project nos. 97-02-16087a, 99-02-16618a, and 00-02-17858a).

REFERENCES

1. R. H. Headryck, J. E. Lynch, J. N. Kemp, *et al.*, J. Acoust. Soc. Am. **107**, 201 (2000).
2. R. H. Headryck, J. E. Lynch, J. N. Kemp, *et al.*, J. Acoust. Soc. Am. **107**, 221 (2000).
3. K. Noble and S. Flatte, J. Acoust. Soc. Am. **107**, 747 (2000).
4. K. Smith, J. Acoust. Soc. Am. **98**, 2330 (1995).
5. D. Rubenstein and M. Brill, in *Ocean Variability and Acoustic Propagation*, Ed. by J. Potter and A. Warn-Warnas (Kluver Academic, Dordrecht, 1991), pp. 215–228.
6. J. Zhou, X. Zhang, and P. Rogers, J. Acoust. Soc. Am. **90**, 2042 (1991).
7. B. G. Katsnel'son, L. G. Kulapin, A. A. Migulin, and V. G. Petnikov, Akust. Zh. **38**, 308 (1992) [Sov. Phys. Acoust. **38**, 164 (1992)].
8. V. A. Zhuravlev, I. K. Kobozev, A. A. Migulin, *et al.*, Akust. Zh. **37**, 1212 (1991) [Sov. Phys. Acoust. **37**, 635 (1991)].
9. B. G. Katsnel'son and V. G. Petnikov, *Acoustics of a Shallow Sea* (Nauka, Moscow, 1997).
10. K. V. Konyaev and K. D. Sabinin, *Waves inside the Ocean* (Gidrometeoizdat, St. Petersburg, 1992).
11. *The Formation of Acoustical Fields in Oceanic Waveguides: Coherence Phenomena*, Ed. by V. A. Zverev (Inst. of Appl. Phys., Nizhni Novgorod, 1997).
12. A. Belov, A. Serebryany, and V. Zhuravlev, in *Proceedings of 8th International Symposium on Acoustic Remote Sensing and Associated Techniques of the Atmosphere and Oceans* (Moscow, 1996).
13. A. Khrekov, A. Semenov, A. Skvortsov, and V. Susarov, in *Proceedings of the European Conference on Underwater Acoustics, Luxembourg, 1992*, Ed. by M. Weydert (Elsevier, London, 1992), pp. 351–355.
14. A. Khrekov, A. Semenov, and V. Susarov, in *Proceedings of the European Conference on Underwater Acoustics, Luxembourg, 1992*, Ed. by M. Weydert (Elsevier, London, 1992), pp. 329–333.

15. B. Katsnelson and S. Pereselkov, in *Proceedings of the International Conference OCEANS'96 MTS/IEEE* (Florida, USA, 1996), pp. 27–31.
16. J. Zhou, X. Zhang, and P. Rogers, in *Proceedings of the International Conference OCEANS'96 MTS/IEEE* (Florida, USA, 1996), pp. 1–8.
17. F. V. Bunkin, Yu. A. Kravtsov, N. N. Omel'chenko, *et al.*, in *Acoustic Waves in the Ocean*, Ed. by L. M. Brekhovskikh and I. B. Andreeva (Nauka, Moscow, 1987), pp. 76–83.
18. *Sound Transmission through a Fluctuating Ocean*, Ed. by S. Flatte (Cambridge Univ. Press, Cambridge, 1979; Mir, Moscow, 1982).
19. L. D. Landau and E. M. Lifshitz, *Course of Theoretical Physics*, Vol. 6: *Fluid Mechanics* (Nauka, Moscow, 1986; Pergamon, New York, 1987).
20. P. Morse and K. U. Ingard, *Theoretical Acoustics* (McGraw Hill, New York, 1968).
21. P. H. Leblond and L. A. Mysak, *Waves in the Ocean* (Elsevier, Amsterdam, 1978; Mir, Moscow, 1981).
22. M. J. Lighthill, *Waves in Fluids* (Cambridge Univ. Press, Cambridge, 1978; Mir, Moscow, 1981).
23. L. M. Brekhovskikh and V. V. Goncharov, *Introduction to the Mechanics of Continuous Media* (Nauka, Moscow, 1982).
24. M. A. Isakovich, *General Acoustics* (Nauka, Moscow, 1973).
25. A. D. Lapin and A. G. Semenov, A Report of the Andreev Acoustics Institute (Moscow, 1988).
26. L. A. Bespalov, A. M. Derzhavin, and A. G. Semenov, Akust. Zh. **44**, 591 (1998) [Acoust. Phys. **44**, 507 (1998)].
27. A. M. Derzhavin and A. G. Semenov, Akust. Zh. **45**, 204 (1999) [Acoust. Phys. **45**, 172 (1999)].
28. J. R. Apel *et al.*, IEEE J. Ocean Eng. **22**, 465 (1997).
29. A. N. Serebryanyĭ, Izv. Ross. Akad. Nauk, Fiz. Atmosf. Okeana **29** (2), 244 (1993).

Translated by E. Kopyl

Acoustical Physics, Vol. 47, No. 2, 2001, pp. 178–183. Translated from Akusticheskiĭ Zhurnal, Vol. 47, No. 2, 2001, pp. 220–226.

REVIEWS

The Equation of State of a Microinhomogeneous Medium and the Frequency Dependence of Its Elastic Nonlinearity

V. Yu. Zaĭtsev, V. E. Nazarov, and I. Yu. Belyaeva

Institute of Applied Physics, Russian Academy of Sciences,
ul. Ul'yanova 46, Nizhni Novgorod, 603600 Russia
e-mail: nazarov@hydro.appl.sci-nnov.ru

Received August 28, 1999

Abstract—In the framework of a rheological model, a nonlinear dynamic equation of state of a microinhomogeneous medium containing nonlinear viscoelastic inclusions is derived. The frequency dependences of the effective nonlinear parameters are determined for the difference frequency and second harmonic generation processes in the case of a quadratic elastic nonlinearity. It is shown that the frequency dependence of the nonlinear elasticity of the medium is governed by the linear relaxation response of the inclusions at the primary excitation frequency, as well as by the relaxation of the inclusions at the nonlinear generation frequencies. © *2001 MAIK "Nauka/Interperiodica".*

In recent years, the theory of media that exhibit a strong acoustic nonlinearity has been extensively developed. These media include different kinds of rock, some metals, and some structural materials. To date, it has been established that the nonlinear properties of such media are connected with various structural inclusions (or microinclusions) whose dimensions are large relative to the interatomic distances and small relative to the characteristic dimension of acoustic disturbances. In acoustics, such media are referred to as microinhomogeneous media [1–4]. As a rule, the acoustic properties of microinhomogeneous media cannot be described in terms of the classical (five- or nine-constant) theory of elasticity [5]. Firstly, the damping constant of such media is frequency-independent within a sufficiently wide frequency band [6], whereas the damping constant of homogeneous media is a linear function of frequency. Secondly, the elastic nonlinearity of homogeneous media is frequency-independent, whereas the nonlinearity of microinhomogeneous media can depend on frequency [7, 8]. Therefore, an adequate model and a corresponding equation of state should be developed to describe the nonlinear wave processes in microinhomogeneous media. The linear and nonlinear rheological models of a microinhomogeneous medium, which were proposed earlier in [9–14], provide the explanation for the frequency-independent behavior of the Q-factor and the strong elastic nonlinearity observed in such media. This paper combines and extends these models to derive a dynamic nonlinear equation of state of a microinhomogeneous medium and analyzes the frequency dependences of some nonlinear effects in the interaction between elastic disturbances in a medium if this kind.

Consider a rheological model of a nonlinear microinhomogeneous medium. As we noted above, microinhomogeneous media contain various inclusions (grains, cracks, dislocations, etc.) whose characteristic dimensions are small relative to the acoustic wavelength. In most cases, the compressibility of these inclusions is higher than that of the surrounding homogeneous material. Due to the higher compressibility of the inclusions, an elastic stress that occurs in their vicinity creates a higher strain (and, accordingly, strain rate), which is much higher than the average strain (and strain rate) in the medium. Therefore, the dissipation and the elastic nonlinearity of the medium are governed by the effect of these highly compliant inclusions. In order to derive the equation of state of the medium, we consider its part of length L much smaller than the characteristic wavelength λ. In such a region, the strain can be treated as quasi-static, which allows us to ignore the inertial properties of the material. Therefore, the rheological model of the microinhomogeneous medium can be represented by a nonuniform chain of linear elastic and nonlinear viscoelastic elements connected in series, as shown in Fig. 1. In this chain model, the uniform parts consisting of stiff elements (with the elastic coefficient κ) correspond to the inclusion-free regions of a perfectly elastic medium, while the nonlinear viscoelastic elements (with the elastic coefficients $\kappa_i \ll \kappa$) correspond to the compliant inclusions. We assume that the stiff and compliant elements of the chain are of equal length l, so that their number within the length L is equal to N, where $Nl = L$, and the number of inclusions is $N_1 = \nu N$, where the dimensionless coefficient ν is the relative (per-unit-volume) concentration of these inclusions.

Rheological models similar to the model shown in Fig. 1 were proposed in [9–14] for describing the dissipation and the nonlinear elastic properties of microinhomogeneous media. These models explain the fre-

1063-7710/01/4702-0178$21.00

quency independence of the Q-factor of such media on the basis of the assumption that the distribution of elastic parameters of the viscoelastic inclusions is wide with the nonlinear properties of the inclusions being ignored [9–11]. Conversely, the analysis of the nonlinear elasticity of the medium [12–14] ignored the viscosity of the inclusions and allowed for their nonlinearity. Clearly, when the viscosity of the nonlinear inclusions is taken into account, their effective stiffness proves to increase with the frequency of the acoustic disturbance, which results in an increase in the sound velocity at high frequencies, i.e., in the acoustic dispersion. An increase in the stiffness of the inclusions also decreases their strain and, therefore, decreases the nonlinearity of the medium, which means that its nonlinear elasticity becomes frequency-dependent. Thus, the origin of the sound velocity dispersion and that of the frequency dependence of the nonlinear elasticity of the medium are closely related.

To derive the dynamic equation of state of the microinhomogeneous medium, we use the model shown in Fig. 1 to calculate the elongation $X^{(t)}$ of the chain under the action of stress σ as a sum of elongations of the stiff and compliant elements:

$$X^{(t)} = (N - N_1)\varepsilon_0 l + \sum_{i=1}^{N_1} X_i^{(s)}, \tag{1}$$

where $\varepsilon_0 l$ is the elongation of a stiff element, $X_i^{(s)} = \varepsilon_i l$ is the elongation of the ith inclusion, and ε_0 and ε_i are their relative strains. Dividing both sides of Eq. (1) by the length of the element $L = Nl$, we obtain the expression for the average strain ε:

$$\varepsilon = (1 - \nu)\varepsilon_0 + \nu\varepsilon_i. \tag{2}$$

As we noted above, the stiff elements of the chain are perfectly elastic and are described by the equation

$$\sigma = E\varepsilon_0, \tag{3}$$

where $E = \kappa l$ is the elasticity modulus of the medium consisting of the stiff elements. The equation of state of the ith inclusion characterized by the viscosity and elastic nonlinearity has the form

$$\sigma = \zeta_i E[\varepsilon_i - F(\varepsilon_i)] + g\dot{\varepsilon}_i, \tag{4}$$

where $\dot{\varepsilon}_i \equiv d\varepsilon_i/dt$ is the inclusion strain rate, ζ_i is a dimensionless coefficient that characterizes the relative elasticity of the inclusions ($\zeta_i = E_i/E \ll 1$), and $F(\varepsilon_i)$ is the small elastic nonlinear correction ($|F(\varepsilon_i)| \ll |\varepsilon_i|$).

Equations (2)–(4) can be used to derive the equation of state of the microinhomogeneous medium, i.e., the function $\sigma = \sigma(\varepsilon)$. For the stiff elements, Eq. (3) yields

$$\varepsilon_0 = \sigma/E. \tag{5}$$

Since the nonlinearity is weak, the strain of the inclusions can be found by the successive approximation technique assuming that $\varepsilon_i = \varepsilon_i^{(1)} + \varepsilon_i^{(2)} + \ldots$, where $|\varepsilon_i^{(2)}| \ll |\varepsilon_i^{(1)}|$. In the linear approximation, the solution to Eq. (4) has the form of the relaxation integral:

$$\begin{aligned}\varepsilon_i^{(1)}(\sigma) &= (\zeta_i\Omega/E_i)\int_{-\infty}^{t}\sigma(\tau)e^{-\zeta_i\Omega(t-\tau)}d\tau \\ &= (\Omega/E)\int_{-\infty}^{t}\sigma(\tau)e^{-\zeta_i\Omega(t-\tau)}d\tau,\end{aligned} \tag{6}$$

where $\Omega = E/g$ has the frequency dimension, so that $\Omega_i = \zeta_i\Omega$ is the relaxation frequency of the ith inclusion.

The expression for the nonlinear correction $\varepsilon_i^{(2)}$ has the form

$$\begin{aligned}&\varepsilon_i^{(2)}(\sigma) \\ &= \Omega\zeta_i\int_{-\infty}^{t}e^{-\zeta_i\Omega(t-\tau)}F\left(\frac{\Omega}{E}\int_{-\infty}^{t}\sigma(\tau)e^{-\zeta_i\Omega(t-\tau)}d\tau\right)d\tau.\end{aligned} \tag{7}$$

Substituting Eqs. (5)–(7) for the strains ε_0 and ε_i into Eq. (2), we obtain the nonlinear dynamic equation of state of the microinhomogeneous medium in the form

$$\begin{aligned}\varepsilon(\sigma) &= \frac{1}{E}\left((1-\nu)\sigma + \nu\Omega\int_{-\infty}^{t}\sigma(\tau)e^{-\zeta_i\Omega(t-\tau)}d\tau\right) \\ &+ \nu\Omega\zeta_i\int_{-\infty}^{t}e^{-\zeta_i\Omega(t-\tau)}F\left(\frac{\Omega}{E}\int_{-\infty}^{\tau}\sigma(\tau')e^{-\zeta_i\Omega(t-\tau')}d\tau'\right)d\tau.\end{aligned} \tag{8}$$

This equation is valid within the entire range of inclusion concentrations $0 \le \nu \le 1$. The concentrations $\nu = 0$ and $\nu = 1$ (at $\zeta_i = \text{const}$) correspond to the homogeneous media: at $\nu = 0$, we obtain a perfectly elastic linear medium and, at $\nu = 1$ and $\zeta_i = \text{const}$, we have a nonlinear elastic medium whose dissipation properties are similar to those of liquids, gases, and homogeneous solids; in this case, the equation of state of the medium coincides with Eq. (4).

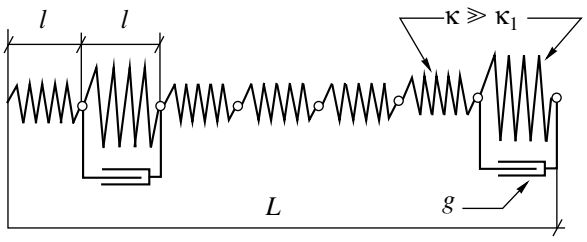

Fig. 1. Rheological model of a microinhomogeneous medium.

When the concentration of the inclusions is small, Eq. (8) can be reduced to the canonical form $\sigma = \sigma(\varepsilon)$:

$$\sigma(\varepsilon) = E\left(\varepsilon - \nu\Omega\int_{-\infty}^{t}\varepsilon(\tau)e^{-\varsigma_i\Omega(t-\tau)}d\tau + \nu\Omega\varsigma_i\int_{-\infty}^{t}e^{-\varsigma_i\Omega(t-\tau)}F\left(\Omega\int_{-\infty}^{\tau}\varepsilon(\tau')e^{-\varsigma_i\Omega(t-\tau')}d\tau'\right)d\tau\right). \quad (9)$$

Note that equations of this kind (i.e., with relaxation kernels) were earlier introduced phenomenologically to describe the imperfectly (inherently) elastic materials [4, 15, 16].

Equation of state (9) can be used to analyze the frequency behavior of the elastic nonlinearity of the microinhomogeneous medium. As can be seen from this equation, the dynamic action manifests itself in the nonlinear response of the medium in two ways. Firstly, this is the effect of the linear relaxation of the medium, because the linear response is the argument of the nonlinear correction $F(\varepsilon_i^{(1)})$. Secondly, the relaxation affects the response of the medium to the nonlinearity-induced secondary sources (the nonlinear correction F), which govern the nonlinearity-induced strain (or stress). These mechanisms (or, rather, components of a single nonlinear relaxation process) are essentially different. The first mechanism is universal for any nonlinear correction and is independent of the nature of the nonlinear process. The second mechanism strongly depends on the time scale of the nonlinear strain; therefore, the particular type of the nonlinearity and of the nonlinear process is significant (for example, it is important whether the process upconverts or downconverts the frequency). Nevertheless, Eq. (9) allows us to make some sufficiently general conclusions. The following estimate is valid for the relaxation integral of the function $f(t)$:

$$|f(t)| \geq \Omega\left|\int_{-\infty}^{t}f(\tau)e^{-\Omega(t-\tau)}d\tau\right|. \quad (10)$$

Then, the elastic nonlinearity of the medium containing relaxing nonlinear inclusions diminishes with increasing frequency of the action, because the argument of the nonlinear function in Eq. (9) decreases.

Below, we consider the basic features of the frequency dependence of the elastic nonlinearity for a medium with a quadratic nonlinearity, $F(\varepsilon_i) = \Gamma\varepsilon_i^2$, by examples of the generation (or demodulation) of the second harmonic and the difference frequency under a harmonic and biharmonic action on the medium.

We begin with analyzing a medium containing identical inclusions ($\varsigma_i = \varsigma$). Consider the downconversion process when the difference-frequency stress is produced under the biharmonic strain of the medium:

$$\varepsilon(t) = \varepsilon_0\cos\omega_1 t + \varepsilon_0\cos\omega_2 t. \quad (11)$$

Substituting Eq. (11) into Eq. (9) and separating the components at $\omega_d = |\omega_1 - \omega_2|$, we derive the expression for the difference-frequency stress σ_d at the difference frequency in the form $\sigma_d(\omega_d) = A_d\cos\omega_d t + B_d\sin\omega_d t = |\sigma_d|\cos(\omega_d t + \varphi_d)$, where the amplitude σ_d and the phase φ_d have the form:

$$|\sigma_d| = (A_d^2 + B_d^2)^{1/2} = \frac{\nu\Gamma\varepsilon_0^2 E}{\varsigma^2[(1 + (\omega_1/\varsigma\Omega)^2)(1 + (\omega_2/\varsigma\Omega)^2)(1 + (\omega_d/\varsigma\Omega)^2)]^{1/2}}, \quad (12)$$

$$\varphi_d = \arctan(\beta_d/A_d) = \arctan\left(\frac{(\omega_d/\varsigma\Omega)[2 + \omega_1\omega_2/(\varsigma\Omega)^2]}{1 + \omega_1\omega_2/(\varsigma\Omega)^2 - (\omega_d/\varsigma\Omega)^2}\right). \quad (13)$$

As can be seen from Eq. (12), in the static limit ω_d, $\omega_{1,2} \ll \varsigma\Omega$, the amplitude is $|\sigma_d| = \sigma_{\text{stat}} = \nu\Gamma\varepsilon_0^2 E/\varsigma^2$. When the frequencies ω_d and $\omega_{1,2}$ reach the order of the characteristic relaxation frequency $\varsigma\Omega$ of the inclusions or higher, the nonlinear response of the medium decreases: $\sigma_d \sim (\omega_1\omega_2\omega_d)^{-1}$. For a low difference frequency ($\omega_d \ll \varsigma\Omega$) and for $\omega_1 \approx \omega^2 = \omega$, Eq. (12) is simplified:

$$|\sigma_d| = \nu\Gamma\varepsilon_0^2 E[\varsigma^2[1 + (\omega/\varsigma\Omega)^2]]^{-1}. \quad (14)$$

This expression shows that, when $\omega \gg \varsigma\Omega$, the amplitude behaves as $|\sigma_d| \sim \omega^{-2}$.

As can be seen from Eq. (13), the relaxation of the inclusions leads to a monotonic variation of φ_d from zero (in the quasi-static limit when $\omega_1, \omega_2, \omega_d \ll \varsigma\Omega$) to $\pi/2$ (when $\omega_1, \omega_2, \omega_d \gg \varsigma\Omega$).

To describe the frequency dependence of the elastic nonlinearity of the microinhomogeneous medium in the case of the difference frequency generation, we introduce the normalized nonlinear parameter N_d defined as the ratio of the amplitude $|\sigma_d|$ given by Eq. (14) to the amplitude value $\sigma_{\text{stat}} = \nu\Gamma\varepsilon_0^2 E/\varsigma^2$ in the static limit:

$$N_d = [1 + (\omega/\varsigma\Omega)^2]^{-1}. \quad (15)$$

The parameter N_d versus frequency ω is shown in Fig. 2 (curve *1*).

Consider the process of the second harmonic generation under the harmonic action on the medium: $\sigma(t) = \sigma_0\cos\omega t$. In this case, Eq. (9) yields the expression for the stress at the double frequency, $\sigma_2 = A_2\cos 2\omega t +$

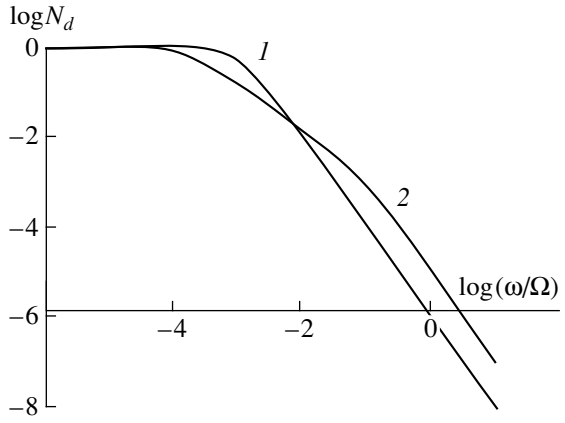

Fig. 2. Normalized nonlinear parameter N_d versus frequency ω_1 for the process of the difference frequency generation ($\omega_d/\Omega = 10^{-5}$): (*1*) a medium with identical inclusions ($\varsigma = 10^{-3}$) and (*2*) a medium with inclusions distributed in elasticity ($a = 10^{-4}$, $b = 10^{-1}$).

$B_2 \sin 2\omega t$, the amplitude and phase of the stress σ_2 being determined as

$$|\sigma_2| = \nu\Gamma\varepsilon_0^2 E \frac{1}{2\varsigma^2[1 + (\omega/\varsigma\Omega)^2][1 + (2\omega/\varsigma\Omega)^2]^{1/2}}, \quad (16)$$

$$\varphi_2 = \arctan\left(\frac{2(\omega/\varsigma\Omega)[(\omega/\varsigma\Omega)^2 - 2]}{5(\omega/\varsigma\Omega)^2 - 1}\right). \quad (17)$$

Figure 3a shows the frequency dependences of the normalized nonlinear parameter N_2 introduced according to Eq. (15) and of the phase σ_2. Curve *1* demonstrates a rapid decrease in the parameter N_2 when the frequency ω is higher than the inclusion relaxation frequency $\varsigma\Omega$. In addition, Eq. (16) shows the above-mentioned effect of the inclusion relaxation on the nonlinearity of the medium at the frequency of the primary excitation ω and at the frequency of its second harmonic, 2ω. Note that the following inequality is valid: $N_2 \leq N_d$.

In contrast to the smooth variation of the phase from 0 to $\pi/2$ in the case of the difference frequency generation, from Eq. (17), it follows that the phase φ_2 of the second harmonic changes rapidly by π in the vicinity of the frequency $\omega = \varsigma\Omega/\sqrt{5}$. This property can be used to change the frequency dependence of the parameter N_2: when the medium contains inclusions with different relaxation frequencies, their nonlinear responses superimpose, which may cause a nonmonotonic frequency dependence of the parameter N_2. Figure 3b shows the dependences of N_2 and φ_2 on frequency for a medium with inclusions of two types (their relaxation frequencies differ by an order of magnitude). These dependences demonstrate the nonmonotonic behavior mentioned above.

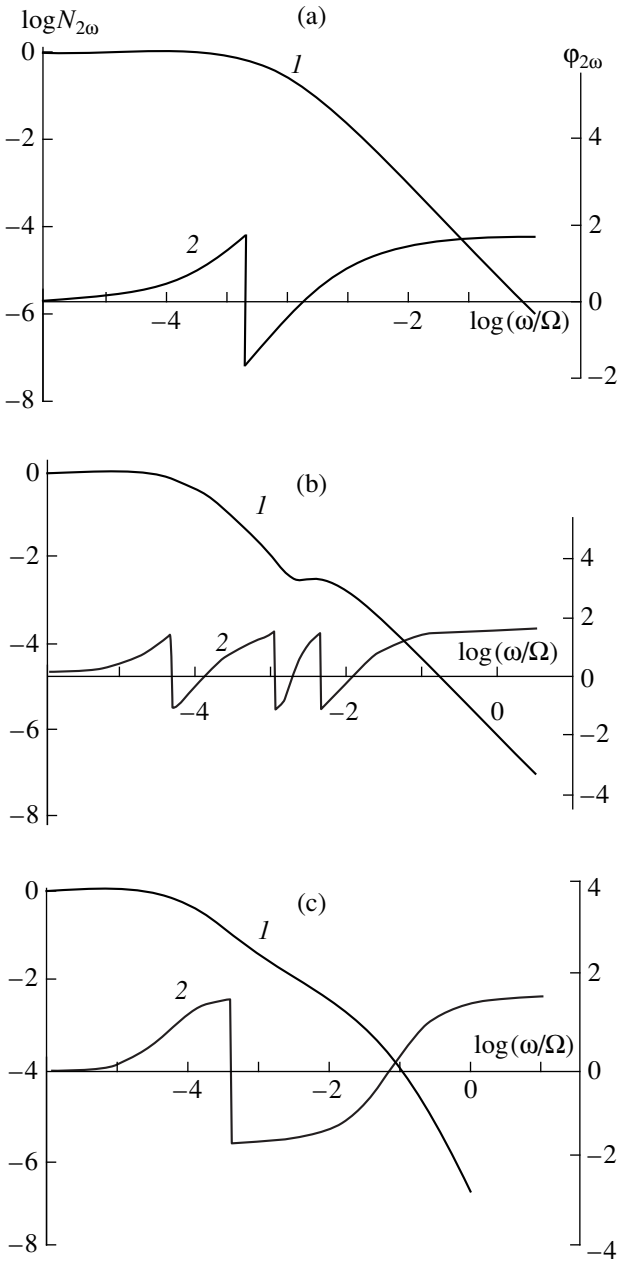

Fig. 3. (*1*) Normalized nonlinear parameter $N_{2\omega}$ and (*2*) phase $\varphi_{2\omega}$ versus frequency ω for the process of the second harmonic generation (a) in a medium with identical inclusions ($\varsigma = 10^{-3}$), (b) in a medium with inclusions of two types ($\varsigma_1/\varsigma_2 = 10^{-1}$), and (c) in a medium with inclusions distributed in elasticity ($a = 10^{-4}$, $b = 10^{-1}$).

In real microinhomogeneous media, inclusions are not identical and are characterized by a certain distribution in elasticity, $\nu = \nu(\varsigma)$, so that $\nu(\varsigma)d\varsigma$ represents the concentration of inclusions with the parameter ς within the interval $[\varsigma, \varsigma + d\varsigma]$. In general, real inclusions are also distributed in the viscosity (or in the relaxation frequency Ω), so that the inclusion distribution function must depend on the parameters ς and Ω: $\nu = \nu(\varsigma, \Omega)$. In

this case, Eqs. (1)–(7) provide an evident generalization of Eq. (9):

$$\sigma(\varepsilon) = E\Bigg\{\varepsilon + \int d\varsigma \int d\Omega \nu(\Omega, \varsigma)\Omega \int_{-\infty}^{t} \varepsilon(\tau) e^{-\varsigma\Omega(t-\tau)} d\tau$$

$$- \int d\varsigma \int d\Omega \nu(\Omega, \varsigma)\Omega\varsigma \int_{-\infty}^{t} e^{-\varsigma\Omega(t-\tau)} \tag{18}$$

$$\times F\left[\Omega \int_{-\infty}^{\tau} \varepsilon(\tau') e^{-\varsigma\Omega(t-\tau')} d\tau'\right]\Bigg\}.$$

It has been shown [9–11] that, to explain the frequency-independent behavior of the Q-factor of microinhomogeneous media, one should assume that the distribution $\nu(\varsigma)$ is sufficiently wide, the wide distribution of inclusions in elasticity being of most importance particularly for the linear dissipation–dispersion properties, while their distribution in viscosity affects the results insignificantly [11]. Since the linear and nonlinear parts of Eq. (18) contain relaxation integrals of similar structure, we will first analyze the nonlinear elasticity as a function of frequency by analogy with [9–11] allowing for the distribution of the inclusions in the parameter ς under the assumption that

$$\begin{aligned} &\nu(\varsigma) = \nu_0 \quad \text{for} \quad \varsigma \in [a, b], \\ &\nu(\varsigma) = 0 \quad \text{for} \quad \varsigma \notin [a, b]; \quad a \le \varsigma \le b < 1. \end{aligned} \tag{19}$$

As above, we consider the processes of the difference frequency and second harmonic generation in a medium with a quadratic elastic nonlinearity.

In the case of the difference frequency generation, one can obtain expressions similar to Eqs. (12) and (13). However, they are rather lengthy. Therefore, below, we present the formulas for the quadrature coefficients A_d and B_d derived for a low difference frequency when the primary-excitation frequencies are approximately equal ($\omega_1 \approx \omega_2 = \omega$) and $\omega_d \ll \omega$:

$$A_d = \nu_0 \Gamma \varepsilon_0^2 E \left(\frac{\Omega}{\omega}\right)^2 \times \left[\frac{\omega_d}{\Omega}\arctan\left(\frac{\varsigma\Omega}{\omega_d}\right) - \frac{\omega}{\Omega}\arctan\left(\frac{\varsigma\Omega}{\omega}\right)\right]\Bigg|_{\varsigma=a}^{\varsigma=b}, \tag{20}$$

$$B_d = \nu_0 \Gamma \varepsilon_0^2 E \frac{\omega_d \Omega}{\omega^2} \ln\left[\frac{1 + (\omega/\varsigma\Omega)^2}{1 + (\omega_d/\varsigma\Omega)^2}\right]\Bigg|_{\varsigma=a}^{\varsigma=b}. \tag{21}$$

These expressions also show the effect of the relaxation at both the excitation and difference frequencies; the medium is characterized by two relaxation frequencies $a\Omega$ and $b\Omega$, which correspond to the lower and higher boundaries of the inclusion distribution in elasticity, respectively. The dependence of the parameter N_d on the frequency ω is shown in Fig. 2 (curve *2*). This plot shows that $N_d = \text{const}$ for $\omega < a\Omega$. When $a\Omega < \omega < b\Omega$, we have $N_d \sim \omega^{-1}$, i.e., N_d decreases more slowly than predicted by Eqs. (12) and (14), which are derived for the medium with identical inclusions. For $\omega > b\Omega$, we have $N_d \sim \omega^{-2}$ (as for the medium with identical inclusions for $\omega > \varsigma\Omega$).

For the second harmonic, one can obtain the following expressions for the coefficients A_2 and B_2 by analogy with Eqs. (15) and (16):

$$A_2 = \nu\Gamma\varepsilon_0^2 E\left[\frac{2}{\omega/\Omega}(\arctan(\varsigma\Omega/2\omega) - \arctan(\varsigma\Omega/\omega)) + \frac{1}{\varsigma[1 + (\omega/\varsigma\Omega)^2]}\right]\Bigg|_{\varsigma=a}^{\varsigma=b}, \tag{22}$$

$$B_2 = \nu\Gamma\varepsilon_0^2 E\left\{\frac{1}{\omega/\Omega}\ln\left[\frac{1 + (\omega/\varsigma\Omega)^2}{1 + (2\omega/\varsigma\Omega)^2}\right] + \frac{\omega/\varsigma\Omega}{\varsigma[1 + (\omega/\varsigma\Omega)^2]}\right\}\Bigg|_{\varsigma=a}^{\varsigma=b}. \tag{23}$$

The effect of the inclusion relaxation at the excitation frequency and at its second harmonic can also be seen here. Figure 3c shows the parameter N_2 and the phase φ_2 versus the frequency ω. One can see that, when $\omega < a\Omega$, $N_2 = \text{const}$; in the range $a\Omega < \omega < b\Omega$, $N_2 \sim \omega^{-1}$; and for $\omega > b\Omega$, $N_2 \sim \omega^{-3}$.

Now, we consider the combined effect of the inclusion distributions in elasticity and viscosity. We assume that the inclusions are uniformly distributed in the parameters ς and Ω:

$$\begin{aligned} &\nu(\varsigma, \omega) = \nu_0 \quad \text{for} \quad \varsigma \in [a, b], \quad \Omega \in [\Omega_a, \Omega_b], \\ &\nu(\varsigma, \omega) = 0 \quad \text{for} \quad \varsigma \notin [a, b], \quad \Omega \notin [\Omega_a, \Omega_b]. \end{aligned} \tag{24}$$

In this case, we failed to study Eq. (18) analytically and generalize Eqs. (20)–(23), though, in principle, the solutions of interest can be obtained numerically. Here, we present the approximate analytical result describing the process of demodulation ($\omega_d = 0$):

$$\sigma_d = \frac{1}{2}\nu_0 \Gamma \varepsilon_0^2 E N_d,$$

$$N_d = \left[\left(\frac{\Omega^2}{\omega} + \frac{\omega}{b^2}\right)\arctan\left(\frac{\Omega b}{\omega}\right) - \left(\frac{\Omega^2}{\omega} + \frac{\omega}{a^2}\right)\arctan\left(\frac{\Omega a}{\omega}\right) + \frac{\Omega(b-a)}{ab}\right]\Bigg|_{\Omega=\Omega_a}^{\Omega=\Omega_b}. \tag{25}$$

Figure 4 represents the parameter N_d versus frequency ω for different values of the parameter Ω_b/Ω_a. As can be seen from Fig. 4, the additional allowance made for the distribution of inclusions in the viscosity (unlike the distribution in elasticity) weakly affects the

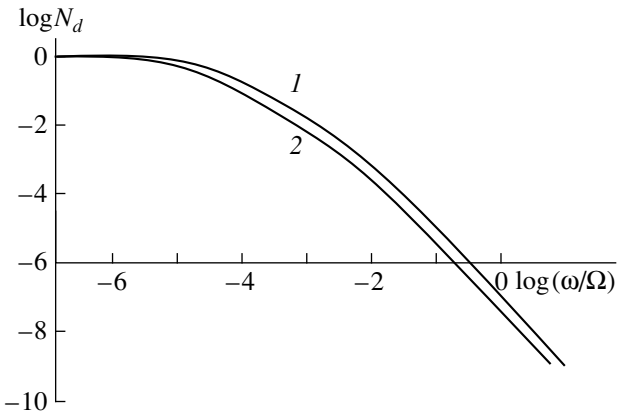

Fig. 4. Normalized nonlinear parameter N_d versus frequency ω for the process of demodulation ($\omega_d = 0$) in the medium with inclusions distributed in elasticity ($a = 10^{-4}$, $b = 10^{-1}$) and viscosity: Ω_b/Ω_a = (*1*) 10 and (*2*) 10^4.

nonlinear parameter N_d, as in the case of the results obtained in [9–11] for linear dissipation and dispersion properties of a microinhomogeneous medium.

Thus, in this paper, in the framework of a rheological model, a nonlinear dynamic equation of state of the microinhomogeneous medium containing viscoelastic inclusions is derived and, for the case of the quadratic elastic nonlinearity, the frequency dependences of the effective nonlinear parameters are determined for the processes of the difference frequency and second harmonic generation. It is shown that the frequency dependence of the nonlinear elasticity of the medium is governed by the combined effect of (i) the linear relaxation response of the inclusions at the frequency of the primary excitation and (ii) their relaxation at the combination frequencies and harmonics. Note that, though the consequences of the equation of state are analyzed for a medium with a quadratic nonlinearity, the approach developed in this paper can also be applied to media with other types of the elastic nonlinearity: cubic, different-modulus, hysteretic, etc. [4, 17, 18].

The equation of state derived above (together with the equation of motion) can be used to study various nonlinear effects that occur in the propagation and interaction of elastic waves in microinhomogeneous media. Due to the above-mentioned specific features of these media, the character of the nonlinear processes in them essentially differs from that of the nonlinear processes in homogeneous media, which can be used as a diagnostic indicator in the remote monitoring of the medium.

ACKNOWLEDGMENTS

This work was supported by the Russian Foundation for Basic Research (project nos. 98-05-64683 and 98-02-17686) and by the Interbranch Center for Science and Engineering (project no. 1369).

REFERENCES

1. M. I. Isakovich, *General Acoustics* (Nauka, Moscow, 1973).
2. V. E. Nazarov, L. A. Ostrovsky, I. A. Soustova, and A. M. Sutin, Phys. Earth Planet. Inter. **50** (1), 65 (1988).
3. K. A. Naugol'nykh and L. A. Ostrovskiĭ, *Nonlinear Wave Processes in Acoustics* (Nauka, Moscow, 1990).
4. V. E. Gusev, W. Lauriks, and E. Thoen, J. Acoust. Soc. Am. **103**, 3216 (1998).
5. L. D. Landau and E. M. Lifshits, *Course of Theoretical Physics*, Vol. 7: *Theory of Elasticity* (Nauka, Moscow, 1965; Pergamon, New York, 1986).
6. S. Ya. Kogan, Izv Akad. Nauk SSSR, Fiz. Zemli, No. 11, 3 (1966).
7. V. E. Nazarov, Fiz. Met. Metalloved. **88** (4), 82 (1999).
8. V. E. Nazarov, Akust. Zh. **46**, 228 (2000) [Acoust. Phys. **46**, 186 (2000)].
9. V. Yu. Zaĭtsev and V. E. Nazarov, Akust. Zh. **45**, 622 (1999) [Acoust. Phys. **45**, 552 (1999)].
10. V. Yu. Zaĭtsev and V. E. Nazarov, Acoust. Lett. **21**, 11 (1997).
11. V. Yu. Zaĭtsev, V. E. Nazarov, and A. E. Shul'ga, Akust. Zh. **46**, 348 (2000) [Acoust. Phys. **46**, 295 (2000)].
12. V. Yu. Zaĭtsev, Acoust. Lett. **19**, 171 (1996).
13. I. Yu. Belyaeva and V. Yu. Zaĭtsev, Akust. Zh. **43**, 594 (1997) [Acoust. Phys. **43**, 510 (1997)].
14. I. Yu. Belyaeva and V. Yu. Zaĭtsev, Akust. Zh. **44**, 731 (1998) [Acoust. Phys. **44**, 635 (1998)].
15. V. A. Pal'mov, *Vibrations of Elastically Plastic Bodies* (Nauka, Moscow, 1976).
16. Yu. N. Rabotnov, *Mechanics of a Deformed Solid* (Nauka, Moscow, 1979).
17. K. E.-A. van Den Abeele, P. A. Johnston, R. A. Guyer, and K. R. McCall, J. Acoust. Soc. Am. **101**, 1885 (1997).
18. V. Gusev, C. Glorieux, W. Lauriks, and J. Thoen, Phys. Lett. A **232**, 77 (1997).

Translated by A. Khzmalyan

Acoustical Physics, Vol. 47, No. 2, 2001, pp. 184–193. Translated from Akusticheskiĭ Zhurnal, Vol. 47, No. 2, 2001, pp. 227–237.

REVIEWS

Experimental Studies of Sound Diffraction by Moving Inhomogeneities under Shallow-Water Conditions

V. A. Zverev, P. I. Korotin, A. L. Matveev, V. V. Mityugov, D. A. Orlov, B. M. Salin, and V. I. Turchin

Institute of Applied Physics, Russian Academy of Sciences, ul. Ul'yanova 46, Nizhni Novgorod, 603600 Russia

e-mail: matveyev@hydro.appl.sci-nnov.ru; turchin@hydro.appl.sci-nnov.ru

Received January 31, 2000

Abstract—The experimental data on the sound propagation and diffraction by moving test inhomogeneities under lake conditions are presented. It is shown that the diffracted signals under multimode propagation are adequately described by simplified theoretical models proposed earlier. The detection of the diffracted signals against the background of a fluctuating direct signal is demonstrated for the reception by a horizontal or vertical array. It is also shown that the direct and diffracted signals observed in the lake are similar in their characteristics to the signals in a shallow sea, which allows one to use the lake experiment for testing various underwater acoustic techniques intended for shallow-sea conditions. *© 2001 MAIK "Nauka/Interperiodica".*

In a series of papers [1–6], a method of diagnostics of moving inhomogeneities by the scattering of the primary acoustic field in the "forward" direction, i.e., in the directions close to that of incidence, is considered.[1] A scheme for the observation of inhomogeneities by such a method is shown in Fig. 1. The acoustic source and the receiving array (a vertical or horizontal one) form the stationary propagation track OA, which is crossed by a moving inhomogeneity at a point *S*. In the absence of a scatterer, the array elements receive the direct signal P_0; if no fluctuations occur in the medium, the amplitude and phase of this signal are constant in time. At the moments close to the time when the inhomogeneity intersects the track OA, the received signal experiences a perturbation, since, in accordance with the Babine principle, the direct field is supplemented by a field diffracted by the inhomogeneity: $P = P_0 + P_d$, where P is the received signal and P_d is the diffracted signal. If the level of radiation is rather high, the fluctuations of the direct signal are the main interference.

To single out a diffracted signal against the background on this interference, several methods were suggested [2–7], which use, to one or another extent, model descriptions of the diffracted signal. A number of experiments carried out in shallow-sea conditions showed that the "forward" scattering is very promising for use in the diagnostics of moving inhomogeneities [2, 3, 8].

However, to develop such a method, systematic experimental investigations were needed. In particular, it is of interest to compare real diffracted signals with the simplified theoretical models [2, 3] and to use a great body of experimental data for testing various algorithms of the signal processing under the conditions of a fluctuating transmission channel, etc. To this end, in summers of 1997 and 1998 at Lake Sankhar (the Vladimir region), a number of experiments were carried out to observe the diffracted signals in the frequency range 1–3 kHz.

In choosing such a method of the experimental investigations, we allowed for its low cost, as compared to the sea experiments, and for the following facts.

First, the regular components of both the direct and the diffracted acoustic fields obey the similarity relations [10]: with a simultaneous increase in frequency by a factor K and a decrease in all geometric dimen-

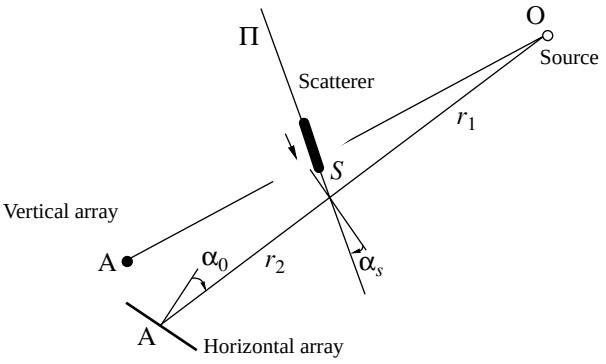

Fig. 1. Disposition of the source, the receiving arrays (A), and the scatterer moving along the trajectory Π in the horizontal plane; α_s is the angle between the normal to the line OA and the trajectory Π, α_0 is the scatterer bearing measured relative to the normal to the array.

[1] In a number of works, the term "bistatic sonar" is also used.

sions by the same factor, the acoustic field structure is not changed, provided that the sound velocity and the density remain invariable. Approximately, this will be valid even with allowance for the sound absorption in the sea bottom, because the absorption coefficient is almost proportional to frequency in a rather broad frequency range. In the lake chosen, the vertical sound velocity profile and the type of the bottom (sand, silt) are specific for a shallow sea (see below). Therefore, the results obtained can be extended to shallow sea conditions with allowance for a corresponding scaling coefficient.[2]

Second, the preliminary observations have shown that the acoustic field fluctuates in the lake conditions, the statistical characteristics of these fluctuations being similar in a qualitative sense to sound fluctuations along a stationary track in shallow sea conditions (see, e.g., [12]). Although the fluctuations of the acoustic field in the lake can be generated by somewhat different hydrophysical processes, only the statistical characteristics of the interference (temporal spectra, spatial correlation scales, etc.) are significant in the detection of useful signals. From this point of view, one can hope that the validation of the signal processing algorithms under lake conditions will to some extent also testify to their applicability in the shallow sea conditions.

Both above-mentioned facts allow one to consider the lake experiment as a rather exact scale model of a sea experiment with the scaling coefficient $K \sim 10$–20. Moreover, in the lake experiment, it is easier to monitor the track parameters, the motion of the scatterer, and the hydrophysical characteristics of a water area.

The experiments were carried out at Lake Sankhar, which is of the karst origin and forms a closed freshwater basin (the salinity is less than 1‰) without sinks and sources. The area of the deep-water part is $\sim 0.6 \times 0.8$ km with the water depths 10–20 m and the sand-silt bottom (the thickness of mud is about 1 m in the region of maximal depths and several to several tens of centimeters in other parts). The map of the lake with isobars and the disposition of the equipment is shown in Fig. 2.

In the experiment, two identical 64-element line receiving hydroacoustic arrays 12 m in length were used. One array was installed horizontally at a depth of ~6 m, the second array was installed vertically and spanned almost the whole propagation channel. The signals from the array hydrophones were brought out to a small pontoon that was anchored near the place of the array installation. The pontoon carried the equipment for the analog conversion of signals (amplification, filtering) and for the digital conversion (heterodyning, low-frequency filtering, and increasing the time lapse between signals). The transformed signals

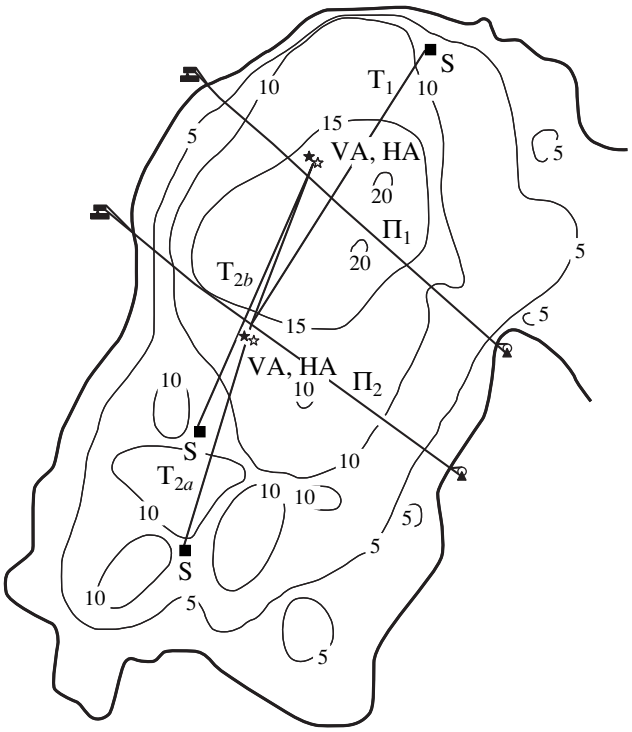

Fig. 2. Map of Lake Sankhar with the isobars (5, 10, 15, and 20 m) and the positions of the equipment: (S) source; (VA) vertical array; (HA) horizontal array; (Π) trajectories of the moving inhomogeneity; and (T) stationary tracks of sound transmission.

were recorded on a hard disk of a computer. The radiated signal had the relative frequency stability no worse than $\sim 10^{-9}$, which allowed one to carry out phase measurements during at least several hours. Basically, we used a continuous multifrequency signal of the form

$$s(t) = \sum_{i=1}^{I} a_i \cos(2\pi f_i t + \phi_i)$$

with the frequencies f_i in the range 0.8–3.0 kHz. A sound source of the piezoceramic type was rigidly fixed at a distance of ~0.7 m from the bottom at different sea depths (see Fig. 2). In some experiments, near this source, an additional hydrophone was installed from which the signal was transmitted by a cable to the pontoon.

To study the sound diffraction, three test scatterers were used. Two of them were the hollow metallic cylinders with an internal diameter of 0.45 m and with the lengths 5.2 and 2.5 m (below, "long" and "short" scatterers, respectively); for streamlining, the 0.6-m conic nozzles were mounted at the ends of the cylinders, these nozzles being partially filled with foam plastic. The third scatterer was a rectangular screen of the foam plastic; it was 5×1 m in area and 0.1 m in thickness. To provide the negative buoyancy of it, a load was attached to its lower side. To move the scatterers in the underwa-

[2] In a lake, as an additional factor, sound reflections may occur from the coastlines, which can introduce some extra difficulties in the signal interpretation.

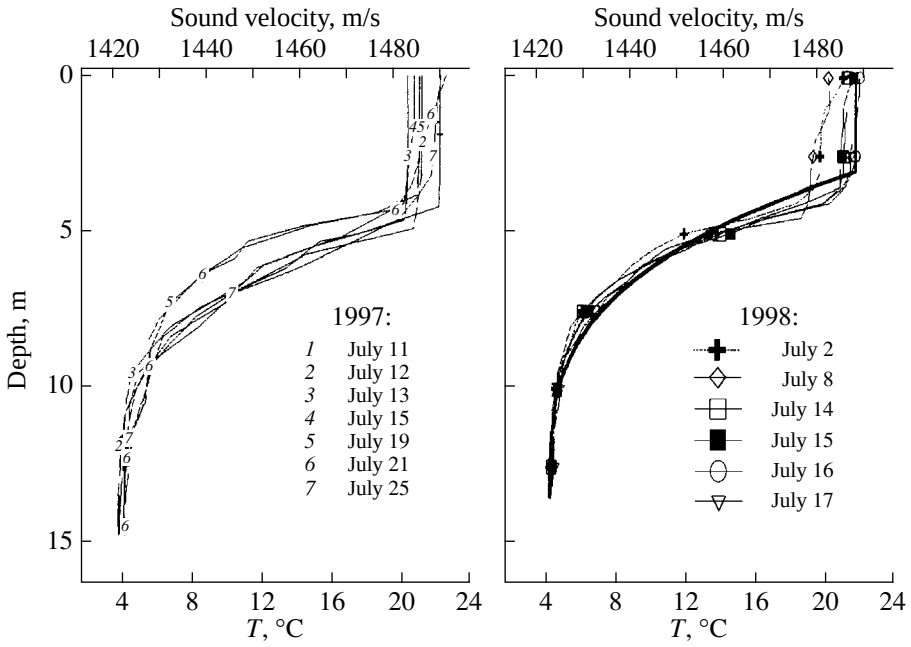

Fig. 3. Profiles of sound velocity and temperature in the lake in 1997 and 1998. The thick line (1998) corresponds to the automodeling solution for an expanding layer of mixed liquid above the thermocline.

ter position with a constant speed, we used a halyard stretched between the shores of the lake and a winch.

In addition to the acoustic equipment, a wave recorder, sensors of temperature fluctuations in water at different depths and a meter of the speed and wind direction were also used. From the depth dependence of the temperature, the sound velocity profile $c(z)$ was determined; some examples of $c(z)$ are shown in Fig. 3. As follows from Fig. 3, the variability of $c(z)$ is mainly related to warming (cooling) of the upper layers due to changes in the weather conditions. Note that the profile in Fig. 3, in general, agrees well with the theoretical automodeling solution for a shallow sea [9].

The main part of observations are the records of signals received by the array elements for three stationary acoustic tracks T_1, T_{2a}, and T_{2b} between the source and the vertical array (VA) and between source and the horizontal array (HA) (see Fig. 2). Most records were obtained when one of the test scatterers moved approximately across the stationary track along the trajectories Π_1 or Π_2; the speed of the movement was in the range 0.3–0.7 m/s at a scatterer depth of 6 or 10 m; the duration of a record was 5–20 min. More than 100 such records were made with one to four intersections of the acoustic track (about 50 records were also made in the absence of the scatterer movement). Every record is a 3D set of complex numbers P_{nji}, where n is the number of the hydrophone of the vertical or horizontal array, j is the number of the time reading, and i is the number of the radiation frequency. The signal readings were made with the frequency 6–10 Hz (in different records); the signal band after demodulation of the carrier frequency f_i was ±(3–5) Hz. A number of specific experiments were also carried out for synthesizing the diffracted signals and measuring the "sections" of the acoustic field; signals were recorded by series within 24 h (without a scatterer).

It is initially assumed that the acoustic field in the lake, as well as in a shallow sea, has the regular (coherent) component determined by a sufficiently large number (~10–20) of propagating modes and a weaker fluctuating component due to the scattering by the surface roughness and the volume fluctuations of the sound velocity.

Figure 4 exhibits some examples of the spatial spectra of the coherent component for the vertical and horizontal arrays (the result of averaging over a ~3-min interval) for the track T_{2b} and the carrier frequency 2.5 kHz. As follows from Fig. 4, the spatial structures of the signals are sufficiently stable in time. The spatial spectrum for the HA has a pronounced main lobe in the direction toward the source ($\sin\alpha_0 = 0.18$).[3] The spatial spectrum of the VA had a quasi-random set of the peaks in the range $\pm\sin\theta_w$, where θ_w is the trapping angle of the waveguide. For the sound velocities in the bottom in the range 1650–1800 m/s and the profiles $c(z)$ shown in Fig. 3, we have $\sin\theta_w \simeq 0.5$–0.6, which agrees well with the results presented in Fig. 4.

Figure 5 exhibits some examples of normalized spectral power densities (SPD), $W^{(norm)}(f)$, (in dB per 1/Hz) of the signals at the hydrophones of the VA and HA

[3] For the larger bearings, the main lobe of the HA is deformed at some frequencies, i.e., the modal structure of the sound field affects the spatial spectrum (see, e.g., [13]).

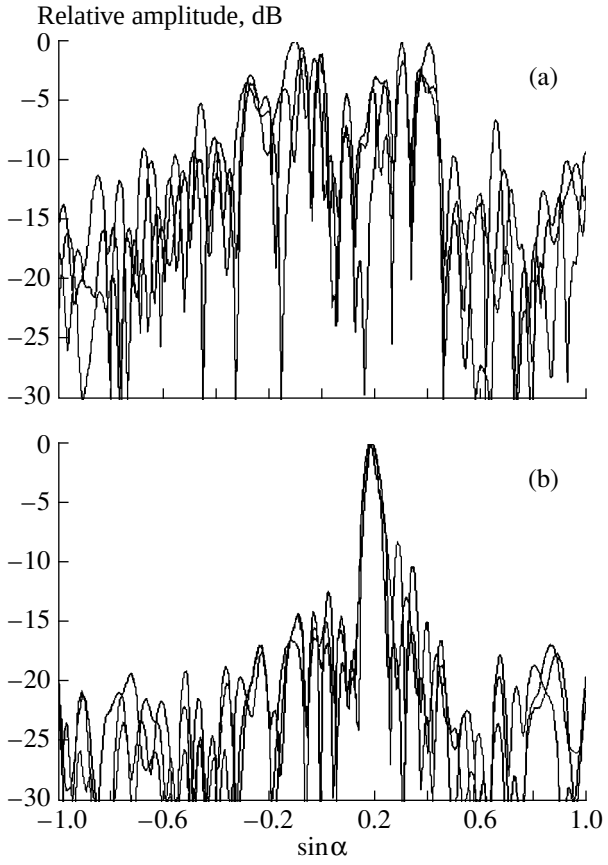

Fig. 4. Spatial spectra of the coherent field component at the (a) vertical and (b) horizontal arrays as functions of $\sin\alpha$, where α is a current bearing: a frequency of 2.5 kHz, track T_{2b}; each plot exhibits three realizations with a time separation of 1.5 h and two days relative to the first record.

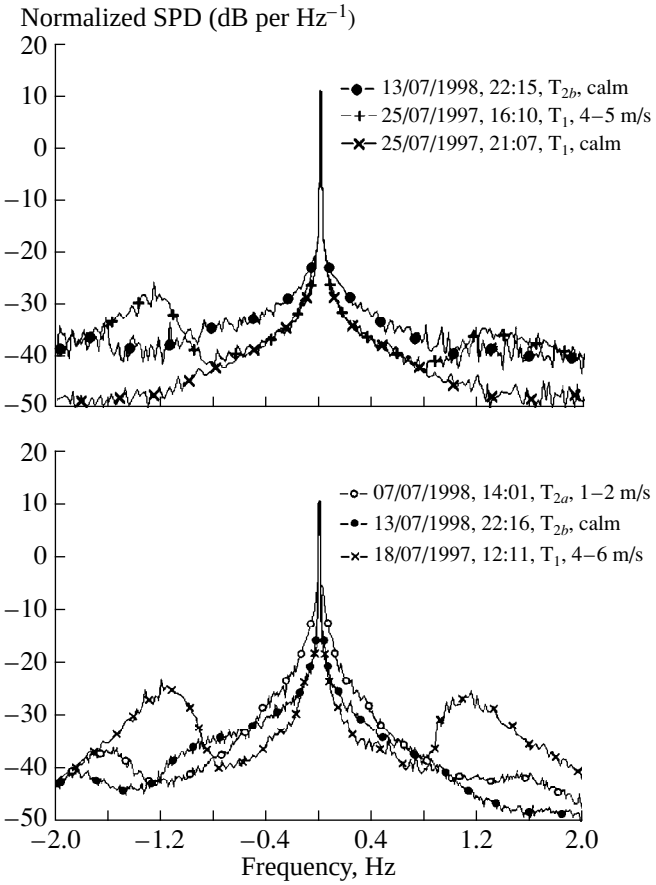

Fig. 5. Examples of normalized SPD averaged over the hydrophones of (a) the vertical and (b) the horizontal arrays: frequency 2.5 kHz; the date and time of the record beginning, the track, and the wind speed are shown in the plot.

with the frequency resolution 2–3 MHz for the same carrier frequency 2.5 kHz. The SPD were determined by averaging the records from all 64 hydrophones for each array over ~15 min intervals with the use of the Hanning window. Since the fluctuations observed have a multiplicative character, in order to exclude the dependence of the estimate on the radiated signal level and the size of the analyzing window (for $f \neq 0$), the normalization was performed by the integrated power, i.e.,

$$W^{(norm)}(f) = W(f)\left[\int_{-F_s/2}^{F_s/2} W(f)df\right]^{-1},$$

where F_s is the sampling frequency.

It is convenient to compare the normalized SPD, with allowance for the frequency band occupied by the diffracted signal $\overline{W^{(norm)}}$, with the dimensionless ratio R of the intensities of the diffracted and direct signals (see below). Since, as mentioned above, the direct signal fluctuations are the main interference for singling out the diffracted signal, then the comparison of $10\log\overline{W^{(norm)}}$ and $10\log R$ allows one to judge the signal-to-noise ratio (SNR) in the experiment. The analysis of the SPD for different tracks, wind speeds, etc., showed the presence of a low-frequency component close to the zero frequency with the rate of decay $\sim f^{-1\ldots2}$ and peaks in the vicinity of frequencies 1.0–2.0 Hz, which are related to the wind-induced waves. The same features (the presence of the low-frequency component and wind-induced peaks) are typical of stationary tracks in a shallow sea (see, e.g., [12]), although the parameters characterizing the SPD are different in the sea and the lake. For example, the peaks corresponding to the sound scattering by the rough surface in the lake are localized in a more high-frequency region due to the fact that wind-induced waves are not fully-developed ones. In spite of such distinctions, the fact itself of the presence of the ambient noise background (fluctuations) in the lake allows one to test different algorithms of signal processing under the lake conditions and, with some corrections, to extrapolate the results to sea conditions.

As a model of a diffracted signal $P_d(t)$ for matched processing in the case of a single receiving element of the VA or HA, we [3] suggested using the following expression

$$P_d(t) = A_d S_d(t - t_c),$$
$$\text{where } S_d(t) = \Phi\left(\frac{t}{T_d}\right)e^{i\gamma t^2}. \quad (1)$$

Here, A_d is the time-independent amplitude of the diffracted signal, which is proportional to the direct signal amplitude A_0 (see below); t_c is the time when the scatterer intersects the track OA (see Fig. 1); and the function $\Phi(x)$ describes the normalized directional pattern of the scattered field (for the scatterer of the rectangular form, $\Phi(x) = \sin\pi x/\pi x$). The parameters T_d and γ characterizing the duration of the diffracted signal and the rate of change of the Doppler frequency shift are described by the expressions

$$T_d = \frac{2\pi h}{\kappa l v}, \quad \gamma = \frac{\kappa v^2}{2h}, \quad (2)$$

where $h = r_1 r_2/r$; r_1 = OS, r_2 = SA (see Fig. 1); $r = r_1 + r_2$ is the acoustic track length; $v = v_s\cos\alpha_s$ and $l = l_s\cos\alpha_s$, where v_s and l_s is the speed and length of the scatterer, respectively, and α_s is the angle between the normal to the track and the scatterer trajectory; and κ is a mean wave number lying within the interval $\kappa_1 < \kappa < \kappa_m$, where κ_m ($m = 1, 2, \ldots, M$) is the wave number of the mth mode. Expression (1) was obtained in the paraxial approximation for sufficiently shallow angles $\sim v T_d/2r_2$, $v T_d/2r_1$.

For the HA, the model of a space–time diffracted signal can be constructed on the basis Eq. (1) [5] in the framework of the same approximations:

$$P_d(x, t) = A_d S_d\left(t - t_c - \frac{x}{v_a}\right)e^{-i\kappa x\sin\alpha_0}, \quad (3)$$

where x is the coordinate along the array ($x = 0$ is in the center of the array), α_0 is the source bearing, and

$$v_a = v\frac{r}{r_1\cos\alpha_0}.$$

The models presented above disregard the multimode behavior of the sound propagation and operate with some average wave number,[4] which makes these models stable with respect to the incompleteness of *a priori* data on the channel. For the VA, a model of the space–time diffracted signal $P_d(z, t)$ (z is the current depth of the receiving elements) cannot be constructed in the framework of such an approximation. Although in a number of problems, the modal expansions for a plane-layered medium (see, e.g., [15]) were used in the processing, it is known that such representations are very critical to the accuracy of *a priori* data on the sound velocity profiles, the bottom parameters, the invariability of the sea depth along the acoustic track, etc. It is most simple to assume that *a priori* data on the vertical structure of the diffracted field are absent. In this case, as a model for the VA, we can take the expression $P_d(z, t) = A_d(z)S_d(t - t_c)$, where $A_d(z)$ is an unknown complex function of depth z.

The statistical models of the diffracted signal can be developed with allowance for a frequency band occupied by this signal. The bandwidth of the spectrum given by Eq. (1) equals $\pm\Delta f_d$, where $\Delta f_d \sim v/l$, provided that $h \gg \kappa l^2$ (in this case, for the LFM-like signal (1), the bandwidth is determined by the frequency deviation γ). At the same time, as follows from Fig. 6, most intense fluctuations of the direct signal together with the coherent component are concentrated in a rather narrow spectral interval in the vicinity of the zero frequency and can be suppressed with the use of a high-pass filter (HPF), provided that the cutoff frequency of the HPF is $f_1 \ll \Delta f_d$; i.e., the diffracted signal is only slightly distorted after filtering. Thus, the received and filtered signal $P^{(F)}(t)$ can approximately be written as

$$P^{(F)}(t) \simeq P_d(t) + \Delta P_0(t), \quad (4)$$

where $\Delta P_0(t)$ represents the residual fluctuations of the direct signal, which now can be considered as a random stationary process with the zero mean[5] and consider Eq. (4) as a classical statistical model involving the additive mixture of the diffracted signal P_d of the known form with several unknown parameters (the time of crossing, the speed, etc.) and the interference ΔP_0. It is well known that for such a model, the optimal procedure is constructed on the basis of the consistent (correlation) processing with the use of models (1)–(3).

Since the described models of the diffracted signal are a very rough approximation of the waveguide propagation, there is a need in the experimental testing of their correspondence to the real diffracted signals, since considerable deviations reduce the efficiency of the consistent processing. The direct testing, i.e., the experimental observation, for example, of the temporal dependence $P_d(t)$ and its comparison with Eq. (1) is not possible because of the smallness of the diffracted component compared to the residual fluctuations of the direct signal. Although, after HPF, the diffracted component was noticeable in some records, the low signal-to-noise ratio (SNR) did not allow estimation of the diffracted signal profile. Therefore, several indirect exper-

[4] In a plane-layered medium, P_d represents M^2 terms of the form of Eq. (1) with various combinations of the wave numbers $\kappa_{m'}$ and $\kappa_{m''}$ (see, e.g., [14]).

[5] Naturally, in a random inhomogeneous waveguide, both the direct and diffracted signals will fluctuate; moreover, the diffracted signal fluctuations have, in a sense, a multiplicative character; for example, a change in the amplitude and phase of the radiated signal causes the same changes in the diffracted signal. However, expression (4) assumes that the fluctuating components of both signals are much less (approximately by the same factor) than the regular components; in this case, one can neglect the fluctuating component of the diffracted signal due to the smallness of the diffracted signal compared to the direct signal.

imental methods were used to verify this correspondence.

First, in order to increase the SNR, according to Eq. (3), we used the coherent summation of the signals $P_n^{(F)}(t)$ received by the elements of the HA and passed through HPF with delays proportional to the coordinate x_n of the nth received element:

$$\hat{P}_d(t) = \frac{1}{N}\sum_{n=1}^{N} P_n^{(F)}\left(t + \frac{x_n}{v_a}\right)e^{i\kappa x_n \sin\alpha_0}, \qquad (5)$$

where N is the number of the elements of the HA. In general, model (1) agrees rather well with the experiment, which can be seen from Fig. 6a, where the estimate of $P_d(t)$ is given, as an example, for the screen of plastic foam. For the long cylinder, an interesting effect was revealed: the difference in time between the maximum in $|\hat{P}_d(t)|$ and the instant of the sign reversal of the first derivative of the phase; i.e., the maximum of the scattering pattern was oriented at some angle to the direction of the signal incidence.[6] For the short cylinder, this effect was also present, but it was less pronounced.

Second, for the experimental estimation of the mismatch between model (1) and the diffracted signal in a real shallow-water channel, an experiment was carried out for synthesizing the diffracted signal. To this end, the source of a cw signal was towed along the trajectory of the scatterer motion at the same depth. The signals were received by the hydrophones of the HA and VA, as well as by a separate hydrophone located close to the source that was used in the experiments with a real moving scatterer. The product of the signal received by every element of the array and that received by the separate hydrophone were subjected to the moving integration over time with a window $T = l/v$, where v if the speed of towing and l is the scatterer length. Thus, we experimentally imitated the Kirchhoff diffraction by a line (one-dimensional) scatterer l in length, which moved with the speed v in a real shallow-water channel (the reciprocity principle was used for determining the current source–scatterer transfer coefficient). Figure 6b shows an example of a synthesized diffracted signal. The correlation coefficients between synthesized signals and model (1) were within ~0.7–0.8 in the range 1.5–2.5 kHz.

The procedures of the selection of the diffracted signal and evaluation of its parameters in the framework of the above-mentioned model describing the forward scattering involved the method of incoherent accumulation over elements of the VA after matched temporal filtering [2, 3] and the method of space–time matched

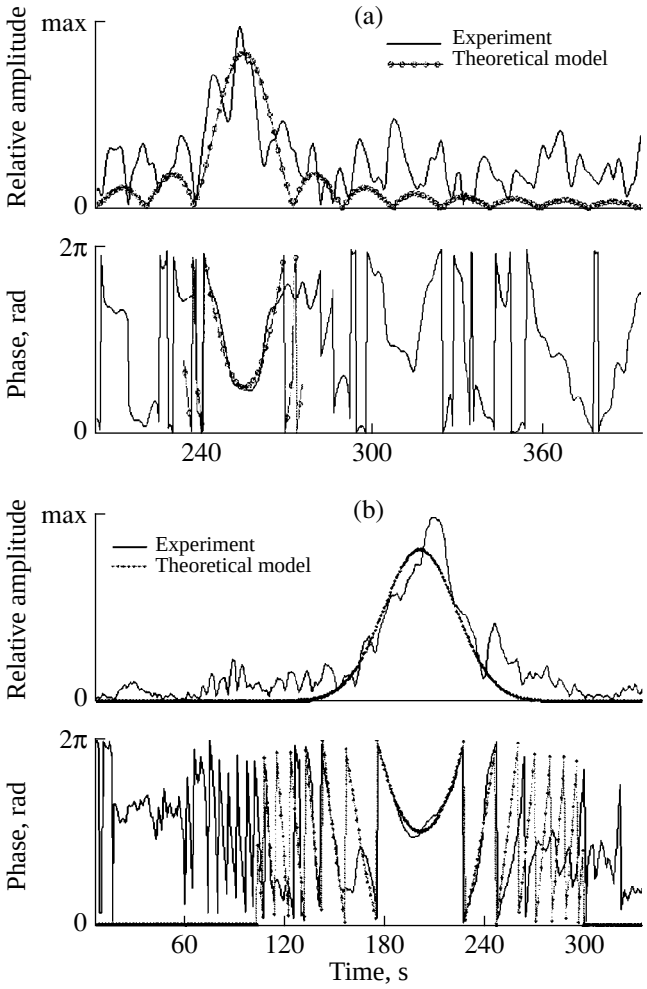

Fig. 6. Theoretical and experimental time dependences of the diffracted signals for (a) the screen of the foam plastic and (b) the synthesized scatterer.

filtering (STMF) for the HA [5]. In the first case, the temporal dependences $F_i(t)$ were constructed for every ith radiation frequency $F_i(t)$:

$$F_i(t) = \sum_{n=1}^{N} \frac{1}{A_{norm,\,i,\,n}}\left|\int P_{ni}^{(F)}(t')S_{d,\,i}^{*}(t'-t)dt'\right|, \qquad (6)$$

where A_{norm} is the normalizing factor independent of time. These dependences have a sharp peak of width $\sim\Delta f_d^{-1}$ at the instant of intersection, $t \simeq t_c$. In the second case, the temporal dependences $F_i(t)$ were constructed as

$$F_i(t) = \frac{1}{A_{norm,\,i}} \times \left|\int\left\{\sum_{n=1}^{N} P_{ni}^{(F)}\left(t' + \frac{x_n}{v_a}\right)e^{i\kappa_i x_n \sin\alpha_0}\right\}S_{d,\,i}^{*}(t'-t)dt'\right|. \qquad (7)$$

[6] The reason is likely to be in the features of diffraction by the elastic shell of the cylinder: its diameter was comparable with the sound wavelength, while the Kirchhoff approximation demands that it be much greater than the wavelength; moreover, the cylinder was composed of different sections, which made the parameters of its shell inhomogeneous.

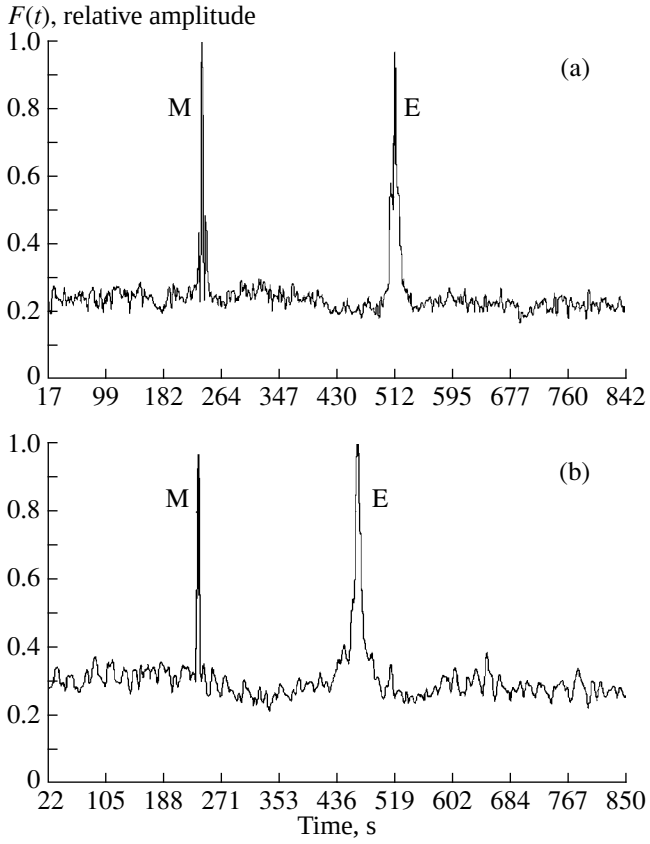

Fig. 7. Examples of the application of procedure (6) for the processing of experimental (E) and model (M) diffracted signals for the VA (track T_1, frequency ~3 kHz): (a) long cylinder, averaging over four frequencies; (b) short cylinder, averaging over five frequencies.

The outputs of the matched filters were averaged incoherently over frequencies: $F(t) = (1/I)\sum_{i=1}^{I} F_i(t)$; thus, we reduced the probability of the disappearance of the diffracted signal when the scatterer got into the sound field minimum with respect to the source or the receiver, and an increase in the output value of the SNR was achieved. Examples of such dependences for the VA and HA are shown in Figs. 7 and 8. Note that the theoretical estimates of the intensity ratio of the diffracted and direct signals $|A_d/A_0|^2$ on the basis of the relationships from papers [3, 4] yielded for our experiment –15…–25 dB for various types of scatterers, depths, and transmission tracks (the experimental estimates of this ratio are mainly in the same limits), while the normalized SDP of the fluctuations of the direct signal were –10…–20 dB in the frequency band of the diffracted signal ~±0.2 Hz (see Fig. 5), which characterizes the input SNR. After processing, the SNR was ~30 dB, as follows from Figs. 7 and 8; the corresponding gain was achieved due to the matched processing.

The third method to verify the efficiency of model (1) was as follows: into the experimental body of data, we introduced the parameters of a model diffracted signal; the parameters of the trajectory (the speed etc.) and the amplitude A_d were taken from the experimental data, while the instant of the intersection, t_c, was chosen so that the responses to the model and experimental diffracted signals did not overlap. As seen from Figs. 7 and 8, the amplitudes of the responses to the experimental and the model diffracted signals differ by 1–2 dB.

Procedures (6) and (7) were also used for the parameter estimation of the diffracted signal: for this purpose, the result of the application of Eqs. (6) and (7) was maximized over an unknown parameter, for example, the scatterer speed, v. Using Eq. (6), one can estimate three unknown parameters, for example, in our experiment, the instant of the intersection, the speed, and the scatterer length, while Eq. (7) allows one to estimate four parameters, for example, the instant of intersection, the speed (including the sign), the scatterer length, and the distance to the intersection point. As an example, Fig. 9 exhibits the dependences of the scattering cross-section on the speed (including its sign) and scatterer length (Eq. (6)) and on the speed and distance (Eq. (7)) at $t = t_c$.

Besides procedures (6) and (7) matched with the form of the diffracted signal at the instant of intersection of the transmission track, more simple methods of processing were also used. In particular, after preliminary filtering in the band $\Delta f = f_h - f_l$ (f_l and f_h are the lower and upper cutoff frequencies of the filter, respectively), the dependence of the signal on time and bearing $s = \sin\alpha$ was constructed for the HA [7]:

$$F(t_j, s) \sim \left| \sum_{n=1}^{N} P_{nj}^{(F)} e^{i\kappa x_n s} \right|,$$

where $P_{nj}^{(F)}$ are the time readings of the signal at the nth element of the HA after preliminary filtering, t_j is the time of the jth reading, and the number of the radiation frequency i is omitted. Figure 10 exhibits an example of such a dependence for the frequency $f_l > \Delta f_d$, i.e., for the case when the diffracted signal corresponding to the forward scattering was considerably suppressed. It can be seen from Fig. 10 that the trajectory of the scatterer motion is quite clearly traced both before and after the time of the track intersection; i.e., the diffracted signal is well observed in the region of the bistatic scattering.[7] In this region, the Doppler frequency shift appeared with the sign corresponding to the direction of the scatterer motion, to or from the track OA shown in Fig. 1. As a result, the spectrum of the diffracted signal was shifted to the left or to the right of the frequency range $\pm\Delta f_d$ corresponding to the forward scattering. Although the amplitude of the diffracted signal decreases significantly in the region of the bistatic scattering, the SPD

[7] In contrast to a classical scheme of the bistatic location, the source and the receiver were on different sides of the scatterer trajectory.

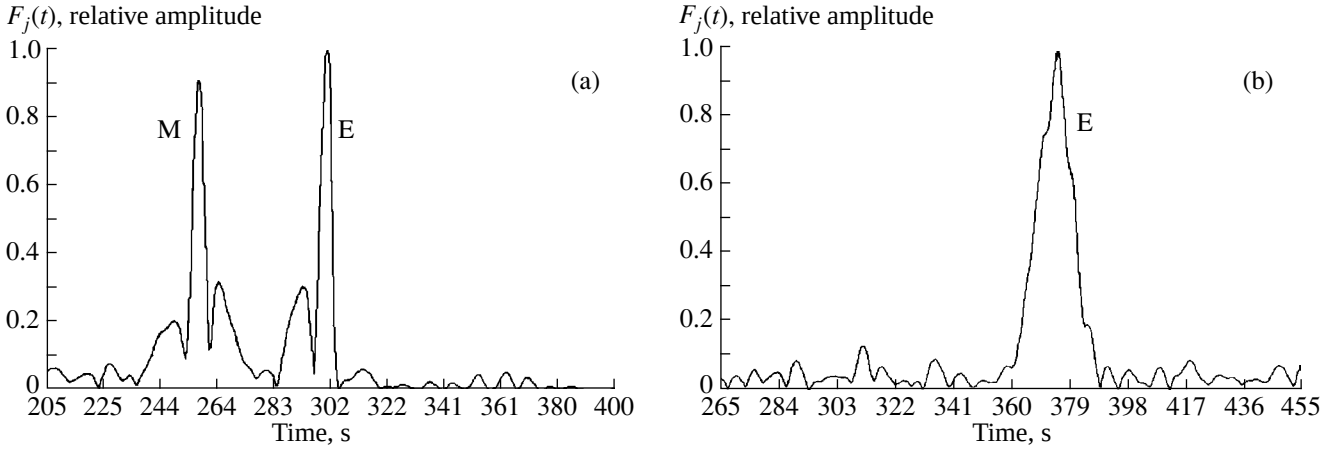

Fig. 8. Examples of the application of procedure (7) for the processing of experimental (E) and model (M) diffracted signals for the HA: (a) track T_{2b}, short cylinder, frequency 2.40 kHz; (b) track T_1, long cylinder, frequency 1.98 kHz.

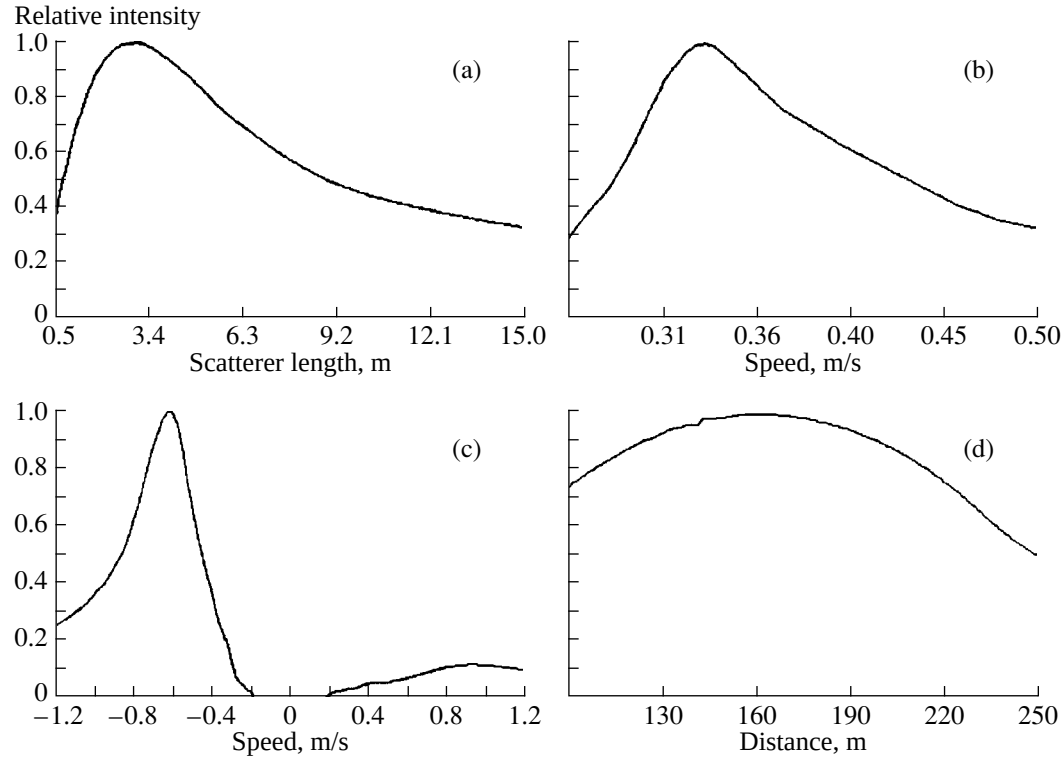

Fig. 9. Dependence of the intensity $F^2(t_c)$ (Eq. (6)) on (a) the scatterer length l and (b) the speed v for the VA (frequency ~3 kHz, track T_1, short cylinder 2.5 m in length, speed of motion 0.34 m/s, incoherent averaging over five frequencies) and the dependence of the intensity (Eq. (7)) on (c) the speed and (d) the distance r_2 for the HA (track T_{2b}, short cylinder moving with a speed of –0.68 m/s and intersecting the track at the distance $r_2 \simeq 150$ m, incoherent averaging over five frequencies in the range 2.0–2.5 kHz).

of the direct signal fluctuations also decreases, as follows from Fig. 5. This fact is the reason of the successful observation of diffraction in the region of the bistatic scattering.

The simplest model of the diffracted signal in this region is the "scattering point." In the framework of this model, if a multimode character of the wave propagation is neglected, the diffracted signal received by the HA in the region of the bistatic scattering can be written as

$$P_d(x, t) \sim e^{i\kappa[r_1(t-t_c)+r_2(t-t_c)]-i\kappa x s(t-t_c)}, \qquad (8)$$

where $r_1(t)$ and $r_2(t)$ are the current distances between the source and the scatterer and between the scatterer and the center of the HA; $s(t)$ is the sine of the current bearing of the scatterer; and the time dependences $r_1(t)$,

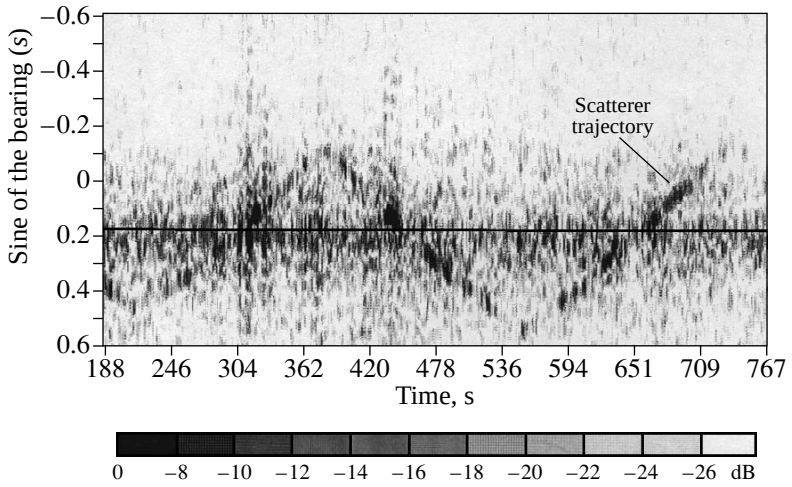

Fig. 10. Example of the reconstruction of the scatterer trajectory as a function of time and bearing in the processing of a signal from the HA after the suppression of the lower frequencies in the range $|f| < 0.3$ Hz and the upper frequencies $|f| > 0.6$ Hz; $s = \sin\alpha$. The horizontal line shows the stationary source bearing ($\sin\alpha_0 = 0.18$). The figure exhibits the second, third, and fourth intersections of the stationary track T_{2b} by the short cylinder; the frequency 2.4 kHz.

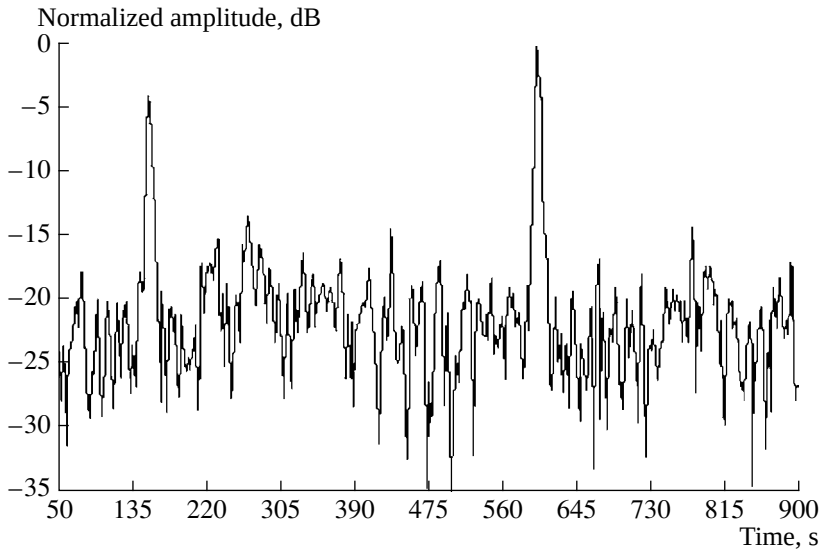

Fig. 11. Time variation of the output of a space–time matched filter in the case of the separation of the diffracted signals in the region of bistatic scattering: HA, track T_{2a}, frequency 2.5 kHz, short cylinder. Two peaks in the plot correspond to two intersections of the stationary track in the same direction.

$r_2(t)$, and $s(t)$ are found from elementary geometric considerations. With allowance for Eq. (8), a space–time matched filter was constructed; its output as a function of time is shown in Fig. 11. As follows from Fig. 11, the diffracted signal correlates well with model (8); the output value of the SNR is close to that of the filter matched with the signal scattered forward (see Fig. 8).

Thus, the preliminary analysis leads to the following conclusions:

(i) The propagation and scattering of acoustic signals under lake conditions at frequencies of the order of units of kilohertz in many respects is similar to that observed in a shallow sea at frequencies from ten to several hundreds of hertz (some differences in the statistical characteristics of fluctuations can easily be taken into account); thus, the fundamental possibility to test various schemes of remote diagnostics of the inhomogeneities under lake conditions is demonstrated, which reduces the cost of the tests;

(ii) The previously developed simplified model of the diffracted signal in the region of the forward scattering and the estimates of the diffraction levels are in good agreement with the experimental data obtained in

the multimode sound propagation, at least, for distances $\sim K \times 500$ m, where $K \sim 10^1$;

(iii) With a suitable procedure of the received signal processing, the diffracted component is clearly observed in the region of the bistatic scattering, which allows one not only to detect the fact of the intersection of the stationary transmission track by an inhomogeneity, but to carry out a trajectory evaluation as well.

The body of the experimental data obtained in our experiment is several Gbytes; the processing and the analysis of these data is continued, and we hope to obtain new results, which will be presented in subsequent publications.

ACKNOWLEDGMENTS

We are grateful to A.V. Lebedev and M.A. Raevskiĭ for the discussions on the sound propagation; to A.Ya. Balalaev, V.V. Bredikhin, V.A. Laukhin, V.V. Papko, V.V. Pikalev, A.I. Potapov, V.A. Tyutin, A.V. Tsiberev, and A.C. Chashchin for their participation in the experiments and in the construction of the equipment; and to G.N. Balandina, O.N. Kemarskaya, and G.E. Fiks for their participation in the data processing.

This work was supported by the Russian Foundation for Basic Research, project no. 99-02-16401.

REFERENCES

1. S. M. Gorskiĭ, V. A. Zverev, *et al.*, Akust. Zh. **34**, 55 (1988) [Sov. Phys. Acoust. **34**, 29 (1988)].
2. S. M. Gorskiĭ, V. A. Zverev, A. L. Matveev, and V. V. Mityugov, Akust. Zh. **41**, 223 (1995) [Acoust. Phys. **41**, 190 (1995)].
3. V. A. Zverev, A. L. Matveev, and V. V. Mityugov, Akust. Zh. **41**, 591 (1995) [Acoust. Phys. **41**, 518 (1995)].
4. V. A. Grigor'ev and V. M. Kuz'kin, Akust. Zh. **41**, 410 (1995) [Acoust. Phys. **41**, 359 (1995)].
5. V. I. Turchin, Preprint No. 416, IPF RAN (Inst. of Applied Physics, Russian Academy of Sciences, Nizhni Novgorod, 1996).
6. V. V. Borodin and M. Yu. Galaktionov, in *Formation of Acoustic Fields in Oceanic Waveguides*, Ed. by V. A. Zverev and A. I. Khil'ko (Inst. of Appl. Phys., Russ. Acad. Sci., Nizhni Novgorod, 1998), Vol. 2, pp. 259–355.
7. V. A. Zverev, Akust. Zh. **46**, 75 (2000) [Acoust. Phys. **46**, 62 (2000)].
8. A. B. Gershman, V. I. Turchin, and V. A. Zverev, IEEE Trans. Signal Process. **43** (10), 2249 (1995).
9. S. S. Zelitinkevich, *Penetrating Turbulent Convection* (Valgus, Tallinn, 1989).
10. A. N. Barkhatov, *Modeling of Sound Propagation in the Ocean* (Gidrometeoizdat, Leningrad, 1982).
11. A. L. Matveev and V. V. Mityugov, *A Report on the 7th Cruise of the Sergeĭ Vavilov Research Vessel* (General Physics Inst., USSR Acad. Sci., Moscow, 1990), Chap. 7.
12. B. G. Katsenel'son and V. G. Petnikov, *Acoustics of a Shallow See* (Nauka, Moscow, 1997).
13. V. A. Eliseevnin, Akust. Zh. **29**, 44 (1983) [Sov. Phys. Acoust. **29**, 25 (1983)].
14. S. M. Gorskii, V. A. Zverev, and A. I. Khilko, in *Formation of Acoustic Fields in Oceanic Waveguides*, Ed. by V. I. Talanov and V. A. Zverev (Inst. of Applied Physics, Russ. Acad. Sci., Nizhni Novgorod, 1995), pp. 63–80.
15. K. Yoo and T. C. Yang, J. Acoust. Soc. Am. **104**, 3326 (1998).

Translated by Yu. Lysanov

Acoustical Physics, Vol. 47, No. 2, 2001, pp. 194–201. Translated from Akusticheskiĭ Zhurnal, Vol. 47, No. 2, 2001, pp. 238–245.

REVIEWS

Particular Features of the Acoustic Wave Propagation in Condensed Media in Different Conditions

S. V. Krivokhizha, I. L. Fabelinskiĭ, and L. L. Chaĭkov

Lebedev Physical Institute, Russian Academy of Sciences, Leninskiĭ pr. 53, Moscow, 117924 Russia

Received June 12, 2000

Abstract—The light spectrum of molecular scattering is used for studying the particular features of the hypersound propagation in a guaiacol–glycerol binary solution with two critical points. The kinetics of the spectrum of scattered light in liquid salol is studied when the viscosity of the latter varies over ten orders of magnitude. Acoustic singularities are revealed in the critical region at the phase transition and at a large viscosity. © *2001 MAIK "Nauka/Interperiodica".*

INTRODUCTION

Acoustic waves are interpreted in this paper as elastic oscillations of particles of a medium, these oscillations propagating with the speed of sound and transferring energy without any mass transfer. The frequencies of acoustic waves existing on the Earth span from 0 Hz[1] to the boundaries of the Debye spectrum, 10^{13} Hz [1]. The part of sound that is perceived by human ear occupies the interval of acoustic frequencies from 16 to 20000 Hz, which constitutes only one ten-billionth (10^{-10}) part of the whole acoustic range.

Low-frequency sound or infrasound (0–16 Hz), as well as high-frequency ultrasound (10^6–10^9 Hz) and hypersound (10^9–10^{13} Hz) (this classification is purely conditional), are widely used for scientific and technological purposes.

The utilization of acoustic waves of different frequencies for scientific purposes calls for finding an adequate method of recording the sound interaction with the phenomenon under investigation and a possibility to retrieve the desired information from the obtained records.

Below, we present some new results concerning the interaction of longitudinal and transverse sound resulting from the pressure fluctuation ΔP and the fluctuation of anisotropy $\Delta\xi_{ik}$. As is known, fluctuations of different thermodynamic quantities such as pressure ΔP, entropy ΔS or temperature ΔT, and concentration ΔC, as well as the fluctuation of such a nonthermodynamic quantity as anisotropy $\Delta\xi_{ik}$, occur as a result of the thermal chaotic motion of atoms or molecules of a medium. The fluctuations of entropy, pressure, concentration, and anisotropy are independent of one another.

We note that such fluctuations as the fluctuations of pressure, entropy or temperature, and concentration do not affect the isotropy of the medium. This means that the light scattered due to such fluctuations is always linearly polarized, the electric vector of the scattered light wave being directed perpendicularly to the scattering plane, independently of the polarization or depolarization of the excitation light.

Pressure fluctuations arising at any point of a body cannot stay there but travel along the body with the sound velocity. Any fluctuation arises and vanishes at any place and time thus filling constantly the whole volume of the body.

Einstein provided a method for calculating the thermodynamic fluctuations [2].

Two years later, Debye [1], while developing the Einstein theory of heat capacity of solids, assumed that 3N degrees of freedom of coupled atomic oscillators of a solid have to be treated as 3N normal elastic waves [here, N is the total number of particles (atoms and molecules) in the whole sample]. Thus Debye [1] treats the energy of thermal motion of particles of a solid as the energy of elastic waves. From this point of view, fluctuations are the result of a superposition (interference) of Debye elastic waves. We also can consider the Debye elastic waves as the Fourier components of the fluctuation, as was done earlier by Einstein [2] and Mandel'shtam [3]. We extend this approach to any condensed medium where the mean free path $\bar{l}$ is much less than the light wavelength λ($\bar{l} \ll \lambda$).

Therefore, in a solid, we have 3N elastic waves, where N is a great number and the thermal elastic waves have different frequencies within the aforementioned interval and different directions. At first glance, it seems impossible to separate a single wave and conduct all necessary investigations with it. Luckily, this is not the case, and it turns out to be possible to separate

[1] Here we consider sound of zero frequency as sound with the wavelength equal to the linear dimensions of the globe, 1.2×10^9 cm, and with the speed of sound being different at different depths; however, if we assume the latter to be equal to 5×10^5 cm/s, we obtain that the zero frequency corresponds to $f_{\min} \sim 5 \times 10^{-4}$ Hz.

any of these waves and study its behavior in the physical phenomenon under investigation.

However, we first need a technique for separating a preset thermal elastic wave.

THERMAL SOUND AND ITS CHARACTERISTICS

Let us direct a beam of light with the wavelength λ at the sample of the continuous medium under investigation ($\bar{l} \ll \lambda$) in which the aforementioned great number of Debye waves are "crowded." In such conditions, there are always some waves with the wave vectors $+\bar{\mathbf{q}}$ and $-\bar{\mathbf{q}}$, where $|\bar{\mathbf{q}}| = \frac{2\pi}{\Lambda}$. Here, Λ is the sound wavelength. The superposition of such waves gives rise to a standing wave. Light incident on such a standing wave is diffracted by it as by a diffraction grating. The direction of the diffracted light is determined by the Bragg condition

$$2n\Lambda\sin\frac{\theta}{2} = \lambda, \tag{1}$$

where n is the refraction index and θ is the angle between the propagation directions of the excitation light and the diffracted light.

From Eq. (1), it follows that it is possible to separate the sound waves with the minimal wavelength $\Lambda_{min} = \lambda/2n$ at $\theta = 180°$, and, for $\theta = 0$, with the wavelength $\Lambda_{max} \cong \infty$ (conditionally, $\Lambda \cong 10^9$ cm).

The time variation of the density in a standing sound wave modulates the scattered light at the frequency of the elastic wave $f = \frac{V}{\Lambda}$, where V is the sound velocity. Such a modulation gives rise to discrete components in the spectrum of scattered light. These are the Mandel'shtam–Brillouin components shifted with respect to the central (Rayleigh) line by $\Delta\omega$. The latter quantity is determined from the sound frequency and Eq. (1):

$$\pm\Delta\omega = \pm 2\pi f = 2n\frac{V}{C}\omega\sin\frac{\theta}{2}. \tag{2}$$

Here, C and ω are the light velocity and frequency, respectively. Thus, two shifted Mandel'shtam–Brillouin components appear in the spectrum of molecular scattering. From their positions and from Eq. (2), it is possible to determine the velocity V. The shape of the shifted line is determined by the form of the function modulating the scattered light. Such a function is determined by the law of the fluctuation variation with time.

The time dependence of the pressure fluctuation in a medium with losses is determined by the solution of the Navier–Stokes equation, while the fluctuations of the entropy and concentration are determined by the solution of the Fourier equation. The problem is treated in detail in the literature [4–6], and here we present the final result of the calculation of the intensity distribution in frequencies, $I(\omega)$, for the Mandel'shtam–Brillouin components:

$$I(\omega) = I_{ad}\frac{(2/\pi)\delta\Omega^2}{(\omega^2 - \Omega^2)^2 + 4\delta^2\omega^2}. \tag{3}$$

Here, I_{ad} is the integral intensity of light scattered by adiabatic fluctuations, δ is the attenuation coefficient of sound, and Ω is the sound frequency.

The total width of the Mandel'shtam–Brillouin component at the half of its maximal intensity is

$$\delta\omega = 2\delta = 2V\alpha, \tag{4}$$

where α is the amplitude attenuation coefficient of sound. One can also see from the theory that α is determined by the shear and bulk viscosities and the heat conductivity:

$$\alpha = \frac{q^2}{2V\rho}\left[\frac{3}{4}\eta + \eta' + \frac{\kappa}{C_p}(\gamma - 1)\right]. \tag{5}$$

Here η, η', κ, γ, and ρ are the shear and bulk viscosities, the heat conductivity coefficient, ratio of the heat capacity at constant pressure to the heat capacity at constant volume, and the density, respectively. Thus, investigation of the light spectrum of molecular scattering provides an opportunity to determine all basic characteristics of an acoustic wave.

The absorption coefficient α (Eq. (5)), as well as the sound velocity (Eq. (2)), can be obtained for any acoustic wave with the wavelength that can vary according to Eq. (1) from the minimal one equal to $\Lambda = \frac{\lambda}{2n}$ (for ordinary liquids, Λ is approximately three times less than the wavelength of the excitation light) to the maximal Λ that is not limited fundamentally, but in practice it is difficult to realize the angles $\theta \sim 0$ because of the proximity to the excitation light, and, therefore, one has to choose $\theta \neq 0$ in an experiment. A typical intensity distribution in the spectrum of molecular scattering is shown in Fig. 1.

In this paper, we consider the cases of the propagation of ultrasound and hypersound in the critical region at phase transitions in binary liquid solutions when two critical points are present and the case of a transverse hypersonic wave propagating in a medium where the shear viscosity varies over a wide range.

VELOCITY AND ATTENUATION OF SOUND IN THE CRITICAL REGION

Experimental and theoretical studies of phase transitions in various media have always been important and remain topical now. The study of such a substance as Rochelle salt, which has two Curie critical points (the higher point at a temperature of 24°C and the lower point at a temperature of –18°C) was of special interest.

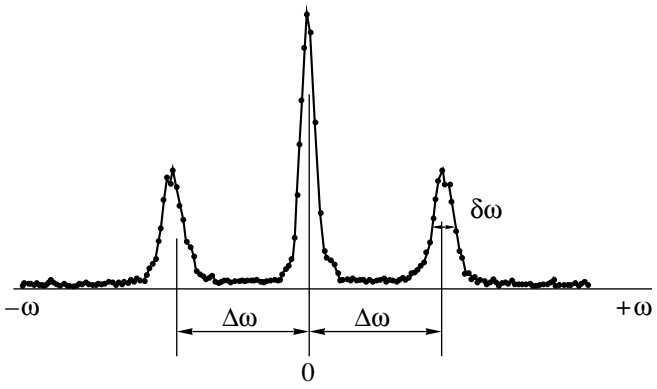

Fig. 1. Typical spectrum of molecular scattering of light: $\pm\Delta\omega$ ($=\pm 2\pi f$) is the shift of the Mandel'shtam–Brillouin components with respect to the central (Rayleigh) line; the shift is determined by the sound velocity, the light frequency, and the scattering angle θ (Eqs. (2) and (3)); $\delta\omega$ is the half-width of the Mandel'shtam–Brillouin component; its value is determined by the absorption coefficient of the thermal sound waves (Eqs. (4) and (5)).

The temperature dependence of absorption in the vicinities of both Curie points in Rochelle salt at a frequency of 5×10^6 Hz was obtained for the first time by Yakovlev, Velichkina, and Baranskiĭ [7]. They observed a rapid growth of the sound absorption coefficient in the vicinities of both critical points. For a detailed investigation of the phenomenon, variations of the positions of the critical points with respect to temperature are necessary, which is connected with great difficulties of crystallographic character. Probably, this was the main reason why the problem was not developed further.

We studied samples of liquid binary solutions of guaiacol and glycerol, which have two critical points under certain conditions. The relative positions of the critical points can be varied easily and arbitrarily within a certain interval. Since the patterns of the second-order phase transitions that occur in various media have many common features, the results obtained by us are of a general character. They are suitable for discussing the critical phenomena accompanying phase transitions in general, and we hope that they will be useful for the development of the microscopic theory of phase transitions [8, 9].

However it turned out that our experimental study brought up more questions than the number of answers we expected to obtain while experimenting. The solution of the carefully purified guaiacol ($CH_3OC_6H_4OH$) and glycerol ($CH_2OHCHOHCH_2OH$) components is homogeneous over the whole temperature–concentration phase plane. However, if we add water to such a solution—one molecule of water per 25 molecules of the solution, or one molecule of CCl_4 per 180 molecules of the solution—a closed region or loop appears in the phase plane within which the solution is stratified (Fig. 2a). It is hard to imagine that the effect of so small a quantity of the third component leads to such radical changes in the solution properties. Most probably, the small quantity of the third component plays the role of a trigger (a trigger effect), but the mechanism of this effect remains to be studied. Two critical points appear in the loop in Fig. 2a. Their relative positions can be varied arbitrarily until they merge into a double critical point. One can see from the three-dimensional phase diagram that the higher and lower critical points form the upper and lower lines of critical points (Fig. 2b).

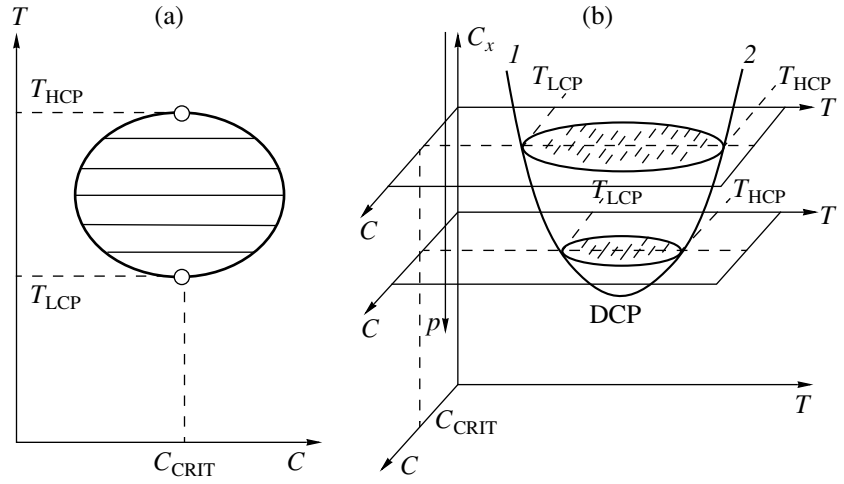

Fig. 2. Phase diagrams for a guaiacol–glycerol solution with a closed region of stratification in the temperature–concentration (T–C) coordinates: T_{HCP} is the temperature of the higher critical point, T_{LCP} is the temperature of the lower critical point, C_{CRIT} is the critical concentration, and $\Delta T = T_{HCP} - T_{LCP}$; the region of stratification is shown by hatching. (a) The two-dimensional diagram and (b) the three-dimensional phase diagram in the T–C–C_x coordinates (C_x is the concentration of the third component) with the lines of the (*1*) lower and (*2*) higher critical points.

VELOCITY AND ABSORPTION OF HYPERSOUND NEAR THE CRITICAL POINTS

Our experimental studies described above have demonstrated that both the critical index of the correlation radius and the purely outward phenomena like the critical opalescence are identical at the higher and lower critical points. However, the presence of the higher and lower critical points in one solution is not a common phenomenon. Therefore, it is necessary to study the behavior of various physical quantities (acoustic quantities in our case) in the region of the homogeneous solution above the higher critical point and below the lower critical point. We use the interference setup designed by us on the basis of a multipass Fabry–Perot interferometer and electronic recording of the spectrum with its subsequent processing by a personal computer. Figure 3 presents the results of measurements of the velocity of hypersound with the frequency $f \sim 10^{10}$ Hz and the results of its calculation by Eq. (4). The temperature dependence of the velocity is linear in both studied regions. The unusual feature is the big difference between the inclinations of the straight lines or the temperature coefficients of the velocity $\beta = dV/dT$: above the higher critical point, $\beta = -6.5$ ms^{-1} deg^{-1} and, below the lower critical point, $\beta = -11.5$ ms^{-1} deg^{-1}. This result is the evidence of the fact that the same solution is described by different equations of state on different sides of the critical points. Such a statement remains valid even when both critical points merge into one double critical point where $\beta_{DCT} = 0$. On different sides of the double critical point, the temperature coefficient of velocity differs almost by a factor of two. Since no chemical reactions occur in the solution, one can assume that the solution structure changes. A detailed study of the temperature dependence of the velocity of hypersound in the whole temperature interval reveals three different regions: above the higher critical point, where $\beta = -6.5$ ms^{-1} deg^{-1}; below the lower critical point, where $\beta = -11.6$ ms^{-1} deg^{-1}; and near the double critical point (within several degrees), where $\beta = 0$. The width of the Mandel'shtam–Brillouin component is determined by the sound absorption (Eq. (4)). Figure 4 shows the experimentally measured temperature dependence of the width of the Mandel'shtam–Brillouin component. The same dependence for the double critical point is presented in Fig. 5.

The behavior of the curves resembles that of the λ-curve of absorption in the case of the second-order phase transition in helium (He I to He II).

MEASUREMENT OF THE VELOCITY OF ULTRASOUND

The observed difference in the temperature coefficients of sound velocity and in the character of the curves of hypersound absorption given above can be explained in our opinion only by the difference between the structures above the higher critical point and below the lower critical point. Such a difference can be determined by the fact that molecular clusters are formed in different ways within different temperature intervals; or, alternatively, they are formed in one region, and the other region has nothing except for the Van der Waals forces and the hydrogen bond forces. If the linear dimensions of the clusters are of the same order of magnitudes as the acoustic wavelength, this should have some effect on the sound propagation. Apparently, in this case, the medium cannot be consid-

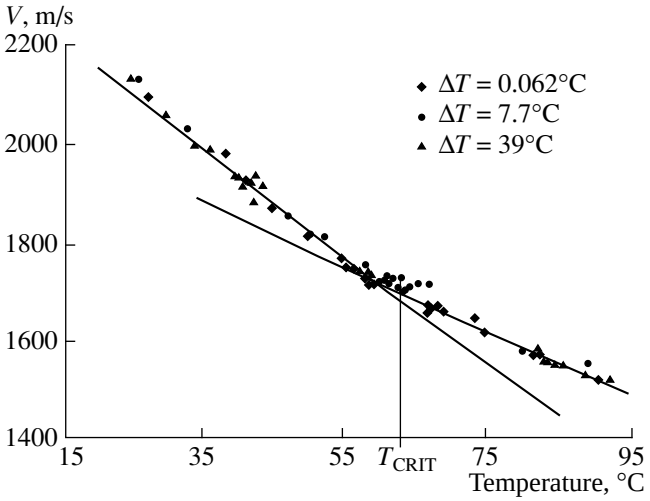

Fig. 3. Temperature dependence of the hypersound velocity V in guaiacol–glycerol solutions with different size of the stratification region ΔT: ΔT = (◆) 0.062, (●) 7.7, and (▲) 39°C. The straight lines show the mean experimental dependences. The temperature coefficient of the velocity, $dV/dT = \beta$, above the higher critical point is equal to –6.5 m s^{-1} deg^{-1}, below the lower critical point it is equal to –11.6 m s^{-1} deg^{-1}, and it remains such for all ΔT. In the immediate vicinity of the double critical point, within a narrow temperature range of ~5°C, $\beta = 0$.

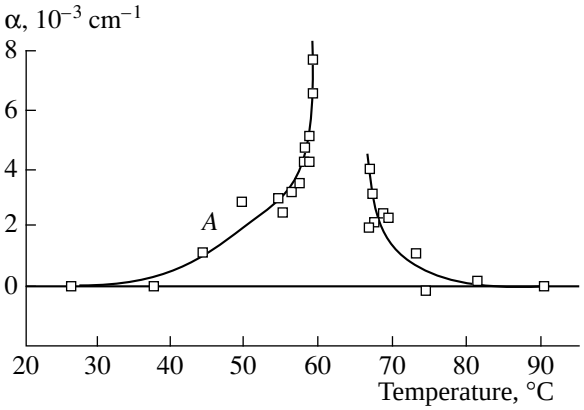

Fig. 4. Temperature dependence of absorption coefficient of hypersound α (in cm^{-1}) in a guaiacol–glycerol solution with ΔT = 7.7°C. The absorption in the absence of the third component is taken as zero. The absorption curve in the critical region has a λ-form.

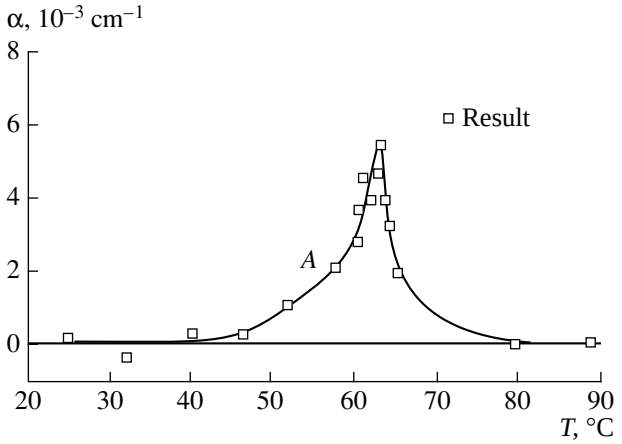

Fig. 5. Temperature dependence of the absorption coefficient α in cm^{-1} in the same solution as in Fig. 4 with ΔT = 0.062°C (almost the double critical point).

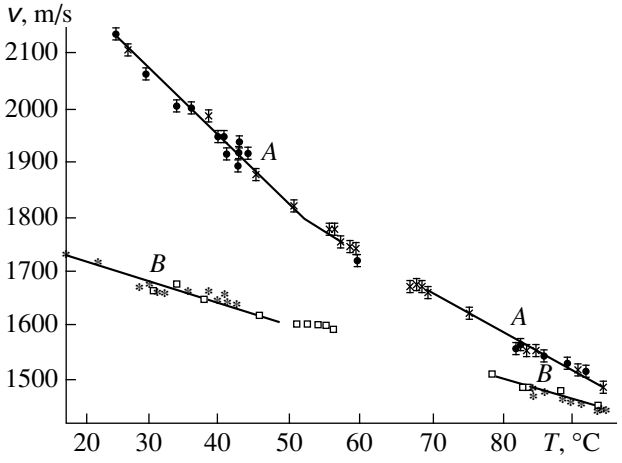

Fig. 6. Temperature dependence of the velocities of hypersound and ultrasound at ΔT = 7.7°C: straight lines *A* correspond to hypersound with the wavelength $\Lambda = 2.4 \times 10^{-5}$ cm and straight lines *B* correspond to ultrasound with the wavelength $\Lambda = 7.6 \times 10^{-2}$ cm. In the case of ultrasound, β is almost the same in both temperature regions and equal to -4 m s^{-1} deg^{-1}. The maximal dispersion of the sound velocity is 22% and decreases down to 4–2% with increasing temperature.

ered as continuous. By contrast, when the sound wavelength is greater than the linear dimensions of the clusters, the sound propagating in the medium will not "notice" the inhomogeneities, and this must also affect the characteristics of the medium. These considerations lead us to the necessity to measure the temperature dependence of the sound velocity in the same regions where we studied the propagation of hypersound, but this time using ultrasound with the frequency four orders of magnitude lower than the frequency of hypersound studied in the experiments presented in Fig. 3, namely, $f_{US} \cong 10^6$ Hz.[2] Ultrasound was generated by piezoelectric quartz, and the measurements were conducted using a special setup designed by us [5, 10]. The results surpassed our expectations. The experimental results demonstrated that, while the temperature coefficients of velocity for hypersound with the wavelength $\Lambda_{HS} \cong 2 \times 10^{-5}$ cm differ by a factor of two, no difference is observed in the temperature coefficients for $\Lambda_{US} \cong 7 \times 10^{-2}$ cm [11]. Figure 6 presents the temperature dependence of the velocity of ultrasound with the frequency 2.8×10^6 Hz on both sides of the critical points. The results obtained for hypersound (Fig. 3) are given in the same plot for comparison. It follows from these results that, in the case of ultrasound, β is the same in both regions, and it is equal to -4 ms^{-1} deg^{-1}. The fact that β is the same in both regions apparently means that $\Lambda \cong 0.1$ cm is greater than the linear dimensions of the expected clusters to such extent that this medium can be considered as homogeneous and continuous for the applied ultrasound. Hypersound with $\Lambda \cong 2 \times 10^{-5}$ cm presumably "feels" the inhomogeneity caused by the clusters, and the medium cannot be considered as continuous for this kind of sound.

It is well known that, if inhomogeneities in a medium are of the size ~0.1 λ, the intensity distribution in the scattering angle will be asymmetric (in the case of a noticeable difference between the refraction indexes). Our angular measurements of intensity showed that, for the angles 45° and 180°–45°, the intensity of the scattered light is the same. Therefore, the linear dimensions of inhomogeneities are less than λ/10. Thus, the question about the size of the clusters is still to be answered. One can notice a wide difference between the values of the sound velocity at ultrasonic and hypersonic frequencies, i.e., the dispersion of the sound velocity. The large dispersion of the sound velocity amounting to 22%, as well as the dependence of the sound velocity on temperature, is observed here for the first time (as far as we know).

If we use the simple version of the relaxation theory of sound propagation in condensed media by Mandel'shtam and Leontovich [12] as the basis, we can write the following expression for the dispersion of the sound velocity:

$$\Delta V = V_{HS} - V_{US}, \quad \text{and} \quad V = \frac{1}{2}(V_{HS} + V_{US}),$$
$$\Delta V/V = \frac{1}{2\rho V^2}\frac{\eta'}{\tau}. \tag{6}$$

Here, τ is the relaxation time of the bulk viscosity. A large value of $\Delta V/V$ means either a large η' or a small τ. The latter is unlikely taking into account the fact that the medium most probably has clusters. We believe that further investigation will give an answer

[2] Here, the subscripts HS and US mean hypersound and ultrasound, respectively.

to this question, as well as to other questions raised by this study.

TRANSVERSE SOUND WAVES AND THE RELAXATION PROCESS

Fluctuations of anisotropy can arise by virtue of their nature only in the case when the thermal chaotic motion occurs with anisotropic molecules or particles constituting the medium. As was mentioned in the introduction, the fluctuation of anisotropy is anisotropic, and, hence, the light scattered because of this fluctuation is depolarized. In the spectrum, this kind of scattered light represents a rather wide band, which extends for 100–150 cm^{-1} and even farther and is usually called the wing of the Rayleigh line. Starting from the discovery of this phenomenon in 1928 and till 1941, it was assumed that this band has a peak at the unshifted frequency. However, in 1967 it was demonstrated that the situation was not as simple [13].

The first quantitative theory of the phenomenon was developed by Leontovich [5, 14]. This theory took into account only one relaxation time of the anisotropy and was fairly complicated. Away from the unshifted frequency, the intensity distribution in frequency was described by the Lorentzian of the form

$$I(\omega) = \frac{\text{const}}{1 + \omega_0^2\tau^2}, \qquad (7)$$

where ω_0 is the frequency measured with reference to the frequency of the excitation light and τ is the relaxation time of the anisotropy. For evaluation purposes, we can assume that $\tau = \Phi\eta/k_B T$, where Φ is the volume of a molecule and k_B is the Boltzmann constant.

A general theory for any number of relaxation times was developed by Rytov [15, 6]. The experimental investigation of the spectra of depolarized scattered light was conducted using the same interference setup that was utilized for the study described above. Salol was selected as the medium for investigation, because its molecules have a large anisotropy and the substance itself can be supercooled and allows a viscosity variation over many orders of magnitude.

The scattered light was observed at an angle of 90°. A polarizer (a Glan prism) was positioned in the path of the scattered light in such way that the light scattered because of the fluctuations of anisotropy and pressure was completely eliminated. The observation and the measurement were conducted only for the depolarized light, I_{VH} (the electric vector of the scattered light lay in the scattering plane).[3] The spectra were recorded when the salol temperature varied from 19 to –70°C. Simultaneously, the viscosity η varied from 29 cP at 19°C to 10^{11} cP at –70°C.

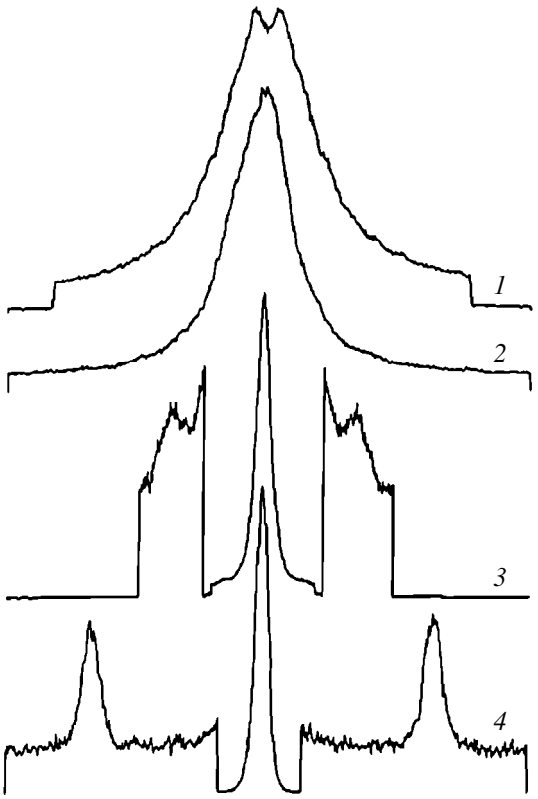

Fig. 7. Spectra of the depolarized scattering of light in salol: (*1*) a doublet structure with the minimum at the frequency of the excitation light in the temperature interval from +90 to +50°C; (*2*) a continuous spectrum of depolarized scattered light in the temperature interval from +50 to 20°C; (*3*) a spectrum of depolarized scattering of light at +19°C, where the doublet of the Mandel'shtam–Brillouin component appears at the wings of the central component; and (*4*) a triplet structure of the spectrum at the temperature –20°C.

The spectral records of the light scattered in salol at different values of temperature and viscosity are presented in Fig. 7. Spectrum *1* corresponds to the temperature interval from +90 to +50°C (the viscosity range from 2 to 7 cP). The fine structure of the Rayleigh line [13] is clearly visible. Spectrum *2* corresponds to the temperature interval from +50 to 20°C (the viscosity from 7 to 27 cP), the fine structure of the wing of the Rayleigh line is not observed. Spectrum *3* is obtained at the temperature 19°C (the viscosity is 29 cP). Spectrum *4* corresponds to the temperature –20°C. The Mandel'shtam–Brillouin components caused by a transverse wave are observed.

[3] The first index in the subscript shows the polarization of the excitation light and the second index corresponds to the polarization of the scattered light; *V* is the vector of the electric field of a light wave and is perpendicular to the scattering plane; and *H* lies in the scattering plane.

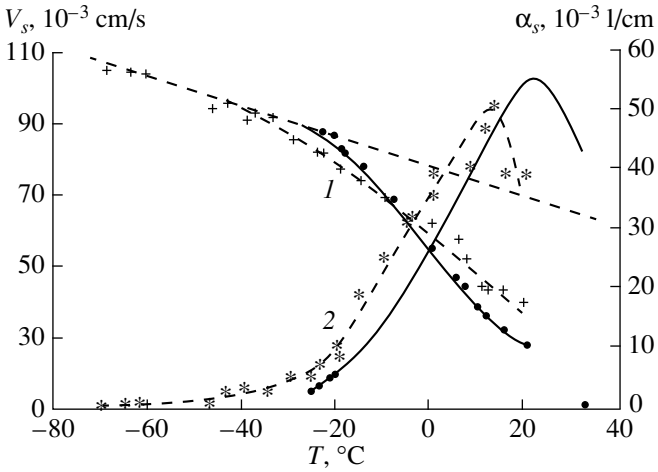

Fig. 8. Results of the experimental studies of (*1*) the transverse sound velocity ((+) the experimental points and (the solid curve) the calculation by the theory [17]) and (*2*) the absorption coefficient of hypersound ((∗) the experimental points and (the solid curve with a peak) the calculations by the theory [17]).

The results obtained by measuring the velocity of transverse sound and its absorption are presented in Fig. 8. In the temperature dependence of the transverse sound velocity (curve *1*), one can clearly distinguish two regions with $\frac{dV_s}{dT}$ = 6.25 ms^{-1} deg^{-1} in the interval from –34 to 19°C and $\frac{dV_s}{dT}$ = 3.3 ms^{-1} deg^{-1} in the interval from –70 to –34°C. Here, V_s is the velocity of transverse sound.

As far as we know, the velocity of transverse hypersound in salol had been studied earlier [13], while the width of the shifted depolarized components was measured by us for the first time [11].

To compare the results of our experiment with the theory, we used the formulas of the nonlocal relaxation theory [17].

The theoretical curves (Fig. 8) describe qualitatively the experimental results (the solid lines). We believe that the observed disagreement between theory and experiment is caused by the imperfection of the theory. We will study this problem further.

If we assume that the thermal Debye wave does not differ from the sound wave generated, e.g., by a quartz radiator of sound,[4] it becomes clear that the discrete Mandel'shtam–Brillouin components should not be observed, because the shear viscosity is too large.

If a half of the total half-width $\delta\omega/2 = \alpha_s V$ is equal to the distance between the orders (Eq. (2)), it is impossible to observe discrete lines, and the corresponding condition of absorption at the wavelength Λ is

$$\alpha_s \Lambda = 2\pi,$$

where α_s is the absorption of a shear wave.

It follows from hydrodynamics that, in the case under consideration, we have $\alpha_s\Lambda \gg 2\pi$ at low temperatures and the discrete Mandel'shtam–Brillouin components must not be observed.

They also must not be observed when the relaxation that occurs at high frequencies is taken into account. However, in our experiment, we observe clearly defined transverse Mandel'shtam–Brillouin components (Fig. 7).

In terms of $\alpha_s\Lambda$, we obtain that the maximal value is $\alpha_s\Lambda = 1.16$. For the temperature –10°C, we obtain $\alpha_s\Lambda = 0.6$, and the Mandel'shtam–Brillouin components are well pronounced.

A possible explanation for the observed discrepancy is that the molecular viscosity noticeably differs from the shear viscosity measured by a viscometer or by the macroscopic viscosity [18].

ACKNOWLEDGMENTS

This work was supported by the Russian Foundation for Basic Research, project no. 99-02-18483.

REFERENCES

1. P. Debya, Ann. Phys. (Leipzig) **39**, 789 (1912).
2. A. Einstein, Ann. Phys. (Leipzig) **33**, 1275 (1910).
3. L. I. Mandel'shtam, Ann. Phys. (Leipzig) **41**, 609 (1913); *Complete Works* (Akad. Nauk SSSR, Leningrad, 1948), Vol. 1, p. 246.
4. G. S. Landsberg, Usp. Fiz. Nauk **36**, 284 (1948).
5. I. L. Fabelinskiĭ, *Molecular Scattering of Light* (Nauka, Moscow, 1965; Plenum Press, New York, 1968).
6. I. L. Fabelinskiĭ, Usp. Fiz. Nauk **164**, 897 (1994).
7. I. A. Yakovlev, T. S. Velichkina, and K. N. Baranskiĭ, Zh. Éksp. Teor. Fiz. **32**, 935 (1957) [Sov. Phys. JETP **5**, 762 (1957)].
8. A. Z. Patashinskiĭ and V. L. Pokrovskiĭ, *Fluctuation Theory of Phase Transitions* (Nauka, Moscow, 1982).
9. L. D. Landau and E. M. Lifshits, *Statistical Physics*, 3rd ed. (Nauka, Moscow, 1976; Pergamon Press, Oxford, 1980), Parts 1 and 2.
10. S. V. Krivokhizha and I. L. Fabelinskiĭ, Zh. Éksp. Teor. Fiz. **50**, 3 (1966) [Sov. Phys. JETP **23**, 1 (1966)].
11. K. V. Kovalenko, S. V. Krivokhizha, and I. L. Fabelinskiĭ, Dokl. Akad. Nauk **333** (5), 603 (1993) [Phys. Dokl. **38** (12), 507 (1993)].

[4] In reality, the Debye wave does not decay in time and space [6], but the phase of such a wave is not constant and changes in time according to a certain law. In the case under consideration, the spectra of the scattered light are almost identical in both cases, and, therefore, we assume for the sake of simplicity that the Debye elastic wave does not differ from the wave generated artificially.

12. L. I. Mandel'shtam and M. A. Leontovich, Zh. Éksp. Teor. Fiz. **7**, 438 (1937).

13. V. S. Starunov, E. V. Tiganov, and I. L. Fabelinskiĭ, Pis'ma Zh. Éksp. Teor. Fiz. **65** (5), 371 (1967) [JETP Lett. **65**, 260 (1967)].

14. M. A. Leontovich, J. Phys. (Moscow) **4**, 499 (1941); *Selected Works* (Nauka, Moscow, 1985), p. 271.

15. S. M. Rytov, Zh. Éksp. Teor. Fiz. **58** (12), 2154 (1970); [Sov. Phys. JETP **31** (6), 1163 (1970)]; **59** (12), 2130 (1970) [**32** (6), 1153 (1970)].

16. L. M. Sabirov, V. S. Starunov, and I. L. Fabelinskiĭ, Zh. Éksp. Teor. Fiz. **60** (1), 146 (1971) [Sov. Phys. JETP **33** (1), 82 (1971)].

17. M. A. Isakovich and I. A. Chaban, Zh. Éksp. Teor. Fiz. **50** (5), 1343 (1966) [JETP **23** (5), 893 (1966)].

18. S. V. Krivokhizha and I. L. Fabelinskiĭ, Dokl. Akad. Nauk **350** (5), 612 (1996) [Phys. Dokl. **41** (10), 457 (1996)].

Translated by M. Lyamshev

Acoustical Physics, Vol. 47, No. 2, 2001, pp. 202–207. Translated from Akusticheskiĭ Zhurnal, Vol. 47, No. 2, 2001, pp. 246–252.

REVIEWS

Space–Time Acoustic Holography of Moving Inhomogeneities

A. L. Matveev, V. V. Mityugov, and A. I. Potapov

Institute of Applied Physics, Russian Academy of Sciences,
ul. Ul'yanova 46, Nizhni Novgorod, 603600 Russia
e-mail: matveyev@hydro.appl.sci-nnov.ru

Received May 10, 2000

Abstract—A method for observing weak diffraction responses on the background of a fluctuating signal from a primary cw source is developed and tested. The possibility to visually observe the dynamics of the secondary field caused by the presence of nonstationary perturbations of the water medium is demonstrated. © *2001 MAIK "Nauka/Interperiodica".*

INTRODUCTION

The method of element-by-element incoherent accumulation of signal responses at a vertical array showed its high efficiency for a noise-immune observation of moving underwater inhomogeneities and for measuring the parameters of their motion in a shallow-water sound channel. One of the important stages of the corresponding signal processing is the quasi-holographic temporal filtering based on the *a priori* theoretical predictions concerning the structure of the desired signal [1–3].

Along with the incoherent accumulation, it seems to be reasonable to use the space-coherence properties of the sound field recorded by a multielement vertical array [4]. In our previous publication [5], we already demonstrated the possibility to reconstruct the spatial distribution of the field and the position of a stationary cw source by using the principle of the wave front reversal realized by numerical computer methods. Similar studies were performed in full-scale conditions [6] and on the basis of computer simulations [7].

The transmission-shadow technique, which we used for the observation of weak diffraction signals, required the development of effective algorithms for the preliminary "subtraction" of the intense signal generated by a remote primary source. The signals remaining after such an operation are those produced by secondary sources, and these signals can also be visualized in the signal plane (the vertical plane that includes the array and the primary source) with the help of the coherent-numerical procedure of the wave front reversal. Below, it will be shown that the use of such an approach provides fuller hydrophysical information than simple localization of a compact inhomogeneity.

By combining the principles of temporal holography (matched filtering) and spatial holography (coherent wave front reversal), it is possible to indicate and localize with a higher contrast the episodes corresponding to the intersection of the signal plane by moving inhomogeneities.

THEORETICAL ANALYSIS OF COHERENT AND INCOHERENT METHODS OF EXTRACTING WEAK SIGNALS

In this section, we analyze the algorithms of extracting secondary signals as applied to different methods of their subsequent processing. We divide the primary signals received by the hydrophones of the array into the following three components. The first component is represented by the temporally constant signals from the primary source, which "illuminates" the underwater spatial region under study. Owing to the interference effects caused by the multimode character of sound propagation in the shallow-water sound channel, these signals considerably vary both in amplitude and in phase, depending on the depth of the receiving element.

The second component corresponds to the interference-related temporal fluctuations caused by the nonstationary propagation conditions (seiches, internal waves, or nonstationary underwater currents). Multiple experiments carried out in lakes and in sea conditions showed that the low-frequency spectral region of these fluctuations exhibits the properties of $1/f$-noise.

The third component is the desired signal itself, which represents the result of the diffraction shadowing of the primary source by a moving screen or related in some other way to the presence of acoustic inhomogeneities in the spatial region under study. In the lake experiments with a moving screen, the characteristic frequencies of the corresponding disturbances were found to vary from several hundredths to several tenths of a hertz.

The aforementioned time characteristics of the three listed components allow one to separate the signal of the primary source together with the most significant low-frequency part of noise fluctuations by way of a conventional moving averaging within time intervals about tens of seconds. Such a procedure will make it possible to eliminate these signals from the subsequent processing, while the structure of the desired signal will

practically remain unaffected. The next stage of signal processing is the matched filtering, which, in addition to the low-frequency noise suppression, will provide the suppression of high-frequency noise.

We denote the current complex amplitudes of the received signals by $x_k(t)$ (where k is the number of hydrophone in the vertical array) and use the conventional exponential representation

$$x_k(t) = X_k(t)\exp[i\varphi_k(t)], \quad (1)$$

where $X_k(t)$ and $\varphi_k(t)$ are the real amplitudes and phases, respectively. In the case under study, we can write

$$x_k(t) = x_{0k}(t) + \delta x_k(t), \quad (2)$$

where $x_{0k}(t)$ is the signal from the primary source together with the interference fluctuations and $\delta x_k(t)$ is the weak desired signal.

We calculate the first variation of representation (1):

$$\delta x_k(t) = [\delta X_k(t) + iX_{0k}(t)\delta\varphi_k(t)]\exp[i\varphi_{0k}(t)]. \quad (3)$$

In accordance with the processing procedure described above, we will identify the "unperturbed" values of the amplitude $X_{0k}(t)$ and phase $\varphi_{0k}(t)$ with the results of the moving averaging

$$\tilde{X}_k(t) = \int X_k(t')g(t-t')dt', \quad (4)$$

$$\tilde{\varphi}_k(t) = \int \varphi_k(t')g(t-t')dt' \quad (5)$$

with the use of the filter-window

$$g(t) = \begin{cases} \tau^{-1} & \text{for } |t| \le \tau/2 \\ 0 & \text{for } |t| > \tau/2. \end{cases} \quad (6)$$

In practice, the data of the full-scale and model lake experiments were processed by using the values of τ within 20–60 s.

Thus, for the subsequent processing, as a desired signal, we take the set of functions

$$\delta x_k(t) = [Y_k^{(a)}(t) + i\tilde{X}_k(t)Y_k^{(\varphi)}(t)]\exp[i\tilde{\varphi}_k(t)], \quad (7)$$

where

$$Y_k^{(a)}(t) = X_k(t) - \tilde{X}_k(t), \quad (8)$$

$$Y_k^{(\varphi)}(t) = \varphi_k(t) - \tilde{\varphi}_k(t). \quad (9)$$

To compare the numerical data, it will be more convenient to use normalized dimensionless functions obtained by dividing the complex amplitudes by the array average value

$$\bar{\tilde{X}}(t) = \frac{1}{N}\sum_{k=1}^{N}\tilde{X}_k(t) \quad (10)$$

(N is the number of the array elements) and introducing the variables

$$y_k(t) = \delta x_k(t)/\bar{\tilde{X}}(t). \quad (11)$$

The dynamical reconstruction of the secondary acoustic field pattern from these complex variables is performed by the method of coherent wave front reversal based on the acoustic reciprocity principle.

For a spatial point located in the signal plane at a depth z (measured from the water surface) and at a distance r from the array in the horizontal direction (toward the "illuminating" primary source), we write a conventional mode expansion [8] for the dimensionless transmission coefficient between this point and the kth element of the array:

$$K(z, z_k, r) = \sum_n (\chi_n r)^{-\frac{1}{2}} U_n(z_k)U_n(z)e^{i\chi_n r}, \quad (12)$$

where χ_n and $U_n(z)$ are the mode wave numbers and the mode functions calculated with given boundary conditions at the bottom and at the water surface with allowance for the measured sound velocity profile $c(z)$. Computer programs for performing such calculations are known (see, e.g., [9]). These programs allow one to take into account the rough bottom relief, while expansion (12) is valid only for a planar waveguide.

If we replace each hydrophone of the array by a source generating a signal that is complex conjugate with respect to the received signal, then, according to the reciprocity principle, the spatial structure of the generated field will reproduce the initial one (correct to the aperture limitations and natural distortions due to the off-duty ratio of the array). In the experiment described below (compare also [3]), the array (12 m long) covered practically the whole depth of the lake, and the distance between neighboring elements (19.5 cm) was approximately three times less than the acoustic wavelength. Taking into account the aforesaid, we write the formula for the sound field amplitude $p(r, z)$ of the reconstructed field of secondary sources:

$$p(r, z, t) = \left|\sum_{k=1}^{N} y_k^*(t)\sum_n (\chi_n r)^{-\frac{1}{2}} U_n(z_k)U_n(z)e^{i\chi_n r}\right|. \quad (13)$$

In what follows, for the reconstruction of the secondary field, we will use not only the variables $y_k(t)$, but also the results of their complex matched filtering, which will allow us to increase the contrast when observing the episodes of the intersection of the (r, z) signal plane by the moving screen. We note that, in the brightness images of the field structure, we represent not the pressure amplitude, but the field intensity, i.e., the quantity $p^2(r, z)$.

Now, we turn to the procedure of extracting weak signals by the method of incoherent accumulation. For this purpose, it is convenient to use the normalized amplitude variables

$$Y_k^{(a\ nor)}(t) = Y_k^{(a)}(t)/\tilde{X}_k(t) \quad (14)$$

and the corresponding normalized complex functions

$$Y_k^{(nor)}(t) = Y_k^{(a\ nor)}(t) + iY_k^{(\varphi)}(t). \quad (15)$$

Here, we omit the exponential phase factor that is involved in Eq. (7), because, in the case of the incoherent accumulation of the signal responses over the array, this factor is insignificant.

We note that the introduction of the normalized variables given by Eqs. (14) and (15) already involves a nonlinear transformation of the initially received signals. The application of this heuristic procedure demonstrated a high efficiency of the latter in nonstationary propagation conditions with a pronounced stratification of the sound field, when the standard methods of the theory of linear filtering are ineffective.

In our previous paper [10], it was shown that already a simple incoherent accumulation with the formation of the output signal

$$S(t) = \frac{1}{N}\sum_{k=1}^{N}\left|Y_k^{(nor)}(t)\right| \tag{16}$$

provides satisfactory results in the case of the observation of a diffracting inhomogeneity with a sufficiently large cross-section.

In observing a moving inhomogeneity, the signal-to-noise ratio can be noticeably increased by applying the complex matched filtering algorithm [1]

$$F_k(t) = \int Y_k^{(nor)}(t')\Phi^*(t-t')dt' \tag{17}$$

with the use of the filter

$$\Phi(t) = C\exp\left[-\frac{V}{h\lambda}\left(i\pi + \frac{2l^2}{h\lambda}\right)t^2\right], \tag{18}$$

where V is the screen velocity component normal to the signal plane, l is the projection of the horizontal screen aperture length onto the same direction, λ is the sound wavelength, and h is the reduced distance between the point of intersection and the array (see [3]). Then, the incoherent accumulation is performed for the transformed responses:

$$F(t) = \frac{1}{N}\sum_{k=1}^{N}|F_k(t)|. \tag{19}$$

The normalization of filter (18) is chosen according to the condition

$$C^{-1}\int|\Phi(t)|^2dt = 1. \tag{20}$$

In this case, the maximal signal spikes that occur in the processing by Eqs. (16) and (19) can be treated as equal.

Returning to the problem of the coherent reconstruction of the secondary field, we note that, in this case, for increasing the contrast of the focal spot corresponding to the moving inhomogeneity, the variables $y_k(t)$ are subjected to the same type of matched filtering. More precisely, we perform transformation (17) only for the pre-exponential parts of the functions $y_k(t)$, after which the phase factors $i\tilde{\varphi}_k(t)$ are reproduced in the initial form. This corresponds to the method known from classical radio engineering, namely, to a linear filtering of variables reduced to the zero stationary phase.

Now, we will proceed to discussing some experimental results.

EXPERIMENTAL RESULTS

In this section, we illustrate the theoretical possibilities discussed above by experimental data obtained in a fresh-water reservoir (a lake). At the site where the vertical receiving array was installed, the depth of the lake was about 14 m and, within the acoustic track under study, the bottom was practically flat. The array contained 64 hydrophones, and its total length was 12 m. The primary source producing a cw "illumination" was positioned near the bottom, at a distance of 300 m from the array; the cw radiation frequency was $f = 2499$ Hz.

Below, we study a five-minute-long record segment that contains one episode of intersection of the signal plane by an acoustically opaque screen (220 s from the beginning of the record). The screen was towed by a boat in the direction perpendicular to the acoustic track (and to the source–array vertical signal plane) at a depth of 4–5 m and at a distance somewhat greater than 40 m from the array. The screen length was $l = 1.7$ m, its cross-sectional area was $\sigma = 1$ m^2, and the speed of towing was $V = 0.4$ m/s. For towing, a special-purpose vertical arm was used, so that the boat and the underwater screen crossed the track practically simultaneously.

Prior to the signal processing, a mathematical model of the moving screen was introduced in the record (the track intersection at the instant $t_1 = 45$ s). The model imitates the intersection of the signal plane by a compact screen with the same parameters $l = 1.7$ m, $\sigma = 1$ m^2, and $V = 0.4$ m/s at a depth of 6 m and at a distance of 40 m from the array.

Figure 1 shows the result of the incoherent accumulation (19) of the transformed signal responses over all array elements. The first (imitated) signal peak at $t_1 = 45$ s (indicated by an arrow) only slightly exceeds the level of random noise spikes and is much lower than the experimental peak observed at $t_2 = 220$ s. This fact immediately suggests that a substantial contribution to the observed signal peak was made by the eddy disturbances that were caused by the boat and accompanied the motion of the underwater screen. We note that the following study of the spatial structure of the secondary acoustic field confirmed this assumption.

Figure 2 shows the half-tint pattern of the intensity of the inverse secondary field $p^2(r, z)$ for the instant t_1 (the time reading has a duration of about 1 s). The pattern was obtained by using algorithm (13). In the figure,

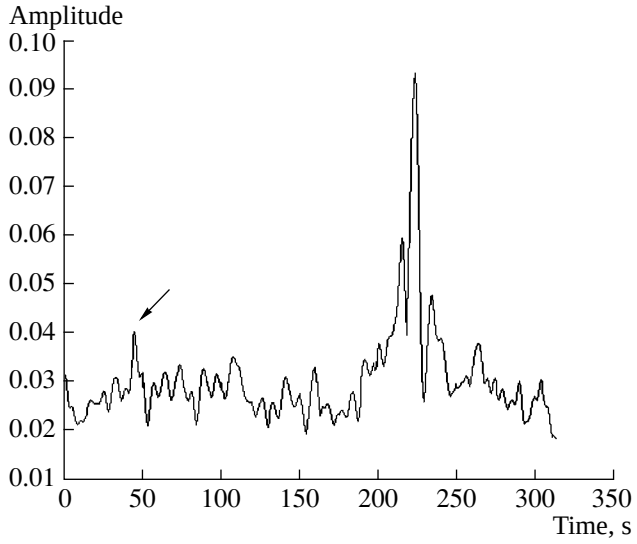

Fig. 1. Result of the incoherent accumulation of signal responses after matched filtering.

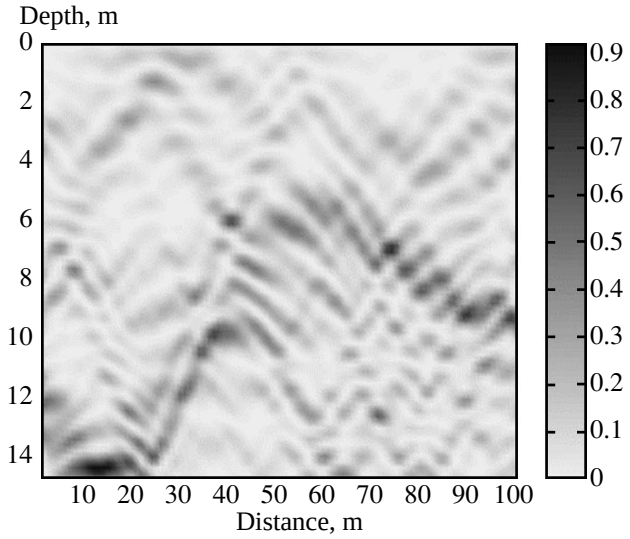

Fig. 2. Secondary field pattern for the instant $t_1 = 45$ s.

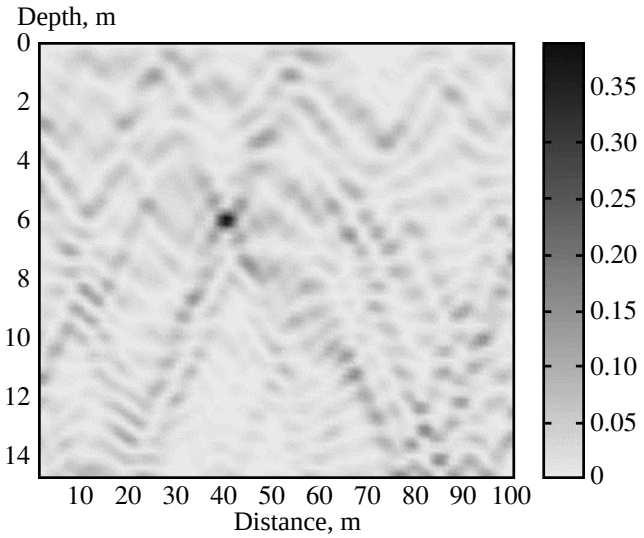

Fig. 3. Secondary field pattern for the instant t_1 after matched filtering.

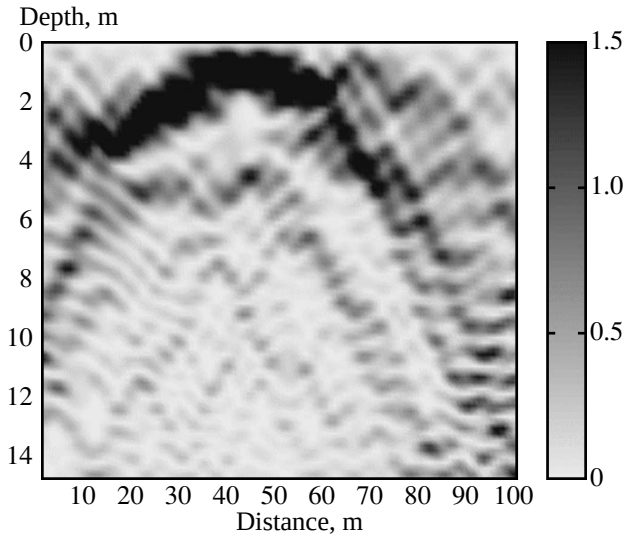

Fig. 4. Secondary field pattern for the instant $t_2 = 220$ s.

one can clearly see the focal spot from the imitated inhomogeneity at the given depth and distance (6 and 40 m, respectively). Simultaneously, more intense interference disturbances can be observed at other points of the pattern.

Figure 3 presents the result of a similar procedure for the same signals subjected to matched filtering described by Eqs. (17) and (18). One can see that, in this case, the imitated inhomogeneity is observed with a noticeably higher contrast. It is important that, from Fig. 3, one can detect with confidence the passage of the moving inhomogeneity, while, after the procedure of incoherent accumulation defined by Eq. (19), the excess of the signal over the noise level (Fig. 1) is obviously insufficient for such a detection.

In addition, the computer simulation allows one to estimate the brightness levels (in arbitrary units, which result from the use of our dimensionless functions) at which one should expect the appearance of the desired spot from by the screen in the real experiment. This estimate is helpful in constructing the patterns of the inverted field, because it allows one to introduce and select the upper threshold limitations of the brightness range in order to observe the expected focal spot from the real screen in the presence of other perturbations of the water medium.

Figure 4 shows the pattern of the inverted secondary field for the time reading t_2; the pattern is obtained with the upper limitation of the brightness range $p^2(r, z)$ at a

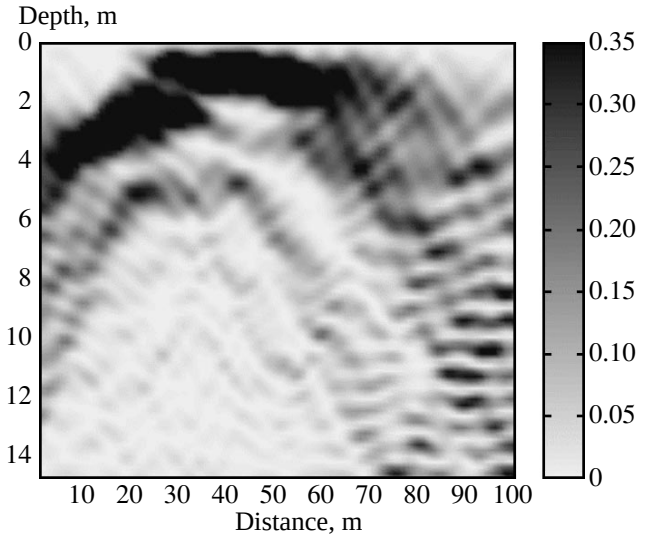

Fig. 5. Secondary field pattern for the instant t_2 after matched filtering.

level of 1.5 (in arbitrary units). One can clearly see the focal spot from the underwater screen at a depth slightly exceeding 4 m and at a distance of 42 m. Simultaneously, closer to the surface, relatively large disturbances caused by the boat motion are observed. Presumably, these disturbances made the maximal contribution to the experimental signal peak near the instant t_2 in Fig. 1. We note that, without using the threshold limitation, one obtains the brightness level of the maximal disturbance in the pattern under discussion as high as 6, and the focal spot produced by the screen will be barely noticeable against this background.

Figure 5 presents the intensity pattern of the inverted field after matched filtering for the same time reading $t_2 = 220$ s. Here, the threshold brightness level is selected to be 0.35, which corresponds to the simulation result shown in Fig. 3. The focal spot from the underwater screen can be clearly distinguished, although the eddy disturbances caused by the boat motion are considerable. The intensity of the maximal secondary field disturbance is about 1.2 (in the same arbitrary units).

An interesting physical effect was observed in studying the pattern structure corresponding to the "precursor" of the intersection of the signal plane by the boat with the towed screen. Figure 6 shows the pattern of the inverted field for the time reading taken 12.7 s prior to the instant t_2. In this figure, one can see an oval-wave structure concentric with respect to the point of the future boat passage. Presumably, here, we observe the result of the Bragg reflection of sound from the surface wave produced by the boat. One should remember that, although we reconstruct only a plane cross-section of the field structure, sound waves from other directions also arrive at the array. If considerable disturbances are present outside the signal plane, these additional components may also be noticeable. Apparently, it is these effects that are observed in the case under study.

One more specific feature was revealed in studying the pattern of the "precursor" signals after matched filtering (17). Such a pattern is shown in Fig. 7 for the same reading $t_2 - 12.7$ s. It was found that, in this case, the filtering procedure completely "erased" the oval-wave disturbances thus allowing one to observe the structure of the unperturbed acoustic field. Specifically, it has become possible to clearly distinguish the difference between the sound propagation in the warm surface layer (about 4 m thick) and the propagation in the colder water bulk below. Since only the sound beams incident on the surface at large angles penetrate into the

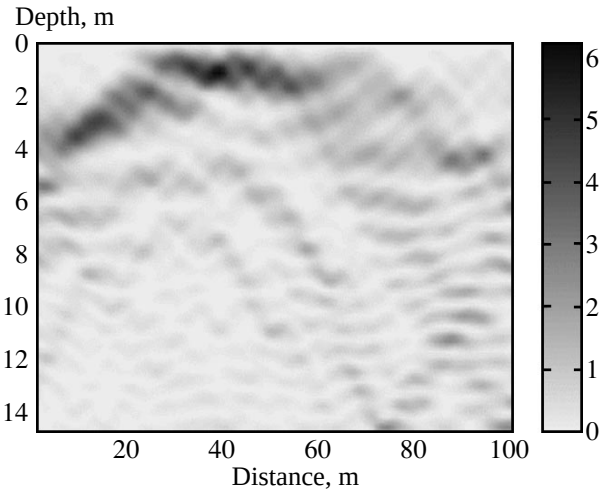

Fig. 6. Secondary field pattern for the instant $t_2 - 12.7$ s.

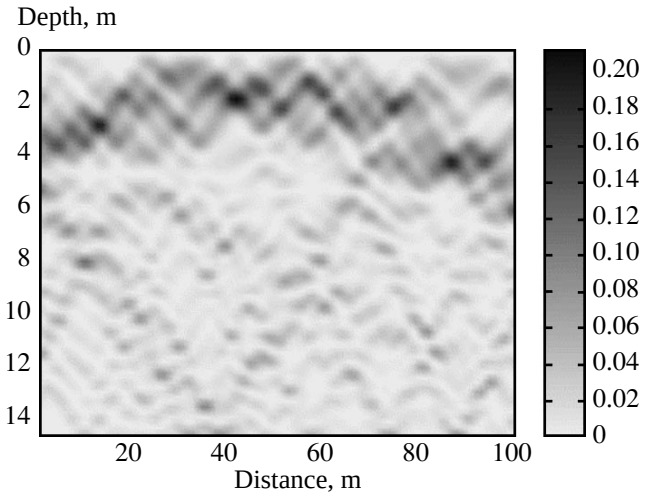

Fig. 7. Secondary field pattern for the instant $t_2 - 12.7$ s after matched filtering.

surface layer, the field formed in this case has a "coarser" cellular structure.

SUMMARY

Thus, the method of the secondary field reversal provides fuller hydrophysical information and allows one to reveal the origin of the observed perturbations. We note that, for its realization, it is necessary to use the same signals as for the observations by the incoherent accumulation scheme, which means that the construction of visual patterns of the secondary field does not require any additional hydroacoustic equipment. However, for calculating the mode eigenfunctions, one needs the fullest possible information on the hydrological conditions of signal propagation, on the relief and physical parameters of the bottom, etc.

For a continuous operation of such a system of observation, it is necessary to continuously monitor the hydrological conditions. With all aforementioned requirements being satisfied, the remaining problems will be easily solved by using the appropriate software and fast-performance computers. In any case, today a visual observation of the dynamics of the underwater medium by acoustic methods seems to be quite feasible.

ACKNOWLEDGMENTS

We are grateful to P.I. Korotin, B.M. Salin, and V.I. Turchin who greatly contributed to the organization of the experiments, and to A.Ya. Balalaev, V.A. Laukhin, V.V. Pikalev, V.A. Tyutin, A.V. Tsiberev, and A.S. Chashchin who participated in the experiment and in the design of equipment.

The work was supported by the Russian Foundation for Basic Research (project no. 99-02-16401).

REFERENCES

1. V. A. Zverev, A. L. Matveev, and V. V. Mityugov, Akust. Zh. **41**, 591 (1995) [Acoust. Phys. **41**, 518 (1995)].
2. A. L. Matveev, V. V. Mityugov, and B. M. Salin, in *Acoustics of the Ocean* (Geos, Moscow, 1998), pp. 151–156.
3. A. L. Matveev and V. V. Mityugov, Akust. Zh. **46**, 115 (2000) [Acoust. Phys. **46**, 80 (2000)].
4. J. A. Fawcett, M. L. Yeremy, and N. R. Chapman, J. Acoust. Soc. Am. **99**, 272 (1996).
5. A. L. Matveev, V. V. Mityugov, and A. I. Potapov, in *Acoustics of the Ocean* (Geos, Moscow, 1998), pp. 309–313.
6. W. S. Hodgkiss, H. C. Song, W. A. Kuperman, *et al.*, J. Acoust. Soc. Am. **105**, 1597 (1999).
7. N. E. Collison and S. E. Dosso, J. Acoust. Soc. Am. **107**, 3089 (2000).
8. E. Skudrzyk, *The Foundations of Acoustics. Basic Mathematics and Basic* (Springer, New York, 1971; Inostrannaya Literatura, Moscow, 1958), Vols. 1 and 2.
9. M. B. Porter, *The KRAKEN Normal Model Program* (SACLANT Undersea Research Center, 1991).
10. S. M. Gorskiĭ, V. A. Zverev, A. L. Matveev, *et al.*, Akust. Zh. **41**, 223 (1995) [Acoust. Phys. **41**, 190 (1995)].

Translated by E. Golyamina

Acoustical Physics, Vol. 47, No. 2, 2001, pp. 208–213. Translated from Akusticheskiĭ Zhurnal, Vol. 47, No. 2, 2001, pp. 253–258.

REVIEWS

Identification of Acoustic Sources in Shallow Water: Errors in the Measured Parameters of the Source Model

A. A. Pudovkin

Andreev Acoustics Institute, Northern Branch, Russian Academy of Sciences, ul. Pochtovaya 3, Severomorsk, Murmansk oblast, 184600 Russia

e-mail: Alexey.Pudovkin@mstu.edu.ru; sfakin@murmansk.rosmail.com

Received June 29, 1998

Abstract—Expressions for the variance of the estimated power of an acoustic source are presented for the case of the source identification in a natural shallow-water environment. The effect of errors in the estimated parameters of a shallow-water waveguide and in the estimated coordinates of the phase center of the source on the confidence interval of the estimated directional characteristics of the source is investigated using a model signal as an example. © *2001 MAIK "Nauka/Interperiodica".*

In the case of the acoustic source identification in the conditions of a natural body of water, the error in the estimated parameters of the source model essentially depends on the errors in the estimated parameters of the model of the shallow-water waveguide.

The literature on the parameter estimation for the models of shallow-water waveguides is quite extensive. Gerstoft and Gingras [1] used the information on the acoustic pressure field measured with a vertical array. Solving the inverse problem in terms of the objective function, they correlated the forecast and the observed fields. The solution provided the estimated model parameters, including the parameters of the ground underlying the water layer. The observations were carried out in the frequency ranges 165–175 and 325–335 Hz. Candy and Sullivan [2] estimated the parameters of the waveguide model by matching the predicted acoustic pressure and sound velocity profile with the observed ones and called their approach the model-based environmental inversion. Correlating the observed and the predicted parameters, they used the objective function to take into account the random character of the field formation. Random signals were processed using the Kalman filtration. The serviceability of the models used was confirmed by testing the statistical hypotheses. The resulting estimates of the parameters in models describing the field formation were used for the source detection [3] and source localization [4, 5], unfortunately, without a sufficient analysis of the measurement errors and their effect on the solution of the detection and localization problems. The *a posteriori* analysis of the experimental results shows that, for a correct processing, one needs to additionally determine the parameters of the medium in processing the information signal [3–5]. Candy and Sullivan [5] reported on the solution of the localization problem together with the determination of some additional characteristics of the data transmission channel. For several points of the water layer, they measured both sound pressure and sound velocity and used this information to repeatedly correct the parameters of the modes propagating in the channel. Using corrected mode parameters, they estimated the distance to the source and the depth of the source. The propagating mode parameters represented the process of state in the extended Kalman filtration version they used.

Consider the estimation of the variance of the radiation power in a given direction from the source. In this case, the pressures measured in the sound channel of a natural water body can serve as the initial data. Power is a scalar parameter; consequently, a scalar variance is sufficient to characterize the errors in the value of the power. However, the power measured in a specified direction relative to the source depends on the vector of the source parameters describing the directional pattern of the radiation. To characterize the errors of a vector, we must use the variance matrix. In the process of estimating the parameter vector of the source, measurements are carried out in a waveguide that, in turn, is characterized by its own vector of parameters. The problem formulated includes, first, the calculation of the variance matrix of the waveguide parameters; second, the calculation of the variance matrix of the source parameters affected by the above errors in the waveguide parameters; and, third, the calculation of the variance of the radiation power.

In solving the inverse problem, one must forecast the observed signal. Forecasting can be conveniently performed using the parametric description of the directional characteristic of the acoustic source $G(\phi, \varphi, \boldsymbol{\beta})$.

1063-7710/01/4702-0208$21.00

Let ϕ and φ be the angles in the vertical and horizontal planes, respectively, and $\boldsymbol{\beta}$ be the vector of the expansion coefficients of the directional characteristic of the observed source in a set of orthogonal functions. The measured pressure depends not only on the vector $\boldsymbol{\beta}$, but also on the vector of the waveguide parameters $\boldsymbol{\eta}$. Such procedures are usually realized under the assumption that the components of the vector $\boldsymbol{\eta}$ are known (they can be estimated, for example, from the special preliminary experiments [6, 7]). The model parameters are estimated as the parameters minimizing the objective function.

In the course of measurements, it is often necessary not only to estimate the parameter vectors of the source $\boldsymbol{\beta}$ and the waveguide $\boldsymbol{\eta}$, but also to reconsider the experimental procedure by determining some additional parameters required for forecasting the measured signal. In the theory of measurements, these parameters are usually called the interference parameters. Designate the vector of interference parameters for the source identification by $\boldsymbol{\varepsilon}$ and the vector of interference parameters for the waveguide identification by $\boldsymbol{\nu}$. In the general case, the vectors of the estimated parameters ($\boldsymbol{\theta}$ for the source identification and $\boldsymbol{\mu}$ for the waveguide identification) are representable in the form $\boldsymbol{\theta} = [\beta^T, \varepsilon^T]^T$ and $\boldsymbol{\mu} = [\eta^T, \nu^T]^T$, where the superscript T denotes the transposition operation. Since the procedure estimates all parameters, including the interference parameters, one should include the error transfer in the variance matrixes of the estimated parameters. By the error transfer, we mean the recalculation of errors in estimating the interference parameters $\boldsymbol{\varepsilon}$ and $\boldsymbol{\nu}$ into the errors in estimating the parameters of the source $\boldsymbol{\beta}$ and the waveguide $\boldsymbol{\eta}$. We designate the resulting variance matrixes of the vectors of estimates $\boldsymbol{\beta}$ and $\boldsymbol{\eta}$ by $D_{\beta/\varepsilon}$ and $D_{\eta/\nu}$, respectively. In estimating the parameters, for example, of the waveguide, the parameters of the model of the measurement situation are adjusted in such a way as to allow forecasting the observed signal. In this adjustment, random deviations of the observed signal from the forecast must be consistent with the model of the measurement situation [8]. The estimation of the parameters of the measurement situation $\boldsymbol{\theta}$ and $\boldsymbol{\mu}$, including the parameters of the autoregression equation characterizing the frequency response of the Kalman filter x_i related to the signal fluctuations, is given in [7]. The variance matrix D_ξ of state x_i is related to the quality of the accomplished estimation and is determined from the solution of the Sylvester equation [9] whose form is uniquely related to the parameters of the autoregression equation. The nonzero diagonal elements of the variance matrix $D_{\xi Y}$ (this matrix corresponds to fluctuations in the processed realization Y relative to the stochastic forecast, and its dimension coincides with the number of readings N in realization Y_i) are formed, according to the procedure described in [10], from the variance matrix D_ξ of state x_i whose dimension coincides with the dimension of the autoregression equation. The cited paper considered the situation of fully coherent mode (or ray) fluctuations. The coherent component of the jth mode (or ray) for the ith reading in the lth signal realization is described by the function $s_{ijl}(\theta, \mu)$, where $i = 1$–N, $j = 1$–m, and $l = 1$–L. If the fluctuations are not fully coherent, the coefficient of the cross-correlation between the fluctuations of signals of different modes R_{jk} is specified in the linear autoregression equation. A consequence of the correlation of fluctuations is the increase of the dimension of the matrix D_ξ. The nonzero diagonal elements of the variance matrix of fluctuations $D_{\xi Yjk}$ are formed from the matrix D_ξ of increased dimension, according to the procedure described in [10].

In order to estimate the model parameters of a towed acoustic source in a natural shallow-water environment, we need the initial information that can be formed, for example, as an array of energies of the sound field measured by the elements of a receiving aperture located in the shallow-water waveguide. In what follows, we assume that a multielement receiving array was used to measure the values of the field energy in the water layer Z_{il} and to determine the source location relative to the aperture at the ith moment. For estimating, we used the objective function composed of two factors. The first factor is formed as the sum $\sum_{i=1}^{N}\sum_{l=1}^{L} F_{il}(Z_{il}, \theta, \eta)$ where the terms $F_{il}(Z_{il}, \theta, \eta)$ are proportional to the energy of the mismatch between the observed parameters and the parameters predicted with the use of the directional characteristic $G(\phi, \varphi, \beta)$. The second factor is determined by the statistics of the tested hypotheses and was calculated by the procedure described in [7].

Let us assume that the variations δZ of the observed pressure in the realization Z processed for estimating the source parameters are uncorrelated with the variations δY of pressure in the realization Y used for estimating the model parameters of the shallow-water sound channel. For the source parameters, the variance matrix can be estimated similarly to the procedure used for estimating the waveguide parameters in [10]. The variance matrix of the measured parameters is formed of the variance matrix of state describing the mismatch between the measurement and the forecast. The resulting expression for the variance matrix of the parameter vector D_θ has the form

$$D_\theta = H_Z^{-1}\left\{Q_Z\left[\sum_{k=1}^{m}\sum_{j=1}^{m}\mathrm{diag}(s_{ijl}(\theta,\eta))\right.\right.$$
$$\left.\left.\times D_{\xi Yjk}\mathrm{diag}(s^c_{ikl}(\theta,\eta)) + D_{wZ}\right]Q_Z^T\right.$$
$$\left.\times K_{Z\theta\eta}D_{\eta/\nu}K_{Z\theta\eta}^T\right\}H_Z^{-1T}, \quad (1)$$

where H_Z is the matrix with the elements $H_{Zpq} = \sum_{i=1}^{N}\sum_{l=1}^{L}\partial^2 F_{il}(Z_{il}, \theta, \eta)/\partial\theta_p\partial\theta_q$, Q_Z is the matrix with the elements $Q_{Zqil} = \partial^2 F_{il}(Z_{il}, \theta, \eta)/\partial\theta_q\partial Z_{il}$, $\mathrm{diag}(S_{ijl}(\theta, \eta))$ is the diagonal matrix with the elements $s_{ijl}(\theta, \eta)$, the superscript in $s^c_{ikl}(\theta, \eta)$ means the complex conjugation, D_{wZ} is the diagonal variance matrix of white noise whose energy is proportional to the energy of the multimode signal of the source under identification, and $K_{Z\theta\eta} = \sum_{i=1}^{N}\sum_{l=1}^{L}\partial^2 F_{il}(Z_{il}, \theta, \eta)/\partial\theta_p\partial\eta_g$ is the sum of terms estimated for the readings of the realization Z used for the identification of the source in the preliminarily identified waveguide. The matrix D_{wZ} describes the noise caused by the fluctuations of the signal propagating in the measurement area of the shallow-water waveguide. The matrix $K_{Z\theta\eta}$ determines how the objective function relates the parameters estimated in the current phase of the measurement process to those estimated in the preceding phase. The subscripts p and q correspond to the parameters of the current phase, and the subscript g corresponds to the parameters of the preceding phase. The variance matrix $D_{\eta/\nu}$ can be obtained from the results of the waveguide identification. In principle, the parameters of the source and the waveguide models can appear simultaneously among the parameters of the measurement situation. However, such a simultaneous appearance is very undesirable, because these parameters are more conveniently estimated in different phases of the experiment. If the source and the waveguide parameters are estimated simultaneously in the same experimental phase, no parameter coinciding with the waveguide parameters measured during the source identification can appear among the preliminarily estimated waveguide parameters η_g. In principle, one can additionally determine the waveguide parameters η_g during the phase of the source measurement. However, in so doing, the objective function must include the information on the variance matrix of the additionally determined parameters, and another expression must be used for the matrix D_θ. If the additional determination of the waveguide parameters during the source identification is nevertheless desirable and if one has to use the objective function in the above form $D_{\eta/\nu}$ neglecting the information on the estimation errors for the waveguide parameters, the additional parameters must appear in the vector $\boldsymbol{\varepsilon}$ rather than in the vector $\boldsymbol{\eta}$; i.e., one should treat them as the interference parameters at the preliminary identification stage. The models used in both experiments for describing the acoustic field formation must coincide and depend on the waveguide parameters η_g. Certainly, one obtains an increased variance for the source parameters estimated from the fields measured in the waveguide for which the parameters of the acoustic model are also measured rather than known exactly, because they are characterized by the variance matrix $D_{\eta/\nu}$. If the parameters of the model are known exactly, one has $D_{\eta/\nu} = 0$.

Then, the variance matrix $D_{\beta/\varepsilon}$ of the vector of the source parameters $\boldsymbol{\beta}$ is calculated from the variance matrix D_θ of the vector of parameters $\boldsymbol{\theta}$ whose components are used for forecasting the observed characteristics of the acoustic field. In the case of estimating the vector of the interference parameters ε from the realization used for estimating the source parameters, the matrix $D_{\beta/\varepsilon}$ takes into account the fact that both these vectors were estimated during the measurement.

Consider the calculation of the matrix $D_{\eta/\nu}$ assuming that the matrix D_μ is known (the matrix $D_{\beta/\varepsilon}$ is similarly determined from the matrix D_θ). Since the measurement is carried out so as to minimize the objective function, the derivative of the objective function with respect to the vector of the estimated parameters must be zero at the point corresponding to the best estimation. Introducing the rectangular matrix $U_{Y\eta} = \sum_{i=1}^{N}\sum_{l=1}^{L}\partial^2 F_{il}(Y_{il}, \eta, \nu)/\partial\mu\partial\eta$ and the similar matrix $U_{Y\nu}$ in which the partial derivative with respect to ν replaces the partial derivative with respect to η, from the condition of the zero derivative of the objective function, we obtain

$$U_{Y\eta}\delta\eta = -U_{Y\nu}\delta\nu.$$

Solving this equation according to the method of least squares, we obtain

$$\delta\eta = -\{U^T_{Y\eta}U_{Y\eta}\}^{-1}U^T_{Y\eta}U_{Y\nu}\delta\nu.$$

We use this formula, which relates the variation $\delta\eta$ of the waveguide parameters to the variation $\delta\nu$ of the parameters considered as the interference ones in the waveguide identification, for deriving the expression for the variance matrix $D_{\eta/\nu}$ composed of the variances of only the waveguide parameters and affected by the variance matrix of the interference parameters. We designate the square matrix corresponding to the matrix D_μ portion related to the vector of the waveguide parameters $\boldsymbol{\eta}$ by D_η and the similar matrix corresponding to the matrix D_μ portion related to the vector $\boldsymbol{\nu}$ composed of the parameters that are considered as the interference ones in the waveguide identification by D_ν. The rest of the matrix D_μ is described by two rectangular Hermitian-conjugated matrixes the right-top of which we designate by $D_{\mu\nu}$. Taking into account the above relationship between the variations $\delta\eta$ and $\delta\nu$ and assuming that the vectors $\boldsymbol{\eta}$ and $\boldsymbol{\nu}$ are estimated during the same experiment, we obtain the following expression for the variance matrix of only the waveguide parameters,

$D_{\eta/\nu}$, with allowance made for the interference parameters:

$$D_{\eta/\nu} = D_\eta - \{D_{\mu\nu}U_{Y\nu}^T U_{Y\eta}[U_{Y\eta}^T U_{Y\eta}]^{-1}\} - \{D_{\mu\nu}U_{Y\nu}^T U_{Y\eta}[U_{Y\eta}^T U_{Y\eta}]^{-1}\}^T + [U_{Y\eta}^T U_{Y\eta}]^{-1}U_{Y\eta}^T U_{Y\nu}D_\nu\{U_{Y\nu}^T U_{Y\eta}[U_{Y\eta}^T U_{Y\eta}]^{-1}\}^T. \quad (2)$$

For the source identification, the effect of the measurement errors in the interference parameters can be taken into account in a similar way. Note that, if the interference parameters are measured without the use of the signal realizations used for the identification, one can perform the calculations with the matrixes D_ν and D_ε obtained from independent measurements. In this case, all elements of the matrixes $D_{\mu\nu}$ and $D_{\theta\varepsilon}$ are zero-valued, because the measurements of the vectors $\boldsymbol{\eta}$ and $\boldsymbol{\beta}$ are independent of the measurements of the vectors $\boldsymbol{\varepsilon}$ and $\boldsymbol{\nu}$.

The variance σ_G^2 of the calculated energy $G(\phi, \varphi, \beta)$ transmitted by the source in the direction specified by the angles ϕ and φ can be estimated using the linear transfer of the error [11]:

$$\sigma_G^2 = \partial G(\phi, \varphi, \beta)/\partial\beta^T D_{\beta/\varepsilon}[\partial G(\phi, \varphi, \beta)/\partial\beta^T]^T, \quad (3)$$

where $\partial G(\phi, \varphi, \beta)/\partial\beta^T$ is the row matrix composed of the derivatives of the directional characteristic with respect to the corresponding parameters.

To demonstrate the use of the above relationships, we consider an example based on the model signal. The model signal was generated according to the model of the acoustic field formation in a natural shallow-water environment [7].

The model signal was defined as energy readings of the tone signal received by an omnidirectional hydrophone from a moving directional local source. The directional characteristic was assumed to be cylindrically symmetric, and its angular dependence was described by the sum of four Legendre polynomials with respective factors of 0.5, –0.16, 0.3, and 0.1. The observed energy of the acoustic signal depends on these factors according to a linear relationship. It is these factors appearing in the directional characteristic that we estimated in the model experiment. We simulated the measurement situation in which the directional source moved along the symmetry axis of its directional characteristic with the velocity coinciding with the velocity of the omnidirectional source in the procedure of the estimation of the waveguide parameters. Such situation occurs, for example, for the sound generated by a propeller in a homogeneous flow. In this case, the directional characteristic is symmetric relative to the rotation axis of the propeller. In the considered model, the source trajectory used for estimating the parameters of the directional characteristic can essentially differ from the source trajectory during the estimation of the waveguide parameters. The simulation was carried out for the case of a uniform rectilinear motion of the source with the receiver located at a distance of 50 m abeam with the motion direction. The coordinates of the phase center of the directional source are nonlinearly related to the observed energy readings of the acoustic signal. We assumed these coordinates to be unknown and estimated them as the interference parameters. In this way, we estimated the waveguide parameters and the variance matrix of the estimation vector from the experimental signal. Then, we used this matrix to estimate the variance matrix of the parameter vector of the directional acoustic source for the model signal.

Calculating the variance matrix of the estimated vector of the waveguide parameters, we used an obvious modification of Eq. (1) for the case of the parameter estimation from the realization Y. Since the estimation of the waveguide parameters does not require any preliminary information, we discarded the second term between braces in Eq. (1). We used Eq. (2) for calculating the variance matrix of the estimated waveguide parameters with allowance made for the effect of the interference parameters. For calculating the variance matrix of the estimated vector of the source parameters, we used Eq. (1). Calculating the variance matrix of the estimated source parameters with allowance for the effect of the interference parameters, we used an obvious modification of Eq. (2) for the case of the parameter estimation from the realization Z. The confidence interval of the estimated value of energy transmitted by the source in a specified direction was evaluated from the variance σ_G^2 calculated by Eq. (3).

The figure shows the polar diagram of the estimated directional characteristic of the source with the corresponding confidence interval in the plane passing through the symmetry axis. The outer and the inner contours correspond to the upper and lower boundaries of the confidence interval, respectively, and the intermediate contour corresponds to the estimate. For all fragments, the distance from the fragment center to the peripheral circle corresponds to 20 dB. We varied the confidence probability in order to fit all three contours characterizing the measurements carried out under different conditions within the 20-dB interval. We set the value of 95% for the confidence probability of the interval calculated under the assumption that the waveguide parameters and the coordinates of the source phase center are known exactly (Fig. 1a). Calculating the confidence interval under the effect of the measurement errors in either the waveguide parameters (Fig. 1c) or the coordinates of the phase center (Fig. 1d) or both (Fig. 1b), we used the 5% confidence probability. In this case, the lower boundary of the confidence interval in Fig. 1b takes the form of narrow lobes directed toward the minima of the contour describing the upper

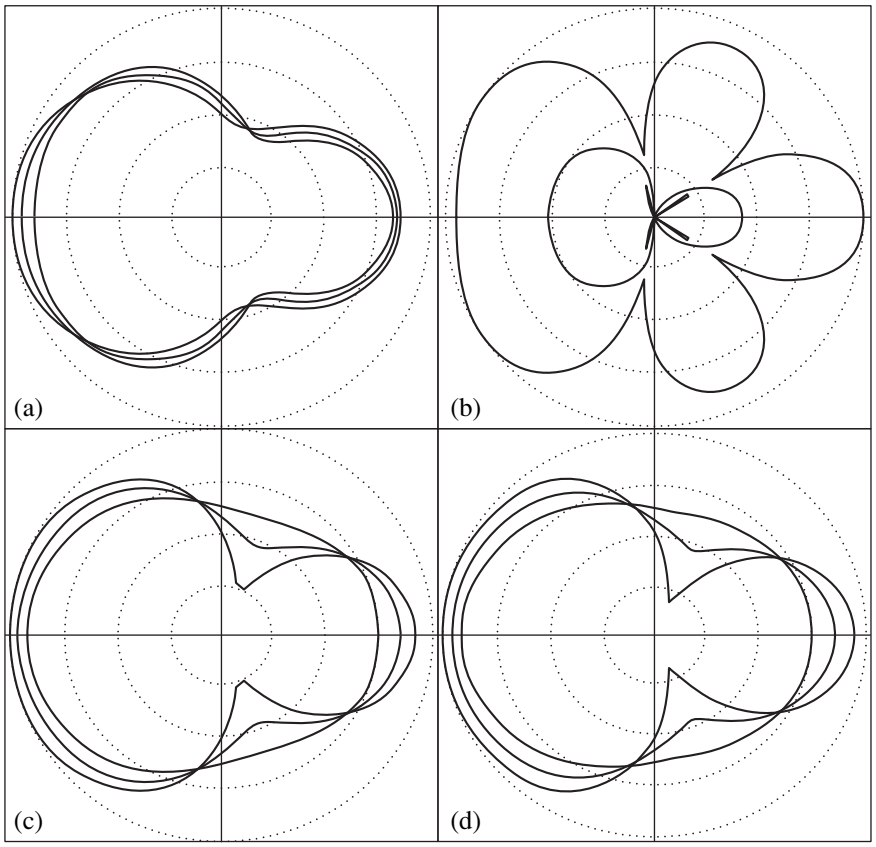

Fig. 1. Estimated directional characteristic of the source. The distance between the dotted circles corresponds to 5 dB. (a) Estimate and the 95% confidence interval calculated under the assumption that the waveguide parameters and the coordinates of the source phase center are exactly known. (b) Estimate and the 5% confidence interval calculated under the assumption that the coordinates of the source phase center are estimated simultaneously with the estimation of the directional characteristic and the parameters of the acoustic waveguide model are estimated in an additional experiment of the same duration. (c) Estimate and the 5% confidence interval calculated under the assumption that the estimate of the directional characteristic is affected by only the errors in the waveguide parameters measured in an additional experiment, and the coordinates of the source phase center are exactly known. (d) Estimate and the 5% confidence interval calculated under the assumption that the coordinates of the source phase center are estimated simultaneously with the directional characteristic, and the parameters of the acoustic waveguide model are exactly known.

boundary of the confidence interval. For the 95% probability of the confidence interval in Figs. 1b–1d, the corresponding contours of the lower and upper boundaries will not appear in the 20-dB interval.

As follows from the figure, the plausible *a priori* information about the phase center of the source under investigation and about the waveguide parameters in the measurement region considerably narrows the confidence interval of the estimated radiation level. If the estimation of the source parameters is accompanied by the estimation of the waveguide parameters or the coordinates of the source phase center, the confidence interval considerably widens, independently of whether the accompanying measurements are carried out in the main experiment or in additional ones. Consequently, the final result of acoustic measurements in shallow water can essentially depend on the errors in the acoustic model of a natural body of water and the errors in the additional determination of the source parameters that are nonlinearly related to the observed characteristics of the field.

ACKNOWLEDGMENTS

I am grateful to A.I. Belov for supplying me with the software used for the sound field calculations, to V.A. Zhuravlev for valuable discussions, and to Yu.I. Ivanov and L.A. Matyukhina for assistance in the software preparation.

REFERENCES

1. P. Gerstoft and D. F. Gingras, J. Acoust. Soc. Am. **99**, 2839 (1996).
2. J. V. Candy and E. J. Sullivan, J. Acoust. Soc. Am. **98**, 1446 (1995).

3. F. B. Shin and D. H. Kil, J. Acoust. Soc. Am. **99**, 2188 (1996).
4. B. F. Harrison, R. J. Vaccaro, and D. W. Tufts, J. Acoust. Soc. Am. **100**, 384 (1996).
5. J. V. Candy and E. J. Sullivan, J. Acoust. Soc. Am. **98**, 1455 (1995).
6. A. I. Belov, A. S. Belogortsev, and E. V. Sharkina, Akust. Zh. **41**, 883 (1995) [Acoust. Phys. **41**, 781 (1995)].
7. A. A. Pudovkin, Akust. Zh. (in press).
8. A. A. Pudovkin, Akust. Zh. **45**, 642 (1999) [Acoust. Phys. **45**, 570 (1999)].
9. A. P. Sage and J. L. Melsa, *Estimation Theory with Applications to Communications and Control* (Huntington, 1971; Svyaz', Moscow, 1976).
10. A. A. Pudovkin, Abstracts of Papers, *6th Session of the Russian Acoustical Society* (Moscow, 1997), pp. 211–214.
11. D. J. Hudson, *Statistics. Lectures on Elementary Statistics and Probability* (Geneva, 1964; Mir, Moscow, 1970).

Translated by A. Vinogradov

Acoustical Physics, Vol. 47, No. 2, 2001, pp. 214–217. Translated from Akusticheskiĭ Zhurnal, Vol. 47, No. 2, 2001, pp. 259–263.

REVIEWS

Nonlinear Raman-Type Acoustic Scattering in Three-Phase Marine Sediments

N. I. Pushkina

Research Computer Center, Moscow State University, Vorob'evy gory, Moscow, 119899 Russia

e-mail: N.Pushkina@post.com

Received April 19, 2000

Abstract—Stimulated Raman-type acoustic scattering by bubble oscillations in three-phase marine sediments, which consist of a solid frame, the pore water, and air bubbles, is considered. A model is developed for the case of the bubbles surrounded by water. The acoustic properties of the sediments are described on the basis of the Biot theory of sound propagation in a fluid-saturated porous medium. Nonlinear wave equations are obtained for marine sediments containing air bubbles. Expressions for the nonlinear scattering coefficient and the threshold intensity of the exciting sound wave are derived. A possibility of an experimental observation of the scattering process is discussed. © *2001 MAIK "Nauka/Interperiodica".*

Multiphase media exhibit specific features of their wave-propagation properties, as compared to single-phase media. Marine sediments consisting of a solid component and water are an example. In recent decades, the studies of the acoustic properties of marine sediments has become urgent, this urgency being caused by the wide application of acoustic techniques in oil exploration and production, in bottom-related environmental activities, in the detection of objects on the sea floor, and so on. Because of the high power of the sound sources used, the nonlinear acoustic properties of the sediments should be investigated. Marine sediments proved to have higher nonlinearity than a homogeneous liquid (see [1]). For example, for water, the so-called second-order nonlinear parameter (which characterizes the degree of the quadratic nonlinearity) is approximately equal to 5–6 while it is about 8–12 for water-saturated sediments. A much higher nonlinearity is characteristic of the marine sediments that contain gas bubbles. It is known [2–4] that, in a liquid, the nonlinearity caused by air bubbles in it is by several orders of magnitude higher that the nonlinearity of the hydrodynamic nature. Thus, the propagation of high-intensity sound waves in marine sediments containing gas bubbles is accompanied by essentially nonlinear processes that are still insufficiently studied.

Recently, studies were reported [5, 6] on the interaction of sound with oscillating bubbles in the ocean bottom. According to Boyle and Chotiros [5], even a very low gas content (the relative concentration of bubbles 10^{-5} or lower) proves to be sufficient for sound scattering by them to predominate over other scattering mechanisms. The same researchers [6] developed a model for a spontaneous sound scattering by the bubble oscillations in marine sediments. Since marine sediments with gas inclusions represent a medium with pronouced nonlinear properties, one can expect that nonlinear acoustic processes similar to the well-known phenomena of nonlinear optics can be observed in such sediments. In this paper, we theoretically study one of these processes, namely, the stimulated Raman-type scattering of a high-intensity sound wave by the bubble oscillations in marine sediments.

To describe the physical properties of the ocean bottom, we use the well-known Biot model [7, 8] for interpenetrating solid and liquid phases. The solid phase consisting of individual mineral grains forms a semirigid frame whose pores are filled with the liquid. In the one-dimensional case, the equations of continuity and momentum conservation for the solid and liquid components have the form [9, 10]:

$$\frac{\partial \rho_m}{\partial t} + \rho_{0m}\frac{\partial v}{\partial x} = 0, \quad \rho_{0m}\frac{\partial v}{\partial t} = -\frac{\partial P}{\partial x},$$

$$\frac{\partial \rho_s}{\partial t} + \rho_{0s}\frac{\partial u}{\partial x} = 0, \tag{1}$$

$$(1-m)\rho_{0s}\frac{\partial u}{\partial t} = \frac{\partial \sigma_{xx}}{\partial x} - (1-m)\frac{\partial P}{\partial x}.$$

In Eqs. (1), only the linear terms are retained, because, as was mentioned above, the nonlinear propagation of sound is mainly governed by the nonlinearity of a single bubble, which is much higher than that of the hydrodynamic nature. The following notations are used in Eqs. (1): ρ_m is the density of the liquid sediment phase, i.e., the mean density of the mix of water and bubbles; ρ_s is the density of the solid phase of the sediment (the subscript "0" indicates the equilibrium values); v and u are the velocities of particles in the liquid and the frame, respectively; P is the pressure in the liquid; m is

the porosity of the sediment; σ_{xx} represents the effective stresses in the porous medium [10]:

$$\sigma_{xx} = -(k + 4/3\mu)\frac{\delta\rho_s}{\rho_{0s}} + \frac{k}{k_s}P,$$

where k and μ are the bulk and shear moduli of the frame of the porous medium, respectively, and k_s is the bulk modulus of individual grains constituting the frame.

By eliminating the velocities v and u from Eqs. (1), we obtain the equations

$$\begin{aligned}\frac{\partial^2\rho_m}{\partial t^2} - \frac{\partial^2 P}{\partial x^2} &= 0.\\ \frac{\partial^2\rho_s}{\partial t^2}(1-m) - \frac{k + 4/3\mu}{\rho_{0s}}\frac{\partial^2\rho_s}{\partial x^2} - \nu\frac{\partial^2 P}{\partial x^2} &= 0.\end{aligned} \tag{2}$$

The density ρ_m of the mix that appears in Eqs. (2) can be expressed in terms of the density ρ_s of the solid phase and the pressure P in the liquid; in addition, it depends on the volume occupied by the bubbles. Let us determine the expression for ρ_m.

In the equilibrium state, the density of the mix with the concentration n of the bubbles can be represented in the form [2]

$$\frac{M}{V_{0m}} = \rho_{0f}(1 - nV_0) + \rho_{0g}nV_0, \tag{3}$$

where M and V_{0m} are the total mass and the volume of the liquid phase of the sediment, i.e., of the water–air mix; ρ_{0f} and ρ_{0g} are the densities of water and air, respectively, in the equilibrium state; and V_0 is the equilibrium volume of a bubble.

In the absence of bubbles, the following expression [11] can be obtained for the relative change in the volume of the liquid phase:

$$\begin{aligned}\frac{\Delta V_{0f}}{V_{0f}} &= \operatorname{div} V = -\frac{1}{m}(GP + \nu\operatorname{div} U)\\ &= -\frac{1}{m}\left(GP - \frac{\nu}{\rho_s}\delta\rho_s\right).\end{aligned} \tag{4}$$

Here, V_f is the volume of water in the sediment, V is the displacement of the liquid, U is the displacement of the frame, $\nu = 1 - m - k/k_s$, and

$$G = \frac{1-m}{k_s} + \frac{m}{k_f} - \frac{k}{k_s^2},$$

where k_f is the bulk modulus for water.

On the other hand, in the equilibrium state with respect to the oscillations of the bubbles, the volume of the liquid is

$$V_{0f} = V_{0m}(1 - nV_0)$$

and, hence,

$$\Delta V_{0f} = -V_{0m}(1 - nV_0)\frac{1}{m}\left(GP - \frac{\nu}{\rho_s}\delta\rho_s\right).$$

In view of this relation, we obtain the following expression for the volume of the liquid phase in the presence of the oscillating bubbles:

$$\begin{aligned}\frac{M}{\rho_m} &= V_f + V_g\\ &= V_{0m}\left[1 - nV_0 - (1 - nV_0)\frac{1}{m}\left(GP - \frac{\nu}{\rho_s}\delta\rho_s\right) + nV\right].\end{aligned} \tag{5}$$

Here, V_f and V_g are the total volumes of water and air in the presence of bubble oscillations and V is the varying volume of an individual bubble.

Expression (5), together with Eq. (3), yields the expression for the water–gas mix:

$$\begin{aligned}\rho_m\left[1 - nV_0 - (1 - nV_0)\frac{1}{m}\left(PG - \frac{\nu}{\rho_s}\delta\rho_s\right) + nV\right]\\ = \rho_{0f}(1 - nV_0) + \rho_g nV_0.\end{aligned}$$

Since the total volume of bubbles is small in the actual sediments, $nV_0 \ll 1$, the relation obtained for the density of the liquid phase can be reduced to the form

$$\rho_m \approx \rho_{0f}\left(1 + \frac{G}{m}P - \frac{\nu}{m}\frac{\delta\rho_s}{\rho_s} - nV\right). \tag{6}$$

By substituting this relation into Eq. (2), we obtain wave equations for the marine sediments with bubbles:

$$\begin{aligned}\frac{\partial^2 P}{\partial t^2} - \frac{m}{\rho_{0f}G}\frac{\partial^2 P}{\partial x^2} - \frac{\nu}{\rho_{0s}G}\frac{\partial^2\rho_s}{\partial t^2} &= \frac{nm}{G}\frac{\partial^2 V}{\partial t^2},\\ \frac{\partial^2\rho_s}{\partial t^2}(1-m) - \frac{k + 4/3\mu}{\rho_{0s}}\frac{\partial^2\rho_s}{\partial x^2} - \nu\frac{\partial^2 P}{\partial x^2} &= 0.\end{aligned} \tag{7}$$

Now, let us consider the bubble oscillations. For a single gas bubble, the equation of motion was derived in [2]:

$$\ddot{V} + \omega_0^2 V + f\dot{V} - \alpha V^2 - \beta(2\ddot{V}V + \dot{V}^2) = \epsilon P, \tag{8}$$

where ω_0 is the natural frequency of the bubble oscillation. The factors appearing in Eq. (8) can be expressed through the equilibrium volume V_0 of the bubble (or through its radius R_0) and the adiabatic index γ:

$$\begin{aligned}\alpha &= \omega_0^2(\gamma + 1), \quad \beta = 1/6V_0,\\ \epsilon &= 4\pi R_0/\rho_{0f}, \quad f = \delta\omega_0,\end{aligned}$$

where δ is the dimensionless absorption coefficient.

In the linear approximation, the volume perturbation has the form

$$V\exp(-i\omega t) = \frac{\epsilon P\exp(-i\omega t)}{\omega^2 - \omega_0^2 + if\omega}. \quad (9)$$

We consider the stimulated Raman-type scattering of the exciting acoustic wave $P_1\exp i(k_1x - \omega_1 t)$ by the bubble oscillations with the natural frequency ω_0. The resulting scattered wave of the difference frequency has the form $P_2\exp i(k_2x - \omega_2 t)$, where $\omega_2 = \omega_1 - \omega_0$. For a liquid, such a process was considered by Zabolotskaya [12]. For the sake of simplicity, we so far restrict our consideration to a situation when all bubbles have the same radius and, hence, the same natural frequency. The system of Eqs. (7) involves the only nonlinear term which is responsible for the Raman-type scattering: the right-hand side of the first equation. To be more precise, the volume V of the bubble, which appears in this term, is the sum of the linear and nonlinear components: $V^l + V^n$. The nonlinear amplitude V_2^n of the bubble oscillations is related to the sound wave P_2 that is produced by the scattering of the exciting wave P_1 by the bubble oscillations, which in turn are enhanced by the nonlinear interaction of the waves P_1 and P_2. This nonlinear amplitude can be obtained from Eq. (8) in the form

$$V_2^n = \frac{\epsilon^3[\alpha - \beta(\omega_1^2 + \omega_0^2 - \omega_1\omega_0)]^2}{2[(\omega_1^2 - \omega_0^2)^2 + \omega_1^2 f^2](\omega_0^2 - \omega_2^2 - i\omega_2 f)^2(-i\omega_0 f)}\left|P_1^2\right|P_2. \quad (10)$$

Note that, because Eq. (10) is obtained by the method of successive approximations, it is valid only far enough from the resonances $\omega_1 = \omega_0$ and $\omega_2 = \omega_0$. Therefore, one can neglect the attenuating terms in the two first factors of the denominator.

With the expression for the nonlinear part of the bubble oscillation amplitude, we can obtain an equation for the dependence of the scattered wave P_2 on distance. Let us eliminate the quantity ρ_s from Eq. (7). To do so, we represent $\delta\rho_s$ in the form

$$\delta\rho_s = \frac{\nu}{c^2}\left(1 - m - \frac{k + 4/3\mu}{\rho_{0s}c^2}\right)\delta P + \lambda, \quad (11)$$

where λ is the nonlinear correction to the linear relation between $\delta\rho_s$ and P, which can be derived, e.g., from the second equation of system (7); c is the sound speed in the sediment. By substituting this relation into system (7), we obtain the following equations:

$$\begin{aligned}
&\delta P_2\left[-1 + \frac{m}{\rho_f Gc^2} + \frac{\nu^2}{\rho_s Gc^2}\left(1 - m - \frac{k + 4/3\mu}{\rho_s c^2}\right)^{-1} - D\right] \\
&\quad - 2i\frac{k_2}{\omega_2^2}\frac{m}{\rho_f Gc^2}\frac{dP_2}{dx} + \frac{\nu}{\rho_s G}\lambda = \frac{nm}{G}V_2^n, \\
&2ik_2\nu\left[\frac{k + 4/3\mu}{\rho_s c^2}\left(1 - m - \frac{k + 4/3\mu}{\rho_s c^2}\right)^{-1} + 1\right]\frac{dP_2}{dx} \\
&\quad + \lambda\omega_2^2\left(1 - m - \frac{k + 4/3\mu}{\rho_s c^2}\right) = 0,
\end{aligned} \quad (12)$$

where D is expressed as

$$D = \frac{nm\epsilon}{G\omega_0^2}\frac{1}{1 - \omega_2/\omega_0}$$

and c is equal to the velocity of the sound wave P_2 for the case at hand. In these and the following equations, the subscript "0" is omitted in the equilibrium values of ρ_f and ρ_s. By linearly approximating Eq. (7), one can show that the expression appearing in the square brackets in the first equation of system (7) is equal to zero. Eliminating λ from these equations and using Eq. (10) for V_2^n, we obtain an equation for the dependence of the amplitude of the scattered wave P_2 on distance, with the natural assumption that it slowly varies within the distance equal to the wavelength

$$\frac{dP_2}{dx} + \tilde{\gamma}P_2 = NP_2, \quad (13)$$

where $\tilde{\gamma}$ is the amplitude attenuation coefficient for the sound wave. Here, N is the "nonlinear force"

$$N = \frac{2}{3}\frac{\pi^2 nV_0 c}{\rho_f^2\delta\omega_0^5 V_0^2 K}F(\Omega)\left|P_1^2\right|, \quad (14)$$

where

$$\begin{aligned}
K &= \frac{\nu^2}{m}\frac{\rho_f}{\rho_s}\left(1 - m - \frac{k + 4/3\mu}{\rho_s c^2}\right) \\
&\quad \times\left[\frac{k + 4/3\mu}{\rho_s c^2}\left(1 - m - \frac{k + 4/3\mu}{\rho_s c^2}\right)^{-1} + 1\right], \\
\Omega &= \omega_1/\omega_0,
\end{aligned} \quad (15)$$

$$F(\Omega) = \frac{[3\gamma + 2 - \Omega(\Omega - 1)]^2}{(\Omega - 1)(\Omega + 1)^2\Omega^2(\Omega - 2)^2}.$$

According to Eq. (13), the threshold intensity of the exciting wave, $I = |P_1|^2/2\rho c_1$, has the form

$$I = \frac{3\tilde{\gamma}\rho_f^2\delta\omega_0^5 V_0^2 K}{4\pi^2 n V_0 c_1 c_2 \rho F(\Omega)}, \qquad (16)$$

where ρ is the mean density of the sediment; the attenuation coefficient δ corresponds to the frequency ω_0: $\delta = \delta(\omega_0)$; and c_1 and c_2 are the velocities of the exciting and scattered sound waves, respectively.

The analysis of the frequency dependence $F(\Omega)$ given by Eq. (15) shows that, far from the resonant values $\Omega = 1$ and $\Omega = 2$, this function is always positive, except for the point $\Omega \approx 3$ where $F(\Omega) = 0$, and it takes its maximal values in the interval $1 < \Omega < 2$ (see figure). For the values of Ω that are higher than approximately 2.6, the function $F(\Omega)$ is small and can barely be distinguished from zero in the figure.

Let us numerically estimate the threshold intensity I. We use the values of the parameters specified for the marine sediments in [13]:

$$m = 0.4; \quad \rho_s = 2.65\ \text{g/cm}^3; \quad \rho_f = 1\ \text{g/cm}^3;$$

$$k = 1.08 \times 10^9\ \text{din/cm}^2;$$

$$\mu = 5.00 \times 10^8\ \text{din/cm}^2; \quad k_s = 3.6 \times 10^{11}\ \text{din/cm}^2.$$

Further, according to [14], we set $V_0 \approx 10^{-4}$ cm^3, $\omega_0 = 2\pi \times 10^4$ s^{-1}, and $\delta \approx 4 \times 10^{-2}$.

If we take $\Omega = 1.5$, we have $\omega_2 = 0.5\omega_0 = 0.5 \times 2\pi \times 10^4$ s^{-1}; for this frequency, $\tilde{\gamma} \approx 3 \times 10^{-3}$ cm^{-1} (see [15]), $\rho \approx \rho_f m + \rho_s(1 - m) \approx 2$ g/cm^3, $c_1 \approx c_2 \approx 1.7 \times 10^5$ cm/s.

With these values of the parameters, we obtain the following estimate for the threshold intensity:

$$I \approx 1.5 \times 10^{-1}(nV_0)^{-1}\ \text{erg cm}^{-2}\ \text{s}^{-1}.$$

For the characteristic values $nV_0 = 10^{-4}$–10^{-5}, this estimate yields

$$I \approx (10^3\text{–}10^4)\ \text{erg/cm}^{-2}\text{s}^{-1} \approx (10^{-4}\text{–}10^{-3})\ \text{W/cm}^2.$$

The results obtained above can be summarized as follows. The nonlinear equations that describe the propagation of a sound wave in marine sediments containing gas bubbles are obtained. The problem of the nonlinear Raman-type scattering by the bubble oscillations in the ocean bottom is solved. Numerical estimates of the threshold intensity of the exciting sound wave are obtained. The estimates show that the nonlinear scattering discussed above can be observed experimentally.

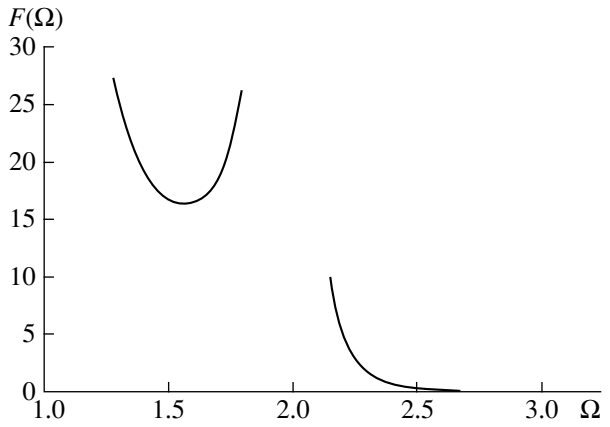

Figure.

REFERENCES

1. J. M. Hovem, J. Acoust. Soc. Am. **66**, 1463 (1979).
2. E. A. Zabolotskaya and S. I. Soluyan, Akust. Zh. **13**, 296 (1967) [Sov. Phys. Acoust. **13**, 251 (1967)].
3. V. G. Welsby and M. H. Safar, Acustica **22** (1), 177 (1969).
4. J. N. Didenkulov, S. W. Yoon, A. M. Sutin, and E. J. Kim, J. Acoust. Soc. Am. **106**, 2431 (1999).
5. F. A. Boyle and N. P. Chotiros, J. Acoust. Soc. Am. **98**, 531 (1995).
6. F. A. Boyle and N. P. Chotiros, J. Acoust. Soc. Am. **103**, 1328 (1998).
7. M. A. Biot, J. Acoust. Soc. Am. **28**, 168 (1956).
8. M. A. Biot, J. Acoust. Soc. Am. **28**, 179 (1956).
9. V. N. Nikolaevskiĭ, Mechanics of Porous and Cracked Media (Nedra, Moscow, 1984).
10. V. G. Bykov and V. N. Nikolaevskiĭ, Akust. Zh. **36**, 606 (1990) [Sov. Phys. Acoust. **36**, 342 (1990)].
11. R. D. Stoll, in *Ocean Seismo-Acoustics. Low Frequency Underwater Acoustics* (Plenum, New York, 1986), pp. 417–434.
12. E. A. Zabolotskaya, Akust. Zh. **31**, 601 (1985) [Sov. Phys. Acoust. **31**, 360 (1985)].
13. A. Turgut and T. Yamamoto, J. Acoust. Soc. Am. **87**, 2376 (1990).
14. H. Medwin, Ultrasonics **15**, 7 (1977).
15. N. P. Chotiros, J. Acoust. Soc. Am. **97**, 199 (1995).

Translated by E. Kopyl

Acoustical Physics, Vol. 47, No. 2, 2001, pp. 218–225. Translated from Akusticheskiĭ Zhurnal, Vol. 47, No. 2, 2001, pp. 264–272.

REVIEWS

Noise of a Turbulent Boundary Layer Flow over Smooth and Rough Plates at Low Mach Numbers

A. V. Smol'yakov

Krylov Central Research Institute, Moskovskoe sh. 44, St. Petersburg, 196158 Russia

e-mail: albert@krylov.spb.su

Received April 19, 2000

Abstract—The spectral levels of the quadrupole noise generated by a boundary layer flow over a smooth surface are calculated. Explicit dependences of the noise levels on the Reynolds number are obtained for the low-frequency and high-frequency ranges. It is shown that the logarithmic zone of the velocity profile is responsible for the region of the quadrupole noise spectrum with a hyperbolic dependence on frequency. A method of calculating the dipole noise of a boundary layer flow over a rough surface is developed. The method is based on the use of the combined probability density for the turbulent velocity fluctuations and the random dimensions of protuberances of the rough surface. The two constants involved in this theory are determined from a special experiment. It is shown that the surface roughness noticeably increases the radiation levels of a boundary layer flow in a certain frequency range. © *2001 MAIK "Nauka/Interperiodica".*

Noise generation by turbulent flows has attracted the attention of many researchers, which can be seen, e.g., from the review published few years ago [1]. Acoustic radiation of a boundary layer flow over an aerodynamically (hydrodynamically) smooth plate was theoretically studied in [2–4]. The results proved to be not fully coincident because of the difference in both the initial experimental data and the theoretical concepts used in these studies. The noise of a boundary layer flow over a rough surface was theoretically studied in [5–7] only for the case of the roughness elements that did not extend beyond the viscous sublayer, so that the flow about them experienced no separations.

In this paper, the approach used for studying the noise of a boundary layer flow over a smooth surface did not undergo any fundamental changes as compared to the approach used earlier [2, 3]. The previous results are quantitatively refined and, what is more important, represented in terms of several new spectrum normalizations, which allow one to clearly demonstrate the role of inertial and viscous forces in the noise generation by the flow at low and high frequencies. The noise of a boundary layer flow over a rough surface is studied for the case of a high degree of roughness, when the roughness elements exceed the thickness of the viscous sublayer by at least an order of magnitude and cause separations of the flow. The method developed for this study is based on new experimental data.

The main idea used earlier in [2, 3] (and later in [8], for the determination of turbulent pseudosound pressures) is as follows. For the characteristic scales of the velocity v and length ℓ of the turbulent fluctuations in a flow with the mean velocity shear $dU/dy \neq 0$, we use the relations

$$v \sim (\overline{u_1 u_2})^{1/2}, \quad \ell = (\overline{u_1 u_2})^{1/2}(dU/dy). \tag{1}$$

Here, U is the mean velocity in the boundary layer at the distance y from the surface and $\overline{u_1 u_2}$ is the single-point correlation between the longitudinal component of turbulent velocity fluctuations u_1 and the component normal to the wall u_2. The calculation of the scales given by Eqs. (1) with the use of simple relations of the semiempirical theory of turbulence [9, 10] allows us to determine the contributions made to the sound radiation by different boundary layer parts whose fluctuating motion depends in different ways on viscous and inertial forces.

As before, the intensity I of the quadrupole acoustic radiation (the radiation power per unit area of the surface contacting the flow) was determined from the relation derived on dimensional grounds:

$$I = k\rho c_0^{-5}\int_0^\infty \varepsilon^{7/2}\left(\frac{dU}{dy}\right)^{9/2} dy, \tag{2}$$

where ρ is the mass density of the medium; c_0 is the sound velocity; $\varepsilon = \overline{u_1 u_2}/(dU/dy)$ is the eddy viscosity; and k is the empirical constant, which was determined after solving a similar problem on the radiation power generated by cold subsonic turbulent jets whose noise could be reliably recorded [11].

Instead of the value $k = 20.4$ used in [2], we take the value $k = 43$, which was obtained after analyzing the experimental data [11] with allowance for the comment

made in [4] in connection with the papers [2, 3] about the necessity to consider the sound reflection from the plate. Some other constants were also refined, but their quantitative refinements were less significant. In calculating the local friction factor c_w at the surface contacting the flow, the Schlichting formula [10] was replaced by the more precise Falkner formula $c_w = 0.0263 R_x^{-1/7}$, where $R_x = U_0 x/\nu$, U_0 is the flow velocity at the outer boundary of the boundary layer, x is the distance from the leading edge of the plate, and ν is the kinematic viscosity. Then, the boundary layer thickness δ, the displacement thickness δ^*, and the momentum thickness θ are calculated by the formulas

$$\delta = (\nu/U_\tau)\exp[0.41(U_0/U_\tau - 7.4)];$$
$$\delta^*/\delta = 0.385 R_x^{-0.07}, \quad \theta/\delta = 0.209 R_x^{-0.05}, \tag{3}$$

where $U_\tau = \sqrt{\tau_w/\rho} = U_0\sqrt{c_w/2}$ is the friction velocity and τ_w is the friction stress at the surface under consideration. The first of expressions (3) was obtained in [8], and the other two are the approximations (Fig. 1) of the results obtained by numerically integrating the corresponding expressions, $(1 - U/U_0)$ and $(U/U_0)(1 - U/U_0)$, over the entire thickness of the boundary layer; the integration was also performed in [8].

Reconsidering the results presented in [2, 3] with allowance for the aforementioned refinements, we obtain that the spectrum of the quadrupole turbulent noise $P(\omega)$ normalized to the "inner" velocity U_τ and length ν/U_τ scales of the boundary layer is now described by the formulas

$$\frac{P(\omega)U_\tau^2}{\tau_w^2\nu} = M^4(c_w/2)^2 \times \begin{cases} 2.208\times 10^{-4}\bar{\omega}^{7/2}R_\tau^{9/2}[3.09 - \ln(\bar{\omega}R_\tau)]^{-1/2} \\ \text{for } \bar{\omega} \le \Omega \\ 50.82\bar{\omega}^{5/2}(1.23/\bar{\omega} - 1)^{7/2} \text{ for } \Omega \le \bar{\omega} \le 1.23. \end{cases} \tag{4}$$

Here, $\bar{\omega} = \omega\nu/U_\tau^2$, $\Omega = 16.0625/R_\tau$, $R_\tau = U_\tau\delta/\nu$, and $M = U_0/c_0$ is the Mach number.

Figure 2 presents the dimensionless spectra (4) for several values of the Reynolds numbers R_x and R_τ; the unique relationship between them, $R_\tau = \exp[0.41(8.72 R_x^{1/14} - 7.4)]$, is easily determined from the aforementioned Falkner formula and the first of Eqs. (3). One can see that the low-frequency radiation spectra, which are caused mainly by the large-scale inertial turbulence in the outer part of the boundary layer, form a family of curves. These curves display a relatively fast increase with frequency and correspond to the dimensionless frequencies $\bar{\omega}$, which are the lower, the higher the Reynolds number is.

As the limiting frequency $\Omega = 16.0625/R_\tau$ is reached, the spectra obtained for all Reynolds numbers acquire the form of a single universal dependence $P(\omega)U_\tau^2/[\tau_w^2\nu M^4(c_w/2)^2] \approx 50.82\ (1.23)^{7/2}/\bar{\omega} = 104.88/\bar{\omega}$, which, according to the calculations, is determined by the turbulent motion in the logarithmic part of the boundary layer. In connection with the result obtained here for the sound pressures, it should be noted that the hyperbolic law ω^{-1} was theoretically predicted by Bradshaw [12] for turbulent pseudosound pressures governed by the logarithmic part of the boundary layer, and this law was later verified by calculations [8]. From Fig. 2, it also follows that the length of the frequency range corresponding to the spectral decrease as $\bar{\omega}^{-1}$ is the smaller, the lower the Reynolds number is. At $R_x \approx 1.76\times 10^5$ ($R_\tau \approx 230$), this range vanishes.

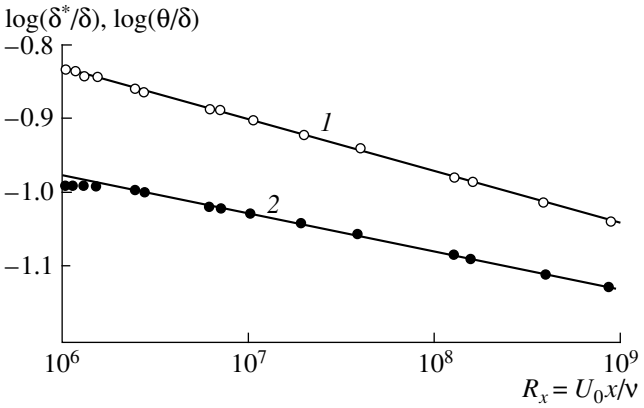

Fig. 1. Ratios of (*1*) the displacement thickness δ^* and (*2*) the momentum thickness θ to the thickness of the boundary layer δ as functions of the Reynolds number R_x: (○), (●) the results of numerical integration and (—) the approximation by Eqs. (3).

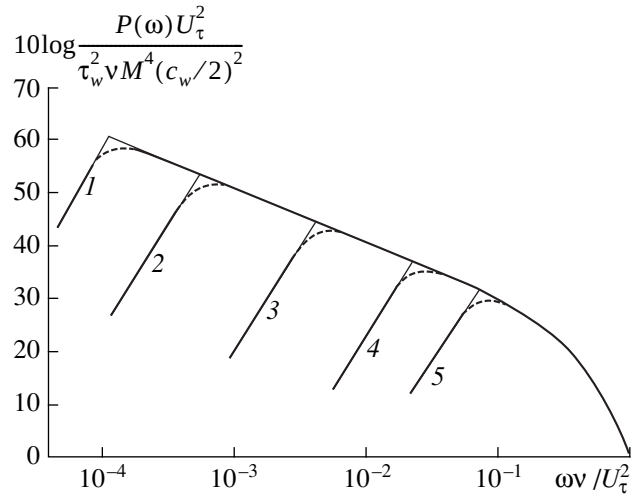

Fig. 2. Quadrupole noise spectra normalized by the "inner" scales: R_x = (*1*) 5×10^8, (*2*) 10^8, (*3*) 10^7, (*4*) 10^6, and (*5*) 1.76×10^5; R_τ = (*1*) 1.5×10^5, (*2*) 2.95×10^4, (*3*) 3.91×10^3, (*4*) 704, and (*5*) 230.

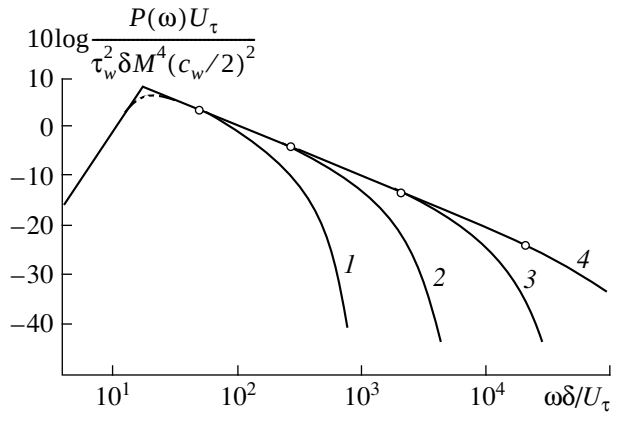

Fig. 3. Quadrupole noise spectra normalized by the "outer" length scale: R_x = (*1*) 10^6, (*2*) 10^7, (*3*) 10^8, and (*4*) 10^9.

Beginning from the frequency $\bar{\omega} \approx 0.07$, the radiation spectra for all Reynolds numbers $R_x \geq 1.76 \times 10^5$ are characterized by a single curve, which decreases more and more steeply with increasing frequency. The calculations show that this part of the spectrum is governed by the smallest scale turbulence in the viscous sublayer and the buffer zone of the boundary layer, which are located in the immediate vicinity of the plate where the viscous forces prevail over the inertial ones.

The presence of breaks in the radiation spectra at the boundaries $\bar{\omega} = \Omega$ between the low and medium frequencies is a consequence of the simplifications that were used in the dimensional analysis and allowed us to obtain solution (4) in a simple analytical form. One should expect that, in reality, the breaks will be replaced by smooth transitions from one part of the spectrum to the other, as, for example, is shown by the dashed lines in Fig. 2.

Figure 3 presents the radiation spectra with another normalization that uses the "outer" length scale, namely, the boundary layer thickness δ governing the motion of large-scale inertial vortex structures in the outer part of the boundary layer. One can see that, with such a normalization, the whole family of the low-frequency spectra shown in Fig. 2 merge into a single curve. This curve describes the dimensionless spectra $P(\omega)U_\tau/[\tau_w^2 M^4(c_w/2)^2\delta]$ in the dimensionless frequency range $0 < \omega\delta/U_\tau \leq 16.0625$ beyond which the spectra decrease first as $(\omega\delta/U_\tau)^{-1}$ and then more steeply. One can also see that, in contrast to the normalization used in Fig. 2, the spectra shown in Fig. 3 exhibit a pronounced splitting in the Reynolds number at medium and, especially, high frequencies $\omega\delta/U_\tau$ and extend the farther into the high-frequency region, the higher the Reynolds number is. The empty circles in Fig. 3 indicate the ends of the hyperbolic spectral regions, these ends corresponding to the dimensionless frequency $\omega\nu/U_\tau^2 \approx 0.07$ in Fig. 2. The formulas used for obtaining the spectra shown in Fig. 3 can be easily derived on the basis of dependences (4) and the evident relationship between the "outer" and "inner" length scales: $\delta = (\nu/U_\tau)R_\tau$.

The normalization of turbulent pseudosound pressures is often performed by using "mixed" (according to the terminology used in [13]) scales of velocity and length, U_0 and δ^*, which allow one to obtain the dimensionless noise spectra in the form

$$\frac{P(\omega)U_0}{\tau_w^2\delta^*} = M^4(c_w/2)^2\Phi\left(\frac{\omega\delta^*}{U_0}, R_x\right). \qquad (5)$$

According to Eq. (2), Eqs. (4) and (5) describe the spectra of the noise generated by a unit area of the plate surface. If the plate dimensions are finite, but sufficiently large for neglecting the additional noise produced by the flow around the plate edges [14], the factor $S/(2\pi r^2)$ should be added on the right-hand sides of Eqs. (4) and (5). This factor indicates that the total radiation energy increases in proportion to the area S of the surface contacting the flow and is approximately uniformly distributed over the surfaces $2\pi r^2$ of all hemispheres located above the plate sufficiently far from it ($r^2 \gg S$). After multiplying the right-hand sides of Eqs. (4) and (5) by $S/(2\pi r^2)$, we can normalize both sides of these equations by the dimensionless ratio (S/r^2). As a result, the radiation spectra (for any, but sufficiently large, values of S and r on condition that $r^2 \gg S$) will be described by the dependences of the type

$$\frac{P(\omega)U_0}{\tau_w^2\delta^*}\left(\frac{r^2}{S}\right) = \frac{M^4}{2\pi}\left(\frac{c_w}{2}\right)^2\Phi\left(\frac{\omega\delta^*}{U_0}, R_x\right). \qquad (6)$$

Such a normalization is used in the alternative estimate [4] of the radiation spectrum of the turbulent noise produced by a boundary layer flow. Figure 4 shows the estimate (Fig. 9.16 in [4]) corresponding to the Mach number $M = 10^{-2}$ and independent of the Reynolds number together with the results of our calculations for different Reynolds numbers. Both estimates depend on the Mach number in the same way, $P(\omega) \sim M^4$, which corresponds to the quadrupole radiation of a boundary layer flow over a smooth surface. One can see that the estimate obtained in [4] predicts higher radiation levels in the region of high dimensionless frequencies $\omega\delta^*/U_0$, but its extrapolation to the low-frequency region, presumably, will provide lower levels than our estimate. These differences are hardly of practical significance for small Mach numbers, because both estimates yield very low levels, which can be considered as some ideal limits in designing engineering structures and cannot be achieved in reality because of the inevitable presence of more powerful acoustic sources of other origins. However, for large Mach numbers, the level of the noise generated by the boundary layer flow is not always negligibly low, and, therefore, the difference in the predictions should not be neglected. By now, it is difficult to indicate the origin of the difference

in the noise levels predicted by different methods. One can only assume that it may be caused by the fact that the estimate given by Eq. (9.52) from [4] is indirectly based on the results of measurements of the wave number–frequency spectra of turbulent pressures at both smooth and rough surfaces (Fig. 8.30 in [4]). As will be shown below (Fig. 9), the surface roughness considerably increases the noise level especially at high frequencies.

Quadrupole sources of sound of different intensities and frequencies occur throughout the entire thickness of the boundary layer, excluding the surface [2, 3] where the turbulent velocity fluctuations are zero. At the surface of a rigid plate, the dipole sources of sound are also absent [15–17], provided that the plate surface is smooth. The presence of roughness on the surface contacting the flow changes the situation both quantitatively and qualitatively. First, the roughness increases the skin friction in the flow thus intensifying the turbulent velocity fluctuations within the entire boundary layer thickness. This, in its turn, leads to an increase in the quadrupole radiation in proportion to the product $\tau_w^2 c_w^2$, according to Eqs. (4)–(6). Second (which is more important), the flow about the protuberances of the rough surface is accompanied by the formation of a set of local flow separations. This gives rise to a dipole radiation, which at low Mach numbers is much more intense than the quadrupole radiation.

Figure 5 shows the schematic diagram of a boundary layer flow near a rough surface. The mean velocity of the flow about protuberances of a rough surface is $8.5U_\tau$ [10] for a fully-developed roughness $R_h^* = U_\tau h/\nu \geq 70$ (h is the statistical mean height of protuberances). It is known that the dipole radiation accompanying a flow separation behind a bluff obstacle, e.g., a cylinder, has a pronounced Strouhal frequency $f = \mathrm{Sh}(U/d)$, where U is the flow velocity; d is the size of the cross-section of the bluff body; and Sh is the Strouhal number, which is approximately equal to 0.2 for a cylinder. It is also known that the radiation power in this case is characterized by the dependence $W \sim \rho U^6 c_0^{-3} Ld$, where c_0 is the sound velocity and L is the cylinder length. Taking into account that the mean velocity of the flow around the surface protuberances is $8.5U_\tau$, where $U_\tau = U_0\sqrt{c_w/2}$, the radiation power produced by one roughness element with the height h and the transverse dimension d can be determined as $W \sim \rho c_w^3 U_0^3 M^3 hd$, where $M = U_0/c_0$ is the Mach number. We assume that, on the average, the size of the protuberances of the rough surface is proportional to their height: $d \sim h$. It is evident that the number of protuberances n on the surface of area S is inversely proportional to their cross-sectional area: $n \sim S/d^2 \sim S/h^2$. With allowance for these simple geometric considerations, the radiation power produced by a flow around n elements lying within the area S can be

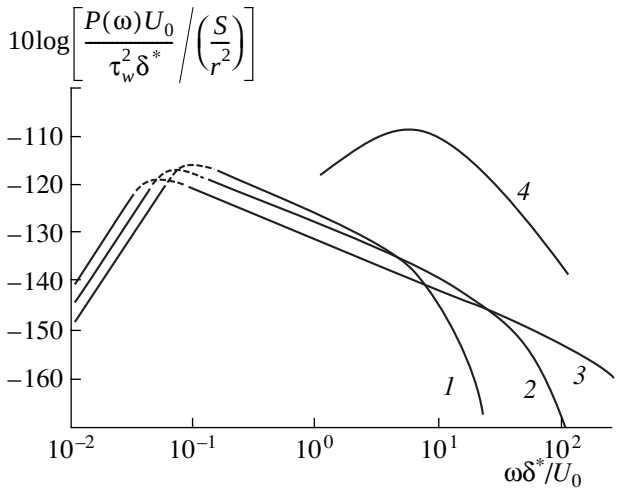

Fig. 4. Quadrupole noise spectra at a distance r from the plate of area S for the Mach number $M = 10^{-2}$: $R_x = (1)\ 10^7$, $(2)\ 10^8$, and $(3)\ 10^9$; and (4) the estimate from [4].

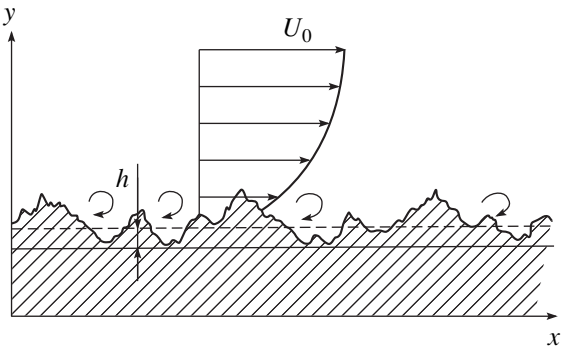

Fig. 5. Schematic diagram of a boundary layer flow over a rough surface.

expressed by the formula $W_{rh} = k_{rh}(S/h^2)\rho c_w^3 U_0^3 M^3 h^2 = k_{rh} S\rho c_w^3 U_0^3 M^3$ and the corresponding radiation intensity, $I_{rh} = W_{rh}/S$, will have the form

$$I_{rh} = k_{rh}\rho c_w^3 U_0^3 M^3, \tag{7}$$

where k_{rh} is the dimensionless coefficient of proportionality, which is to be determined from the experiment.

In a turbulent boundary layer flow over a surface with a uniform roughness, a statistical set of local flow separations from the roughness elements is formed. The accompanying radiation of vortex sound presumably occurs not at the single Strouhal frequency, but in a fairly wide frequency range. This is explained by two factors. First, the velocity of the flow around every protuberance continuously varies due to the turbulent fluctuations in the boundary layer. Second, the radiation should occur at different frequencies, because each pro-

tuberance has its individual dimensions, which randomly vary near the statistical mean height h. Both these factors should cause the appearance of a whole spectrum of different radiation frequencies in the flow about a rough surface.

The random turbulent velocity U_s of the flow about the roughness elements can be described with a sufficient accuracy by the normal law of the probability distribution with the mathematical expectation $8.5U_\tau$ and variance U_τ^2:

$$w_1(U_s) = \frac{1}{U_\tau\sqrt{2\pi}}\exp\left[-\frac{(U_s - 8.5U_\tau)^2}{2U_\tau^2}\right]. \quad (8)$$

For the probability distribution $w_2(h_s)$ of the random dimensions h_s of the rough surface protuberances, no reliable data are available, but it seems to be reasonable to assume that this distribution obeys the Rayleigh, Maxwell, or χ^2-distribution law, which excludes the probability of negative heights of protuberances and determines an almost unrealizable probability for too large values of the random quantity h_s. We will use the specific type of the χ^2-distribution [18]:

$$w_2(h_s) = \frac{6}{h\Gamma(6)}\left(\frac{6h_s}{h}\right)^5\exp\left(-\frac{6h_s}{h}\right), \quad (9)$$

where $\Gamma(x)$ is the gamma-function and $h = \int_0^\infty h_s w_2(h_s)dh_s$ is the statistical mean height of protuberances of the rough surface.

The distribution functions (8) and (9) correspond to the mutually independent random quantities U_s and h_s. Therefore, the combined two-dimensional probability density is characterized by the multiplicative property:

$$w_3(U_s, h_s) = w_1(U_s)w_2(h_s). \quad (10)$$

In a flow with the velocity U_s around a protuberance of height h_s, the radiation occurs mainly at the frequency $\omega = m(U_s/h_s)$, where m is a coefficient, which has the same meaning as the Strouhal number for a cylinder, Sh = 0.2, but may have another numerical value. Then, according to the known laws of mathematical statistics, the probability distribution function for the radiation frequencies will have the form

$$w(\omega) = \int_0^\infty w_3(U_s, h_s)\frac{dh_s}{\left|\frac{\partial}{\partial U_s}\left(m\frac{U_s}{h_s}\right)\right|} = \frac{1}{m}\int_0^\infty h_s w_3\left(\frac{\omega h_s}{m}, h_s\right)dh_s. \quad (11)$$

Substituting Eqs. (8)–(10) in Eq. (11) and introducing the notations $z = 6h_s/h$ and $\xi = \omega h/(U_0\sqrt{c_w}\,6m)$, we derive the expression

$$w(\omega) = \frac{1.604\times10^{-19}}{m}\frac{h}{U_0\sqrt{c_w}}\varphi(\xi). \quad (12)$$

The function

$$\varphi(\xi) = \int_0^\infty z^6\exp[-\xi^2z^2 + (8.5\sqrt{2}\xi - 1)z]dz \quad (13)$$

involved in Eq. (12) is shown in Fig. 6 by the solid curve. For obtaining the estimates, we can perform the calculations with the use of the approximate functions

$$\varphi \approx \begin{cases} 1.625\times10^{19}\xi^5 10^{-3.83\log^2(1.367\xi)} & \xi < 0.602 \\ 9.975\times10^{17}\times10^{-3.83\log^2(1.367\xi)} & \xi > 0.602, \end{cases}$$

which are shown in Fig. 6 by the dashed curve.

As any probability density, the distribution function (12) satisfies the conventional normalization condition

$$\int_0^\infty w(\omega)d\omega = 1. \quad (14)$$

Evidently, the probability $w(\omega)$ is proportional to the spectrum $P_{rh}(\omega)$ of the dipole radiation caused by the flow about a rough surface just as integral (14) is proportional to the integral of the spectrum $P_{rh}(\omega)$ over all frequencies. To determine the relationship between $w(\omega)$ and $P_{rh}(\omega)$, we take into account that the radiation intensity given by Eq. (7) is related to the mean square sound pressure $\overline{p_{rh}^2}$ and the spectrum $P_{rh}(\omega)$ in the following way:

$$\int_0^\infty P_{rh}(\omega)d\omega = \overline{p_{rh}^2} = I_{rh}\rho c_0 = k_{rh}\rho^2c_w^3U_0^4M^2, \quad (15)$$

which yields

$$\int_0^\infty \frac{P_{rh}(\omega)d\omega}{k_{rh}c_w^3\rho^2U_0^4M^2} = 1.$$

Comparing this result with Eqs. (14) and (12), we obtain

$$P_{rh}(\omega) = K_{rh}(c_w)^{5/2} \times h\rho^2U_0^3M^2\varphi[\omega h/(U_0\sqrt{c_w}6m)], \quad (16)$$

where K_{rh} denotes a new empirical constant replacing the old one k_{rh}: $K_{rh} = 1.604\times10^{-19}k_{rh}/m$. From Eq. (16), it follows that the form of the radiation spectrum is determined by function (13) shown in Fig. 6. The posi-

tion of the spectrum on the dimensionless frequency axis, $\omega h/(U_0\sqrt{c_w})$, is determined by the value of the yet unknown constant m, and the spectral levels are governed by the other constant K_{rh}. Both constants are determined experimentally.

The measurements were performed on the lower wall of the closed-jet part of the low-noise, low-turbulence wind tunnel belonging to the Krylov Central Research Institute (the description of the wind tunnel can be found in [19]). The sand-type roughness of the surface contacting the flow was formed by abrasive paper pasted on one of the four walls along the entire working section of the wind tunnel. Two kinds of abrasive paper were used: no. 50 with $h = 0.5$ mm and no. 80 with $h = 0.9$ mm. The flow velocity in the working section was set at intervals of 10 m/s: $U_0 = 20$, 30, 40, and 50 m/s. The measurements covered the ranges of the Reynolds numbers: with respect to the displacement thickness, $U_0\delta^*/\nu$, from 4.5×10^3 to 3.3×10^4; with respect to the height of protuberances of the rough surface, $U_\tau h/\nu$, from 80 to 160; and with respect to the dimensionless frequencies, $\omega\delta^*/U_0$, from 0.4 to 12.5. The pressure fluctuations were measured by piezoceramic transducers whose receiving surfaces 1.2 mm in diameter were mounted flush with the wall and by B&K plane capacitor microphones with the diameters 1/8 and 1/4 inches (3.175 and 6.35 mm).

The turbulent pseudosound pressures that occurred in the boundary layer flow at the rough surface acted on the receiving surfaces of the transducers simultaneously with the sound pressures caused by the dipole vortex sound that accompanied the flow separation from the protuberances of the rough surface. The analysis of the results showed that the turbulent pseudosound pressures prevailed in the low-frequency range, from the lowest frequencies to 1–5 kHz (in the given experimental conditions), while the sound pressures were dominant in the frequency range from 10 to 30–40 kHz. In the intermediate frequency range, from 5 to 8–10 kHz, the levels of the pseudosound and sound pressures were comparable. Figure 7 schematically depicts the typical frequency spectrum and cross-spectrum measured in the experiment. In the low-frequency range *1*, the frequency spectrum (Fig. 7a) exhibits a monotonic behavior typical of turbulent pseudosound pressures; in the intermediate frequency range *2*, the spectral curve breaks, and, at higher frequencies (frequency range *3*), one can see an increase in the spectral levels, which is not typical of pseudosound spectra. This fact alone cannot reliably prove that the spectrum observed in region *3* corresponds to the acoustic radiation of the boundary layer flow. Such a proof can be obtained from the measurements of the cross-spectra (Fig. 7b). It was found that, at low frequencies, the dimensionless longitudinal cross-spectrum, which was adequately normalized by the phase velocity close to the flow velocity, practically vanished at frequencies of 3–5 kHz. In other words, in the low-frequency range *1*,

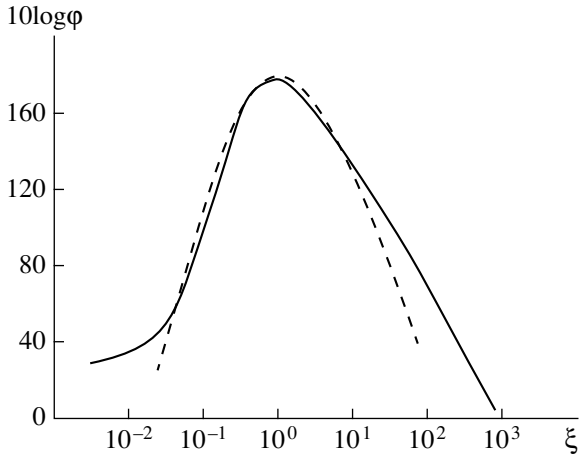

Fig. 6. The function φ(ξ) (the solid line) and its approximation (the dashed line).

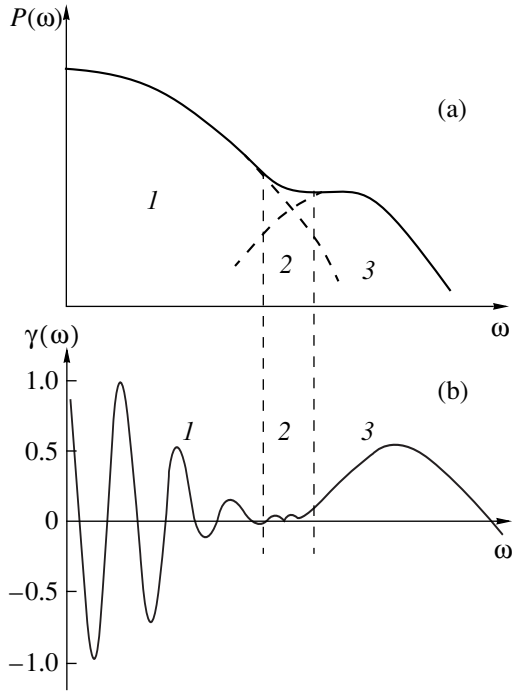

Fig. 7. Typical results obtained by measuring the pseudosound and sound pressure fluctuations at a rough surface: (a) the frequency spectrum and (b) the dimensionless cross-spectrum at a constant separation; (*1*) the pseudosound region, (*2*) the intermediate region, and (*3*) the sound region.

the behavior of the longitudinal cross-spectrum corresponds to its behavior in the field of turbulent pseudosound pressures [4, 19–21]. In the high-frequency region *3*, the cross-spectrum has the form of an oscillatory function with the dimensionless oscillation amplitude reaching relatively large values of 0.35–0.40, which points to a strong correlation of pressure fluctuations at higher frequencies. Such a correlation is quite unnatural for pseudosound [19–21]. The analysis

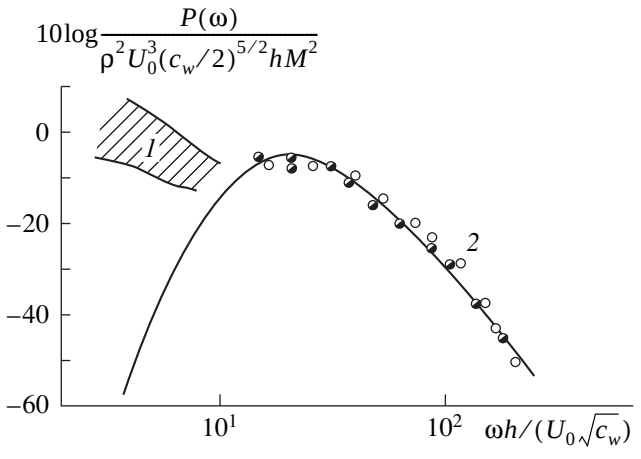

Fig. 8. Dimensionless spectrum of the dipole noise at a rough surface: (*1*) the pseudosound region; (*2*) the dipole noise; (○), (●) the results of measurements for the flow velocity U_0 = 20 and 50 m/s; and (—) the results of the calculations.

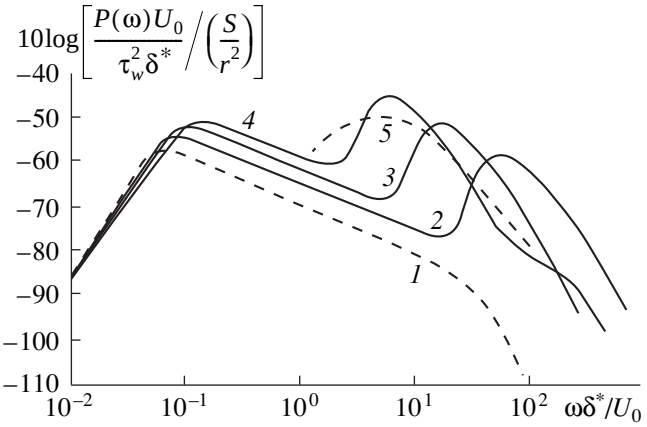

Fig. 9. Spectra of the total (quadrupole and dipole) noise for the Mach number M = 0.3 and the Reynolds number $R_x = 10^8$: (*1*) a smooth surface ($R_h^* = 0$); a rough surface with R_h^* = (*2*) 100, (*3*) 500, and (*4*) 2000; and (*5*) the estimate from [4].

showed that the normalizing phase velocity for the oscillations in the high-frequency region exceeds the flow velocity by an order of magnitude and reaches 300–350 m/s, which is close to the sound velocity in air. Hence, in our experiment with the flow about the rough surface, in the high-frequency region *3* we actually recorded the sound pressure fluctuations, which were absent in the experiments in a low-noise wind-tunnel with a flow over a smooth surface [19]. The statement that, in our experiment, we observed the acoustic radiation of the boundary layer rather than pseudosound is also confirmed by the fact that transducers with different dimensions, e.g., 1/4- and 1/8-inch microphones, perceived the spectral components at these frequencies in the same way. The turbulent pseudosound fluctuations that occur at frequencies above 20–30 kHz are caused by such small vortices that an increase in the transducer diameter by a factor of two should lead, due to the averaging effect, to a decrease in the measured spectral levels by approximately 6 dB [20, 21]. This must not occur (and did not occur in reality) when the pressure fluctuations are caused by sound waves whose wavelengths exceed those of pseudosound pressure-fluctuation waves by about an order of magnitude.

In the experiments, it was found that, in the high-frequency region, the spectral levels increase in proportion to the size of the roughness elements h and to the fifth power of the flow velocity U_0, in compliance with Eq. (16). Figure 8 compares the measured spectral levels of the turbulent noise at a rough surface with the levels calculated by Eq. (16). The friction coefficient c_w at the rough surface was calculated by the Schlichting formula [10] $c_w = [2.87 + 1.58\log(R_x/R_h)]^{-2}$, where $R_h = U_0 h/\nu$. The constant m involved in Eq. (16) and determining the position of the spectral maximum on the frequency axis was obtained by fitting the computations to the experimental data: $m \approx 3.81$. Thus, the maximum of the noise spectrum of the boundary layer flow occurred at the dimensionless frequency $\omega h/(U_0\sqrt{c_w}) \approx 16.7$. As was expected, the spectrum of the dipole noise of the boundary layer flow over a rough surface proved to be a broadband one: it covered almost two decades of the frequency range for a spectral level drop of 45–50 dB relative to the maximum. In determining the other empirical constant K_{rh}, which governs the levels of the spectra given by Eq. (16), it was necessary to take into account the effect of the walls of the closed-jet section of the wind tunnel on the results of the turbulent noise measurements. Using the statistical theory of room acoustics [22], we obtained an approximate estimate of the increase in the measured noise levels because of the noise accumulation inside the channel, which consisted of four thick metal plates with the dimensions 1.3×4.0 m^2 [19] (in the calculations, the plates were assumed to be perfectly rigid). The estimate showed that the measured levels were by approximately 11 dB higher than the radiation levels in a free space. With allowance for this correction for the results of measurements (Fig. 8), one should set $K_{rh} \approx 2.53 \times 10^{-20}$ in Eq. (16).

Figure 9 presents the frequency spectra of the noise generated by the boundary layer flow over a rough surface with the normalization (6) for the Mach number M = 0.3; the Reynolds number $R_x = U_0 x/\nu = 10^8$; and three different numbers $R_h^* = U_\tau h/\nu$ = 100, 500, and 2000 characterizing the degree of roughness. This figure also shows the radiation spectrum of a boundary layer flow over a smooth surface ($R_h^* = 0$) for the same values of M and R_x. In the calculations, it was assumed that the ratio of the displacement thickness to the boundary layer thickness was the same for the smooth

and rough surfaces, and the displacement thickness for the rough surface was expressed through the displacement thickness for the smooth surface by the formula $\delta^*_{rh} = 0.523\delta^*(U_0h/\nu)^{-1/7}$ [23]. Curve *5* in Fig. 9 corresponds to the estimate obtained in [4, Fig. 9.17] on the basis of the experimental data for both smooth and rough surfaces. From Fig. 9, one can see that, in a certain frequency range, the roughness of the surface contacting the flow noticeably increases the levels of noise generated by the turbulent boundary layer flow.

ACKNOWLEDGMENTS

I am grateful to V.P. Marshov for his participation in the experiment.

REFERENCES

1. J. E. Ffowcs Williams, J. Sound Vibr. **190**, 387 (1996).
2. A. V. Smol'yakov, Akust. Zh. **19**, 251 (1973) [Sov. Phys. Acoust. **19**, 65 (1973)].
3. A. V. Smol'yakov, Akust. Zh. **19**, 420 (1973) [Sov. Phys. Acoust. **19**, 271 (1973)].
4. W. K. Blake, *Mechanics and Flow-Induced Sound and Vibration* (Academic, New York, 1986).
5. M. I. Rabinovich, V. P. Reutov, and G. V. Rybushkina, Akust. Zh. **30**, 105 (1984) [Sov. Phys. Acoust. **30**, 60 (1984)].
6. M. S. Howe, J. Sound Vibr. **104**, 29 (1986).
7. M. S. Howe, Proc. R. Soc. London, Ser. A **415**, 141 (1988).
8. A. V. Smol'yakov, Akust. Zh. **46**, 401 (2000) [Acoust. Phys. **46**, 342 (2000)].
9. J. O. Hinze, *Turbulence, an Introduction to Its Mechanism and Theory* (McGraw-Hill, New York, 1959; Fizmatlit, Moscow, 1963).
10. H. Schlichting, *Grenzschicht-Theorie* (G. Braun, Karlsruhe, 1965; McGraw-Hill, New York, 1968; Nauka, Moscow, 1974).
11. A. G. Munin, V. M. Kuznetsov, and E. A. Leont'ev, *Aerodynamical Sources of Sound* (Mashinostroenie, Moscow, 1981).
12. P. Bradshaw, J. Fluid Mech. **30**, 241 (1967).
13. W. L. Keith, D. A. Hurdis, and B. M. Abraham, J. Fluids Eng. **114**, 338 (1992).
14. J. E. Ffowcs Williams and L. H. Hall, J. Fluid Mech. **70**, 657 (1970).
15. M. S. Howe, J. Sound Vibr. **65**, 159 (1979).
16. A. V. Smol'yakov, Akust. Zh. **35**, 506 (1989) [Sov. Phys. Acoust. **35**, 296 (1989)].
17. A. V. Smol'yakov, Acustica **80**, 541 (1994).
18. G. Korn and T. Korn, *Mathematical Handbook for Scientists and Engineers*, 2nd ed. (McGraw-Hill, New York, 1961; Nauka, Moscow, 1968).
19. A. V. Smol'yakov and V. M. Tkachenko, Akust. Zh. **37**, 1199 (1991) [Sov. Phys. Acoust. **37**, 627 (1991)].
20. G. M. Corcos, J. Acoust. Soc. Am. **35**, 192 (1963).
21. A. V. Smol'yakov and V. M. Tkachenko, *The Measurement of Turbulent Fluctuations* (Énergiya, Leningrad, 1980; Springer-Verlag, Berlin, 1983).
22. V. K. Iofe, V. G. Korol'kov, and M. A. Sapozhkov, *A Handbook on Acoustics* (Svyaz', Moscow, 1979).
23. L. G. Loĭtsyanskiĭ, *Fluid Mechanics* (Fizmatlit, Moscow, 1973).

Translated by E. Golyamina

Acoustical Physics, Vol. 47, No. 2, 2001, pp. 226–235. Translated from Akusticheskiĭ Zhurnal, Vol. 47, No. 2, 2001, pp. 273–282.

REVIEWS

Sound Propagation in a Planar Channel in the Presence of a Two-Layer Flow

A. F. Sobolev

State Research Center Zhukovskiĭ Central Aerohydrodynamics Institute, ul. Radio 17, Moscow, 107005 Russia

Received April 25, 2000

Abstract—Expressions describing the field of a point source in a planar channel with admittance walls enclosing a two-layer nonuniform flow are obtained. The dispersion equation that determines the eigenvalues in a wide range of flow velocities in the layers (including supersonic velocities) is studied. The effect of the admittance of the channel walls on the growth rate of unstable disturbances is considered for different frequencies. It is established that the effect of the admittance of the channel walls on the growth rate of the instability waves decreases with increasing frequency and essentially depends on the type of admittance. It is shown that, in the presence of the admittance, new unstable disturbances are formed with a growth rate that can exceed that of the Kelvin–Helmholtz instability wave. © *2001 MAIK "Nauka/Interperiodica".*

An effective means for suppressing the low-frequency noise of an aircraft engine is an ejector nozzle for the exhaust jet. The noise suppression occurs owing to the decrease in the mean velocity and temperature of the average flow formed in the ejector channel as a result of the mixture of the cold ejected air and the hot jet. This kind of silencer had always attracted the interest of engineers, and, in recent years, this interest has grown in connection with the development of a supersonic passenger airplane of the second generation [1–4]. The central place is occupied by the studies of disturbances originating from the unstable shear layer formed between the ejected flow and the fast jet [5]. The analysis of the instability nature was performed in [6] on the basis of the study of the supersonic mixing layer inside a rectangular channel with rigid walls. It was found that the interaction of this layer with the acoustic modes reflected from the walls gives rise to a new family of supersonic unstable solutions in addition to the known Kelvin–Helmholtz (K–H) instability [7]. Attempts were made to affect the unstable disturbances and to reduce the degree of instability by applying a sound-absorbing lining (SAL) to the channel walls [8–10]. It was found that, in some cases, the rate of growth of unstable waves can be reduced, and this effect is largely determined by the choice of the appropriate parameters of the SAL. In particular, it is important that the impedance of the SAL has a negative imaginary part [9].

The studies mentioned above were concerned only with the unstable modes formed in a channel with perfectly rigid walls, because it was believed that just these modes are responsible for the low-frequency noise. However, it is also of interest to study the effect of the admittance of the walls on the whole set of modes existing in the ejector channel, including the unstable modes, in a wider frequency range and a wider range of Mach numbers, as compared to the previous studies. On the other hand, the ejection of air in the channel leads to an increase in the high-frequency noise component, which can be even more unfavorable from the ecological point of view [11]. The other important question that should be answered in this connection arises from the strict limitations imposed on the ejector dimensions, namely the following: How effective is the use of the SAL for reducing the degree of instability of modes in view of the fact that this method leads to a loss of the possibility of noise suppression at high frequencies? It may be more expedient to use other methods for suppressing the unstable modes, and the SAL should be used for the noise suppression in the high-frequency range.

In this paper, we use a point source model to study the modal structure of the acoustic field in a lined planar channel with a two-layer flow whose layers are characterized by different parameters. Taking into account the rather high velocities of the flows in the layers, the real mixing layer can be replaced for simplicity by a tangential discontinuity boundary, at least within a relatively long initial part of the channel. As is known, the flows with tangential discontinuities are unstable with respect to the initial excitation [7]. However, the results obtained on the basis of this representation have a certain domain of applicability [12, 13] and can be useful in studying the sound propagation in moving layered media, including the study of unstable solutions.

Let us consider the propagation of sound in a planar channel of height H. The sound is generated by a simple point source. The flow consists of two layers with the parameters V_j, ρ_j, c_j, and H_j, where V_j is the flow velocity, ρ_j is the density of the medium, c_j is the sound

1063-7710/01/4702-0226$21.00

velocity, H_j is the layer thickness, and the subscript $j = 1$ or 2 corresponds to the lower or the upper layer, respectively. The channel walls are described by the complex admittance β_j. The acoustic field formed in each of the layers satisfies the convective wave equation

$$-\frac{1}{c_j^2}\frac{D_j^2 p_j}{Dt^2} + \nabla^2 p_j = -A_0\delta(x - x_0, y - y_0)\exp(-i\omega t), \quad (1)$$

where p_j is the sound pressure, A_0 is the source amplitude, (x, y) are the coordinates of the point of observation, (x_0, y_0) are the source coordinates, ω is the circular frequency, and $D_j/Dt = -i\omega + V_j\partial/\partial x$ ($j = 1, 2$). The boundary conditions at the lower ($y = 0$, $j = 1$) and upper ($y = H$, $j = 2$) walls of the channel have the form [14]

$$i\omega\partial p_j/\partial y = (-1)^j(\beta_j/c_j)D_j^2 p_j/Dt^2. \quad (2)$$

If we represent the vortex layer as a thin membrane that is permeable for sound but impermeable for the flow, then, for the regions under the membrane and over it, we obtain the respective relationships [12]

$$\partial p_j/\partial y = -\rho_j D_j^2 \eta/Dt^2; \quad j = 1, 2, \quad (3)$$

where η is the normal displacement of the membrane. In addition, in the vortex layer region, the condition of the pressure continuity must be satisfied: $p_1 = p_2$. The boundary-value problem represented by Eqs. (1)–(3) is solved by applying the Fourier transform, as in the previous publications [14, 15]. Assuming that the source is in region *1*, for the Fourier transform we obtain the following expressions:

$$P_1 = \begin{cases} \dfrac{\tilde{A}_0}{\chi_1}\dfrac{\cos(\chi_1 y_0 - \phi_1)}{\sin(\phi_1 - \phi_2)}\cos(\chi_1 y - \phi_2), & y_0 \le y \le H_1 \\ \dfrac{\tilde{A}_0}{\chi_1}\dfrac{\cos(\chi_1 y_0 - \phi_2)}{\sin(\phi_1 - \phi_2)}\cos(\chi_1 y - \phi_1), & 0 \le y \le y_0, \end{cases} \quad (4)$$

$$P_2 = \frac{\tilde{A}_0\cos(\chi_1 y_0 - \phi_1)\cos(\chi_1 H_1 - \phi_2)}{\chi_1\sin(\phi_1 - \phi_2)\cos(\chi_2 H_2 - \varphi_2)} \times \cos(\chi_2(H - y) - \varphi_2), \quad H_1 \le y \le H, \quad (5)$$

where

$$P_j = \int_{-\infty}^{\infty} p_j\exp(-i\xi x)d\xi, \quad \tilde{A}_0 = A_0\exp(-i\omega t - i\xi x_0),$$

$$\tan(\phi_1) = -G_1, \quad \tan(\varphi_2) = -G_2,$$

$$G_j = ik_j\beta_j S_j/\chi_j, \quad S_j = (1 - M_j\xi/k_j)^2, \quad k_j = \omega/c_j,$$

$$M_j = V_j/c_j, \quad \tan(\phi_2) = \frac{\tan(\chi_1 H_1) - R}{1 + R\tan(\chi_1 H_1)},$$

$$R = -Z\tan(\chi_2 H_2 - \varphi_2), \quad Z = \chi_2\rho_1 S_1/\chi_1\rho_2 S_2,$$

$$\chi_j^2 = (k_j - M_j\xi)^2 - \xi^2, \quad j = 1, 2, \quad (6)$$

$$\sin(\phi_1 - \phi_2) = -F(\xi)\cos(\chi_1 H_1 - \phi_1)/\cos(\chi_1 H_1 - \phi_2), \quad (7)$$

$$F(\xi) = \sin(\chi_1 H_1 - \phi_2)\cos(\chi_2 H_2 - \varphi_2) + Z\cos(\chi_1 H_1 - \phi_2)\sin(\chi_2 H_2 - \varphi_2). \quad (8)$$

Formally, the acoustic field in the channel is determined by the inverse Fourier transforms of Eqs. (4) and (5). These expressions have singular points in the form of the poles that are the solutions to the dispersion equation $F(\xi) = 0$, where $F(\xi)$ is determined by Eq. (8). Hence, the integration can be reduced to the summation over the poles. Since these expressions contain no branching points, the spatial spectrum will be discrete. It should be noted that, at $M_1 = M_2$, the dispersion equation, as well as Eqs. (4) and (5), pass into the equation and the Fourier transforms obtained earlier for a channel with a uniform flow [15]. From Eq. (7), it follows that, at the poles, we have $\phi_1 = \phi_2$. The residues at the poles, which correspond to Eqs. (4) and (5), have the form

$$\mathrm{Res}_{P_1} = -\frac{\tilde{A}_0}{\chi_1}\frac{\cos(\chi_1 y_0 - \phi_1)\cos(\chi_1 y - \phi_1)\cos(\chi_2 H_2 - \varphi_2)}{\cos(\chi_1 H_1 - \phi_1)\partial F/\partial\xi}\bigg|_{\xi = \xi_n}, \quad 0 \le y \le H_1, \quad (9)$$

$$\mathrm{Res}_{P_2} = -\frac{\tilde{A}_0}{\chi_1}\frac{\cos(\chi_1 y_0 - \phi_1)\cos[\chi_2(H - y) - \varphi_2]}{\partial F/\partial\xi}\bigg|_{\xi = \xi_n}, \quad H_1 \le y \le H. \quad (10)$$

If the source is located in the upper part of the channel, $H_1 \le y_0 \le H$, the solution is obtained in the same way, and the residues at the poles are expressed as

$$\mathrm{Res}_{P_1} = -\frac{\tilde{A}_0 Z}{\chi_2}\frac{\cos[\chi_2(H-y_0)-\varphi_2]\cos(\chi_1 y-\phi_1)}{\partial F/\partial\xi}\bigg|_{\xi=\xi_n}, \quad 0 \le y \le H_1, \tag{11}$$

$$\mathrm{Res}_{P_2} = -\frac{\tilde{A}_0 Z}{\chi_2}\frac{\cos(\chi_2(H-y_0)-\varphi_2)\cos(\chi_2(H-y)-\varphi_2)\cos(\chi_1 H_1-\phi_1)}{\cos(\chi_2 H_2-\varphi_2)\partial F/\partial\xi}\bigg|_{\xi=\xi_n}, \quad H_1 \le y \le H. \tag{12}$$

It should be noted that Eqs. (10) and (11) exhibit a certain kind of reciprocity; namely, to obtain Eq. (11) from Eq. (10), one should interchange the positions of y and y_0 and multiply the result by $\rho_1 S_1/\rho_2 S_2$.

The success in calculating the field of the source by means of the theory of residues largely depends on how quickly and accurately one obtains the roots of the dispersion equation determined by Eq. (8): $F(\xi; \beta_1, \beta_2, M_1, M_2, \omega) = 0$. If, in the latter equation, we set $\xi = \xi(\beta_j)$ or $\xi = \xi(M_j)$ or $\xi = \xi(\omega)$ and consider all other variables as external parameters, this equation will have singular points at certain values of β_j or M_j or ω, respectively. At these points, which actually are second-order branching points, two roots of the equation merge. For example, for $\xi = \xi(\beta_j)$, the behavior of the roots near a given point $\xi = \xi_0(\beta_j^0)$ is determined by the relationship

$$dF = 0 = \frac{\partial F}{\partial \xi_0}(\xi-\xi_0) + \frac{1}{2}\frac{\partial^2 F}{\partial \xi_0^2}(\xi-\xi_0)^2 + \frac{\partial F}{\partial \beta_j^0}(\beta_j-\beta_j^0).$$

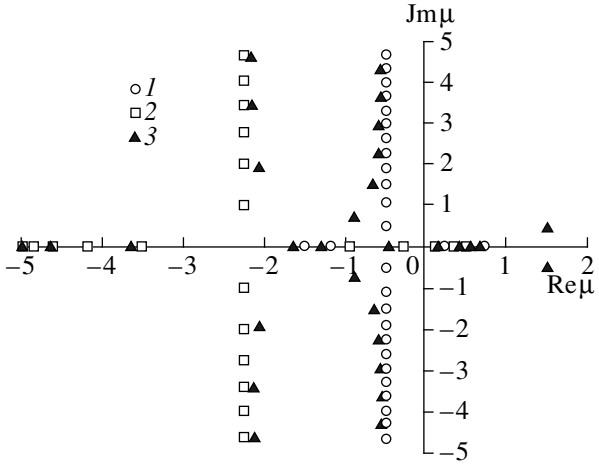

Fig. 1. Positions of the poles in the complex plane for three variants of the flow velocities in the channel: *1*—a uniform flow with $M = 0.4$; *2*—a uniform flow with $M = 0.8$; and *3*—a two-layer flow with $M_1 = 0.8$ and $M_2 = 0.4$.

When $\partial F/\partial\xi_0 \ne 0$, we have $\xi - \xi_0 = -\left(\frac{\partial F}{\partial \beta_j^0}(\beta_j - \beta_j^0)\right)/\frac{\partial F}{\partial \xi_0}$, and (β_j^0) is a regular point. When $\partial F/\partial\xi_0 = 0$, we have $\xi - \xi_0 = \pm\sqrt{-2\frac{\partial F}{\partial \beta_j^0}(\beta_j - \beta_j^0)/\frac{\partial^2 F}{\partial \xi_0^2}}$ and (β_j^0) is a second-order branching point. Similar relationships can be written for $\xi = \xi(M_j)$ and $\xi = \xi(\omega)$. Below, we will show that singular points in M_1 also exist, which leads to the appearance of unstable solutions at supersonic flow velocities.

In the following, for simplicity we will assume that $\rho_1 = \rho_2$ and $c_1 = c_2$; i.e., the layers differ in only the flow velocity. We will consider different combinations of the flow velocities in the layers. For definiteness, we assume that $M_2 < M_1$.

SUBSONIC FLOWS IN THE UPPER AND LOWER LAYERS

In the specific calculation of the field in the channel with the use of the theory of residues, a question arises of how to select an appropriate path of integration along the real axis in the complex plane ξ so that the poles lying above the path correspond to the field in the channel region $x - x_0 > 0$ and the poles lying below the path correspond to the field in the region $x - x_0 < 0$. For a channel with rigid walls, the dispersion equation can be represented as follows:

$$\chi_1 \sin(\chi_1 H_1)\cos(\chi_2 H_2)/S_1 + \chi_2 \cos(\chi_1 H_1)\sin(\chi_2 H_2)/S_2 = 0. \tag{13}$$

Figure 1 shows the positions of the dispersion equation determined by Eq. (8), $\mu = \xi/k$, for three types of the flow: a flow that is uniform within the entire channel cross-section with the velocity corresponding to $M = 0.4$, a similar flow with the velocity corresponding to $M = 0.8$, and a two-layer flow with the aforementioned values of the flow velocity in the upper and lower layers, respectively. In the calculations, we used the parameters $H = 0.36$ m, $H_1 = H_2 = H/2$, and the wave parameter $kH = 10.639$. When the flow is uniform throughout the channel cross-section, the roots of the

dispersion equation lie on the real axis within the range $-k/(1 - M_{1,2}) < \xi < k/(1 + M_{1,2})$ and on the line that is parallel to the imaginary axis and intersects the real axis at the point $\xi_{1,2} = -M_{1,2}k/(1 - M_{1,2}^2)$ (the subscript indicates the flow velocity). The roots of the first kind correspond to the homogeneous modes, and the roots of the second kind correspond to the inhomogeneous modes. In the case of a two-layer flow, the roots lie on the real axis within the range $-k/(1 - M_1) < \xi < k/(1 + M_2)$ and in the complex plane in the region between the straight lines parallel to the imaginary axis and intersecting the real axis at the points $\xi_{1,2}$. The roots of the latter type asymptotically approach the aforementioned straight lines. In addition, in the case of a two-layer flow, we obtain two complex roots: $\mu_0 = 1.5112 \pm i0.4847$. It can be shown that one of them corresponds to the K–H hydrodynamic instability. To prove this statement, we divide the equation $F(\xi) = 0$ by the quantity $\cos(\chi_1 H_1 - \phi_2)\cos(\chi_2 H_2 - \varphi_2)$. As a result, we obtain

$$F_1(\xi) = \tan(\chi_1 H_1 - \phi_2) + Z\tan(\chi_2 H_2 - \varphi_2) = 0. \quad (14)$$

We assume that, in this equation, the quantities $\chi_j H_j$ ($j = 1, 2$) are fairly large, which may occur because of the large values of either H, or χ, or both of them. Then, we obtain $\tan(\chi_j H_j) \longrightarrow -i$. Substituting this value in Eq. (14) and using the well-known trigonometric formulas, we derive

$$Z = -(G_1 + G_2 + i(G_1G_2 - 1))/(G_1 + G_2 + i(G_1G_2 - 1)) \equiv -1 \quad (15)$$

or, in an explicit form, we obtain $1 + (\chi_2\rho_1(1 - V_1\xi/\omega)^2)/(\chi_1\rho_2(1 - V_2\xi/\omega)^2) = 0$. With the search for a hydrodynamic solution in mind, we set $c \longrightarrow \infty$. This yields $\xi/\omega = (1 \mp iq)/(V_1 \mp iqV_2)$, where $q = \sqrt{\rho_2/\rho_1}$. Setting $q = 1$, $\mu = \xi/k$, $\omega = kc$, and $V = Mc$, we obtain

$$\mu = (M_1 + M_2 \mp i(M_1 - M_2))/(M_1^2 + M_2^2). \quad (16)$$

For $M_1 = 0.8$ and $M_2 = 0.4$, the calculation by Eq. (16) yields $\mu = 1.5 \pm 0.5$, which is fairly close to the exact value. In the case $M_2 = 0$, from Eq. (16) we obtain the well-known relation between ξ and ω [7]. It should be noted that the condition obtained in [15] for the formation of pseudosound solutions in a channel with a uniform subsonic flow corresponds to the condition that the numerator (as well as the denominator) in Eq. (15) be equal to zero.

For $H_1, H_2 \longrightarrow \infty$ and $M_2 = 0$, the analytical solutions to the dispersion equation in the form of Eq. (13) were first obtained by L.D. Landau in 1944. These solutions can be generalized to the case $M_2 \neq 0$ by transforming the corresponding dispersion equation

$$F_1(\xi) = \chi_1/S_1 + \chi_2/S_2 = 0 \quad (17)$$

to the equation of the following type:

$$\frac{(k - M_1\xi)^2 - (k - M_2\xi)^2}{(k - M_1\xi)^2(k - M_2\xi)^2} \times \left(1 - \frac{\xi^2}{(k - M_1\xi)^2} - \frac{\xi^2}{(k - M_2\xi)^2}\right) = 0.$$

The root of the first cofactor $\mu = 2/(M_1 + M_2)$ is always real, and the roots of the second cofactor have the form

$$\mu = \left(\frac{M_1 + M_2}{2} \pm \sqrt{\frac{(M_1 - M_2)^2}{4} + 1 \pm \sqrt{1 + (M_1 - M_2)^2}}\right)^{-1}, \quad (18)$$

where $\mu = \xi/k$. Of these four roots, two roots corresponding to the plus sign should be rejected, because they do not satisfy the initial equation. From Eq. (18), it follows that, when $(M_1 - M_2)^2 < 8$, we have two complex conjugate roots. When $(M_1 - M_2)^2 > 8$, the roots become real. The presence of the real roots suggests the stability of the tangential discontinuity for the Mach numbers $|M_1 - M_2| > 2\sqrt{2}$. However, this conclusion (derived on the basis of solving the dispersion equation with allowance for the compressibility) contradicts the result obtained above without regard for the compressibility (see Eq. (16)) and testifies to the fact that the tangential discontinuity is always unstable. To reveal the origin of this contradiction, solutions (18) were numerically studied as functions of M_1 and M_2. The problem was alleviated owing to the fact that it was unnecessary to seek any new solutions to Eq. (17) by numerical methods, because one can state that any solution to Eq. (17) should be expressed by formula (18). The numerical analysis showed that it is not for all values of M_1 and M_2 that formula (18) yields a correct result, i.e., a result that makes $F_1(\xi)$ equal to zero. Specifically, it was found that the condition of the existence of solutions to Eq. (17) satisfies the inequality $|M_1 - M_2| < 1.7$ when M_1 or M_2 is equal to zero. As M_1 (or M_2) increases, this range narrows and, thus, never exceeds the value $2\sqrt{2}$. Hence, we can conclude that, on the basis of solution (18), it is inappropriate to consider the stability or instability of the tangential discontinuity for $|M_1 - M_2| > 2\sqrt{2}$, because, for the Mach numbers satisfying this condition, Eq. (17) has no solutions. In the allowed region of Mach numbers, two complex conjugate solutions are present, one of which corresponds to the instability of the tangential discontinuity. For a more detailed study of the K–H instability, it is necessary to consider the model with a finite thickness of the mixing layer. In the presence of the bounding walls, the multiple reflections from them result in the formation of dis-

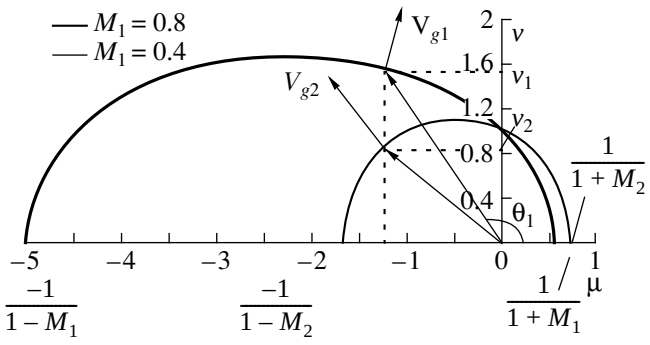

Fig. 2. Graphical representation of Eq. (6) in a two-layer channel with subsonic flows in the layers.

turbances at the discontinuity surface. These disturbances are unstable for any large Mach numbers, although the degree of their instability decreases with an increase in the velocities of the concurrent flows and a decrease in the velocity difference between them.

Important characteristics that allow one to identify the modes in a uniform channel are the energy flux and the group velocity. Although the group velocity is determined for a wave packet, it can be used in application to individual modes, provided that this involves no contradictions with the physical meaning. The energy flux density can be represented in the form [16]

$$\mathbf{W} = (p^2/\rho_0 c)(1 + \mathbf{M}\cdot\mathbf{n})(\mathbf{n} + \mathbf{M}), \quad (19)$$

where $\mathbf{n}$ is the unit vector in the direction of the wave propagation. The relation of the energy flux density to the energy density and the group velocity is determined by the equation $\mathbf{W} = E\mathbf{V}_g$, where

$$E = (p^2/\rho_0 c^2)(1 + (\mathbf{n}\cdot\mathbf{M})), \quad (20)$$

$$\mathbf{V}_g = c(\mathbf{n} + \mathbf{M}). \quad (21)$$

The projections of the group velocity and the energy flux density on the x axis are as follows:

$$V_{gx} = c(M + \mu(1 - M^2))/(1 - \mu M), \quad (22)$$

$$W_x = (p^2/\rho c)(M + \mu(1 - M^2)/(1 - \mu M)^2). \quad (23)$$

For complex values of μ, the expression for the energy density flux can be generalized:

$$W_x = (p^2/\rho c)\mathrm{Re}(M + \mu(1 - M^2))/|(1 - \mu M)|^2. \quad (24)$$

Let us represent each mode that is a solution to the dispersion equation determined by Eq. (8) as a superposition of plane waves propagating in a layered medium. The relationship between the real values of the wave numbers along the channel axis, $\mu = \xi/k$, and along the direction toward the wall, $\nu = \chi/k$, is determined by Eq. (6). Figure 2 shows the graphical representation of this relationship. As μ varies, the ends of the wave vectors describe the respective ellipses. Figure 2 corresponds to the data shown in Fig. 1. Each of the ellipses in Fig. 2 can be considered independently in order to reveal the specific features of a channel with a uniform flow. Specifically, it can be shown that, for a wave with the wave numbers (μ, ν), the group velocity vector is directed along the normal to the ellipse at the corresponding point. This means that the projection of the group velocity vector and the energy flux are positive (i.e., directed along the flow) when $\mu > -M/(1 - M^2)$; otherwise, the projection of the group velocity vector and the energy flux are negative (i.e., directed against the flow). In the case $-M/(1 - M^2) < \mu < 0$, the phase and group velocities are of opposite sign. At the critical frequency determined from the condition $\mu = -M/(1 - M^2)$, the projection of the group velocity on the z axis is zero and the wave propagates normally to the wall with the velocity $V_g = c\sqrt{1 - M^2}$. From Eq. (24), it follows that the energy flux of the inhomogeneous waves is equal to zero. Therefore, in the case of a uniform flow, the path of integration (see Fig. 1) should be selected in such a way that the points lying on the real axis to the right of the point $\mu = -M/(1 - M^2)$ be above the path and the points lying to the left of this point be below the path. In addition, if $(x - x_0) > 0$, the integration path should be closed in the upper half-plane, and, if $(x - x_0) < 0$, it should be closed in the lower half-plane.

From Fig. 2 for a two-layer flow, it follows that, when $-1/(1 - M_1) < \mu < -1/(1 - M_2)$, the wave corresponding to a given mode and incident from medium 1 on medium 2 experiences a total internal reflection, and in medium 2 we obtain a field that is nonuniform along the y axis (a superposition of exponentially decaying and exponentially growing waves). When $-1/(1 - M_2) < \mu < 1/(1 + M_1)$, the wave penetrates into the second medium. In this case, the initial angle of incidence of the wave is determined by the relation $\cos(\theta_1) = -1/(1 + M_1 - M_2)$ (the angles are measured relative to the positive direction of the x axis) and the refracted wave propagates in the direction $\theta_2 = \pi$. At $\mu = 1/(1 + M_1)$, the wave excited in the first medium propagates in the direction $\theta_1 = 0$ and the refracted wave propagates in the direction determined by the relation $\cos(\theta_2) = 1/(1 + M_1 - M_2)$. When $1/(1 + M_1) < \mu < 1/(1 + M_2)$, a nonuniform field consisting of a superposition of waves exponentially decaying and exponentially growing along the y axis is formed in medium 1. In the case $M_1 > M_2$, the angle of incidence is smaller than the angle of refraction, except for the case $\mu = 0$, when the angle of incidence is equal to the angle of refraction.

In a two-layer flow, the identification of modes encounters some difficulties. The energy flux and the group velocity provide no unique result. For example, when $-M_1/(1 - M_1^2) < \mu < -M_2/(1 - M_2^2)$ (Fig. 2), the energy flux corresponding to the given mode is positive in the lower layer and negative in the upper layer. Similarly, the calculation of the energy flux corresponding to the K–H mode shows that the energy flux is positive in both layers, but the group velocity determined as the real part of Eq. (20) can have different signs in different

layers and be positive or negative depending on the sign of the energy density determined by Eq. (20). If the energy density is negative, the group velocity is also negative, and vice versa.

For a unique identification of modes, one should use the Briggs criterion [17], which is equivalent to the causality principle [18]. According to this criterion, it is not necessary to assume that the frequency and, hence, the wave number are real numbers in the dispersion equation. Moreover, if any solution to the dispersion equation corresponds to a wave propagating in the positive direction and having a real wave number, the same solution will also correspond to a wave propagating in the positive direction and having a complex wave number with a positive imaginary part. If we take a wave number with a fairly large positive imaginary part, the solutions to the dispersion equation that lie in the upper half-plane of the complex plane $\xi(\mathrm{Im}\,\xi > 0)$ will correspond to the waves that occur to the right of the source and the solutions lying in the lower half-plane ($\mathrm{Im}\,\xi < 0$) correspond to the waves to the left of the source. Thus, we should select a complex frequency whose real part is equal to the true frequency and the imaginary part is a sufficiently large positive number and, by decreasing the imaginary part down to zero, study the motion of the roots in the complex plane. The roots that intersect the real axis by moving downward correspond to the modes propagating in the positive direction and exponentially growing in this direction. The roots that intersect the real axis while moving upward correspond to the modes growing in the negative direction. As an example, Fig. 3 shows the motion of the roots in the complex plane for Im(kH) decreasing from 4 to zero and Re(kH) = 10.639. According to this figure, some of the roots moving along their trajectories remain in the complex plane, other roots move downward or upward approaching the real axis, and only one root, which corresponds to the K–H instability, intersects the real axis in the downward direction. Hence, in calculating Green's function, the integration path should be selected so as to leave this root on the left while going around the path in the counterclockwise direction. In terms of physics, the appearance of a growing solution is caused by the fact that the mode takes the energy from the two-layer flow, which, in its turn, leads to a spreading of the boundary between the layers and to an increase in the boundary layer thickness.

The question arises as to how strongly the growth rate of the K–H instability waves can be affected by the SAL mounted on the walls of an ejector. From the studies [8–10] of supersonic flows, it was found that the use of SAL leads to a decrease in the rate of growth of the instability waves. However, the effect was obtained for relatively low frequencies and for a flow with a diffuse structure that is observed at a relatively large distance from the inlet. These studies showed that the effect of the SAL on the growth rate of the instability wave is possible only at low frequencies, and this effect

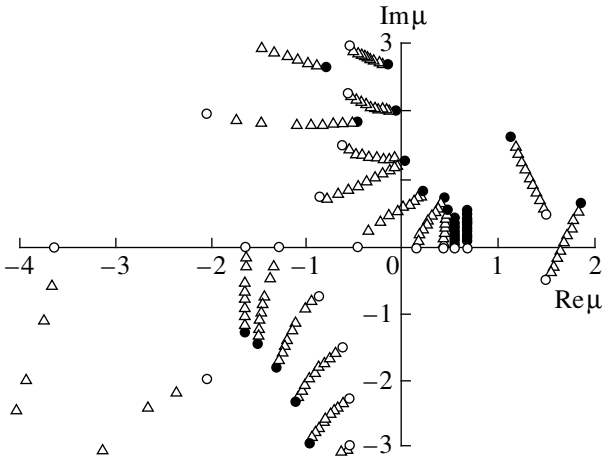

Fig. 3. Motion of the roots in the complex plane when Im(kH) decreases from 4 to 0 for a channel with perfectly rigid walls; Re(kH) = 10.639, $H_1 = H_2 = H/2$, $M_1 = 0.8$, and $M_2 = 0.4$.

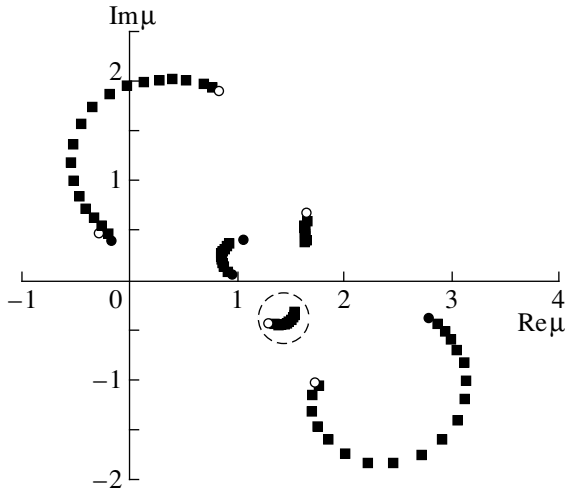

Fig. 4. Motion of the roots of the dispersion equation in the complex plane when the imaginary part of the admittance varies within the interval $-2 \le \mathrm{Im}\beta_{1,2} \le 2$; $\mathrm{Re}\beta_{1,2} = 1$, $H_1 = H_2 = H/2$, $M_1 = 0.8$, $M_2 = 0.4$, and $kH = 0.665$.

depends on the type of the admittance; namely, when the imaginary part of the admittance is negative, the growth rate decreases, and, when the imaginary part of the admittance is positive, the growth rate of the instability wave can even increase. At high frequencies, the effect is practically absent. What is more important, the presence of SAL gives rise to another growing mode (or several modes) and this mode appears at both low and high frequencies independently of the type of the admittance. This phenomenon is illustrated in Fig. 4, which shows the motion of some of the roots of the dispersion equation with the variation of the imaginary part of the admittance at a low frequency for kH = 0.665. The root corresponding to the K–H instability is

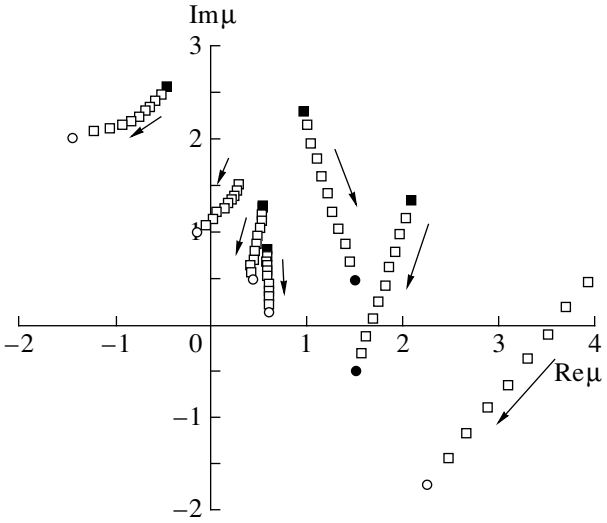

Fig. 5. Motion of the roots in the complex plane when the imaginary part of the wave parameter decreases from 0.2 to zero; Re(kH) = 3.325, $\beta_{1,2} = 1$, $H_1 = H_2 = H/2$, $M_1 = 0.8$, and $M_2 = 0.4$.

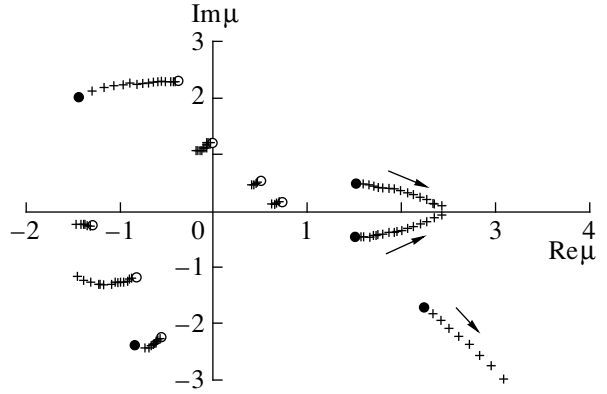

Fig. 6. Motion of the roots of the dispersion equation when the flow velocity in the lower layer decreases from $M_1 = 0.8$ to $M_1 = 0.4$; $M_2 = 0.4$, $kH = 3.325$, and $H_1 = H_2 = H/2$.

enclosed in a dashed circle. In the entire range of variation of the imaginary part of the admittance, the new mode has a greater imaginary part and, hence, a higher growth rate, as compared to the K–H mode. At higher frequencies, no qualitative changes are observed, except for the region of the variation of the K–H roots. With increasing frequency, this region is contracted to a point, which confirms that the K–H instability is independent of the admittance at high frequencies. To show that the new mode is similar in character to the K–H mode and that it satisfies the Briggs criterion, we consider Fig. 5, which represents the motion of the roots in the complex plane with a decrease in the imaginary part of the wave parameter from 0.2 to zero at a constant real part of 3.325 and at $\beta_{1,2} = 1$ at which the imaginary part μ of the new mode is maximal in magnitude. From Fig. 5, it follows that two roots are present and these roots begin their motion from the upper half-plane and intersect the real axis. One of these roots corresponds to the K–H mode, and the other to the new mode. According to the Briggs criterion, they are unstable. It is of interest to consider the motion of the unstable solutions with the decrease in the flow velocity in the lower layer down to the value of the flow velocity of the upper layer. Figure 6 shows the motion of the roots for the selected admittance values $\beta_{1,2} = 1$. When $M_1 \longrightarrow M_2$, the roots corresponding to the K–H instability tend to a real value, which, however, cannot be a root of the dispersion equation in a channel with a uniform flow, because this value, $\mu = 2.42$, exceeds the upper bound of the roots of the dispersion equation, $\mu = 1/(1 + M_2) = 0.71$. The new unstable root tends to infinity. There are reasons to believe that the appearance of the new unstable solutions is related to the singular points of the dispersion equation, if we assume that, in this equation, $\xi = \xi(\beta_1, \beta_2)$. A detailed analysis of these solutions will be the subject of our following study.

A SUBSONIC FLOW IN THE UPPER LAYER AND A SUPERSONIC FLOW IN THE LOWER LAYER

The Difference between the Flow Velocities in the Layers Is Less than Twice the Velocity of Sound

In a channel with rigid walls, the relationship between the values of the wave numbers along the channel axis, $\mu = \xi/k$, and in the direction toward the wall, $\nu = \chi/k$, will be determined according to Eq. (6) by an equation for an ellipse in the upper layer and by an equation for a hyperbola in the lower layer (Fig. 7). From Fig. 7, one can see that real values of the roots can exist in the entire range $-\infty < \mu < \infty$. As in the case of the subsonic flow, using Fig. 7 we can trace the changes in the directions of the wave vectors in the layers and get an idea of the field structure for the whole range of values of μ. The roots corresponding to the K–H instability have their real parts belonging to the interval $1/(1 + M_2) < \mu < 1/(M_1 - 1)$ in which the real roots of the dispersion equation are absent. As in the case of the subsonic flow, the direction of the group velocity is determined by the direction of the normal to the curve at a given point. From Fig. 7, it follows that, in the upper layer, the direction of the group velocity can vary within $0 \le \vartheta_2 \le \pi$ when μ varies within $-1/(1 - M_2) \le \mu \le 1/(M_1 + 1)$. In the lower layer, the direction of the group velocity varies within the Mach cone: $0 \le \vartheta_1 \le \arccos(\sqrt{M_1^2 - 1}/M_1)$. The group velocity is positive in the lower layer for all real values of μ, and, in the upper layer, it is negative for $-1/(1 - M_2) \le \mu \le -M_2/(1 - M_2^2)$. In the case of a uniform channel, this interval of the values of μ corresponds to the acoustic energy transfer against the flow.

From the analysis presented above, it follows that, in choosing the path of integration along the real axis from $-\infty$ to $+\infty$, it is necessary to pass it to the right of the singular points lying on the real axis except for the singular points within the interval $-1/(1 - M_2) \le \mu \le -M_2/(1 - M_2^2)$ and to the left of the latter points. It is also necessary that the integration path passes to the right of the points corresponding to the K–H instability. This conclusion is confirmed by the use of the Briggs criterion.

When the walls have a finite admittance, the roots move to the complex plane. As in the case of a subsonic flow in the upper layer, unstable solutions due to the finite wall admittance appear in addition to the unstable solutions of the K–H type. The degree of instability of these additional modes depends on the admittance and can exceed the degree of the K–H instability. At high frequencies, the K–H instability is also independent of the wall admittance. However, in the presence of a supersonic flow, we obtain other unstable solutions related to the presence of this flow. In the case of a finite admittance with $\mathrm{Re}\beta > 0$, when $\mathrm{Re}\mu > 1/(M - 1)$, which corresponds to the right branch of the hyperbola (see Fig. 7), the roots of the dispersion equation move downward from the real axis and, thus, become unstable.

The Difference between the Flow Velocities in the Layers Is Greater than or Equal to Twice the Velocity of Sound

In a channel with perfectly rigid walls, an increase in M_1 will lead to the leftward motion of both branches of the hyperbola (Fig. 7). When $M_1 - M_2 > 2$, the right branch of the hyperbola intersects the ellipse. It is evident that, at the point of intersection, we have $\chi_1 = \chi_2$, which yields $\mu_0 = 2/(M_1 + M_2)$. In this case, in the interval $\mu_0 < \mu < 1/(1 + M_2)$, an anomalous phenomenon is observed: in passing from the lower layer to the upper one, the wave vector deviates toward smaller rather than larger angles. One can easily see that, when $M_1 = M_1^{(0)} = M_2 + 2\mu_0$ is a root of the dispersion equation. Moreover, we can show that this point is a second-order root with respect to the velocity M_1; i.e., $(\mu - \mu_0)^2 \approx M_1 - M_1^{(0)}$, or $M_1^{(0)}$ is a second-order branching point. This means that, in passing through this point, the corresponding two roots merge on the real axis into a double root and then diverge moving at an angle of 180° to the upper and lower half-planes. Thus, the new class of unstable solutions, which were studied in [6], can be considered as a result of the branching of roots at the singular points of the dispersion equation, if we assume that, in this equation, $\xi = \xi(M_1)$. Figure 8 illustrates the formation of unstable solutions as a result of the branching of the roots of the dispersion equation for M_1 varying from 1.4 to 3.15, M_2 being constant and equal to 0.4 and $H = 10.639$. For comparison, the same figure

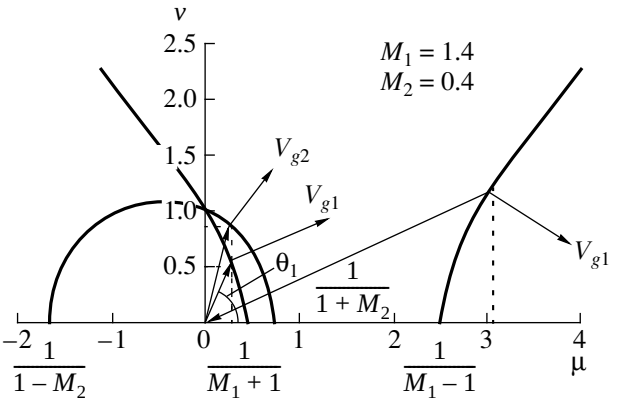

Fig. 7. Graphical representation of Eq. (6) in a two-layer channel with a subsonic flow in the upper layer and a supersonic flow in the lower layer.

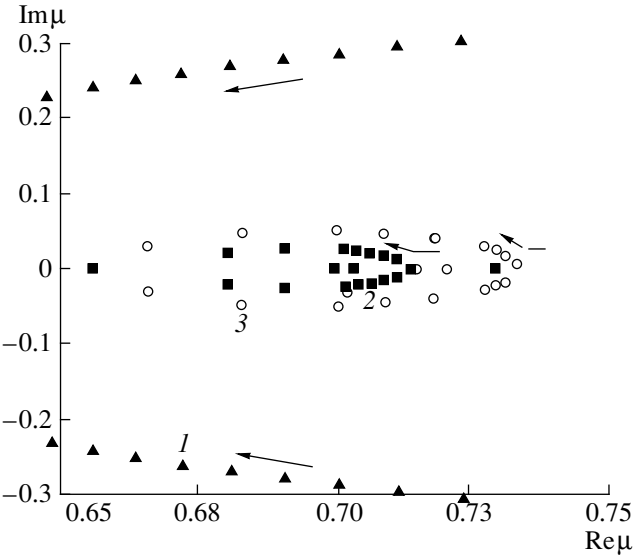

Fig. 8. Motion of the roots corresponding to the unstable solutions to the dispersion equation in the complex plane: *1*—the K–H instability and *2*, *3*—the instabilities of the new type.

presents the solutions corresponding to the K–H instability. In the whole range of values of M_1 specified above, the K–H instability exceeds the instability of the new type, although the degree of the K–H instability decreases according to Eq. (16). The new type of instability appears at $M_1 = 2.4$. With a further increase in M_1, this instability reaches some maximal value. At $M_1 = 2.65$, the two complex roots return to the real axis and then diverge by moving on different sides of the real axis. Within the interval $2.65 < M_1 < 2.70$, the instability of the new type is absent. As M_1 increases further, the roots come closer to each other and the instability of the new type again comes into play. It should be noted that the coalescence and the bifurcation of

modes, which were obtained at a fixed frequency with the variation of the Mach number, can also be obtained by continuously varying the frequency at fixed values of $M_{1,2}$ [6].

SUPERSONIC FLOWS IN THE LOWER AND UPPER LAYERS

In this case, the situation is much the same as that with a subsonic flow in the upper layer. For a channel with perfectly rigid walls, the roots of the dispersion equation lie on the real axis, except for the two roots corresponding to the K–H instability. However, the roots lying on the real axis are spaced at half the intervals corresponding to a subsonic flow in the upper layer. In the case under study, the modes are not separated into homogeneous and inhomogeneous ones, and, in calculating Green's function, it is necessary to take into account the whole infinite set of modes. The path of integration should be selected so as to leave all roots on the left and to close the path in the upper half-plane. This means that the field is concentrated to the right of the source and is absent to the left of it. The relationship between the real values of the wave numbers along the channel axis and in the direction toward the wall is determined by the equations describing the hyperbolas. The left branches of the hyperbolas correspond to the wave numbers oriented in both positive and negative directions, depending on the value of the root of the dispersion equation; the right branches of the hyperbolas correspond to the negative direction of the wave vectors and, hence, of the phase velocities. Otherwise, the case under study is similar to the case of a subsonic flow in the upper layer, which was described above. As in the latter case, the direction of the group velocity coincides with the normals to the hyperbola branches. The maximal angle of the deviation of the hyperbola normal from the μ axis is determined by the formula $\cot(\vartheta) = \sqrt{M^2 - 1}$ or $\sin(\vartheta) = 1/M$. Thus, we have a set of modes propagating in the positive direction within the Mach angle with the group velocities determined by Eq. (21): $V_{g1,2} = c\sqrt{M_{1,2}^2 + (1 + \mu M_{1,2})/(1 - \mu M_{1,2})}$. As in the case with a subsonic flow, the admittance of the channel walls weakly affects the K–H instability at low frequencies and does not affect it at high frequencies. For complex values of the admittance with $\mathrm{Re}\beta > 0$, all roots of the dispersion equation that correspond to the right branches of the hyperbolas are shifted to the lower half-plane, and this shift is greater than in the case with a subsonic flow. In terms of the Briggs criterion, these roots correspond to unstable solutions and the integration path should lie to the right of them.

As in the case with a subsonic flow in the upper layer, when $M_1 - M_2 > 2$, unstable solutions related to the singular points of the dispersion equation are present, if we assume that, in the dispersion equation, $\xi = \xi(M_1)$.

Thus, we have studied unstable disturbances in a wide range of Mach numbers, from subsonic to supersonic ones, in a lined channel with a two-layer flow in it.

It is established that the effect of the admittance of the channel walls on the growth rate of the K–H instability waves decreases with increasing frequency and depends on the type of the admittance.

It is shown that, in the presence of the admittance, new unstable disturbances are formed, and the growth rate of these disturbances can exceed the growth rate of the K–H instability wave. There are reasons to believe that the appearance of such growing solutions is related to the singular points of the dispersion equation, provided that, in this equation, $\xi = \xi(\beta_1)$ or $\xi = \xi(\beta_2)$.

It is shown that the appearance of growing solutions in a channel with rigid walls in the case $M_1 - M_2 > 2$ is related to the presence of the singular points of the dispersion equation, if one assumes that, in the latter, $\xi = \xi(M_1)$.

On the whole, the studies described above show that the use of SAL for reducing the growth rate of the unstable waves is ineffective, because the character of the waves remains the same, i.e., unstable. A better method of reducing the growth rate of unstable waves should be the intensification of the intermixing of the flows at the ejector inlet, which provides the most rapid equalization of the flow velocities in the layered medium. This can be achieved by using corrugated nozzles, special windows, etc. Although their application leads to an increase in the high-frequency noise, the latter can be suppressed by using an SAL, which is much more efficient in this spectral region.

REFERENCES

1. W. K. Lord, C. W. Jones, V. L. Head, and E. A. Krejsa, AIAA Pap., No. 95-1909 (1995).
2. T. G. Tillman, R. W. Paterson, and W. M. Presz, J. Propul. Power **8**, 513 (1992).
3. Y. J. Nakamura and T. Oishi, AIAA Pap., No. 99-1928, 1 (1999).
4. Y. Nakamura, T. Oishi, J. Julliard, and A. Dravet, AIAA Pap., No. 98-2325, 1 (1998).
5. T. Z. Dong and R. R. Mankbadi, AIAA Pap., No. 96-1731, 1 (1996).
6. C. K. W. Tam and F. Q. Hu, J. Fluid Mech. **203**, 51 (1989).
7. L. D. Landau and E. M. Lifshitz, *Course of Theoretical Physics*, Vol. 6: *Fluid Dynamics* (Nauka, Moscow, 1988; Pergamon, New York, 1987).
8. F. Q. Hu, AIAA Pap., No. 93-4350, 1 (1993).
9. M. D. Dahl, AIAA Pap., No. 97-1600, 127 (1997).
10. M. Zhuang, AIAA Pap., No. 99-1848, 1 (1999).

11. V. M. Kousnetsov, A. F. Sobolev, and E. G. Maslova, AIAA Pap., No. 98-2324, 1 (1998).
12. L. M. Lyamshev, Akust. Zh. **28**, 367 (1982) [Sov. Phys. Acoust. **28**, 217 (1982)].
13. M. A. Mironov, Akust. Zh. **21**, 79 (1975) [Sov. Phys. Acoust. **21**, 48 (1975)].
14. A. F. Sobolev, Akust. Zh. **40**, 837 (1994) [Acoust. Phys. **40**, 742 (1994)].
15. A. F. Sobolev, Akust. Zh. **45**, 404 (1999) [Acoust. Phys. **45**, 357 (1999)].
16. M. E. Goldsteĭn, *Aeroacoustics* (Sci. Tech. Information Office, Washington, 1974; Mashinostroenie, Moscow, 1981).
17. R. J. Briggs, *Electron-Stream Interaction with Plasmas* (MIT Press, Cambridge, 1964).
18. L. D. Landau and E. M. Lifshitz, *Course of Theoretical Physics*, Vol. 10: *Physical Kinetics* (Nauka, Moscow, 1979).

Translated by E. Golyamina

Acoustical Physics, Vol. 47, No. 2, 2001, pp. 236–238. Translated from Akusticheskiĭ Zhurnal, Vol. 47, No. 2, 2001, pp. 283–285.

SHORT COMMUNICATIONS

On the Fractal Nature of Sea Surface Reverberation

L. M. Lyamshev

Andreev Acoustics Institute, Russian Academy of Sciences, ul. Shvernika 4, Moscow, 117036 Russia

e-mail: bvp@akin.ru

Received September 11, 2000

An empirical frequency-angular dependence characterizing the high-frequency backscattering of sound by a rough sea surface is known. This dependence was obtained by Schulkin and Shaffer on the basis of the analysis and generalization of results of multiple experiments [1].

It has the form

$$N_s = 10\log(fh\sin\Theta)^{0'99} - 45.3. \quad (1)$$

Here, N_s is the so-called strength of sound scattering by the sea surface in decibels, f is the sound frequency, h is the amplitude of sea waves, and Θ is the glancing angle.

Up to now there has been no explanation of the physical mechanisms of the "origin" or nature of this dependence. Meanwhile, the fact that dependence (1) is described by a power law with a fractional (nonintegral) index attracts one's attention. This kind of dependence is typical of the wave scattering by fractal structures and surfaces (see, e.g., [2, 3]). It is known that a power dependence of the intensity of wave scattering on the frequency (the wavelength) and the scattering angle with a fractional power index is characteristic of fractals. It is natural to associate dependence (1) with the fractal characteristics of the sea surface.

Rather convincing evidence of the fact that the sea surface is characterized by fractal properties exists now. For example, Barenblatt and Leĭkin [4] have demonstrated the self-similarity of the high-frequency spectrum of the wind waves on the sea surface and presented a formula describing the frequency spectrum of wind waves. The wind wave spectrum [4] is characterized by a power law with the index ν which can take on fractional or integral values, and, in particular, at $\nu = 5$, it describes the Phillips spectrum [5] and, at $\nu = 4$, the Zakharov–Filonenko spectrum [6]. Barenblatt and Leĭkin [4] focused their attention on the many existing experimental observations which indicate that the index ν for the frequency spectrum of the waves on the sea surface assumes a nonintegral (i.e., fractional) value. In other words, the spectrum of the sea-surface waves is described by a fractal law.

Expressions characterizing the elevations and the frequency spectrum of a rough sea surface in the space $E = 3$ were obtained by West [7] on the basis of the modified Weierstrass–Mandelbrot function, which is frequently used for describing fractal surfaces. It was shown that the sea surface in the presence of strong roughness is fractal within the interval of the scales of surface waves 0.1–100 m. In this case, the fractal dimension of the surface is $D \approx 2.25$. The frequency spectrum of waves is described by an expression that matches with the formulas obtained by Barenblatt and Leĭkin [4], Zakharov and Filonenko [6], Glasman and Weichman [8], and Kitaĭgorodskiĭ [9].

Zaslavskiĭ and Sharkov [10] studied the fractal properties of the zones of breaking waves on the sea surface. The experimental data were obtained by remote optical probing of the sea surface. Large-scale photography of a rough sea surface with foam formations that accompany the breaking surface gravity waves was performed. In other words, the experimental data represented the results of the backscattering of light by the sea surface in the process of wave breaking. It was established that the distribution of the wave breaking zones was fractal and had the fractal dimension $D = 0.5$. As is well known, the dimension $0 < D < 1$ characterizes the Cantor fractal set [11].

A paper was published recently [12] where an attempt to theoretically relate dependence (1) to the fractal properties of the sea surface was made. The sound scattering by a fractal surface in the space $E = 2$ was considered under the condition that the surface was characterized by the generalized Koch fractal curve. This curve is characterized by the following parameters:

$$n = 0, \quad a^{(0)} = \Lambda,$$
$$n = 1, \quad a_1^{(1)} = \frac{\Lambda_0}{4}(1-\alpha)^{1/2}, \quad (2)$$
$$a_2^{(1)} = 2a_1^{(1)} \quad a_3^{(1)} = 2a_1^{(1)}.$$

Here,

$$\alpha = \frac{4A_0}{\Lambda_0}\cot\frac{\Theta}{2}; \quad (3)$$

n is the number of the sequence (step) of the fractal curve formation; Λ_0 is the primer; $a_1^{(1)}$, $a_2^{(1)}$, and $a_3^{(1)}$ are the elements constituting the leader of the Koch curve; A_0 is the amplitude; and Θ is the angle between the neighboring elements of the fractal set (the Koch

1063-7710/01/4702-0236$21.00

curve). The Hausdorff measure for the indicated generalized fractal curve is expressed by the formula

$$(2^{1-D} + 1)(a_2^{(1)})^D = 1, \quad (4)$$

where D is the fractal dimension and $1 < D < 2$. The calculation of the sound scattering was conducted in the Kirchhoff approximation when the condition $\lambda \ll \Lambda_0$, A_0, where λ is the sound wavelength, is satisfied. Essentially, the calculation of the sound scattering by the surface approximated by the Koch prefractal was conducted in the Kirchhoff approximation. The calculation of the scattered field was conducted using the procedure proposed by Freedman [13] in order to exclude the specific properties of the prefractal from consideration. The expression for the strength of the sound backscattering by a fractal rough surface (the Koch prefractal), which was obtained by Qian [12], has the form

$$N_s = N_0 + 10\log\left[fh\tan\left(\frac{\Theta}{2}\right)\sin\Theta\right]^{2D}, \quad (5)$$

where f is the frequency, h is the average height of roughness, and Θ is the glancing angle. Expression (5) almost coincides with Eq. (1), if we assume that the conditions $\Theta \approx \pi/2$ and $D \approx 0.5$ are satisfied.

The dimension D of the Koch prefractal obeys the condition $1 < D < 2$. According to Qian [12], the necessity to satisfy the condition $D \cong 0.5$ in Eq. (5) can be explained by the fact that, in the case of the backscattering of sound, a quasi-degeneration of the continuous Koch fractal curve into the Cantor set occurs. Such an explanation can seem quite reasonable in the light of the above-mentioned results of the optical experiments [10].

Comparing Eqs. (1) and (5), one can arrive at a conclusion that the conditions with the sound backscattering occurring by individual troughs of the sea surface waves corresponded to the results of the acoustical experiments generalized by Schulkin and Shaffer [1]. However, the state of the sea surface in this case was such that, even in the presence of breaking waves, which were observed in the optical experiments by Zaslavskiĭ and Sharkov [10], no effective formation of a subsurface layer of air bubbles takes place. Otherwise, when a layer of air bubbles is formed under the sea surface, the dependence described by Eq. (1) is violated. However, as Gilbert demonstrated [14], in this case the sound backscattering by the sea surface also obeys the fractal laws. The sound scattering is caused in this case not by the sea surface itself, but by the layer of air bubbles. As it turned out, the spectrum of the sound velocity fluctuations in the subsurface bubble layer obeys the Kolmogorov–Obukhov law, which (as is well known now) reflects the fractal structure of turbulence. The calculations of the strength of the sound backscattering made by Gilbert [14] agree with the experimental data even for rather low frequencies (from 0.1 kHz) and for a wide range of glancing angles.

Schulkin and Shaffer [1] have noted that earlier many researchers obtained power laws for the variations of the intensity of the sound backscattering by the sea surface. As above (see Eq. (1)), the experimental dependences obtained by them can be represented in the form

$$N_s = 10\log(fh\sin\Theta/K_i)^{\nu_i}, \quad (6)$$

where $K_1 = 3.28 \times 10^2$ and $\nu_1 = 2.03$ [15]; $K_2 = 5.57 \times 10^3$ and $\nu_2 = 1.52$ [16]; $K_3 = 1.81 \times 10^3$ and $\nu_3 = 1.43$ [17]; and $K_4 = 6.88 \times 10^3$ and $\nu_4 = 1.03$ [18]. Correspondingly, $K = 3.649 \times 10^4$ and $\nu = 0.99$ for dependence (1) by Schulkin and Shaffer [1].

One could treat the dependences given by Eq. (6) as single and, in a certain sense, incidental facts. Apparently, Schulkin and Shaffer [1] treated them in just this way, and, generalizing, they obtained the average dependence given by Eq. (1).

In our opinion, in reality these results are quite natural when taken separately. Each time, they reflect the experimental conditions or, in other words, the state of the sea surface and its fractal properties, while the value of the power index reflects the fractal dimension. This conclusion agrees well with the idea of Shaefer and Keefer [2] that the approximation of the experimental spectrum of the sea surface waves obeys a power (fractal) law

$$F = A\omega^{-n}, \quad (7)$$

where ω is the frequency of waves and A is a constant.

The analysis of a large number of experimental spectra of fully developed waves [19] (see [1]) demonstrated that, for the frequency interval $\omega = 1.5$–$3.8\ s^{-1}$, the values of n lie within the interval $n = 2.5$–4.3.

The fact that the fractal properties of waves at the sea surface can be characterized by different values of the fractal dimension depending on the external conditions is confirmed, for example, by the results of optical experiments [20] and by their comparison with the results of the experiments by Zaslavskiĭ and Sharkov [10]. Zosimov and Naugolnykh [20] presented the results of an experimental study of the statistical characteristics of wind waves at the ocean surface. The studies were conducted by scanning over the surface by a laser beam. It turned out that the set of specular points at the rough ocean surface was the Cantor set with the fractal dimension $0 < D = 0.8 < 1$. Recall that the optical experiments by Zaslavskiĭ and Sharkov [10] provided the fractal dimension $D = 0.5$. The results of the experiments by Zaslavskiĭ and Sharkov [10] and Zosimov and Naugolnykh [20] not only agree but also indicate the variety of the fractal properties of the rough sea surface.

Finally, it is necessary to note that, as was expected, in the case of small-amplitude waves at the surface or relatively large wavelengths of sound, Rayleigh scattering is observed and the power index in the power law

governing the sound intensity variation with frequency is $\nu = 4$. The sea surface behaves as a Euclidean surface, and, even if it is fractal and not Euclidean, its fractal properties may not manifest themselves in the low-frequency sound scattering.

Thus we can state that the high-frequency surface reverberation observed in the sea in a wide range of variation of sea waves is characterized by fractal properties or has a fractal nature. The frequency dependence of the reverberation intensity obeys a power law with the fractional value of the power index. The value of the index contains information on the fractal properties of the sea surface and on its fractal dimension and can serve for characterizing the wind waves.

ACKNOWLEDGMENTS

This work was supported by the Russian Foundation for Basic Research, project no. 99-02-16334.

REFERENCES

1. M. Schulkin and M. Shaffer, J. Acoust. Soc. Am. **36**, 1699 (1964).
2. D. Shefer and K. Kefer, in *Fractals in Physics*, Ed. by L. Pietronero and E. Tosatti (North-Holland, Amsterdam, 1986; Mir, Moscow, 1988), pp. 62–71.
3. H. D. Bale and P. W. Schmidt, Phys. Rev. Lett. **53**, 596 (1984).
4. G. I. Barenblatt and V. A. Leĭkin, Izv. Akad. Nauk SSSR, Fiz. Atmos. Okeana **17**, 50 (1981).
5. O. M. Phillips, *Dynamics of the Upper Ocean* (Cambridge Univ. Press, Cambridge, 1966; Mir, Moscow, 1969).
6. V. E. Zakharov and N. N. Filonenko, Dokl. Akad. Nauk SSSR **170**, 1292 (1966) [Sov. Phys. Dokl. **11**, 881 (1966)].
7. B. J. West, J. Opt. Soc. Am. A **7**, 1074 (1990).
8. R. E. Glasman and P. B. Weichman, J. Geophys. Res. **94**, 4998 (1989).
9. S. Kitaĭgorodskiĭ, J. Phys. Oceanogr. **13**, 816 (1983).
10. G. M. Zaslavskiĭ and E. A. Sharkov, Dokl. Akad. Nauk SSSR **294**, 1362 (1987) [Sov. Phys. Dokl. **32** (6), 499 (1987)].
11. J. Feder, *Fractals* (Plenum, New York, 1988; Mir, Moscow, 1991).
12. Z. W. Qian, J. Acoust. Soc. Am. **107**, 260 (2000).
13. A. Freedman, Acustica **12** (1), 10 (1962).
14. K. E. Gilbert, J. Acoust. Soc. Am. **94**, 3325 (1993).
15. *Principles of Underwater Sound*, Watl. Defence Res. Council Div. 6, Sum. Tech. Rept. (Washington, DC, 1946), Vol. 7, Chap. 5, pp. 99–109.
16. R. J. Urick and R. M. Hoover, J. Acoust. Soc. Am. **28**, 1038 (1956).
17. G. R. Garisson, S. R. Murphy, and D. S. Potter, J. Acoust. Soc. Am. **32**, 104 (1960).
18. R. P. Chapman and R. P. Harris, J. Acoust. Soc. Am. **38**, 1592 (1962).
19. P. L. Grose, K. L. Warsh, and M. Garstang, J. Geophys. Res. **77** (21), 3902 (1972).
20. V. V. Zosimov and K. A. Naugolnykh, Chaos **4**, 21 (1994).

Translated by M. L. Lyamshev

Acoustical Physics, Vol. 47, No. 2, 2001, pp. 239–240. Translated from Akusticheskiĭ Zhurnal, Vol. 47, No. 2, 2001, pp. 286–287.

CHRONICLE

Oleg Pavlovich Galkin (On His 70th Birthday)

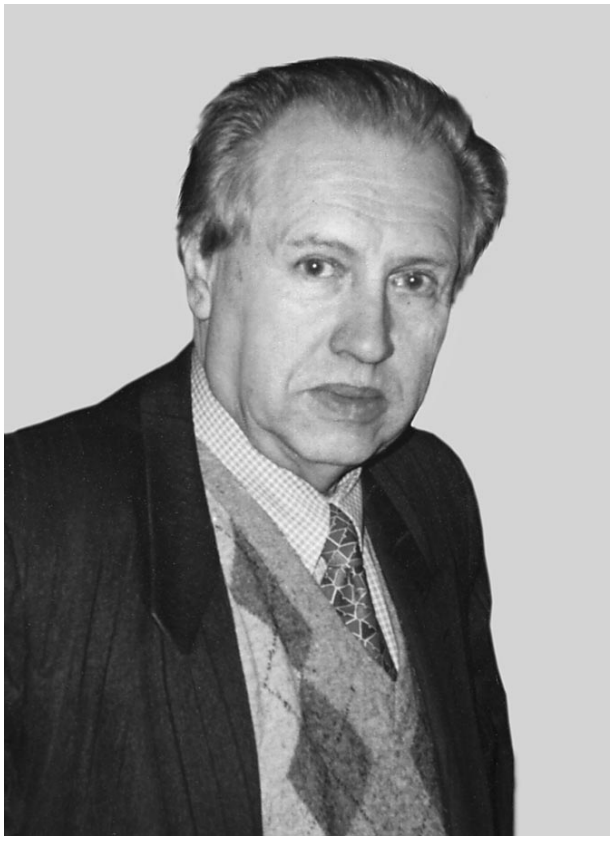

On September 6, 2000, Oleg Pavlovich Galkin—a well-known specialist in ocean acoustics and underwater acoustic engineering and one of the leading scientists of the Andreev Acoustics Institute—turned seventy.

In 1953, Galkin graduated from the Physics Department of Moscow State University and started working at the Acoustics Institute of the Academy of Sciences of the USSR. His whole scientific career has been related to the Acoustics Institute where he was promoted from the position of radio engineer to head of a research department.

The scope of Galkin's scientific interests covers a wide range of problems of underwater acoustics. Long-term studies of sound fields in the ocean are related to his name, including the fundamental works on the horizontal refraction of sound, the form of the phase front of sound waves in an oceanic waveguide, the frequency dependence of the positions of convergence zones, etc. Galkin supervised the design and manufacture of unique research systems for the ships of the Acoustics Institute. He is responsible for a number of developments without which up-to-date underwater acoustic experiments would be difficult to perform. He proposed a method for precise measurement of the distance between submerged transmitting and receiving systems in the open ocean, a method for exploding charges at a strictly predetermined depth from on board a drifting ship, and a method for determining the coordinates of a sound source from the structure of the sound field received at relatively long distances.

Galkin supervised many oceanic experiments which were carried out with the help of research vessels in various regions of the ocean. The geography of the expeditions where Galkin performed his experiments includes the coastal regions of the Black Sea, the Kola Peninsula, and Kamchatka; he also took part in a polar expedition on a floating research station.

Galkin pays much attention to the practical applications of scientific results. He supervised important research and development works aimed at designing underwater acoustic weapons for the navy, including the development of the first Soviet underwater acoustic systems for long-range operation.

The results of the studies carried out by Galkin are presented in his ~200 publications including papers in leading Russian journals and collections of papers and in reports. Galkin is the author of many inventions. The most important results obtained by Galkin were presented at international, all-Union, and all-Russian conferences and meetings.

Several candidate dissertations in physics and mathematics were prepared and defended under Galkin's supervision. He was the editor of many issues of the Proceedings of the Acoustics Institute.

Galkin's characteristic features are a thorough approach to the analysis of scientific results, the desire to consider in close detail all problems arising in his work, and high standards for the reliability of his conclusions and recommendations.

In communicating with his colleagues, as well as in solving various difficult problems, Galkin is always guided by high moral principles.

In 1967, Galkin defended his candidate dissertation in physics and mathematics. In 1970, he received the title of senior researcher. Since 1972, he has been a member of the Scientific Council of the Acoustics Institute.

1063-7710/01/4702-0239$21.00 © 2001 MAIK "Nauka/Interperiodica"

Galkin combines research with tutorial activity. He delivers lectures to the students of the Moscow State Institute (Technical university) of Radio Engineering, Electronics and Automation.

Galkin's views on the problems of the formation of sound fields in the ocean, as well as on other problems of underwater acoustics, are highly respected by specialists from many institutions involved in the development of underwater acoustic equipment. His collaboration with these organizations substantially contributed to the development of Russian underwater acoustics. Galkin's activity in science and engineering was praised by the government: he was awarded two orders of merit and four medals.

Celebrating his 70th birthday, Oleg Pavlovich Galkin is full of energy and creative ideas. We wish him health and more success in science and in his other areas of interest.

Translated by E. Golyamina

Acoustical Physics, Vol. 47, No. 2, 2001, p. 241. Translated from Akusticheskiĭ Zhurnal, Vol. 47, No. 2, 2001, p. 288.

INFORMATION

International Editorial Forum

The 2000 International Editorial Forum was held in New York on October 4 and 5, 2000. It was a meeting of Editors-in-Chief of physical science journals of the Russian Academy of Sciences with the managers of the American Institute of Physics (AIP) and the International Publishing Company "Nauka/Interperiodica" (MAIK "Nauka/Interperiodica"). The forum was organized by the AIP and MAIK "Nauka/Interperiodica." It was a regular event in a series of meetings that have been held over the last ten years.

Now the English language versions of almost all physics journals of the Russian Academy of Sciences such as *Acoustical Physics, Astronomy Reports, Journal of Experimental and Theoretical Physics, Technical Physics, Physics of Atomic Nuclei* and many others are published by MAIK "Nauka/Interperiodica" and distributed worldwide (including electronic versions) by the AIP.

The forum was opened with addresses by Academician R. Petrov, Vice-President of the Russian Academy of Sciences; M. Brodsky, Executive Director of the AIP; and N. Avanesov, First Deputy Director General of MAIK "Nauka/Interperiodica." The significant progress in the joint activities of the AIP and MAIK "Nauka/Interperiodica" was noted. N. Avanesov and D. Walters (AIP) presented reports on the state of publication and translation of journals. M. Flikop, the manager of the department of translations of the AIP, delivered a detailed report on the translation and publication activities of the AIP. The English language versions of physics journals of the Russian Academy of Sciences are refereed by the research consultants of the AIP, who give their opinions on each issue of each journal characterizing the quality of translation and scientific level of the published articles. The general conclusion was that the level of articles is high and the quality of translation meets the requirements.

A special report was devoted to marketing and the state of subscriptions. The necessity for more active work on expanding subscriptions in countries such as Singapore, Malaysia, the Philippines, Thailand, and Vietnam was noted.

F. Perugini (AIP) made a report on the electronic versions of the AIP journals and their presentation on the Internet. Significant progress in the distribution of electronic versions of papers was noted. Now about six million electronic copies of papers from AIP journals are requested per year! Special attention was given to the AIP initiatives in the development of electronic forms of physics journals published by the AIP and the realization of these initiatives in practice. One of these initiatives is the publication of so-called virtual journals. Another initiative is the organization of references on web sites. The AIP has started the publication of a virtual monthly journal "Biophysics." This journal published monthly in electronic (virtual) form compiles multiple articles in biophysics from various journals of different publishers (not only the AIP) from all over the world. The AIP made special contracts with all these publishers. These contracts secure the copyright. An advantage of this virtual journal lies in the fact that an expert in biophysics does not need to search for necessary articles in various journals. The virtual journal includes the overwhelming majority of papers published in leading journals from many countries over the last month.

It was noted in particular that starting from 2000 almost all English-language versions of physical journals of the Russian Academy of Sciences will be published in electronic form, not only the abstracts of articles as was done before.

The 2000 International Editorial Forum was closed by the final addresses by M. Brodsky, Executive Director of AIP and Academician R. Petrov, Vice-President of the Russian Academy of Sciences. Both speeches stressed the fruitfulness of the joint work done by the AIP and MAIK "Nauka/Interperiodica" and the good prospects of adopted decisions on further joint publishing activities.

The forum sessions were well organized. This provided an opportunity to maintain their tight schedule. The participants could exchange their views in official and unofficial discussions and consider specific plans of joint publishing activities.

L. M. Lyamshev

Translated by M. Lyamshev

1063-7710/01/4702-0241$21.00